

# PE&RS

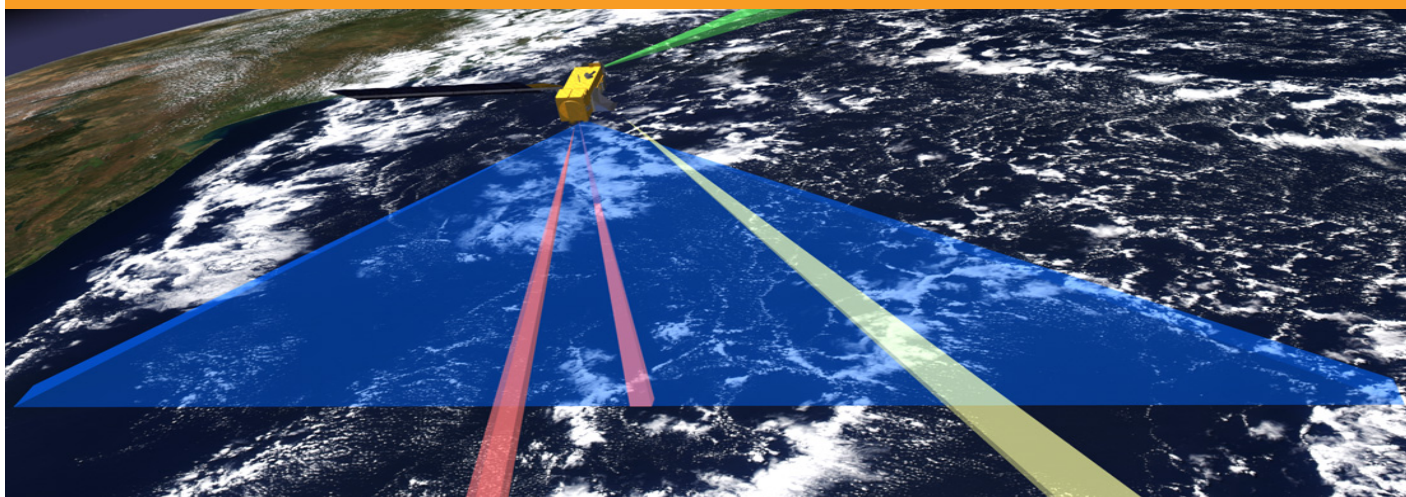
February 2021

Volume 87, Number 2

**PHOTOGRAMMETRIC ENGINEERING & REMOTE SENSING** *The official journal for imaging and geospatial information science and technology*

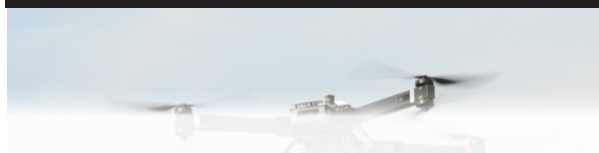


The 4<sup>th</sup> Edition of the *Manual of Remote Sensing*!



# MANUAL OF REMOTE SENSING

## *Fourth Edition*



The *Manual of Remote Sensing, 4th Ed.* (MRS-4) is an “enhanced” electronic publication available online from ASPRS. This edition expands its scope from previous editions, focusing on new and updated material since the turn of the 21st Century. Stanley Morain (Editor-in-Chief), and co-editors Michael Renslow and Amelia Budge have compiled material provided by numerous contributors who are experts in various aspects of remote sensing technologies, data preservation practices, data access mechanisms, data processing and modeling techniques, societal benefits, and legal aspects such as space policies and space law. These topics are organized into nine chapters. MRS4 is unique from previous editions in that it is a “living” document that can be updated easily in years to come as new technologies and practices evolve. It also is designed to include animated illustrations and videos to further enhance the reader’s experience.

MRS-4 is available to ASPRS Members as a member benefit or can be purchased by non-members. To access MRS-4, visit <https://my.asprs.org/mrs4>.



edited by: Stanley A. Morain,  
Michael S. Renslow and Amelia M. Budge



**asprs** THE IMAGING & GEOSPATIAL  
INFORMATION SOCIETY

# ASPRS 2021

## Annual Conference

March 29- April 2, 2021



*The Call for Abstracts is now open through February 15, 2021!*

<http://conferences.asprs.org/asprs-2021/call-for-abstracts/>

## SAVE THE DATE!

Due to the ongoing COVID pandemic, ASPRS is going to be conducting its 2021 Annual Conference virtually. The conference program will consist of:

- » a multi-day series of technical sessions, including oral presentations, Ignite-Style talks, and invited panel discussions
- » 2-hour and 4-hour workshops conducted as live, instructor-led webinars
- » vendor spotlights and product demos\*
- » the ASPRS Annual Business Meeting, which includes the Installation of Officers and Directors, Presidential Address, and presentation of 2021 Awards and Scholarships.
- » annual Division, Council, and Committee meetings
- » The entire conference program will be recorded and made available on-demand for all registrants on the ASPRS online learning platform.

<http://conferences.asprs.org/asprs-2021/>

## ANNOUNCEMENTS

GeoCue Group has partnered with the Geospatial Division of consulting firm, Ayres, in their acquisition of a GeoCue True View 620 3D Imaging System (3DIS®). GeoCue's True View 620 is equipped with RIEGL's miniVUX-2UAV laser scanner integrated with dual photogrammetric cameras. Extreme accuracy is provided by Applanix APX-20 Position and Orientation System. All True View 3D Imaging Systems are bundled with Applanix POSPac, True View EVO post-processing software and True View Reckon data management solution.

The True View 620 system is a compact, survey grade 3D Imaging Sensor designed for small Unmanned Aerial Systems (UAS). The 200 kHz, 5 return RIEGL laser scanner and dual photogrammetric cameras (providing 40 megapixels of imagery) have been carefully configured to provide a fused lidar/imagery field of view of 120°. All components are contained within a rigid machined mount and carefully calibrated to provide true sensor fusion. The system includes full post-processing software that generates a stunning ray-traced 3D colorized point cloud ("3D Image") and geocoded images that can be used in photogrammetric workflows.

The True View product line gives mappers and surveyors the ability to deliver high quality analytic data with exacting accuracies. These deliverables can be generated using workflows and tools within True View EVO. Examples of derived products include classified ground models, profiles, cross sections, digital elevation models, topographic contours, volumetric analysis, classified wires and more.

UAS-based lidar is particularly effective on medium-size projects that span the niche between conventional survey and manned aircraft and provides fast turnaround of highly accurate data with the option of colorized point clouds. An example of the power of UAS lidar is its flexibility in challenging situations, such as topographic mapping for flood mitigation on the west shore of Wisconsin's Green Bay, which has large areas of wetland bog. The legwork involved in covering this area with traditional survey equipment would last over a week, while the necessary UAS lidar flights and ground control could be accomplished in hours.

Here are some of the strategic advantages of the UAS-mounted GeoCue system:

- Fast and flexible mobilization.
- An alternative for survey in locations where terrain is challenging using other methods.
- Solid integration of the lidar sensor, cameras and inertial measurement unit (IMU) ensures a smooth workflow and quality results.
- Less constrained by low clouds than manned aircraft.
- Ability to penetrate heavily forested areas to reach the ground and create an accurate terrain model quickly.
- Targeted management of vegetation along utility corridors rather than costly on-the-ground deployments.

GeoCue's President, Lewis Graham, stated, "Ayres has been a valued partner since the formation of our company. It is an honor that they have selected us to provide their drone survey technology."

Paul Crocker, who manages Ayres' UAS program, said, "We are already seeing the benefits of using the GeoCue True View 620 system integrated tightly with our long-endurance aircraft. Clients are impressed with the high accuracy of the data, and the well-designed sensor package ensures consistency that we can count on. Their customer support has been top notch as we begin to roll out this service to our clients."

## ACCOMPLISHMENTS

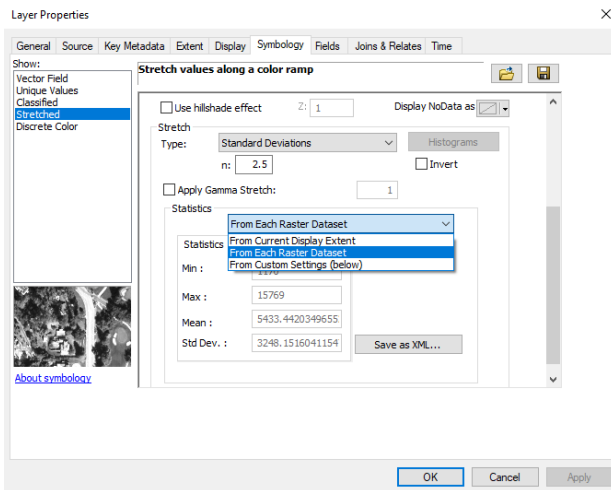
Atlantic is pleased to announce that Mike Dooley has joined our team as a Vice President and he will be based in San Antonio, TX. Dooley, a strategic hire for Atlantic, has spent most of his 34-year geospatial career focusing on the infrastructure and energy markets. Our company recently achieved pre-certification with TXDOT, FDOT, and GDOT to go along with numerous other existing DOT pre-certifications. Dooley's key focus will be expanding and enhancing Atlantic's A/E market offerings for infrastructure and energy clients. His knowledge and expertise in those markets, coupled with Atlantic's significant technology investments, will be invaluable to Atlantic's plans for growth.

"I have followed Mike's career since his early days in the northeastern US and am excited to finally have him on the same team after competing for so long," said Tim Stagg, Atlantic Executive Vice President. "He brings expertise that our team needs to take the next step in our growing infrastructure and energy markets. He will make great contributions to Atlantic and our clients".

"Atlantic is an impressive company with clear vision and passion that is unmatched," said Mike Dooley. "I am excited to work alongside so many top professionals that strive daily to best serve clients throughout the US."

## CALENDAR

- 29 March - 2 April, **ASPRS 2021 Annual Conference**, For more information, visit [www.asprs.org/](http://www.asprs.org/).
- 23-25 April, **GISTAM 2021**, Prague, Czech Republic. For more information, visit [www.gistam.org/](http://www.gistam.org/).
- 7-11 June, **URISA GIS Leadership Academy**, Minneapolis, Minnesota. For more information, visit [www.urisa.org/education-events/urisa-gis-leadership-academy/](http://www.urisa.org/education-events/urisa-gis-leadership-academy/).
- 16-20 August, **URISA GIS Leadership Academy**, Portland, Oregon. For more information, visit <https://www.urisa.org/education-events/urisa-gis-leadership-academy/>.



## 73 GIS Tips & Tricks—Never use the Defaults

## Publishing a Peer-review Article in *PE&RS* is now Easier! 80

### COLUMNS

- 75 Book Review—*GIS for Science: Applying Mapping and Spatial Analytics*
- 77 Grids and Datums Update  
This month we look at The Kingdom of the Netherlands
- 79 Signatures  
The Column of the Student Advisory Council

### ANNOUNCEMENTS

- 74 ASPRS Certifications
- 80 Headquarters News— Publishing a Peer-review Article in *PE&RS* is now Easier!
- 80 New ASPRS Members  
Join us in welcoming our newest members to ASPRS.

### DEPARTMENTS

- 70 Industry News
- 70 Calendar
- 90 Who's Who in ASPRS
- 104 In-Press *PE&RS* Articles
- 124 ASPRS Sustaining Members
- 143 ASPRS Media Kit

### 81 Monitoring the Spatiotemporal Dynamics of Urban Green Space and Its Impacts on Thermal Environment in Shenzhen City from 1978 to 2018 with Remote Sensing Data

*Yue Liu, Hui Li, Peng Gao, and Cheng Zhong*

In a developing city, urban green space (UGS) plays an increasingly significant role in improving the urban environment and beautifying the urban landscape. In the meantime, UGS has been substantially and frequently interfered with by human activities. Taking Shenzhen City (a great metropolis of China) as an example, this article investigated the spatio-temporal dynamics of UGS and its influence on the urban thermal environment with Landsat images.

### 91 A Soil and Impervious Surface Adjusted Index for Urban Impervious Surface Area Mapping

*Yanyi Zhang, Yugang Tian, and Lihao Zhang*

Index-based methods are widely applied to urban impervious surface area (ISA) mapping, but the confusion between ISA and soil remains unsolved. In this article, the near-infrared (NIR)-blue bands were selected as feature space by analyzing the spectra from the US Geological Survey spectral library, and a simple impervious surface ratio index (ISRI) was developed by shifting the NIR-blue coordinate origin toward the convergence point of the fitting lines of ISA and soil. The ISRI was then validated for threshold simulation, separability, and correlation analysis.

### 105 Reclaimed-Airport Surface-Deformation Monitoring by Improved Permanent-Scatterer Interferometric Synthetic-Aperture Radar: A Case Study of Shenzhen Bao'an International Airport, China

*Lu Miao, Kaiqiang Deng, Guangcai Feng, Kaifeng Li, Zhiqiang Xiong, Yuedong Wang, and Shuiyuan He*

Reclaimed airports usually have fragile geological structures and are susceptible to the uneven ground settlements caused by filling-material consolidation, underground construction, and dynamic loading from takeoff and landing of aircrafts. Therefore, deformation monitoring is of great significance to the safe operation of reclaimed airports. This article adopts an improved permanent-scatterer interferometric synthetic-aperture radar strategy to map the spatiotemporal deformation of Shenzhen Bao'an International Airport in China and then provides new ideas for studying deformation in similar fields, and technical references for the future construction of Shenzhen Airport.

### 117 Fully Convolutional Neural Network for Impervious Surface Segmentation in Mixed Urban Environment

*Joseph McGlinchy, Brian Muller, Brian Johnson, Maxwell Joseph, and Jeremy Diaz*

The urgency of creating appropriate, high-resolution data products such as impervious cover information has increased as cities face rapid growth as well as climate change and other environmental challenges. This article explores the use of fully convolutional neural networks (FCNNs)—specifically UNet with a ResNet-152 encoder—in mapping impervious surfaces at the pixel level from WorldView-2 in a mixed urban/residential environment.

### 125 An Improved GPU-Based Parallel Computing Method for Landscape Index Calculation in Urban Area

*Mengjun Kang, Yunlong Ma, Qingyun Du, and Min Weng*

With the development of urbanization in the world, dealing with the problems caused by urban expansion is becoming more and more important. The data that need to be processed in urbanization studies have increased with the improvement of the spatial and temporal resolution of remote sensing satellites, exerting considerable pressure on traditional software used for landscape index computation. In this article, an improved landscape index-computing algorithm is proposed.

### 133 Exploring the Performance of Different Texture Information and Polarization Features from PolSAR Images in Urban Land Cover Classification

*Songjing Guo, Jiahua Teng, and Qimin Cheng*

In this article, the performance of combining polarization features with texture features extracted by four descriptors, respectively, in land cover classification is explored.

**See the Cover Description on Page 72**

# COVER DESCRIPTION

Trees play a vital role in Earth's carbon and water cycles. They also contribute food, firewood, and other resources important to human activity. But while forests are easy to spot from above, smaller stands of trees have often gone undercounted because they have been harder to detect with the satellite imagers usually available to scientists.

Now an international team of scientists has used artificial intelligence and commercial satellites to identify an unexpectedly large number of trees spread across arid and semi-arid areas of western Africa. These drylands were previously classified as having little to no tree cover, but new analysis techniques proved otherwise. The findings could help scientists better understand and quantify the role drylands have in the storage and cycling of carbon.

The research team used the Blue Waters supercomputer at the University of Illinois and an artificial intelligence technique called "deep learning" to map the trees. Led by Martin Brandt of the University of Copenhagen, the team first spent a year examining commercial satellite imagery by eye and identifying 90,000 individual trees in order to build a training dataset for the computer. Ankit Kariryaa of the University of Bremen led the development of the deep learning computer processing.

Once Brandt and colleagues developed and tested their dataset, Blue Waters—one of the fastest supercomputers in the world—took just a few days to identify nearly 2 billion trees across 1.3 million square kilometers (500,000 square miles) of sub-Saharan Africa.

Previous land cover mapping studies of the region relied on satellite imagery with 10– or 30–meter resolution (the distance visible within each pixel). Such studies classified large swaths as grassland or bare soil whenever trees covered less than 20 percent of the land area.

For the new study, Brandt and colleagues used commercial, high-resolution (0.5 meter) imagery from DigitalGlobe satellites, including QuickBird-2, GeoEye-1, WorldView-2, and WorldView-3. Brandt gained access to the images through the Commercial Smallsat Data Acquisition (CSDA) program, which acquires data from commercial sources that can support NASA's Earth science research and application goals.

Brandt's machine-learning method identified 1.8 billion individual trees standing outside of areas classified as forests. It also measured the crown diameter of each tree. Tree cover was, predictably, higher in areas with more rainfall. "The canopy cover increases from 0.1 percent (0.7 trees per hectare) in hyper-arid areas, through 1.6 percent (9.9 trees per hectare) in arid and 5.6 percent (30.1 trees per hectare) in semi-arid zones, to 13.3 percent (47 trees per hectare) in sub-humid areas," the researchers wrote in *Nature*. "Although the overall canopy cover is low, the relatively high density of isolated trees challenges prevailing narratives about dryland desertification and even the desert shows a surprisingly high tree density."

Mapping trees outside of forests at this level of detail would take months or years with traditional analysis methods, so the use of very high-resolution imagery and machine learning represents a significant breakthrough. The next steps for the research team include expanding their study area to survey more of Africa and estimating the carbon contained within these trees. "We don't know much about the role of these dryland areas in the global carbon cycle," said Brandt. "This research is a step towards filling that knowledge gap."

Brandt and colleagues have published their dataset—which includes the location and crown diameter of trees in western Africa—through the Oak Ridge National Laboratory Distributed Active Archive Center (ORNL DAAC). Users can also find it through a NASA Earthdata search.

For more information, visit <https://landsat.visibleearth.nasa.gov/view.php?id=147612>.



## PHOTOGRAMMETRIC ENGINEERING & REMOTE SENSING

JOURNAL STAFF

Publisher ASPRS

Editor-In-Chief Alper Yilmaz

Assistant Director — Publications Rae Kelley

Electronic Publications Manager/Graphic

Artist Matthew Austin

*Photogrammetric Engineering & Remote Sensing* is the official journal of the American Society for Photogrammetry and Remote Sensing. It is devoted to the exchange of ideas and information about the applications of photogrammetry, remote sensing, and geographic information systems. The technical activities of the Society are conducted through the following Technical Divisions: Geographic Information Systems, Photogrammetric Applications, Lidar, Primary Data Acquisition, Professional Practice, and Remote Sensing Applications. Additional information on the functioning of the Technical Divisions and the Society can be found in the Yearbook issue of *PE&RS*.

Correspondence relating to all business and editorial matters pertaining to this and other Society publications should be directed to the American Society for Photogrammetry and Remote Sensing, 425 Barlow Place, Suite 210, Bethesda, Maryland 20814-2144, including inquiries, memberships, subscriptions, changes in address, manuscripts for publication, advertising, back issues, and publications. The telephone number of the Society Headquarters is 301-493-0290; the fax number is 225-408-4422; web address is [www.asprs.org](http://www.asprs.org).

**PE&RS.** *PE&RS* (ISSN0099-1112) is published monthly by the American Society for Photogrammetry and Remote Sensing, 425 Barlow Place, Suite 210, Bethesda, Maryland 20814-2144. Periodicals postage paid at Bethesda, Maryland and at additional mailing offices.

**SUBSCRIPTION.** For the 2021 subscription year, ASPRS is offering two options to our *PE&RS* subscribers — an e-Subscription and the print edition. E-subscribers can plus-up their subscriptions with printed copies for a small additional charge. Print and Electronic subscriptions are on a calendar-year basis that runs from January through December. We recommend that customers who choose both e-Subscription and print (e-Subscription + Print) renew on a calendar-year basis.

The rate of the e-Subscription (digital) Site License Only for USA and Non-USA is \$1000.00 USD. e-Subscription (digital) Site License Only for Canada\* is \$1049.00 USD. e-Subscription (digital) Plus Print for USA is \$1365.00 USD. e-Subscription (digital) Plus Print for Canada\* is \$1424.00 USD. e-Subscription (digital) Plus Print for Non-USA is \$1395.00 USD. Printed-Subscription Only for USA is \$1065.00 USD. Printed-Subscription Only for Canada\* is \$1124.00 USD. Printed-Subscription Only for Non-USA is \$1195.00 USD. \*Note: e-Subscription/Printed-Subscription Only/e-Subscription Plus Print for Canada include 5% of the total amount for Canada's Goods and Services Tax (GST #135123065). **PLEASE NOTE: All Subscription Agencies receive a 20.00 USD discount.**

**POSTMASTER.** Send address changes to *PE&RS*, ASPRS Headquarters, 425 Barlow Place, Suite 210, Bethesda, Maryland 20814-2144. CDN CPM # (40020812)

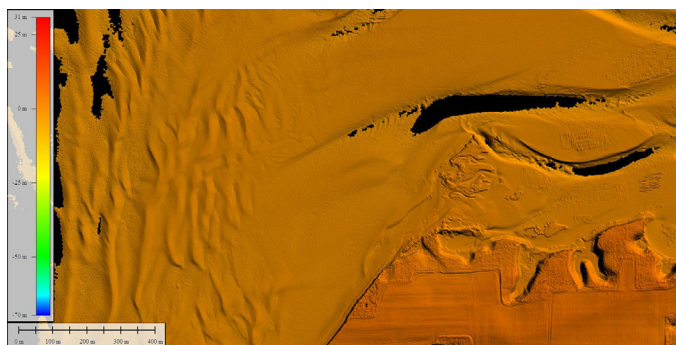
**MEMBERSHIP.** Membership is open to any person actively engaged in the practice of photogrammetry, photointerpretation, remote sensing and geographic information systems; or who by means of education or profession is interested in the application or development of these arts and sciences. Membership is for one year, with renewal based on the anniversary date of the month joined. Membership Dues include a 12-month electronic subscription to *PE&RS*. Or you can receive the print copy of *PE&RS* Journal which is available to all member types for an additional fee of \$60.00 USD for shipping USA, \$65.00 USD for Canada, or \$75.00 USD for international shipping. Dues for ASPRS Members outside of the U.S. will now be the same as for members residing in the U.S. Annual dues for Regular members (Active Member) is \$150.00 USD; for Student members \$50.00 USD for USA and Canada \$53.00 USD; \$60.00 USD for Other Foreign members. A tax of 5% for Canada's Goods and Service Tax (GST #135123065) is applied to all members residing in Canada.

**COPYRIGHT 2021.** Copyright by the American Society for Photogrammetry and Remote Sensing. Reproduction of this issue or any part thereof (except short quotations for use in preparing technical and scientific papers) may be made only after obtaining the specific approval of the Managing Editor. The Society is not responsible for any statements made or opinions expressed in technical papers, advertisements, or other portions of this publication. Printed in the United States of America.

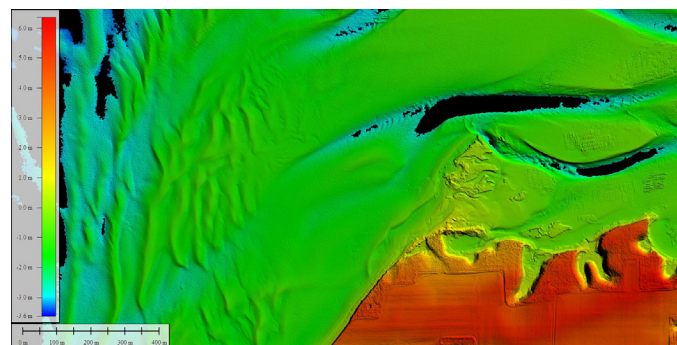
## Never use the Defaults

How many times has one of these scenarios played out for you? You just got a new computer and you have to reinstall all the software that you have been using for the past three years, or you finally get that upgrade to a piece of software that you have using “forever” that upon installation, wipes out all your favorite settings. In either of these scenarios, the software may be set to the “manufacturer defaults”, and if you are like Emily and me, it’s a real stretch of your memory to remember where to customize your GIS experience. A similar scenario just played out here at Dewberry when Emily logged-in to a new (to her) Virtual Machine. Emily fired up a session of Global Mapper, and all of the familiar settings that she has been using and tweaking over the past several years were suddenly gone and the software defaults in place.

While GlobalMapper is an excellent GIS system for viewing 3D data, like topobathymetric lidar, the default for displaying the raster color ramp defaults to show the elevation range for the full extent of the loaded dataset. While that is great when you are viewing the entire dataset, if you zoom in to a smaller extent, the default color ramp shrinks to the range of values in that extent, as in this bathymetric DEM, below, where the elevation range is small and displayed in a narrow color range of orange(s).



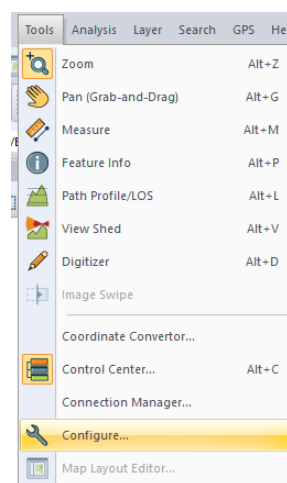
Here is the same extent symbolized by the color ramp of the entire dataset. Obviously, when the entire color ramp is used to render the smaller extent, additional bathymetric detail is easily seen. Changing the way GlobalMapper displays the elevations to the range in the view really enhances the way the data are perceived.



To customize the default display range, simply click on ‘Configure’ (the wrench icon located in tool bar.)



Alternatively, you could click on ‘Tools’ and then ‘Configure’

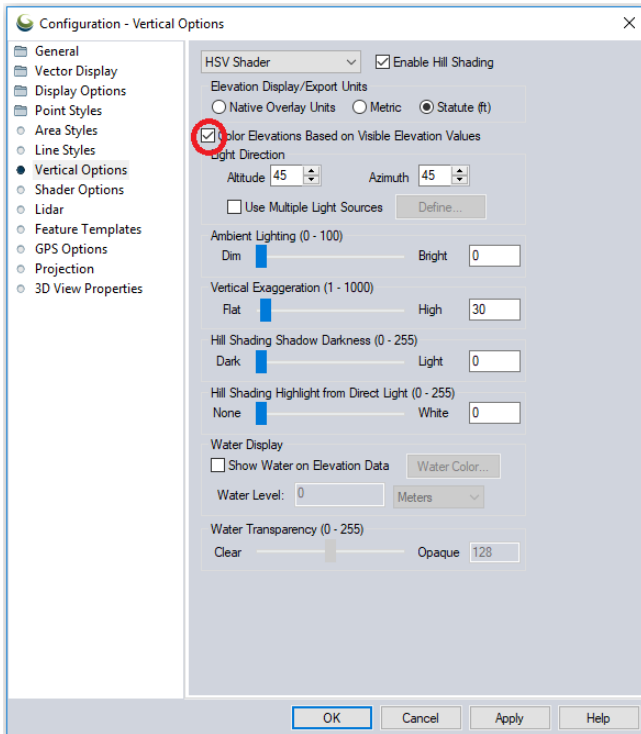


(Remember, there is always more than one way to fix something in GIS). Either way, once activated a GUI will open. Navigate to ‘Vertical Options’ and check the box next to

Photogrammetric Engineering & Remote Sensing  
Vol. 87, No. 2, February 2021, pp. 73–74.  
0099-1112/21/73–74

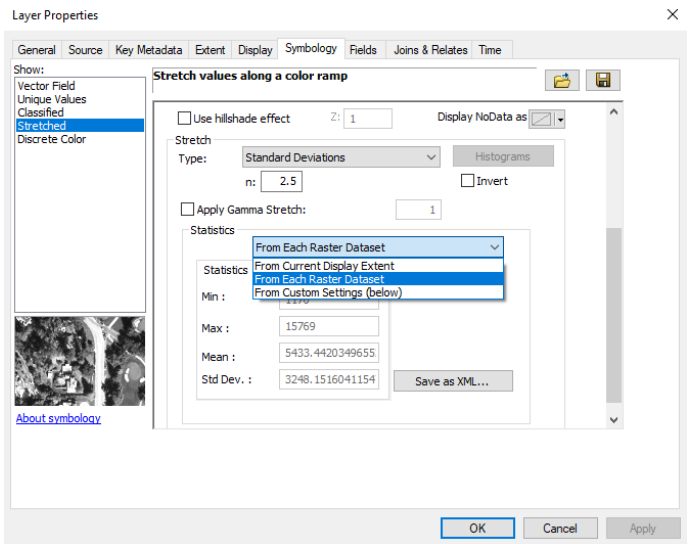
© 2021 American Society for Photogrammetry  
and Remote Sensing  
doi: 10.14358/PERS.87.2.73

'Color Elevation Based on Visible Elevation Values', press "Apply" and "OK".



And it is that easy!

By the way: There is similar control in Esri-ArcGIS Desktop that renders the entire color ramp for the displayed extent. The



ArcGIS control is in the Layer Properties | Symbology tab, and choose from the dropdowns: "From Current Display Extent" to render the entire color ramp for your smaller extent.

*Emily Klipp and Al Karlin, Ph.D., CMS-L, GISP are with Dewberry's Geospatial and Technology Services group in Tampa, FL. Emily is a project manager with Dewberry with a passion for all-things in the marine environment and especially topobathymetric lidar. As a senior geospatial scientist, Al works with all aspects of Lidar, remote sensing, photogrammetry, and GIS-related projects.*

Please e-mail questions or comments to [GISTT@ASPRS.org](mailto:GISTT@ASPRS.org).

## STAND OUT FROM THE REST

### EARN ASPRS CERTIFICATION

ASPRS congratulates these recently Certified and Re-certified individuals:

#### CERTIFIED PHOTOGRAMMETRIST

**Roman Shults, Certification #1654CP**

Effective December 28, 2020, expires December 28, 2025

#### RECERTIFIED PHOTOGRAMMETRISTS

**Marvin Miller, Certification #R1025CP**

Effective August 7, 2019, expires August 7, 2024

**Branko Hricko, Certification #R1486CP**

Effective December 6, 2020, expires December 6, 2025

**David Beattie, Certification #R1417CP**

Effective August 26, 2019, expires August 26, 2024

#### CERTIFIED MAPPING SCIENTIST LIDAR

Jason Jung, Certification #CMS-L060

Effective December 28, 2020, expires December 28, 2025

#### RECERTIFIED MAPPING SCIENTISTS REMOTE SENSING

Lloyd Coulter, Certification #R187RS

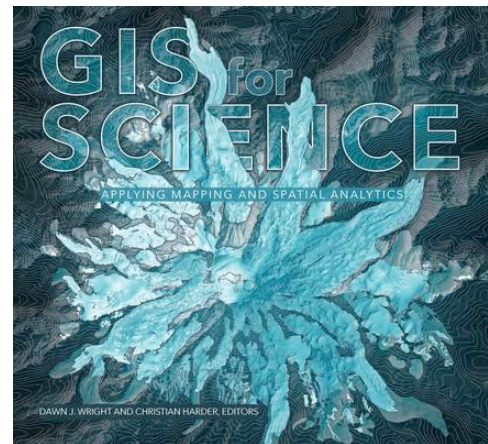
Effective December 18, 2020, expires December 18, 2025

ASPRS Certification validates your professional practice and experience. It differentiates you from others in the profession. For more information on the ASPRS Certification program: contact [certification@asprs.org](mailto:certification@asprs.org), visit <https://www.asprs.org/general/asprs-certification-program.html>.



At first glance *GIS for Science* (Harder and Wright, 2019) has the look and feel of a coffee table book, one that is occasionally picked up and leafed through to look at the pictures and rarely read. The full-color images and maps are abundant and large and beautifully illustrate the power of spatial imagery. However, this oversized, landscape orientated paperback makes it unwieldy to wrangle, reducing the amount of time a browser might spend examining any of the content details. Having said that, *GIS for Science* is an excellent resource and its usefulness far outweighs the initial awkward handling. This first volume of *GIS for Science* is a compilation of GIS applications at different spatial and temporal scales from a variety of disciplines of both social and physical sciences. Each chapter in this edited volume is written by experts of the subject matter, so the writing style and framework of each chapter is different which keeps a reader's interest. The five-part organization: "How Earth Works," "How Earth Looks," "How We Look at Earth," "Training Future Generations of Scientists," and "Technology Showcase," provide GIS examples from a variety of perspectives. This is useful because the intended audience broadly encompasses professional scientists, citizen scientists, and "anyone interested in geography and science". As an Earth and Environmental Science student, my approach to integrating GIS was as a tool to facilitate interpretation of science. Because I had a previous career in computer programming and data analysis, technology and the science of geographic information were not foreign to me and I quickly realized the power of spatial data science. However, as an educator, I see firsthand the lack of awareness and understanding of the applications of GIS to interpret science both with my colleagues and with students. In fact, my professional interest in this "textbook" was as a potential resource to provide examples of applications and elicit additional interest in our GIS program. This challenge of striking a balance between broad applicability across multiple disciplines and providing discipline-specific applications is what makes GIS so perennially interesting. *GIS for Science* beautifully illustrates current research as well as exciting possibilities for further investigation. The book also links to supplemental digital resources that promote inquiry and provides inspiration for incorporating the book and the digital resources into teaching activities.

On the whole, *GIS for Science* contains a variety of applications that provide detailed background in a particular discipline (see for example *The Anatomy of Supervolcanoes* by Brandmeier) and/or specific information about the use of different GIS components, such as the use of machine-learning in *Predicting Global Seagrass Habitats* by Aydin and Butler. However, there are some inconsistencies in the level of detailed explanations and definitions. For example, in *Global Ecosystem Mapping* by Sayer, an excellent explanation of the development and generalization of categories is



## GIS for Science: Applying Mapping and Spatial Analytics

Christian Harder and Dawn J. Wright, Editors.

ESRI Press, Redlands, CA. 2019. 237 pp., diagrams, maps, photos, images. Paperback. \$39.99. ISBN 978-1-58948-530-3.

**Reviewed by** M.Kathryn Rocheford, Assistant Professor, School of Natural Resources and Environment, Lake Superior State University, Sault Ste. Marie, Michigan.

provided but statistical clustering is not explained. Similarly, a detailed description of how Light Detection and Ranging (lidar) works and the subsequent products from the data is provided in *What Lies Beneath* by Coe, but interpolation is undefined. The inclusion of a glossary of GIS terminology would alleviate these issues for readers that are beginning their GIS journey.

If a user were to pick up *GIS for Science* and read one chapter because a particular topic piqued their interest, it would hit or miss as to whether the reader would learn about the wealth of supplemental information that supports this book on the accompanying website, [gisforscience.com](http://gisforscience.com). This is because some of the individual chapters have no mention of the available digital resources. For example, the background scientific information presented in *Extreme Heat Events and Changing Climate* by Boehnert and Wilhelmi is very well explained, and a specific case study is presented. However, there is no indication that digital materials are available

Photogrammetric Engineering & Remote Sensing  
Vol. 87, No. 2, February 2021, pp. 75–76.  
0099-1112/21/75–76

© 2021 American Society for Photogrammetry  
and Remote Sensing  
doi: 10.14358/PERS.87.2.75

Table 1. Index of topic disciplines and GIS applications by chapter.

Author(s)	Topic Discipline	GIS Component
Sayer	Ecosystems: Land & Marine; Sustainability	Mapping; Classification
Coe	Natural Hazards	LiDAR interpretation
Brandmeier	Volcanology	Machine Learning; Workflow
Aydin & Butler	Oceanography; Biology	Machine Learning; Python Modeling
Wilhelmi & Boehnert	Climate Change: Extreme Heat	Model Builder; Workflow
Griffen & Geraghty	Homelessness	Workflow; Survey 123; Hotspot analysis
Ferdaña et al.	Coastal Resilience	Decision Support System; Machine Learning; 3D Geoprocessing
Bennet et al.	Bird Migration: Climate Change	Modeling; Interactive tools for citizen scientists
Ur & Blossom	Archaeology; Urbanization	Historical Image analysis; UAV
Allenby, Joppa & Jojic	Watershed Conservation	Artificial Intelligence; Satellite Imagery
Klancher, Guenther & Wells	Glaciology; Hydrology	GPR, Kite Aerial Photography
Klooster, Smith & Strout	Conservation; Socioeconomics	UAV; Land cover mapping; watershed risk analysis

to further explore the topic, including the Learn ArcGIS Lessons: “Explore Future Climate Projections” by Frye and “Predict Weather with Real Time Data” by Kerski. Further, it is disappointing that the digital resource “Field Notes” specifically featured in *Global Ecosystem Mapping* by Sayer has either been taken down or did not make it into production.

Finally, the variety of applications across different disciplines is engaging for GIS professionals and scientists, and this volume succeeds in providing the scientific background for each discipline. However, a scientist from a particular discipline (e.g. wildlife ecology) is not likely to utilize this printed volume to learn more about how GIS would assist them with spatial data analysis or aid with student engagement. For readers that may fall in this category, compiled for your edification is an index (Table 1) of the chapters from Parts I-III.

In conclusion, *GIS for Science* is a great resource for the spatially aware reader to enhance their understanding of the science behind the use of GIS components. However, this author finds the details about some of the GIS components to be too vague for a non-spatially aware reader to engage in learning more about GIS. Therefore, missing the mark for the intended audience (professional scientists, citizen scientists, and “anyone interested in geography and science”) and relegates the book to coffee table status. I will, however, make full use of the available digital resources to engage my colleagues and students.



## Too young to drive the car? Perhaps! But not too young to be curious about geospatial sciences.

The ASPRS Foundation was established to advance the understanding and use of spatial data for the betterment of humankind. The Foundation provides grants, scholarships, loans and other forms of aid to individuals or organizations pursuing knowledge of imaging and geospatial information science and technology, and their applications across the scientific, governmental, and commercial sectors.

Support the Foundation, because when he is ready so will we.

[asprsfoundation.org/donate](https://asprsfoundation.org/donate)





# & GRIDS & DATUMS

BY Clifford J. Mugnier, CP, CMS, FASPRS

## THE KINGDOM OF THE NETHERLANDS

The Grids & Datums column has completed an exploration of every country on the Earth. For those who did not get to enjoy this world tour the first time, *PE&RS* is reprinting prior articles from the column. This month's article on The Kingdom of The Netherlands was originally printed in 2003 but contains updates to their coordinate system since then.

The kingdom was established in 1815 by French Emperor Napoleon, and initially controlled Belgium and Luxembourg. Inhabited since Paleolithic time, the region has been subjected to influences from early Celts, Germanic peoples, and Romans. The Netherlands is located at the mouths of three major European rivers: the Rhine, the Maas or Meuse, and the Schelde. With an area slightly less than twice the size of New Jersey, the kingdom borders the North Atlantic Ocean to its north and west (451 km), Belgium to its south (450 km), and Germany to its east (577 km). The terrain is mostly coastal lowland and reclaimed land (lowest point is Zuidplaspolder at  $-7$  m); there are some hills in the southeast and the highest point is Vaalservedg (322 m).

Willebrord Snell van Roijen (*Snellius*) was born in 1580 in Leiden, the Netherlands, and studied law at the University of Leiden although he taught mathematics there while he studied law. Snell's father was a professor of mathematics, and in 1613 he succeeded his father as professor of mathematics at the University of Leiden. The following year, he innovated the first classical triangulation based on his discovery of the Law of Sines. Using a brass Quadrant with a radius of 60 cm and by measuring an initial baseline of 328 m (total of five bases), he observed a quadrangle starting at Leiden and proceeded to complete a chain of quadrilaterals between Bergen op Zoom and Alkmaar. Later *Snellius* measured noontime shadows of towers in order to determine the length of a degree of the meridian. In 1617, he published *Eratosthenes Batavus De Terrae Ambitus Vera Quantitate*, which detailed his proposed techniques that established the science of Geodesy. He also discovered optical refraction (Snell's Law) and explored the loxodrome, a word he coined.

Before 1790, there was no systematic large-scale mapping in the Netherlands, either national or regional. The first mapping efforts, from 1791 to 1794 and from 1807 to 1811, were made to support cadastral mapping for taxation. In 1811, Napoleon



I decreed that the entire country be surveyed and registered for the establishment of a cadastre. The Dutch Cadastre was established in 1832 and remained in the Ministry of Finance until 1973. Between 1809 and 1822, complete topographic mapping coverage of the Netherlands at a scale of 1: 115,200 was achieved based on the first primary triangulation, published in 1861, on older cartographic materials, and on plane table foils. The Topografisch Bureau was founded in 1815 under the Ministry of Defense and was renamed Topografisch Dienst Nederlands (TDN) in 1931. The old triangulation and mapping was cast on the ellipsoidal Bonne projection where the latitude of origin  $\Phi_0 = 51^\circ 30' N$ , the central meridian was based on the (then) Prime Meridian at Amsterdam, and the scale factor at origin was unity. The ellipsoid of reference was the Bessel 1841 where the semi-major axis ( $a$ ) = 6,377,397.155 m, and the reciprocal of flattening ( $1/\rho$ ) = 299.1528128. (I think the old Amsterdam Datum of 1802 was first referenced to the Krayenhoff 1827 ellipsoid.) The kilometeric grid squares on the old series are numbered over each 1:50,000- scale sheet 0 to 40 West to East and 50 to 75 South to North, and a reference coordinate is given by sheet number and square number. The graticule was referenced to Amsterdam. The TDN has used aerial photogrammetry for mapping since 1932.

Photogrammetric Engineering & Remote Sensing  
Vol. 87, No. 2, February 2021, pp. 77–78.  
0099-1112/21/77–78

© 2021 American Society for Photogrammetry  
and Remote Sensing  
doi: 10.14358/PERS.87.2.77

A new triangulation was surveyed from 1886 to 1913 and published in *Triangulation du Royaume Des Pays-Bas*, the first volume in 1903 and the second volume in 1921. The origin of the Rijksdriehoeksmeting van het Kadaster of 1918 Datum (RD 1918) at the *Lieve Vrouwe* (Holy Virgin) Church tower in Amersfoort is  $\Phi_0 = 52^\circ 09' 22.178''$  N,  $\Lambda_0 = 5^\circ 23' 15.5''$  East of Greenwich, ( $0^\circ 30' 15.522''$  East of Amsterdam), and  $h_0 = 0$  m. The ellipsoid of reference for RD 1918 is the Bessel 1841, and the Schreiber Stereographic double projection was chosen for the kingdom. The Stereographic Grid origin is at the RD 1918 origin; the False Easting is 155 km, the False Northing is 463 km, and the scale factor at origin is unity. The result of this particular choice for the false origin is that no East to West reference can be more than 280 km, and no North to South reference can be less than 300 km. A comparison was made by the Dutch between values of 12 trigonometric stations along the border, as determined by the new Dutch triangulation on the Bessel ellipsoid and the new Belgian (*PE&RS*, October 1998) values on the Hayford ellipsoid. The Dutch triangulation lies 2.95 and 10.0 centesimal seconds South and East, respectively, of the Belgian triangulation. According to Jacob A. Wolkeau of the U.S. Army Map Service, these differences were mainly due to residual differences in the respective Datum origins and the reduction of the triangulations on different ellipsoids of reference. Comparisons made by the Belgians showed varying differences of 4.4" to 5.2" in latitude and 6.1" to 10.2" in longitude. The figures used in the 1950s British map series revision of the Dutch maps to the adjacent Belgian maps were 4.6" in latitude and 10.2" in longitude determined from a number of primary stations along the border. The transformation of the RD1918 Datum to WGS84 Datum is defined by a seven-parameter Bursa-Wolfe shift using the standard NIMA *right-hand rotation* sign convention:  $\Delta X = +565.036$  m,  $\Delta Y = +49.914$  m,  $\Delta Z = +465.839$  m,  $R_x = +0.4094''$ ,  $R_y = -0.3597''$ ,  $R_z = +1.86854''$ , and  $\delta s = -4.0772$  ppm. A test point offered by Maarten Hooijberg in *Practical Geodesy*, 1997 is  $\phi_{RD1918} = 51^\circ 59' 13.3938''$ ,  $\lambda_{RD1918} = 4^\circ 23' 16.9953''$ ,  $h_{RD1918} = 30.696$  m  $\rightarrow$   $\phi_{WGS84} = 51^\circ 59' 09.9145''$ ,  $\lambda_{WGS84} = 4^\circ 23' 15.9533''$ , and  $h_{WGS84} = 74.312$  m. Incidentally, Hooijberg also states that the WGS84 coordinates of *Lieve Vrouwe* tower are  $\phi_{WGS84} = 52^\circ 09' 18.62''$ ,  $\lambda_{WGS84} = 5^\circ 23' 13.9327''$ , and  $h_{WGS84} = 43.348$  m. The reader is cautioned that the parameters given above are expressed in the standard NIMA *right-handed rotation* sign convention. European software commonly utilizes a left-handed rotation sign convention that appears to be mysteriously favored by NATO countries *in lieu* of the standard that is recognized and used by the United States, Australia, and most (I guess) of the Western Hemisphere. The best explanation I have heard for this curious disparity is a certain senior geodesist in the U.S.

National Geodetic Survey once mused, "They probably didn't understand the math!"

The RD 1918 was recomputed on the European Datum of 1950 (EU50) and referenced to the Hayford 1909 (International 1909) ellipsoid where  $a = 6,377,388$  and  $1/f = 297$ . To transform from EU50 to WGS84, NIMA lists the three-parameter values as  $\Delta X = 87 \pm 3$ m,  $\Delta Y = -96 \pm 3$ m,  $\Delta Z = -120 \pm 3$ m, and the mean solution was based on 52 stations. To transform from EU79 to WGS84, NIMA lists the three-parameter values as  $\Delta X = -86 \pm 3$ m,  $\Delta Y = -98 \pm 3$ m,  $\Delta Z = 119 \pm 3$ m, and the mean solution was based on 22 stations.

The first known elevation benchmark in Europe was the Amsterdam City Watermark (*Amsterdams Peil* or *AP*). Although now lost, the original was set in 1684! In 1707, the city watermark (*AP*) was already indicated on a water gauge near Bilderham — 25 km from the original mark. Extensions of precise levels were not performed until Napoleonic times. General C.R.T. Krayenhoff supervised the extension of the vertical datum from Amsterdam to the rivers Rhine, Meuse, and IJssel, and along the coast of the Zuiderzee. Ramsden's leveling instrument was used which utilized a spirit level vial attached to a telescope. Krayenhoff's initial point was the water gauge at Amstel Lock. The *AP* was decreed to be the general datum plane of the Netherlands in 1818, and by 1860 the *AP* was published as the datum reference for some 550 benchmarks of the Prussian Railroad system. In 1876, a level loop was run among the original five stones and the deviation from the mean height for these 200-year-old benchmarks amounted to a maximum of 4 mm! Because of subsequent confusion with various levelings carried into Germany, the Dutch introduced new leveling results in January of 1891 as *Normaal Amsterdams Peil*, or *NAP*. At that same time, the Germans changed the name for their usage to *Normal-Null*. By 1928, the German and Dutch levels were compared anew with the result being  $NN = NAP - 0.021$  mm. The *NAP* is now extended from Lapland to Gibraltar and from Scotland to Sicily, based on the original Dutch work in 1684.

### The Kingdom of The Netherlands Update

Detailed information on updates to the geodetic coordinate systems of the Netherlands can be found at:

#### Reference Systems for Surveying and Mapping

[http://gnss1.tudelft.nl/pub/vdmarel/reader/CTB3310\\_RefSystems\\_1-2a\\_print.pdf](http://gnss1.tudelft.nl/pub/vdmarel/reader/CTB3310_RefSystems_1-2a_print.pdf)

#### National Report of the Netherlands 2019 - EUREF

<http://euref.eu/symposia/2019Tallinn/05-16-Netherlands.pdf>

#### EUREF Permanent GNSS Network

[http://www.epncb.eu/\\_networkdata/siteinfo4onestation.php?station=DELFO0NLD](http://www.epncb.eu/_networkdata/siteinfo4onestation.php?station=DELFO0NLD)

The contents of this column reflect the views of the author, who is responsible for the facts and accuracy of the data presented herein. The contents do not necessarily reflect the official views or policies of the American Society for Photogrammetry and Remote Sensing and/or the Louisiana State University Center for GeoInformatics (C<sup>4</sup>G).

This column was previously published in *PE&RS*.

# GREETINGS FROM THE ASPRS STUDENT ADVISORY COUNCIL (SAC)!

As we continuously network with our ASPRS Student Chapter community, we would like to highlight one of our newest members, North Carolina Agricultural and Technical State University, in Greensboro, North Carolina. Their ASPRS Student Chapter assisted in hosting the 2020 North Carolina Association for Photogrammetry and Remote Sensing Student Research Virtual Symposium. Go Aggies!



As students, we were honored to help the NC ASPRS host their Student Research Virtual Symposium. It was the first time many students helped host a virtual symposium. Our team worked under the direction of Ms. Hope Morgan (NC ASPRS) and Dr. Leila Hashemi-Beni (NCAT ASPRS Faculty Advisor). We advertised the event, developed the event agenda, moderated the event, and participated in the event. Student presenters consisted of undergraduate and graduate students. Event attendees and presenters were also able to gain career insights and

professional advice from three dynamic keynote panelists. Anthony Puzzo, Business Development Team Lead, State Government at Esri, Kirk Waters, Physical Scientist at NOAA Office for Coastal Management, and Silvia Terziotti, GIS Specialist at U.S. Geological Survey (USGS). Dr. Leila Hashemi-Beni, Asmamaw Gebrehiwot, Saurabh Dhamankar, and Terra McKee are part of our inaugural NCAT ASPRS Team.

NCAT ASPRS Team			
			
Dr. Leila Hashemi-Beni Faculty Advisor	Asmamaw Gebrehiwot President	Saurabh Dhamankar Vice President	Terra McKee, Secretary/Treasurer Symposium Moderator

## Symposium Presenters

### Crop Growth Study using UAV Remote Sensing Method

Freda Elikem Dorbu, *North Carolina A&T State University*

### Assessment of Vertical Vegetation Structure Metrics in Complex Forested Wetlands using UAS-borne Lidar Technology

Asami Minei and Narcisa G. Pricope, *University of North Carolina Wilmington*

### Deep Learning For Flood Extent Mapping Using Uav Optical Imagery

Asmamaw Gebrehiwot, *North Carolina A&T State University*

### Using Remote Sensing to Detect Urban Transformation in China Between the Years 1999 and 2018

James Duncan, *Fayetteville State University*

### Agent Based Modeling for Active Farm-Land Transition to Support Food Desert

Saurabh S. Dhamankar, *North Carolina A&T State University*

### A Remote Sensing Approach: Mapping and Linking Desertification with Conflicts in Darfur, Sudan, in 2001-2019

Ivy Knapp, *Fayetteville State University*

#### ASPRS STUDENT ADVISORY COUNCIL

YOUSSEF KADDOURA  
COUNCIL CHAIR

EVAN VEGA  
DEPUTY COUNCIL CHAIR

JASON MCGLAUGHLIN  
EDUCATION COUNCILOR

GERARDO ROJAS  
DEPUTY EDUCATION COUNCILOR

TERRA MCKEE  
COMMUNICATIONS COUNCILOR

JEFF PU  
DEPUTY COMMUNICATIONS COUNCILOR

MADISON FUNG  
SOCIAL MEDIA COMMITTEE CHAIR

AUSTIN STONE  
NETWORKING COUNCILOR

VICTORIA SCHOLL  
DEPUTY NETWORKING COUNCILOR

LAUREN MCKINNEY-WISE  
CHAPTERS COMMITTEE CHAIR

DAVID LUZADER  
SAC ECPC LIASON

## JOURNAL STAFF

### Editor-In-Chief

Alper Yilmaz, Ph.D., PERSeditor@asprs.org

### Associate Editors

Rongjun Qin, Ph.D., qin.324@osu.edu  
 Michael Yang, Ph.D., michael.yang@utwente.nl  
 Petra Helmholz, Ph.D., Petra.Helmholz@curtin.edu.au  
 Bo Wu, Ph.D., bo.wu@polyu.edu.hk  
 Clement Mallet, Ph.D., clemallet@gmail.com  
 Jose M. Pena, Ph.D., jmpena@ica.csic.es  
 Prasad Thenkabil, Ph.D., pthenkabil@usgs.gov  
 Ruisheng Wang, Ph.D., ruisheng@ucalgary.ca  
 Desheng Liu, Ph.D., liu.738@osu.edu  
 Valérie Gouet-Brunet, Ph.D., valerie.gouet@ign.fr  
 Dorota Iwaszczuk, Ph.D., dorota.iwaszczuk@tum.de  
 Qunming Wang, Ph.D., wqm11111@126.com  
 Filiz Sunar, Ph.D., fsunar@itu.edu.tr  
 Norbert Pfeifer, np@ipf.tuwien.ac.at  
 Jan Dirk Wegner, jan.wegner@geod.baug.ethz.ch  
 Hongyan Zhang, zhanghongyan@whu.edu.cn  
 Dongdong Wang, Ph.D., ddwang@umd.edu  
 Zhenfeng Shao, Ph.D., shaozhenfeng@whu.edu.cn  
 Ribana Roscher, Ph.D., ribana.roscher@uni-bonn.de  
 Sidike Paheding, Ph.D., spahedin@mtu.edu

### Contributing Editors

#### Highlight Editor

Jie Shan, Ph.D., jshan@ecn.purdue.edu

#### Feature Articles

Michael Joos, CP, GISP, featureeditor@asprs.org

#### Grids & Datums Column

Clifford J. Mugnier, C.P., C.M.S., cjmce@lsu.edu

#### Book Reviews

Sagar Deshpande, Ph.D., bookreview@asprs.org

#### Mapping Matters Column

Qassim Abdullah, Ph.D., Mapping\_Matters@asprs.org

#### Sector Insight

Lucia Lovison-Golob, Ph.D., lucia.lovison@sat-drones.com  
 Bob Ryerson, Ph.D., FASPRS, bryerson@kimgeomatics.com

#### GIS Tips & Tricks

Alvan Karlin, Ph.D., CMS-L, GISP akarlin@Dewberry.com

### ASPRS Staff

#### Assistant Director — Publications

Rae Kelley, rkelley@asprs.org

#### Electronic Publications Manager/Graphic Artist

Matthew Austin, maustin@asprs.org

#### Advertising Sales Representative

Bill Spilman, bill@innovativemediasolutions.com

## PUBLISHING A PEER-REVIEW ARTICLE IN *PE&RS* IS NOW EASIER!

### Open Access

Authors can opt for open access to their published peer-review article, which makes it immediately available on public, open access platforms such as ResearchGate, Academia.edu, or your own research website. The fee for this publishing option is \$1,500 for ASPRS members and \$2,000 for non-members.

### Extra Pages and Color Fees

Each article is allowed nine (9) journal pages before being assessed extra page fees. This is an increase of two (2) journal pages per article. Color fees in the printed version will continue to be \$500 for up to three (3) color pages, \$1,000 for up to six (6) color pages, and \$1,500 for seven (7) or more color pages. Color on the web is complimentary.

For more information on publishing in *PE&RS*, visit <https://www.asprs.org/asprs-publications/pers/manuscript-submission>.

## NEW ASPRS MEMBERS

ASPRS would like to welcome the following new members!

### Cascadia

Peder Nelson

### Central New York

Lisa Casey  
 Jason Olivier

### Eastern Great Lakes

Benjamin Vander Jagt, PhD  
 Jinfei Wang, PhD

### Florida

Jackson Alan Beebe  
 Savannah Rae Carter  
 Jackson McGraw

### Heartland

Brad Mathison

### Mid South

Vince Clause  
 Joseph Davis  
 Garrett Foster

Brian Paul Nietfeld

Balaji Ramachandran, PhD  
 Brittany Wood

### Potomac

Christopher Scott Godwin  
 Chuck Heazel  
 Garrett Shields  
 Lee A. Sweetapple  
 Brian Wilson

### Rocky Mountain

Austin Anderson  
 Eric Clay  
 Andrew J. Holbert

Juan Ridout

Michael P. Scanlan, CP  
 Yusuf I. Siddiqui, CMS

### Western Great Lakes

Phillip Blaine Merrill, CP

FOR MORE INFORMATION ON ASPRS MEMBERSHIP,  
 VISIT [HTTP://WWW.ASPRS.ORG/JOIN-NOW](http://www.asprs.org/join-now)

*Your Path To Success In The Geospatial Community*

# Monitoring the Spatiotemporal Dynamics of Urban Green Space and Its Impacts on Thermal Environment in Shenzhen City from 1978 to 2018 with Remote Sensing Data

Yue Liu, Hui Li, Peng Gao, and Cheng Zhong

## Abstract

*In a developing city, urban green space (UGS) plays an increasingly significant role in improving the urban environment and beautifying the urban landscape. In the meantime, UGS has been substantially and frequently interfered with by human activities. Taking Shenzhen city (a great metropolis of China) as an example, this study investigated the spatio-temporal dynamics of UGS and its influence on the urban thermal environment with Landsat images. From 1978 to 2018, all croplands and more than 50% of water bodies disappeared, while the built-up area increased more than 6 times. The rapid expansion of impervious surface and loss of UGS led to the spread of a surface urban heat island. The study shows that UGS has a significantly mitigating impact on urban land surface temperature, with cold islands mainly located at city parks. The results will be of great significance for improving UGS management, alleviating the urban heat island effect, and establishing a sustainable eco-environment.*

## Introduction

Urbanization is an inevitable eco-social process of human society in the 21st century. At present, more than 50% of the global population lives in urban areas, and it is projected that the proportion will increase to about 70% by 2050 (Intergovernmental Panel on Climate Change 2014). Hence, cities, including their built-up areas and surrounding suburbs, are becoming increasingly important to human beings, as more and more people live in and rely on urban natural, economic, and social environments (Dewan *et al.* 2012; Ding *et al.* 2016). Compared with natural ecosystems, urban ecosystems are characterized by their vulnerability, instability, openness, and dependence (Su *et al.* 2012; D. Li *et al.* 2019). On the one hand, urbanization has the potential to improve the well-being of societies by offering more equal education, employment, and health treatment opportunities; on the other hand, poorly planned urbanization often leads to serious

---

Yue Liu is with the Three Gorges Research Center for Geohazards, Ministry of Education, China University of Geosciences, Wuhan, China.

Hui Li is with the School of Earth Sciences, China University of Geosciences, Wuhan, China.

Peng Gao is with the Department of Earth and Ocean Sciences, University of North Carolina, Wilmington, NC 28403.

Corresponding Author: Cheng Zhong is with the Three Gorges Research Center for Geohazards, Ministry of Education, China University of Geosciences, Wuhan, China (zhonglxm@cug.edu.cn).

threats to local ecological environments, such as air pollution, water contamination, the urban heat island (UHI) effect, and biodiversity loss (H. Li, Wang, Zhong, Su *et al.* 2017; H. Li, Wang, Zhong, Zhang, and Liu 2017; Zhong *et al.* 2018). Today, alleviating the adverse effects of urbanization and keeping development sustainable has become an essential task for city managers.

Urban green space (UGS), consisting of vegetation (woods and grasslands), croplands, and water, plays an increasingly significant role in regulating the urban ecological balance, improving the urban environment, and beautifying the urban landscape (H. Zhang *et al.* 2019). It can effectively alleviate many environmental problems caused by the acceleration of urbanization, such as air pollution, the UHI effect, and biodiversity loss (Hunter and Luck 2015; Chen *et al.* 2018). UGS has been widely considered a significant part of urban ecosystems and an important indicator of urban livability, sustainability, and civilization (Di *et al.* 2019). Thus, planning and research regarding UGS become vital to urban planning, environmental protection, and balancing the urban ecosystem.

Currently, simple indicators such as green rate (percentage area of green lands), green coverage rate (percentage of urban trees), and green space area per capita are widely used in evaluating urban livability and sustainability. Considering that UGS is often limited or even reduced in terms of area and number in the process of urban sprawl, greatly improving the ecological benefits of UGS becomes important and urgent (Qian, Zhou, and Li 2015; Bandyopadhyay *et al.* 2017). Therefore, more investigations should be carried out on the ecological functions of specific vegetations and the rationality of UGS spatial distribution.

UGS landscape patterns and their dynamics have great effects on local ecological processes and urban animal and plant communities, climate, hydrology, soil, and so on, by influencing regional material and energy flow (World Health Organization 2016; Threlfall *et al.* 2017). Thus, it is necessary to pay special attention to UGS distribution, structure, function, and development, and the interaction mechanism between the UGS landscape and the ecological environment (Grêt-Regamey *et al.* 2014; Shih 2017). Given that the spatio-temporal dynamics of the UGS landscape and its influences are complex and dynamic, specific studies on them could deepen our understanding of urban environmental problems

---

Photogrammetric Engineering & Remote Sensing  
Vol. 87, No. 2, February 2021, pp. 81–89.  
0099-1112/21/81–89

© 2021 American Society for Photogrammetry  
and Remote Sensing  
doi: 10.14358/PERS.87.2.81

and help authorities develop more rational and effective policies (Jim 2013; Moseley *et al.* 2013).

As the first special economic zone of China, Shenzhen has experienced dramatic economic development and urban expansion since 1978. The former rural village has completely upgraded to a world-class modern metropolis. In the process of this urbanization and modernization, the urban landscapes (including UGS) have been substantially and frequently disturbed, transformed and reconstructed by human activities (Shao, Ding *et al.* 2020). Recently, many studies have been carried out on rapid urbanization processes and related topics, such as land use/land cover change, landscape pattern dynamics, environmental change, and ecological security (Damodaran, Höhle, and Lefèvre 2017; Zhou and Chen 2018; Shao, Li *et al.* 2020). However, the dynamics of UGS landscape patterns and related ecological environment responses, which are vital to UGS protection and development, are still poorly understood for this city.

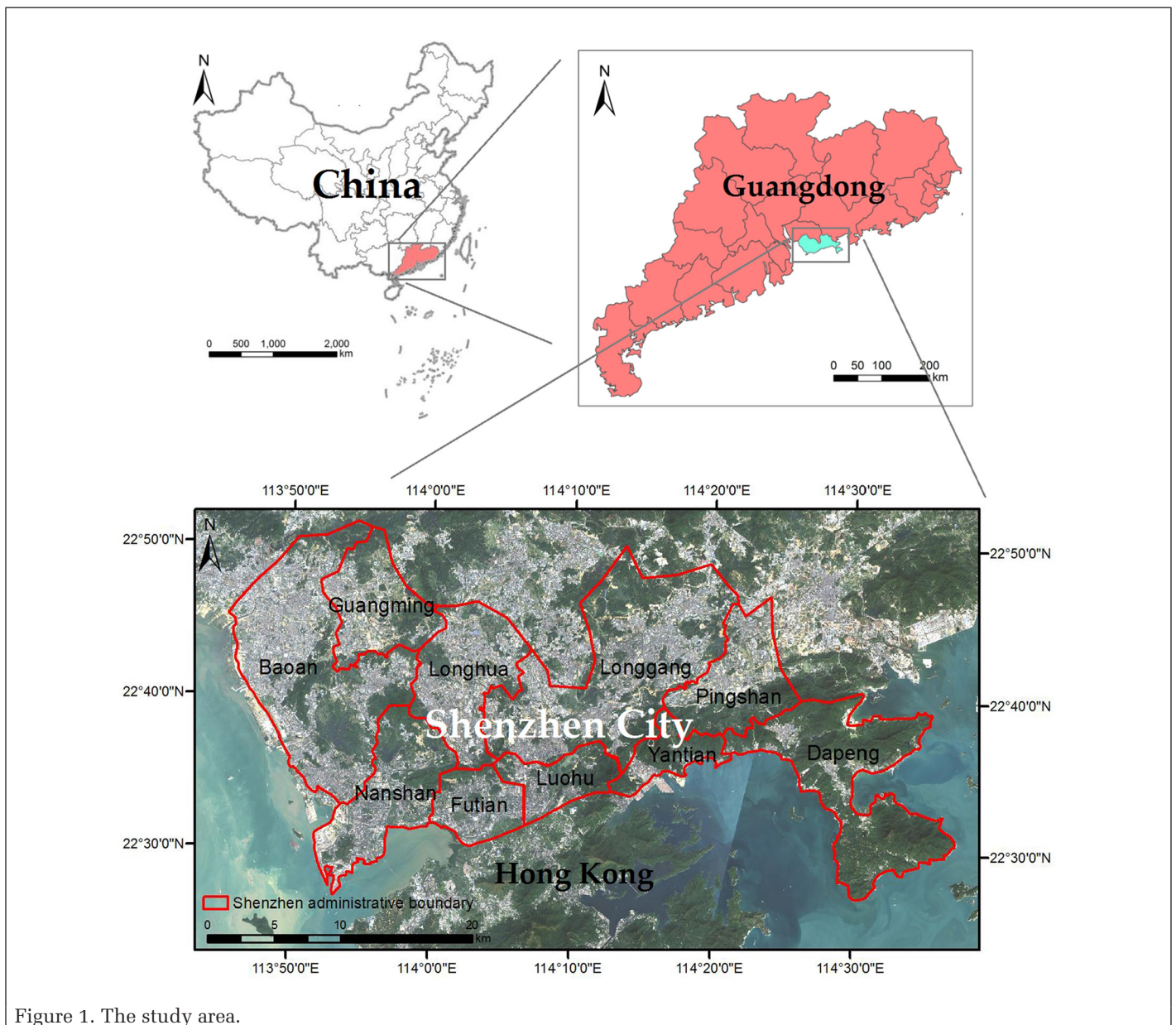
This study aims to discover the spatiotemporal dynamics of the UGS landscape and its influence on the urban thermal

environment in the rapid urbanization process of the city using Landsat images from 1978 to 2018.

## The Study Area and Data

### The Study Area

Shenzhen is located in the south of Guangdong Province, China, adjacent to Hong Kong, as shown in Figure 1. It is known as the first special economic zone, a national economic center, an international metropolis, and “the Silicon Valley of China” (“The rise of China’s ‘Silicon Valley’” 2018). By 2018, the city had a land area of 1996.85 km<sup>2</sup> and a population of 13.02 million (Rivers 2019). In that year, the gross domestic product of Shenzhen was more than \$34 billion, fifth among all Asian cities. The city has a subtropical marine climate characterized by a hot and rainy season from April to September, due to the East Asian monsoon and tropical cyclones, and a warm and dry season from October to March influenced by the northwest monsoon. The annual average precipitation, temperature, and sunshine duration



are 1933.3 mm, 22.4°C, and 2120.5 hr, respectively (“Top 50 World Container Ports” n.d.; Yeandle and Wardle 2019). Besides the coastal plain in the west, most of the city occupies low hilly areas decorated with gentle terraces. The city is rich in vegetation resources, including *Pinus massoniana*, shrubs in the hills, mangroves on the coastal mud band, and artificial forest in the developed regions (“Overview of Shenzhen” 2016).

## Data Set

### Landsat Images

The Landsat project is the longest-running global record of Earth observations from space, running from 1972 to present. The 48-year archive of satellite images can meet the requirements of this study well. The level 2 images were downloaded from the United States Geological Survey official website (<http://www.usgs.gov/>), where radiation correction and geometric correction have already been done. Considering that in winter the city has lower precipitation, stable weather conditions, relatively stable UHI, and evergreen plants, images captured in the winter were selected, as shown in Table 1. It is expected that the data are conducive to investigating the relationship between the city’s UGS and thermal environment (E.-J. Zhang *et al.* 2008; Tan *et al.* 2010).

Table 1. Landsat images used in this study.

Capture Date	Sensor	Bands	Spatial Resolution (m)	Cloud Cover (%)
2 Nov. 1978	MSS	4 (no TIR)	80	4
22 Nov. 1984	TM	7	80	0
8 Nov. 1988	TM	7	30	1
15 Nov. 1993	TM	7	30	11
4 Nov. 1998	TM	7	30	0.4
26 Oct. 2003	TM	7	30	0
15 Nov. 2008	TM	7	30	15
29 Nov. 2013	OLI and TIRS	11	30	0.12
3 Oct. 2018	OLI and TIRS	11	30	3.15

MSS = multispectral scanner; OLI = operational land imager; TIR = thermal infrared band; TM = thematic mapper.

In order to cover the whole study area, two adjacent scenes—Path 122, Row 44 and Path 121, Row 44—captured at similar times were merged and then cut with the city’s administrative boundary. In addition, the Landsat Multispectral Scanner images were rescaled to 30 m to match the resolution of Thematic Mapper and Operational Land Imager.

### Other Data

Vector-map, meteorological, and socioeconomic data were collected from the Bureau of Land and Resources, the Bureau of Meteorology, and the statistical yearbook of the city, respectively.

High-resolution images—including aerial images before 2001, QuickBird images in 2003 and 2008, and WorldView images in 2013 and 2018—were obtained from the Bureau of Land and Resources. Hundreds of samples were interactively and randomly collected from these images, 60% of which were selected as training samples and 40% assigned as validation samples.

## Methods

### UGS Change Detection

The postclassification (thematic) change detection technique was used to monitor UGS spatiotemporal dynamics during the 40 years in question. Landsat images were first classified into UGS and non-UGS, then the classification results at different times were compared to detect changed pixels and related variation. This method can effectively reduce the impacts of atmosphere and illumination noise (Hermosilla *et al.* 2015). More importantly, it can directly find the transfer direction of changed pixels and then rapidly help reveal the general change of the UGS (Martha *et al.* 2010). This method is significantly affected by the accuracy of the classifications.

At each mapping year, 100 samples (60% for training and 40% for validation) for each UGS subtype (vegetation, water, and croplands) and non-UGS subtype (built-up and barren) were carefully selected from high-resolution images by experienced experts. Then the random forest classifier was used to classify Landsat images and produce UGS maps (Gislason, Benediktsson, and Sveinsson 2006). Many studies have proved that this classifier has excellent classification accuracy and computation efficiency and is immune to abnormal data and noises (Lawrence, Wood, and Sheley 2006; Clark and Roberts 2012; Rodriguez-Galiano *et al.* 2012; Xu, Ye, and Nie 2012). The spatiotemporal dynamics of UGS were then detected by comparing UGS classification results at different mapping years (Duro, Franklin, and Dubé 2012; Rodriguez-Galiano *et al.* 2012).

### UGS Landscape Pattern Analysis

Landscape pattern analysis was used to learn detailed morphological and structural characteristics of UGS patches. Monitoring the dynamics of the UGS landscape pattern is expected to reveal more details of UGS changes over the 40 years (Hargis, Bissonette, and David 1998; “FRAGSTATS” n.d.). Typical landscape indexes—the percentage of landscape (PLAND), landscape shape index (LSI), Euclidean area-weighted mean nearest-neighbor distance (ENN\_AM), and cohesion index (COHESION)—were selected to conduct quantitative investigations on UGS heterogeneity, fragmentation, diversity, and evenness.

$$PLAND = \frac{\sum_{j=1}^n a_{ij}}{A} (100), \quad (1)$$

where  $a_{ij}$  is the area of patch  $j$  of type  $i$ , and  $A$  indicates the area of the study area. Equation 1 calculates the proportion of a land type to the whole study area.

$$LSI = \frac{0.25E}{\sqrt{A}}, \quad (2)$$

where  $E$  represents the total length of all UGS patch boundaries and  $A$  indicates the total area of all UGS patches. A large LSI means that the UGS shape is complex.

$$ENN\_AM = \sum_{i=1}^n \sum_{j=1}^m \left( \frac{a_{ij} h_{ij}}{A} \right), \quad (3)$$

where  $h_{ij}$  indicates the nearest distance between patch  $j$  and other patches of type  $i$ ,  $a_{ij}$  is the area of patch  $j$  of type  $i$ , and  $A$  indicates the area of the study area. Equation 3 is used to describe the spatial distance of patches belonging to the same type. A small value implies that patches are clustered, while a large value suggests that patches are far away from each other.

$$\text{COHESION} = \left[ 1 - \frac{\sum_{j=1}^n p_{ij}}{\sum_{j=1}^n p_{ij} \sqrt{a_{ij}^*}} \left[ 1 - \frac{1}{\sqrt{A^*}} \right]^{-1} \right] (100), \quad (4)$$

where  $a_{ij}$  and  $p_{ij}$  indicate the area and perimeter of patch  $j$  of type  $i$  and  $A^*$  represents the total number of patches. COHESION describes the spatial connectedness of patches of a land type. A large value means patches are closely connected.

### Land Surface Temperature Retrieval

Several typical methods for retrieving land surface temperature (LST) from Landsat images have been developed, including the radiative transfer equation, single-channel algorithm, and mono-window algorithm (Jiménez-Muñoz *et al.* 2014; Rozenstein *et al.* 2014). For the radiative transfer equation and single-channel algorithm, accurate atmospheric profile data and meteorological parameters are needed (X. Yu *et al.* 2014). Considering that it is hard to obtain those parameters from images captured before 2000 from the United States Geological Survey official website, these two algorithms could not be used to retrieve the LST for all the study years. The mono-window algorithm is able to retrieve LST from the infrared band simply and accurately, with three standard parameters (land surface emissivity, atmospheric transmittance, and average atmospheric temperature; Qin, Karnieli, and Berliner 2001; Sobrino, Jiménez-Muñoz, and Paolini 2004; Cai *et al.* 2017). In this method, real-time atmospheric parameters are not required.

We tested and compared the three algorithms with images captured after 2000 and found that all retrieval results matched ground values well. Specifically, the retrieval error of the radiative transfer equation and single-channel algorithm are about 0.8 K, while that of the mono-window algorithm is about 1.0 K. Therefore, the mono-window algorithm is suitable for retrieving LST for the whole study period. LST is calculated as (Qin, Karnieli, and Berliner 2001)

$$T_s = \frac{a(1-C-D) + [b(1-C-D) + C + D]T - DT_a}{C}, \quad (5)$$

where  $C = \varepsilon\tau$  and  $D = (1-\tau)[1+(1-\varepsilon)\tau]$ ;  $T_s$  indicates the LST in K;  $a = 67.355351$  and  $b = 0.458606$  when  $T_s$  is in the range of [273.15, 343.15];  $C$  and  $D$  are intermediate variables;  $\varepsilon$ ,  $\tau$ , and  $T_a$  represent the land surface emissivity, atmospheric transmittance, and average atmospheric temperature, respectively; and  $T$  is the temperature transferred from the brightness of a thermal infrared image pixel. More details about how to calculate these parameters are given by Qin, Karnieli, and Berliner (2001).

### Urban Heat Islands

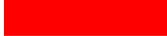
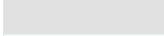
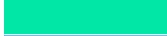
An urban heat island (UHI) is the phenomenon in which the air or surface temperature in urban areas is higher than that in the surrounding suburban areas (Tan *et al.* 2010; Ramamurthy and Bou-Zeid 2017). At present, UHIs are one of the most concerning urban-environment issues, as they pose serious threats to human health in developing cities, especially in Asia (Intergovernmental Panel on Climate Change 2014). Thus, it is of great significance to analyze the impacts of UGS dynamics on UHIs (Founda and Santamouris 2017; Navigant Consulting n.d.).

In this study, the difference between the temperature value at a pixel ( $T_i$ ) and the average temperature of the study area ( $T_{\text{mean}}$ ) is considered the surface urban heat island intensity at the pixel (SUHII; Liu *et al.* 2020):

$$\text{SUHII}_i = T_i - T_{\text{mean}}. \quad (6)$$

If  $\text{SUHII}_i > 0$ , pixel  $i$  is classified as a UHI pixel; if  $\text{SUHII}_i < 0$ , pixel  $i$  is classified as a cold island pixel. More specifically, pixels are divided into seven categories and rendered with different colors according to their SUHII values, as shown in Table 2. This illustrated the city's thermal environment clearly.

Table 2. Surface urban heat island index (SUHII) categories.

SUHII (K)	Category	Color
>5	Strong heat island (SHI)	
3 to 5	Moderate heat island (MHI)	
1 to 3	Weak heat island (WHI)	
-1 to 1	Normal area (NA)	
-3 to -1	Weak cold island (WCI)	
-5 to -3	Moderate cold island (MCI)	
<-5	Strong cold island (SCI)	

### The Impacts of UGS on UHIs

In order to investigate the impacts of UGS on the urban thermal environment, the relationships between UGS characteristics (vegetation coverage, PLAND, and subtypes) and SUHI is analyzed with the Spearman correlation coefficient (Chapman *et al.* 2017; Peng *et al.* 2018). This coefficient is an effective way to investigate the relationship of two variables ( $X$  and  $Y$ ) without considering their distribution and sample size. The method can be described as follows: First sort  $X$  and  $Y$  in ascending or descending order synchronously to get two ranking sets  $x$  and  $y$ , then calculate the correlation coefficient between  $X$  and  $Y$  as follows (Lehman 2005):

$$r_{xy} = \frac{\sum_{i=1}^n (x_i - \bar{x})(y_i - \bar{y})}{\sqrt{\sum_{i=1}^n (x_i - \bar{x})^2} \sqrt{\sum_{i=1}^n (y_i - \bar{y})^2}}, \quad (7)$$

where  $x_i$  and  $y_i$  are the rank of  $X_i$  in  $X$  and of  $Y_i$  in  $Y$ , respectively, and  $\bar{x}$  and  $\bar{y}$  represent the average value of  $X$  and  $Y$ , respectively. According to Equation 7,  $r = 1$  means the strongest positive correlation,  $r = -1$  means the strongest negative correlation, and  $r = 0$  indicates that there is no correlation between  $X$  and  $Y$ .

## Results

### The Spatiotemporal Dynamics of UGS

At first, quinquennial UGS maps for the study years were produced, with hundreds of training samples selected by experienced experts and classified using the random forest classifier. The overall accuracies and results of the classifications are shown in Table 3 and Figure 2, respectively. In Figure 2, the dynamics of UGS subtypes (water, forest, and cropland) and non-UGS subtypes (built-up and barren) are displayed. The transfers between UGS and non-UGS were aggregated and are displayed in Figure 3. Furthermore, the dynamics of the UGS landscape pattern were analyzed and are shown in Table 4.

Table 3 shows that all classifications achieve very high accuracies (overall accuracy and  $\kappa$  coefficient greater than 0.93), which suggests that the results are suitable for further analysis.

Figure 2 shows the dynamics of UGS subtypes (vegetation, water, and croplands) and non-UGS subtypes (built-up and barren), along with the development of the city from 1978 to 2018. Several changes are noticeable: First, croplands, which accounted for about 17% of the total area in 1978, have

Table 3. Accuracies of quinquennial classifications.

Year	1978	1983	1988	1993	1998	2003	2008	2013	2018
OA	0.958	0.955	0.949	0.938	0.946	0.939	0.944	0.932	0.949
$\kappa$	0.947	0.943	0.932	0.938	0.936	0.945	0.955	0.929	0.931
Separability <sup>a</sup>	1.99	1.97	1.88	1.99	1.98	1.95	1.97	1.87	1.99

OA = overall accuracy.

<sup>a</sup> The separability of training samples was tested with the ENVI 5.4 ROI tool.

Table 4. The dynamics of urban green space landscape patterns.

Index	1978	1983	1988	1993	1998	2003	2008	2013	2018
PLAND	67.42	66.51	64.7	56.7	52.65	50.99	50.22	48.38	46.81
LSI	169.93	170.91	170.17	192.6	181.76	128.83	126.26	109.3	94.45
ENN_AM	60.67	60.71	60.81	61.33	61.24	61.48	61.38	61.08	60.99
COHESION	99.62	99.41	99.3	99.06	99.47	99.45	99.46	99.11	99.49

PLAND = percentage of landscape; LSI = landscape shape index; ENN\_AM = Euclidean area-weighted mean nearest-neighbor distance; COHESION = cohesion index.

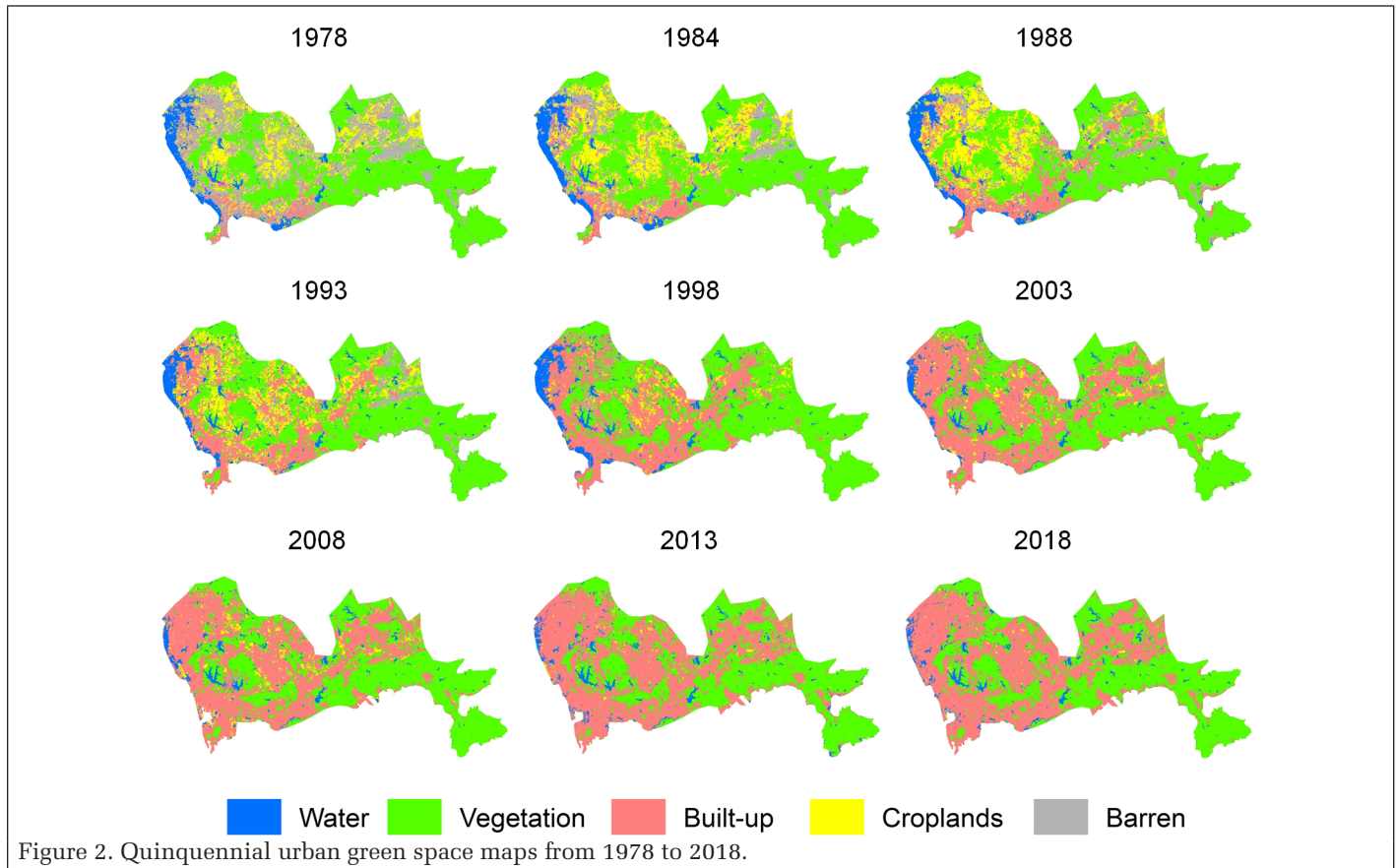


Figure 2. Quinquennial urban green space maps from 1978 to 2018.

almost disappeared in 2018, as the city has become a completely developed metropolis; second, built-up area, which occupied just the southwest coastline (only 6% of the study area) in 1978, has dramatically expanded all over the city and accounts for more than 50% in 2018; third, the area of vegetation (forest, grass, and so on) has barely changed since 1978, which reflects the endeavor of local government in environment protection; and fourth, the water body around the west, which is a part of the Pearl River Estuary, is occupied and built up in 2018, suggesting that the expansion of the city partly comes from marine reclamation.

According to Figure 3, lands transferring from UGS to non-UGS are distributed all over the city, and account for about 24% of the study area, which is even greater than the area of croplands in 1978. By contrast, lands transferring from non-UGS to UGS are just about 0.45%, and mainly happen around city parks, with reconstruction or enlargement.

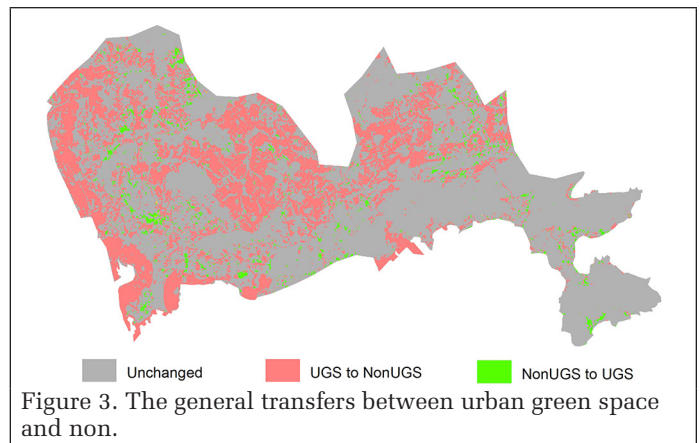


Figure 3. The general transfers between urban green space and non-UGS.

According to Table 4, the PLAND of UGS gradually decreased from 67.42% in 1978 to 46.81% in 2018, which indicates that lots of UGS lands have been transferred into built-up areas. LSI remained unchanged from 1978 to 1988, and then dramatically increased to 192.6 in 1993, followed by a gradual decrease to 94.45 in 2018. This suggests that human activities have great influence on the shapes of UGS patches. Specifically, in the city's developing period when croplands were ruined for built-up construction, UGS shapes became complex; after that, the awareness of and endeavor for UGS protection were enhanced, which helped lower the LSI.

The ENN\_AM and COHESION of UGS are unchanged over the 40 years, which means that the levels of spatial connectedness and spatial distance of UGS patches were maintained.

### UGS Impacts on the Urban Thermal Environment

The quinquennial LST maps of the city were retrieved from Landsat images according to Equation 5 and then transformed into SUHI maps (Figure 3). There is no LST/SUHI map for the year 1978, because the Landsat Multispectral Scanner had no thermal infrared band at that time. Related accuracy validation suggests that the mean difference between the retrieved LST and ground observations is about 1 K.

Before 2003, there was no evident SUHI (strong, moderate, or weak) in the study area, and some regions having lower LST were considered cold islands. After 2003, SUHIs gradually appeared, expanded, and connected. In 2018, most of the city was covered by SUHIs, and only several city parks were covered by cold islands. In Figure 2, the distribution and dynamics of SUHIs are in accordance with those of built-up areas, while the spatiotemporal dynamics of cold islands (strong, moderate, and weak) are identical with those of UGS. The two figures illustrate the mitigating effect of UGS on the urban thermal environment, as well as the positive reinforcement of built-up area.

Strong heat islands are mainly located in the middle areas of the city, including Nanhu, Dongmen, Cuizhu, Dongxiao Street in Luohu District, and Buji Street in Longgang District. The area of UHI with an intensity of more than 1 K expanded in Longcheng and Longshan Districts, Yuanshan Street, and Nantou Street in Nanshan District. A weak UHI is still mainly located in the north of Futian District in the middle and west, the north of Nanshan District, the south of Baoan District, the east of Yantian District, the north of Longgang and Pingshan Districts, and Dapeng New District.

In Nanshan District, high-density and high-strength land development is a common state of urban development and construction over the past 40 years. For instance, the building coverage rate is often higher than 90%. Thus, heat islands are originated from the central part of Nanshan District and then cover most of the area of the district, namely Shekou, Yuehai, and Shahe Streets, not counting several city parks. Most of these places are covered by business districts, including Dongmen Commercial Mall, Huaqiangbei Commercial Mall, and other well-known and established commercial areas in Shenzhen, as well as major tourist attractions such as the Window of the World and Happy Valley and transportation hubs such as railway stations and ports. These heat islands are also characterized by high population density, which can be understood as a heating emission source. A more concentrated crowd will consume more energy, some of which is used to deal with high temperatures, such as air conditioning. This will then enhance the heat island effect in this area.

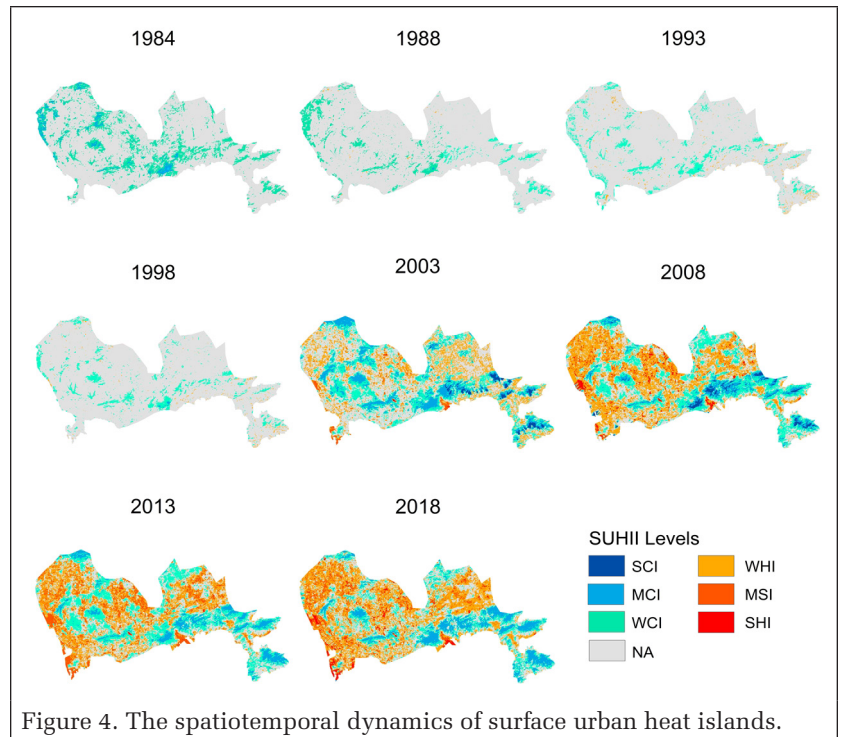


Figure 4. The spatiotemporal dynamics of surface urban heat islands.

If effective measures are not taken, these places are bound to get hotter, and local microclimates will be affected. For instance, a heavy shower will be caused by convection when the air rises due to the increase in temperature and encounters the cooler air around it in a local block. In order to slow down the heat island effect, a district can try to increase vegetation coverage, promote energy conservation and environmental protection, build green roofs, and increase surface permeability.

The quantitative relationship between UGS and SUHI was analyzed with the Spearman correlation coefficient. Figure 5 shows that the vegetation fractional coverage (VFC) and PLAND of UGS have significantly mitigating influences on SUHI ( $r = -0.696$  and  $-0.744$ , respectively), which means patches with higher VFC and greater area can alleviate local SUHIs more effectively. This is helpful for improving plans on environment protection and urban sustainable development. Here, VFC indicates the percentage of the vertical projected area of vegetation on the ground in the total area. Details and formulas for VFC are given by Zhao, Zheng, and He (2004).

In order to analyze the impact of a UGS subtype (water, cropland, or vegetation), the mean SUHI of the each subtype of UGS in each mapping year was calculated (Figure 6). All UGS subtypes have negative SUHI values, while the two non-UGS subtypes (barren and built-up) have positive values. This verifies the fact that UGS alleviates local LST, and non-UGS enhances it. It is noticeable that the SUHI of some types changed during the study period. With regard to built-up areas, SUHI increased dramatically from less than 1 K in 1998 to about 4 K in 2018. This implies that the growth of built-up area not only enlarges the area of SUHI but also enhances the intensity of heat islands. On the contrary, with a decrease in water area, SUHI decreased. Given that the area of vegetation has barely changed, the decrease of SUHI is mainly due to the growth of the temperature difference between vegetation and built-up area, which results from the fact that the growth of built-up area could enhance local LST.

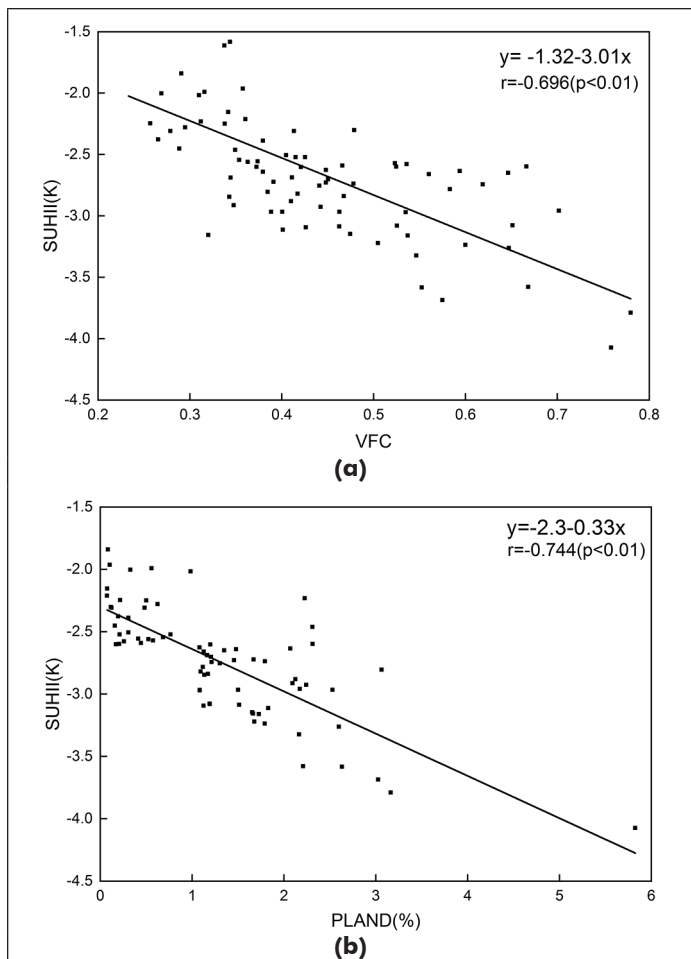


Figure 5. Relationships between urban green space characteristics and surface urban heat island index: (a) vegetation fractional coverage and (b) percentage of landscape.

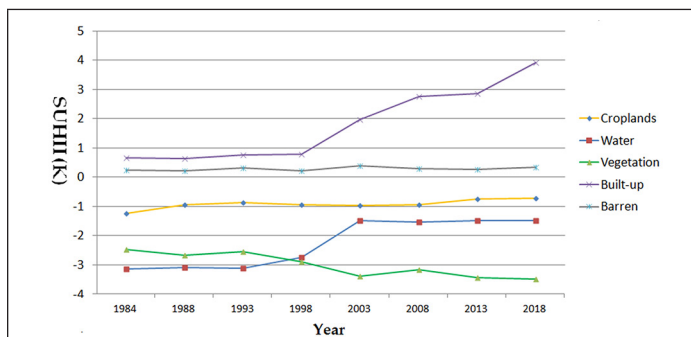


Figure 6. Mean surface urban heat island index of urban green space subtypes in each mapping year.

## Discussion

Rapid urbanization brings tremendous unprecedented pressures to a city's resources, environment, and eco-systems. The fragmentation of habitat caused by built-up construction severely influences the living environment of animals and plants. The invasion of alien plants also causes threats to native plants (Miao *et al.* 2012). UGS can significantly improve the urban environment by means of cooling, reducing noise, maintaining water and soil, and protecting biodiversity. In the urbanization process, the integrity, diversity, and distribution of UGS are being intensively interfered with by human activities (Shao and Liu 2014; Shao *et al.* 2019). Quantitative

analysis on the spatiotemporal dynamics of UGS composition and distribution is helpful for understanding the development history of UGS and the impacts of urbanization on local eco-systems and environments (Carlson and Arthur 2000).

From 1978 to 2018, about 35% of UGS was transferred into built-up area. Specifically, all croplands and more than 50% of water bodies disappeared, while the area and VFC of vegetation were kept unchanged. Among them, 5% of cropland was changed into city parks. On the other hand, built-up area increased to 6 times what it was in 1978, reflecting the dramatic speed of the city's development. It is noticeable that about 100 km<sup>2</sup> of barren land was transferred into UGS, which probably results from the endeavors of local government in UGS protection and enlargement. We also notice that most changes happened between 1992 and 2003, following the famous visitation and speech of President Xiaoping Deng in 1992. During that time, about 70% of croplands disappeared, and built-up area increased from about 400 km<sup>2</sup> to more than 800 km<sup>2</sup>.

Although the area of vegetation did not expand, the number and density of its patches increased. This shows that the relatively natural state was intensively interfered with by human activities (e.g., traffic systems and community constructions) and then changed into an artificial form. The fluctuating tendency of UGS patch shapes was evidently influenced by the changing awareness of local government regarding the priority balance between economic development and environmental protection. Nowadays, UGS is well protected and utilized, as sustainable development and environmental protection have become popular.

With regard to the urban thermal environment, both LST and SUHII display clear upward trends according to the temperature retrieval results and meteorological observations. The rapid expansion of impervious surface and loss of UGS led to the spread of SUHIs. This brings serious threats to citizens' health and economic activities and the urban environment (Connors *et al.* 2013; Ren 2015; Mariani *et al.* 2016). During the study period, the city's SUHIs gradually expanded from several isolated patches to a great connected heat region, accounting for about 50% of the whole area. Its spatiotemporal dynamics are in accordance with the growth of built-up areas. In 2003, SUHIs were mainly located in Longgang and Baoshan Districts, and the mean SUHII was about 1 K. Since then, the SUHIs have grown to all other districts and the mean SUHII has increased to about 3 K. Strong heat islands mainly occur in residential areas, commercial areas, industrial areas, and transportation roads, as their surfaces are mainly impermeable materials such as metal, asphalt, and cement. Furthermore, higher population density and human activities there have led to more heat emissions. On the other hand, the LST of UGS (water, parks, forests, and cropland) is much lower. Great cold islands were found at city parks, such as Yangtashan Park, Bijiashan Park, and Wutongshan Forest Park. The study shows that UGS has a significantly mitigating impact on urban LST, while non-UGS strongly enhances SUHI. It is noticeable that the growth of built-up area not only enlarged the area of SUHIs but also intensified heat islands (Sun *et al.* 2016; Z. Yu *et al.* 2019). Thus, relocating dense industrial parks and enlarging UGS should be implemented to alleviate SUHIs.

Although UGS is of significance for improving the urban living environment, its adverse effects should not be ignored (Niinemets, Loreto, and Reichstein 2004; Terra, Campos, and Martins 2018). The volatile organic compounds emitted by plants are prone to photooxidation reactions. These reactions generate harmful air pollutants, such as secondary organic aerosols (Mazzatenta *et al.* 2015). Given that volatile organic compounds released by plants account for more than 90% of all emissions, improper design of vegetation types and distributions would lead to great threats to human health.

Therefore, UGS constructions and rebuilding must be carefully carried out based on comprehensive and detailed investigations into the city's economy, culture, landscape, climate, and environment.

## Conclusions

Shenzhen has experienced dramatic economic development and urban expansion since 1978. In the process, UGS has been substantially and frequently interfered with by human activities. This study investigated the spatiotemporal dynamics of the UGS landscape and its influence on urban thermal environment. From 1978 to 2018, all croplands and more than 50% of water bodies disappeared; the area of vegetation remained unchanged, while built-up area increased more than six times. During the study period, the city's SUHIs gradually expanded from several isolated patches to a great connected heat region, accounting for about 50% of the whole area. Its spatiotemporal dynamics are accordance with the growth of built-up areas. The study reveals that UGS is vital to mitigating urban heat islands, but volatile organic compounds emitted by plants are prone to photooxidation reactions. Therefore, UGS construction must be carefully planned based on comprehensive investigations. The results will be of great significance for improving UGS management, alleviating UHI effects, and establishing a sustainable eco-environment for developing cities.

## Acknowledgments

We thank the editors and three anonymous reviewers for their careful reading of our manuscript and their many constructive comments and suggestions. This study was sponsored by the Open Fund of Key Laboratory of Urban Land Resources Monitoring and Simulation, Ministry of Natural Resources (KF-2018-03-055), and by the Natural Science Foundation of China under grant 41772352. The authors declare no conflict of interest.

## References

- Bandyopadhyay, M., J.A.N. van Aardt, K. Cawse-Nicholson and E. Ientilucci. 2017. On the fusion of LiDAR and aerial color imagery to detect urban vegetation and buildings. *Photogrammetric Engineering and Remote Sensing* 83 (2):123–136.
- Cai, D., K. Fraedrich, Y. Guan, S. Guo and C. Zhang. 2017. Urbanization and the thermal environment of Chinese and US-American cities. *Science of the Total Environment* 589:200–211.
- Carlson, T. N. and S. T. Arthur. 2000. The impact of land use-land cover changes due to urbanization on surface microclimate and hydrology: A satellite perspective. *Global and Planetary Change* 25 (1–2):49–65.
- Chapman, S., J.E.M. Watson, A. Salazar, M. Thatcher and C. A. McAlpine. 2017. The impact of urbanization and climate change on urban temperatures: A systematic review. *Landscape Ecology* 32 (10):1921–1935.
- Chen, W., H. Huang, J. Dong, Y. Zhang, Y. Tian and Z. Yang. 2018. Social functional mapping of urban green space using remote sensing and social sensing data. *ISPRS Journal of Photogrammetry and Remote Sensing* 146:436–452.
- Clark, M. L. and D. A. Roberts. 2012. Species-level differences in hyperspectral metrics among tropical rainforest trees as determined by a tree-based classifier. *Remote Sensing* 4 (6):1820–1855.
- Connors, J. P., C. S. Galletti and W.T.L. Chow. 2013. Landscape configuration and urban heat island effects: Assessing the relationship between landscape characteristics and land surface temperature in Phoenix, Arizona. *Landscape Ecology* 28 (2):271–283.
- Damodaran, B. B., J. Höhle and S. Lefèvre. 2017. Attribute profiles on derived features for urban land cover classification. *Photogrammetric Engineering and Remote Sensing* 83 (3):183–193.
- Dewan, A. M., M. H. Kabir, K. Nahar and M. Z. Rahman. 2012. Urbanisation and environmental degradation in Dhaka Metropolitan Area of Bangladesh. *International Journal of Environment and Sustainable Development* 11 (2):118–147.
- Di, S., Z.-L. Li, R. Tang, X. Pan, H. Liu and Y. Niu. 2019. Urban green space classification and water consumption analysis with remote-sensing technology: A case study in Beijing, China. *International Journal of Remote Sensing* 40 (5–6):1909–1929.
- Ding, L., Z. Shao, H. Zhang, C. Xu and D. Wu. 2016. A comprehensive evaluation of urban sustainable development in China based on the TOPSIS-entropy method. *Sustainability* 8 (8):746.
- Duro, D. C., S. E. Franklin and M. G. Dubé. 2012. Multi-scale object-based image analysis and feature selection of multi-sensor earth observation imagery using random forests. *International Journal of Remote Sensing* 33 (14):4502–4526.
- Founda, D. and M. Santamouris. 2017. Synergies between urban heat island and heat waves in Athens (Greece), during an extremely hot summer (2012). *Scientific Reports* 7:10973.
- FRAGSTATS: Spatial Pattern Analysis Program for Categorical Maps. n.d. <<https://www.umass.edu/landeco/research/fragstats/fragstats.html>> Accessed 10 May 2019.
- Gislason, P. O., J. A. Benediktsson and J. R. Sveinsson. 2006. Random Forests for land cover classification. *Pattern Recognition Letters* 27 (4):294–300.
- Grêt-Regamey, A., S.-E. Rabe, R. Crespo, S. Lautenbach, A. Ryffel and B. Schlup. 2014. On the importance of non-linear relationships between landscape patterns and the sustainable provision of ecosystem services. *Landscape Ecology* 29 (2):201–212.
- Hargis, C. D., J. A. Bissonette and J. L. David. 1998. The behavior of landscape metrics commonly used in the study of habitat fragmentation. *Landscape Ecology* 13 (3):167–186.
- Hermosilla, T., M. A. Wulder, J. C. White, N. C. Coops and G. W. Hobart. 2015. An integrated Landsat time series protocol for change detection and generation of annual gap-free surface reflectance composites. *Remote Sensing of Environment* 158:220–234.
- Hunter, A. J. and G. W. Luck. 2015. Defining and measuring the social-ecological quality of urban greenspace: A semi-systematic review. *Urban Ecosystems* 18 (4):1139–1163.
- Intergovernmental Panel on Climate Change. 2014. *Contribution of Working Group II to the Fifth Assessment Report of the Intergovernmental Panel on Climate Change*. Cambridge, UK: Cambridge University Press.
- Jim, C. Y. 2013. Sustainable urban greening strategies for compact cities in developing and developed economies. *Urban Ecosystems* 16 (4):741–761.
- Jiménez-Muñoz, J. C., J. A. Sobrino, D. Skokovi, C. Mattar and J. Cristóbal. 2014. Land surface temperature retrieval methods from Landsat-8 thermal infrared sensor data. *IEEE Geoscience and Remote Sensing Letters* 11 (10):1840–1843.
- Lawrence, R. L., S. D. Wood and R. L. Sheley. 2006. Mapping invasive plants using hyperspectral imagery and Breiman Cutler classifications (randomForest). *Remote Sensing of Environment* 100 (3):356–362.
- Lehman, A. 2005. *JMP for Basic Univariate and Multivariate Statistics: A Step-by-Step Guide*. Cary, N.C.: SAS Press.
- Li, D., J. Ma, T. Cheng, J. L. van Genderen and Z. Shao. 2018. Challenges and opportunities for the development of megacities. *International Journal of Digital Earth* 12 (12):1382–1395.
- Li, H., C. Wang, C. Zhong, A. Su, C. Xiong, J. Wang and J. Liu. 2017. Mapping urban bare land automatically from Landsat imagery with a simple index. *Remote Sensing* 9 (3):249.
- Li, H., C. Wang, C. Zhong, Z. Zhang and Q. Liu. 2017. Mapping typical urban LULC from Landsat imagery without training samples or self-defined parameters. *Remote Sensing* 9 (7):700.
- Liu, Y., H. Li, P. Gao and C. Zhong. 2020. Monitoring the detailed dynamics of regional thermal environment in a developing urban agglomeration. *Sensors* 20 (4):1197.
- Mariani, L., S. G. Parisi, G. Cola, R. Laforteza, G. Colangelo and G. Sanesi. 2016. Climatological analysis of the mitigating effect of vegetation on the urban heat island of Milan, Italy. *Science of the Total Environment* 569–570:762–773.

- Martha, T. R., N. Kerle, V. Jetten, C. J. van Westen and K. V. Kumar. 2010. Characterising spectral, spatial and morphometric properties of landslides for semi-automatic detection using object-oriented methods. *Geomorphology* 116 (1–2):24–36.
- Mazzatenta, A., M. Pokorski, F. Sartucci, L. Domenici and C. Di Giulio. 2015. Volatile organic compounds (VOCs) fingerprint of Alzheimer's disease. *Respiratory Physiology & Neurobiology* 209:81–84.
- Miao, X., J. S. Heaton, S. Zheng, D. A. Charlet and H. Liu. 2012. Applying tree-based ensemble algorithms to the classification of ecological zones using multi-temporal multi-source remote-sensing data. *International Journal of Remote Sensing* 33 (6):1823–1849.
- Moseley, D., M. Marzano, J. Chetcuti and K. Watts. 2013. Green networks for people: Application of a functional approach to support the planning and management of greenspace. *Landscape and Urban Planning* 116:1–12.
- Navigant Consulting. XXXX. *Assessment of International Urban Heat Island Research*. Report to U.S. Department of Energy. <URL>. Accessed 30 April 2014.
- Niinemets, Ü., F. Loreto and M. Reichstein. 2004. Physiological and physicochemical controls on foliar volatile organic compound emissions. *Trends in Plant Science* 9 (4):180–186.
- Overview of Shenzhen. Shenzhen People's Government. 2016. <URL>. Accessed 25 October 2018.
- Qian, Y., W. Zhou, W. Li and L. Han. 2015. Understanding the dynamic of greenspace in the urbanized area of Beijing based on high resolution satellite images. *Urban Forestry & Urban Greening* 14 (1):39–47.
- Qin, Z., A. Karnieli and P. Berliner. 2001. A mono-window algorithm for retrieving land surface temperature from Landsat TM data and its application to the Israel-Egypt border region. *International Journal of Remote Sensing* 22 (18):3719–3746.
- Peng, J., J. Jia, Y. Liu, H. Li and J. Wu. 2018. Seasonal contrast of the dominant factors for spatial distribution of land surface temperature in urban areas. *Remote Sensing of Environment* 215:255–267.
- Ramamurthy, P. and E. Bou-Zeid. 2017. Heatwaves and urban heat islands: A comparative analysis of multiple cities. *Journal of Geophysical Research: Atmospheres* 122 (1):168–178.
- Ren, G. 2015. Urbanization as a major driver of urban climate change. *Advances in Climate Change Research*, vol.6 (1): 1–6.
- Rivers, M. Inside China's Silicon Valley: From copycats to innovation. CNNXXXX. <URL>. Retrieved Accessed 1 September 2019.
- Rodriguez-Galiano, V. F., B. Ghimire, J. Rogan, M. Chica-Olmo and J. P. Rigol-Sanchez. 2012. An assessment of the effectiveness of a random forest classifier for land-cover classification. *ISPRS Journal of Photogrammetry and Remote Sensing* 67:93–104.
- Rozenstein, O., Z. Qin, Y. Derimian and A. Karnieli. 2014. Derivation of land surface temperature for Landsat-8 TIRS using a split window algorithm. *Sensors* 14 (4):5768–5780.
- Shao, Z., L. Ding, D. Li, O. Altan, M. E. Huq and C. Li. 2020. Exploring the relationship between urbanization and ecological environment using remote sensing images and statistical data: A case study in the Yangtze River Delta, China. *Sustainability* 12 (14):5620.
- Shao, Z., H. Fu, D. Li, O. Altan and T. Cheng. 2019. Remote sensing monitoring of multi-scale watersheds impermeability for urban hydrological evaluation. *Remote Sensing of Environment* 232:111338.
- Shao, Z., C. Li, D. Li, O. Altan, L. Zhang and L. Ding. 2020. An accurate matching method for projecting vector data into surveillance video to monitor and protect cultivated land. *ISPRS International Journal of Geo-Information* 9 (7):448.
- Shao, Z. and C. Liu. 2014. The Integrated use of DMSP-OLS nighttime light and MODIS data for monitoring large-scale impervious surface dynamics: A case study in the Yangtze River Delta. *Remote Sensing* 6 (10):9359–9378.
- Shih, W. 2017. Greenspace patterns and the mitigation of land surface temperature in Taipei metropolis. *Habitat International* 60:69–80.
- Sobrino, J. A., J. C. Jiménez-Muñoz and L. Paolini. 2004. Land surface temperature retrieval from Landsat TM 5. *Remote Sensing of Environment* 90 (4):434–440.
- Su, S., R. Xiao, Z. Jiang and Y. Zhang. 2012. Characterizing landscape pattern and ecosystem service value changes for urbanization impacts at an eco-regional scale. *Applied Geography* 34:295–305.
- Sun, Y., X. Zhang, G. Ren, F. W. Zwiers and T. Hu. 2016. Contribution of urbanization to warming in China. *Nature Climate Change* 6 (7):706–709.
- Tan, J., Y. Zheng, X. Tang, C. Guo, L. Li, G. Song, X. Zhen, D. Yuan, A. J. Kalkstein, F. Li and H. Chen. 2010. The urban heat island and its impact on heat waves and human health in Shanghai. *International Journal of Biometeorology* 54 (1):75–84.
- Tan, M. Y., C. Li, H. Li and L. Zhang. 2010. Study on the characteristics of spatio-temporal changes of Shenzhen urban heat island based on Landsat TM. Annual meeting of China Meteorological Society.
- Terra, W. C., V. P. Campos, S. J. Martins, L.S.A.S. Costa, J.C.P. da Silva, A. F. Barros, L. E. Lopez, T.C.N. Santos, G. Smant and D. F. Oliveira. 2018. Volatile organic molecules from *Fusarium oxysporum* strain 21 with nematocidal activity against *Meloidogyne incognita*. *Crop Protection* 106:125–131.
- L. J. A. A. K. Hahs, N. E. Stork, N.S.G. Williams and S. J. Livesley. *Journal of Applied Ecology*:The rise of China's "Silicon Valley" (Narrator). XX Month XXXX, CNN video. <https://xxxx.xxxx>. Accessed 1 December 2018.
- Threlfall, C. G., L. Mata, J. A. Mackie, A. K. Hahs, N. E. Stork, N.S.G. Williams and S. J. Livesley. 2017. Increasing biodiversity in urban green spaces through simple vegetation interventions. *Journal of Applied Ecology* 54 (6):1874–1883.
- World Shipping Council. XXXX. <URL>. Accessed World Health Organization. 2016. Urban Green Spaces and Health: A Review of the Evidence. <URL>. Accessed XX Month XXXX.
- World Shipping Council. XXXX. Top 50 World Container Ports. XXXX. <URL>. Accessed 16 October 2019.
- Xu, B., Y. Ye and L. Nie. 2012. An improved random forest classifier for image classification. Pages XXX–XXX in *2012 IEEE International Conference on Information and Automation*, held in Shenyang, China, 6–8 June 2012. Edited by J. Editor. City, St.: Publisher.
- Yeandle, M. and M. Wardle. 2019. *The Global Financial Centres Index 26*. City, Country: Long Finance. <URL>. Accessed 3 October 2019.
- Yu, X., X. Guo and Z. Wu. 2014. Land surface temperature retrieval from Landsat 8 TIRS—comparison between radiative transfer equation-based method, split window algorithm and single channel method. *Remote Sensing* 6 (10):9829–9852.
- Yu, Z., Y. Yao, G. Yang, X. Wang and H. Vejre. 2019. Strong contribution of rapid urbanization and urban agglomeration development to regional thermal environment dynamics and evolution. *Forest Ecology and Management* 446:214–225.
- Zhang, E.-J., J.-J. Zhang, X.-Y. Zhao and X.-L. Zhang. 2008. Study on urban heat island effect in Shenzhen. *Journal of Natural Disasters* 17 (2):19–24.
- Zhang, H., X. Ning, Z. Shao and H. Wang. 2019. Spatiotemporal pattern analysis of China's cities based on high-resolution imagery from 2000 to 2015. *ISPRS International Journal of Geo-Information* 8 (5):241.
- Zhao, C., D. Zheng and W. He. 2004. Vegetation cover changes over time and its effects on resistance to wind erosion. *Acta Phytocologica Sinica* 29 (1):68–73.
- Zhong, C., C. Wang, H. Li, W. Chen and Y. Hou. 2018. Mapping inter-annual land cover variations automatically based on a novel sample transfer method. *Remote Sensing* 10 (9):1457.

# WHO'S WHO IN ASPRS

## BOARD OF DIRECTORS

### BOARD OFFICERS

#### President

Jeff Lovin  
*Woolpert*

#### President-Elect

Jason M. Stoker, Ph.D.  
*U.S. Geological Survey*

#### Vice President

Christopher Parrish, Ph.D.  
*Oregon State University*

#### Past President

Thomas Jordan, Ph.D.  
*University of Georgia*

#### Treasurer

Stewart Walker, Ph.D.  
*photogrammetry4u*

#### Secretary

Lorraine B. Amenda, PLS, CP

### BOARD MEMBERS

#### Sustaining Members Council – 2021

Chair: Joe Cantz  
[www.asprs.org/About-Us/Sustaining-Members-Council.html](http://www.asprs.org/About-Us/Sustaining-Members-Council.html)

#### Committee Chairs Council – 2022

Chair: Mike Zoltek  
Vice-Chair: TBA

#### Early-Career Professionals Council – 2021

Chair: Bobby Arlen  
Vice Chair: Melissa Martin

#### Region Officers Council – 2021

Chair: Lorraine B. Amenda, PLS, CP  
Vice Chair: Demetrio Zourarakas

#### Student Advisory Council – 2021

Chair: Youssef Kaddoura  
<http://www.asprs.org/Students/Student-Advisory-Council.html>

#### Technical Division Directors Council – 2021

Chair: Bandana Kar, Ph.D.  
Vice Chair: Denise G. Theunissen

### TECHNICAL DIVISION OFFICERS

#### Geographic Information Systems Division – 2021

Director: Xan Fredericks  
Assistant Director: Denise G. Theunissen  
[www.asprs.org/Divisions/GIS-Division.html](http://www.asprs.org/Divisions/GIS-Division.html)

#### Lidar Division – 2022

Director: Joshua Nimetz, CMS  
Assistant Director: Ajit Sampath  
[www.asprs.org/Divisions/Lidar-Division.html](http://www.asprs.org/Divisions/Lidar-Division.html)

#### Photogrammetric Applications Division – 2022

Director: Kurt Rogers  
Assistant Director: Benjamin Wilkinson  
[www.asprs.org/Divisions/Photogrammetric-Applications-Division.html](http://www.asprs.org/Divisions/Photogrammetric-Applications-Division.html)

#### Primary Data Acquisition Division – 2021

Director: Jon Christopherson  
Assistant Director: J. Chris Ogier  
[www.asprs.org/Divisions/Primary-Data-Aquisition-Division.html](http://www.asprs.org/Divisions/Primary-Data-Aquisition-Division.html)

#### Professional Practice Division – 2022

Director: Harold W. Rempel, III, CP  
Assistant Director: Bill Swope  
[www.asprs.org/Divisions/Professional-Practice-Division.html](http://www.asprs.org/Divisions/Professional-Practice-Division.html)

#### Remote Sensing Applications Division – 2022

Director: Raechel A. Portelli, Ph.D.  
Assistant Director: Amr Abd-Elrahman  
[www.asprs.org/Divisions/Remote-Sensing-Applications-Division.html](http://www.asprs.org/Divisions/Remote-Sensing-Applications-Division.html)

#### Unmanned Autonomous Systems (UAS) – 2022

Director: Megan Ritelli, Ph.D.  
Assistant Director: Dan Hubert

### REGION PRESIDENTS

#### Alaska Region

David Parret  
<http://www.asprsalaska.org/>

#### Cascadia Region

Robert Hairston-Porter

#### Eastern Great Lakes Region

Shawana P. Johnson, Ph.D, GISP  
<http://egl.asprs.org/>

#### Florida Region

Xan Fredericks  
<http://florida.asprs.org/>

#### Heartland Region

Whit Lynn  
<http://heartland.asprs.org/>

#### Mid-South Region

<https://www.asprs.org/all-regions/mid-south.html>

#### Northeast Region

(representing the merger of The New England and Central New York Regions)  
Trevis Gigliotti, Interim President

#### North Atlantic Region

Richard W. Carlson, Jr., P.L.S., C.P.  
<http://natlantic.asprs.org/>

#### Pacific Southwest Region

Omar G. Mora  
<https://pswasprs.org/>

#### Potomac Region

Dave Lasko  
<http://www.asprspotomac.org/>

#### Rocky Mountain Region

<http://www.asprs-rmr.org/>

#### Western Great Lakes Region

Brandon Krumwiede  
<http://wgl.asprs.org/>

# A Soil and Impervious Surface Adjusted Index for Urban Impervious Surface Area Mapping

Yanyi Zhang, Yugang Tian, and Lihao Zhang

## Abstract

*Index-based methods are widely applied to urban impervious surface area (ISA) mapping, but the confusion between ISA and soil remains unsolved. In this article, the near-infrared (NIR)-blue bands were selected as feature space by analyzing the spectra from the US Geological Survey spectral library, and a simple impervious surface ratio index (ISRI) was developed by shifting the NIR-blue coordinate origin toward the convergence point of the fitting lines of ISA and soil. The ISRI was then validated for threshold simulation, separability, and correlation analysis. Results demonstrated that ISRI had a good performance for ISA mapping in four cities in China with different geographic environments, with all extraction accuracies all above 90%. ISRI had a high separability between ISA and soil and was better than other indices (normalized difference built-up index and biophysical composition index). Further, ISRI has a close relationship with the ISA proportion. Therefore, ISRI would be a simple and reliable index for urban ISA mapping.*

## Introduction

Rapid global urbanization over past 50 years has led to great changes in global land cover, manifesting as a large number of previously natural landscapes being replaced by urban impervious surfaces, exerting negative effects on natural ecosystems, hydrology, climate, and biodiversity (Turner *et al.* 1994; Deng and Wu 2012). As a result, the ecological environment is facing severely high pressure (Blair 1996; Elvidge *et al.* 2007; Grimm *et al.* 2008; Utz *et al.* 2011). Therefore, advance well urban planning is urgently needed, for which mapping the distribution of impervious surface in a timely manner and accurately is critically important. A growing number of studies on the distribution estimation and expansion of urban impervious surfaces have been done in many developed countries (Xian and Homer 2010).

Impervious surface area (ISA), as an important indicator of the urban eco-environment, refers to a surface covering that lacks water permeability, including asphalt, cement roads, roofs, airports, and other building facilities that are closely related to human life, as well as other natural impervious surfaces in the city (Arnold and Gibbons 1996; Blair 1996; Sloanecker *et al.* 2001; Matsushita *et al.* 2014). For ISA mapping, manpower- and material resources-consuming traditional methods are apparently completely incompetent to meet the progressively increasing current demands, which require fast, large-scale covering and real-time measurement. With the development of satellites, remote sensing technology has been widely used in research on urban impervious surfaces with its advantages of dynamicity, rapidity, periodicity, and wide coverage (Shao and Liu 2014; Cooper *et al.* 2017; Shao *et al.* 2019). On the basis of the vegetation-impervious surface-soil (V-I-S) urban conceptual distribution model, which was

proposed by Ridd (1995) using three main physical components to summarize urban environments, methods for ISA mapping can be roughly divided into four categories: spectral mixture analysis (SMA), regression analysis, image classification, and spectral index.

SMA extracts ISA based on the assumption that a pixel is composed of different but fixed endmembers in proportion (Phinn *et al.* 2002; Wu and Murray 2003; Wu 2004). Further modification for it has been proposed as multiple-endmember spectral mixture analysis, considering that different pixels should have different endmembers (Roberts *et al.* 1998; Rashed *et al.* 2003; Powell *et al.* 2007; Franke *et al.* 2009). However, the computational complexity and difficulty in obtaining pure endmembers under complex environments hinders SMA's application in mapping a wide range of ISA (Plaza *et al.* 2004; Somers *et al.* 2011). Regression analysis calculates ISA mainly using the relationship between ISA proportions and other urban component characteristics (Bauer *et al.* 2002; Esch *et al.* 2009), such as the negative correlation existing between vegetation and ISA (Weng *et al.* 2004). A positive correlation of the extraction results has been found between the high-resolution and low-resolution images (Lu *et al.* 2011). Some of the data for regression analysis, for instance, season-dependent vegetation cover, may vary greatly, which definitely affects the stability and accuracy of the ISA extraction results (Weng 2012). Image classification includes maximum likelihood classification (McIver and Friedl 2002; Richards 2013), support vector machine (Bazi and Melgani 2006; Durbha *et al.* 2007; Turker and Koc-San 2015), object-oriented classification (Miller *et al.* 2009; Bhaskaran *et al.* 2010; Cai and Jin 2016; Nagel and Yuan 2016), artificial neural network (Hu and Weng 2009; Van de Voorde *et al.* 2009), random forest classifier (Shao *et al.* 2016), and deep learning classification (Kussul *et al.* 2017). Its accuracy for ISA mapping depends mainly on the model accuracy, which is affected mostly by sample size, quality, and segmentation threshold (Foody and Arora 1997; Lu and Weng 2007).

A common problem of the first three methods is algorithm complexity at a certain degree, which prevents them from being implemented in mapping large areas. Therefore, relatively simple spectral indices with high efficiency have been proposed. According to the composition of indices, they can be divided into two categories. The first is constructed by the original spectral band, including impervious surface area index (ISAI) (Carlson and Traci Arthur 2000), normalized difference built-up index (NDBI) (Zha *et al.* 2003), normalized difference impervious surface index (NDISI) (Xu 2010), biophysical composition index (BCI) (Deng and Wu 2012), normalized difference impervious index (NDII) (Wang *et al.* 2015), and perpendicular impervious surface index (PISI) (Tian *et al.* 2018). The second is constructed by the existing

Photogrammetric Engineering & Remote Sensing  
Vol. 87, No. 2, February 2021, pp. 91–104.  
0099-1112/21/91–104

© 2021 American Society for Photogrammetry  
and Remote Sensing  
doi: 10.14358/PERS.87.2.91

Yanyi Zhang, Yugang Tian, and Lihao Zhang are with the School of Geography and Information Engineering, China University of Geosciences, Wuhan, China (ygangtian@cug.edu.cn).

indices, namely, composite indices, including index-based built-up index (IBI) (Xu 2008), modified normalized difference impervious surface index (MNDISI) (Liu *et al.* 2013), normalized urban area composite index (NUACI) (Liu *et al.* 2015), normalized difference urban index (NDUI) (Zhang *et al.* 2015), combinational built-up index (CBI) (Sun *et al.* 2016), and combinational biophysical composition index (Zhang *et al.* 2018). However, most spectral indices cannot efficiently separate soil from ISA because of their similar spectral characteristics and the complexity of urban compositions. For instance, NDBI's mid-infrared and near-infrared (NIR) bands theoretically enhance the impervious surface information but also highlight soil information, which makes NDBI extraction results often affected by sparse vegetation and bare soil (Chen and Chen 2006). Therefore, good extraction results could be obtained only if indices focusing on a specific area or with special assistance: ISAI, an index being applicable to building areas, may overestimate ISA in nonbuilding areas with less vegetation coverage; BCI needs the tasseled cap (TC) transformation, which is not available in all sensors; NDISI and MNDISI can efficiently map building areas by utilizing the thermal infrared band that is also not provided by most sensors; MNDISI is not suitable for wide application due to its complex calculation; and NDBI application requires bare soil being masked out in advance due to its incapability to extract bare soil. Other indices mentioned above also have their respective defects. The composite indices solve the problem of the confusion between bare soil and ISA to a certain extent but with the accuracy dependent on the constituent indices and requiring relatively complicated calculations. Some indices' applying scopes are limited by the data they use, such as NUACI and NDUI.

As mentioned, the present indices with respective shortcomings are not yet perfect enough to efficiently apply for large-area ISA mapping, and the problem of confusion between ISA and bare soil is far from being completely resolved. Therefore, this article proposed a simple index, the impervious surface ratio index (ISRI), which is derived by coordinate transformation to enhance the separability between ISA and other urban components, especially soil.

The remainder of this article is structured as follows. The next section introduces the study area and data. The following section presents the methodology of ISRI development in detail, including band selection, ISRI development, and ISRI threshold determination. The methodology of ISRI evaluation, including accuracy analysis, separability analysis, correlation analysis, and comparative analysis, is reported next. Finally, results and a discussions and conclusions are provided. A flowchart of the proposed ISRI is shown in Figure 1.

## Study Area and Data

### Study Area

Four cities are selected as study areas that represent different states of soil and impervious surface under different geographic environments (Figure 2). Xi'an (33.43°N, 107.44°E), located in the western part of China, is the core city of the Guanzhong Plain urban agglomeration and the starting point of the Silk Road, with a total area of 9983 km<sup>2</sup>, and has a complex and diverse landscape, with a warm temperate semihumid continental monsoon climate. Xining (36.56°N, 101.74°E), located in the northwest part of China, is the largest city in the Tibetan Plateau, with a land area of 7679 km<sup>2</sup>, and belongs to a cold semiarid climate. Wuhan (30.52°N, 114.31°E) is not only the central city in central China but also the core city of the Yangtze River Economic Belt with a land area of 8561 km<sup>2</sup>, and its central terrain is low and flat, but the south part is hilly, with the Yangtze and Han rivers flowing through the city. Moreover, Wuhan has a humid subtropical monsoon climate with abundant rainfall and four distinct seasons. Fuzhou (26.08°N, 119.30°E), located on the southeast coast of China, is a central city in the economic zone on the west side of the straits with the total land area of 11 968 km<sup>2</sup>.

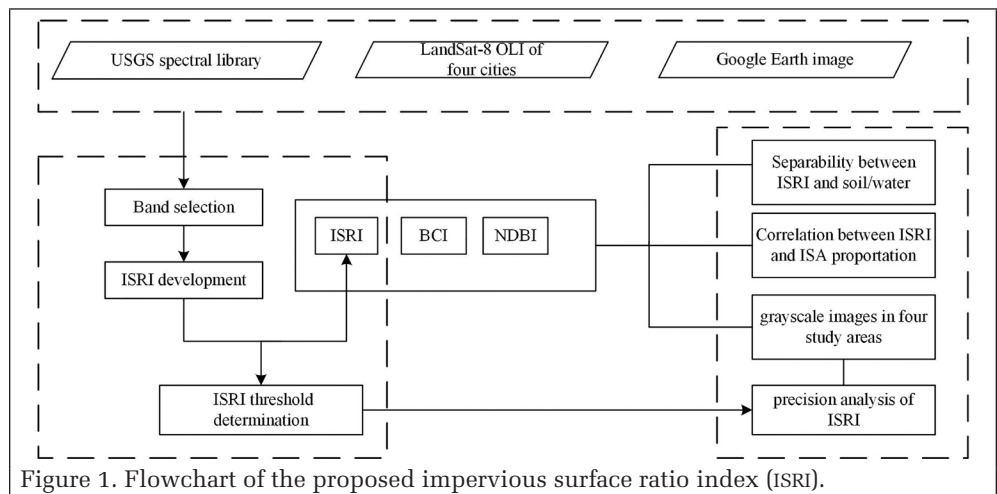


Figure 1. Flowchart of the proposed impervious surface ratio index (ISRI).

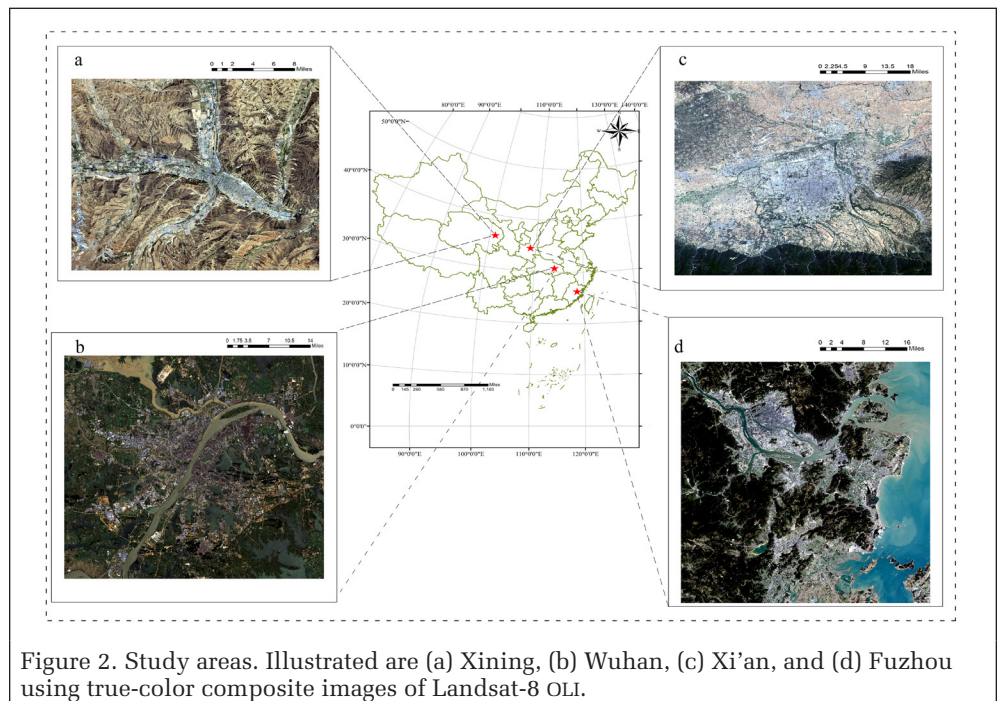


Figure 2. Study areas. Illustrated are (a) Xining, (b) Wuhan, (c) Xi'an, and (d) Fuzhou using true-color composite images of Landsat-8 OLI.

It belongs to subtropical monsoon climate and has abundant rainfall and high vegetation coverage.

### Data

Data used in this article are from the US Geological Survey (USGS) spectral library (Kokaly *et al.* 2017) and Landsat-8 OLI images, mainly for the purpose of experiments and verifications.

The data in the spectral library are compiled by researchers in the spectroscopy laboratory through measuring the spectral reflectance of hundreds of materials. The USGS spectral library was developed based on the JPL spectral library by the USGS for the remote sensing of mineral resources. Samples included in the library contain minerals, rocks, soils, physically constructed as well as mathematically computed mixtures, plants, vegetation communities, microorganisms, and man-made materials. In order to ensure the consistency of spectral resolution, in this article only the spectra that have been resampled to the spectral response functions of Landsat-8 Operational Land Imager (OLI) were selected from the USGS spectral library. The library also provided the data used for index development and standard samples that are relatively pure and undisturbed by the atmosphere for later threshold simulation experiments of ISRI.

Landsat-8 OLI images of the four cities that are clear and cloud free were downloaded (Table 1), including visible, NIR, shortwave infrared (SWIR), cirrus band in 30-m resolution, and thermal infrared band in 100-m resolution. The Landsat-8 OLI level 1 images are already geometrically corrected. The projection coordinate system of Landsat-8 OLI imagery is Universal Transverse Mercator, and the geographic coordinate system is World Geodetic System 1984.

Table 1. Acquisition data of images.

Image	Area			
	Xi'an	Xining	Fuzhou	Wuhan
Landsat-8 OLI	17 Jun. 2016	10 May 2016	11 Mar. 2018	23 Jul. 2016
Google Earth	12 Aug. 2016	25 Feb. 2016	13 Jan. 2018	27 Jul. 2016

High-resolution images (0.54 m) free of clouds from Google Earth corresponding to the Landsat-8 OLI images were selected as the verification data (Figure 3). The geographic coordinates and projection coordinates of the high-resolution images are consistent with the Landsat-8 OLI imagery. The high-resolution images are used for correlation analysis and separability analysis of the proposed ISRI.

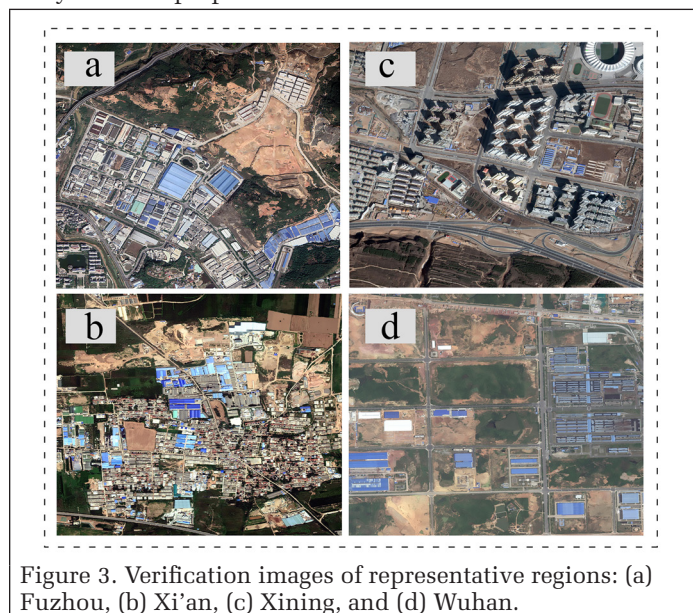


Figure 3. Verification images of representative regions: (a) Fuzhou, (b) Xi'an, (c) Xining, and (d) Wuhan.

As shown in Table 1, the acquisition data of high-resolution verification data that we selected are close to that of the corresponding Landsat-8 OLI images in order to reduce the vegetation coverage errors.

### Data Preprocessing

Prior to the spectral analysis experiment, the ISA samples, which consist of common city scenes, were selected out from the USGS spectral library, such as asphalt, metal materials, concrete, cement, plastic, and glass. Radiation calibration and atmospheric correction were performed in advance if the pixel value (DN value) was used in order to avoid the loss of the difference information between the reflectance properties of different land cover types (Haboudane *et al.* 2002; Thiemann and Kaufmann 2002). Radiometric calibration and atmospheric calibration were completed by using ENVI Radiometric Calibration and FLAASH module in this article.

## Methodology of ISRI Development

### Band Selection

Land cover types of the city are complex and diverse. In this study, urban biophysical compositions were roughly divided into three types, namely, impervious surface, vegetation, and soil, according to the V-I-S model. In order to obtain the accurate spectral characteristics of ISA and reduce spectra errors caused by the heterogeneity, the ISAs were divided into the bright ISA and the dark ISA according to their reflectance values. Specifically, the reflectance of the bright ISA is high, and the reflectance of the dark ISA is low. We selected 200 samples for each class from Landsat-8 OLI image and calculated the average of each class to plot their spectral curves, as shown in Figure 4a.

We found that the spectral curve of urban ISA is different from others in NIR-blue feature space. Specifically, the spectral curve of the dark ISA shows a gently upward trend, the spectral curve of the bright ISA rises more slowly than that of the dark ISA, and the spectral curves of both soil and vegetation are steeper than those of the ISA, where the vegetation curve is steeper than the soil curve. If the reflectance value of each urban component in NIR and blue bands is connected with a straight line, then the slopes of the reflectance of the bright and dark ISAs in NIR blue feature space are significantly smaller than those of vegetation and soil. Although there is the same pattern in blue-red feature space, the vegetation cannot be distinguished from the ISA because its spectral curve is similar to ISAs. To sum up, ISAs and other land cover types have the best separability in the NIR-blue feature space.

To further verify this phenomenon, 184 pure samples representing four kinds of urban components from the USGS spectral library were picked out (dark ISAs: 40 samples, e.g., dark paints, concrete, asphalt, dark gray brick paving, black plastic; bright ISAs: 43 samples, e.g., bright paints, glass, metal material, medium red brick, white plastic; soil: 87 samples, e.g., brown loam, silty loam, brown sand, pale brown silty loam, gray silty clay; vegetation: 14 samples, e.g., grass, conifer, redwood, weed, bush). The spectral curves of the four types of samples from the USGS are shown in Figure 4b. It is clear that the spectral curves from the USGS spectral library are very similar to those from Landsat-8 OLI images. Therefore, the ISAs can be discriminated from others according to the difference in slopes of the NIR-blue feature space. The NIR and blue bands can be selected as the feature bands for ISA spectral index development.

As shown in Figure 4, the spectral curves of each type from both kinds of data had the consistent trend. Meanwhile, when the correlation analysis between the USGS spectral library and Landsat-8 OLI is made (as shown in Table 2), it is obvious that there is a very high correlation between them. Therefore, the

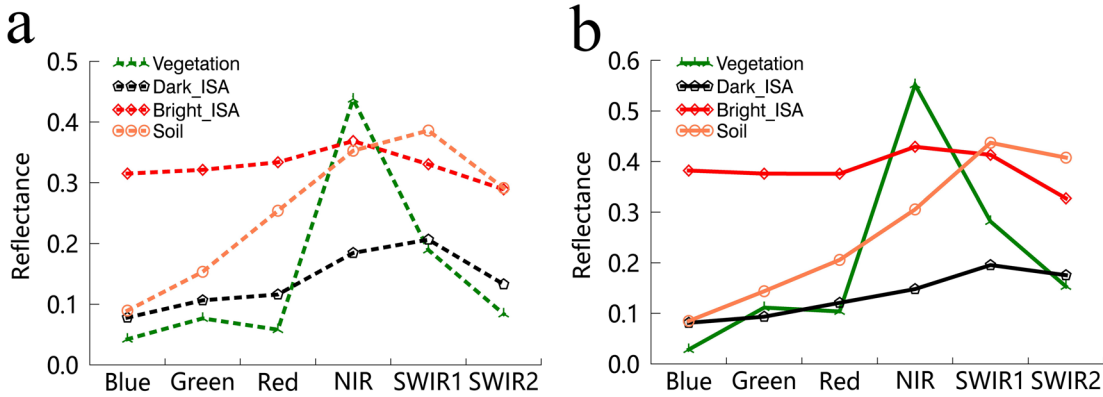


Figure 4. Spectral curves of vegetation, soil, dark ISAs, bright ISAs from the (a) Landsat-8 OLI and (b) USGS spectral library. ISA = impervious surface area; NIR = near-infrared; SWIR = short-wave infrared; USGS = US Geological Survey

Table 2. Pearson correlation coefficient between USGS spectral library and Landsat-8 OLI images.

Data Source	Urban Component			
	Bright ISA	Dark ISA	Soil	Vegetation
Spectral library with Landsat-8 OLI	0.9087	0.8573	0.8919	0.9214

ISA = impervious surface area;  
USGS = US Geological Survey.

samples from the USGS spectral library can be used for the development and the threshold simulation of the following new index.

#### ISRI Development

Based on the spectral characteristics found, the slopes of the ISAs in the NIR-blue feature space is different from those of the others. Hence, a new ratio index is proposed by using the ratio of the blue and NIR bands as follows:

$$\text{Index1} = \left( \frac{\rho_{\text{NIR}}}{\rho_{\text{Blue}}} \right), \quad (1)$$

where  $\rho_{\text{Blue}}$  and  $\rho_{\text{NIR}}$  represent the reflectance of the blue and NIR bands, respectively.

The pure spectra of the USGS spectral library are selected as the experimental samples, including 87 soil, 40 dark ISA, 43 bright ISA, and 14 vegetation samples, and then the scatter plot is drawn with  $\rho_{\text{NIR}}$  as the horizontal axis and  $\rho_{\text{Blue}}$  as the vertical axis (Figure 5a). Figure 5a shows that vegetation is distributed over soil. Accordingly, ISAs could be efficiently exacted only if ISAs and soil can be separated. However, the confusion between ISA and soil is serious when they are near the coordinate origin. The geometric form of Index1 shows straight lines passing through the coordinate origin with different slopes. Regardless of how the slope of the line is changed, ISA and soil gathering near the coordinate origin are hard to distinguish. Therefore, Index1 should be slightly adjusted.

In order to make the index easier to distinguish between ISA and soil, the coordinate origin should be translated, and then a new impervious surface ratio index is developed in the new coordinate (Figure 5b) as follows:

$$\text{Index1}' = (\rho_{\text{NIR}} + I_1) / (\rho_{\text{Blue}} + I_2). \quad (2)$$

In order to obtain the new coordinate system, the soil line and the ISA line should be fitted in advance. The samples used for fitting of the soil line and the ISA line are from the USGS spectral library. To fit the ISA line, the dark ISA and

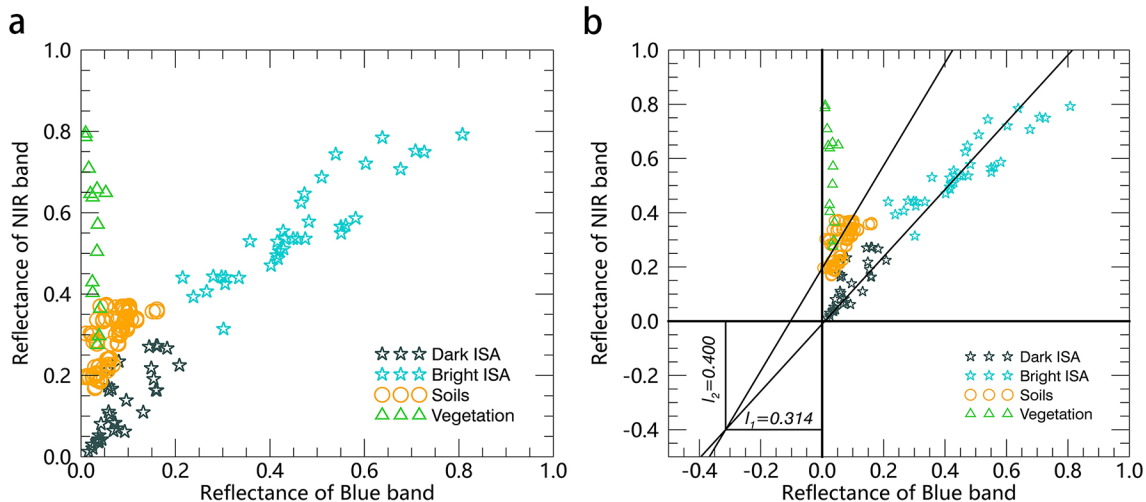


Figure 5. Scatter plot with the NIR-blue feature space: (a) original coordinate axis and (b) transformed coordinate axis. ISA = impervious surface area; NIR = near-infrared.

bright ISA samples are merged into one category. As we can find from Figure 5b, if the intersection of two fitted lines is regarded as the new coordinate origin, a reference line to distinguish the dark ISA from the soil can be easily obtained.

The Index1 coordinate is transformed by shifting the NIR-blue feature space origin toward the fitting lines convergence point of the ISA and the soil (Figure 5b). The coordinate of the new origin in the original feature space is the values of the adjustment coefficients  $I_1$  and  $I_2$ , respectively (Figure 5b).

We can further find that the Index1' value of ISA is smaller than the value of soil and vegetation. To highlight the ISAs in remotely sensed images, a reciprocal operation is performed, and the ISRI is developed as Equation 3. The corresponding result is shown in Figure 6:

$$\text{ISRI} = (\rho_{\text{blue}} + 0.314) / (\rho_{\text{NIR}} + 0.400). \quad (3)$$

In order to verify the reasonableness of ISRI development, some samples of bright ISAs, dark ISAs, bright soil, and dark soil were selected from Landsat-8 OLI images (the DN value of each pixel has been converted into reflectance). For each type, 100 pure pixels were picked out. Then index operations were performed according to Equations 1 and 3 on these samples, and the maximum and minimum index value of each type was recorded, as shown in Figure 7. The range

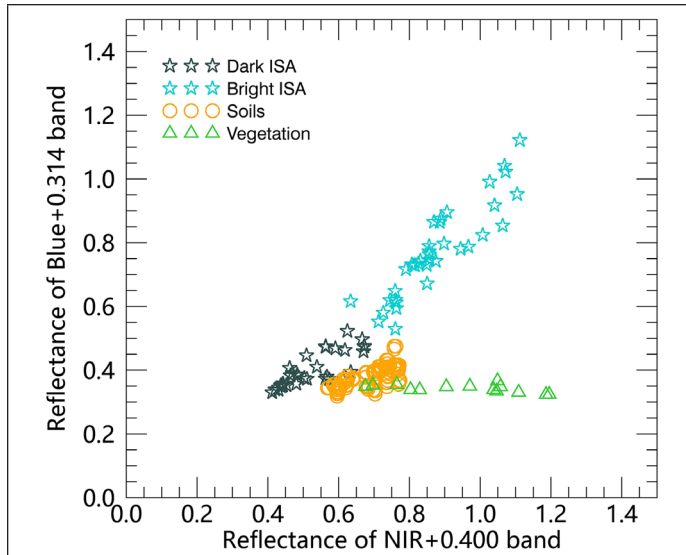


Figure 6. Scatter plots in the (Blue+0.314) and (NIR+0.400) feature space. ISA = impervious surface area; NIR = near-infrared

of the ISA Index1 value is large, and the range of the Index1 value between the dark soil and dark ISA had a significant overlap, as shown by the dotted line in Figure 2a. However, the ISRI values of ISAs (both the dark ISA and the bright ISA) in Figure 2b do not overlap with that of soil (both dark soil and bright soil), and there is a clear dividing line between them. Meanwhile, the ranges of ISRI of ISAs are less than those of Index1. These phenomena indicate that ISRI can reduce ISA's heterogeneity and that ISRI is better than Index1 in separability between ISA and soil.

### ISRI Threshold Determination

The threshold simulation experiment of ISRI is also conducted by using pure samples from the USGS spectral library. For medium-resolution images, such as Landsat-8 OLI, pure pixels are uncommon; that is, the land cover types in one pixel are complex and diverse, and the proportions of ISA, soil, and vegetation may have influences on the ISRI value. The experiment assumes that urban scenes contain only three components: ISA, soil, and vegetation; the spectral value of each pixel can be linearly mixed by a certain proportion of the spectral values of the three components. In this experiment, we regard ISA as the foreground and vegetation and soil as the background. The composition of one pixel satisfies the following equations:

$$\rho_{\text{img}} = a^* \rho_{\text{ISA}} + b^* \rho_b, \quad (4)$$

$$\rho_b = c^* \rho_{\text{soil}} + d^* \rho_{\text{veg}}, \quad (5)$$

$$a + b = 1, c + d = 1, \quad (6)$$

where  $\rho_{\text{img}}$  is the reflectance of the pixel;  $\rho_b$  denotes the reflectance of the background;  $\rho_{\text{ISA}}$  refers to the reflectance of ISA;  $\rho_{\text{soil}}$  and  $\rho_{\text{veg}}$  represent the reflectance of soil and vegetation, respectively;  $a$  and  $b$  indicate the proportions of ISA and background, respectively; and  $c$  and  $d$  signify the proportions of soil and vegetation in the background, respectively. The proportions of components in one pixel are adjusted with a unit of 0.1 according to Equation 4. A total of 11 simulation conditions were performed, and the experimental results are plotted in Figure 8.

Experimental results show that the ISRI value increases with the increasing ISA proportion in all simulation cases. When the ISA proportion is a constant, the ISRI value is directly proportional to the soil proportion in the background. We also find that the overall range of the ISRI values is [0.4961, 0.8879]. If the ISA proportion is 0, the ISRI value ranges from 0.4961 to 0.6631. Hence, when the ISRI value is within this range, the actual components may contain only soil or a

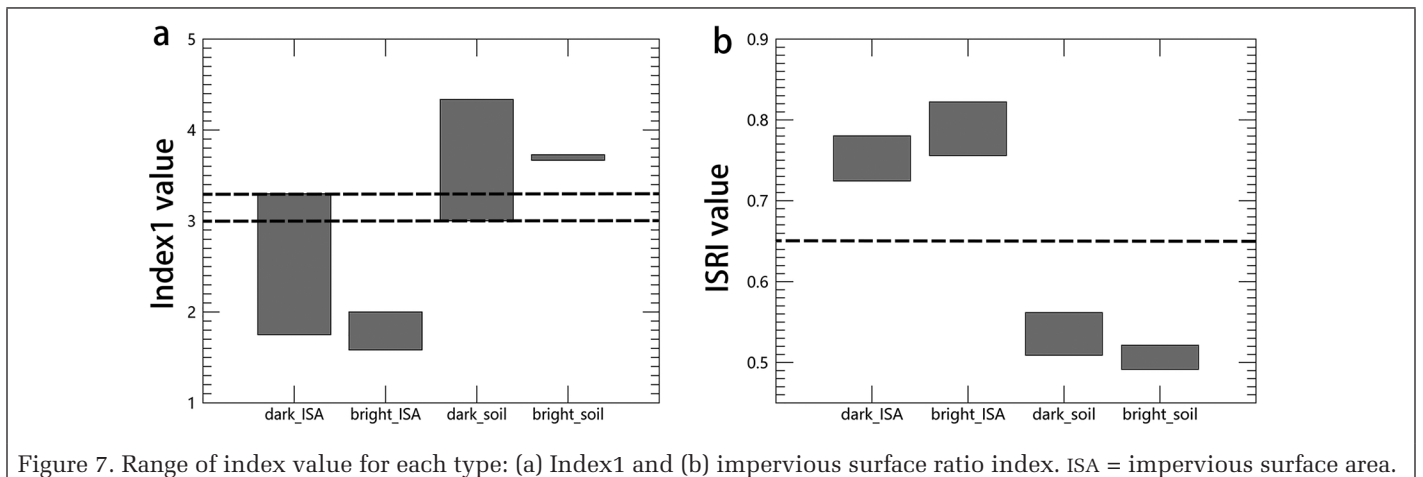


Figure 7. Range of index value for each type: (a) Index1 and (b) impervious surface ratio index. ISA = impervious surface area.

mixture of soil and vegetation. When the ISA proportion is greater than 0 and less than 0.5 and the threshold is less than 0.6631, the pixel type is unclear; that is, whether the pixel must contain ISA is not known. However, when the ISRI value is greater than 0.6631, the proportion of ISA must be greater than 0 regardless of the proportions of soil and vegetation; that is, in this case, the pixel must contain ISA. Furthermore, the ISRI value in all cases must be greater than 0.6631 if the ISA proportion is greater than 0.5. If a certain type in one pixel has the proportion of more than 0.5, then the pixel could be classified as such a type. Therefore, one pixel with an ISA proportion of 0.5 or more must be extracted by the threshold 0.6631.

The proposed threshold 0.6631 is only the result of simulation experiments and is performed using the average spectral value of pure samples from the USGS spectral library, which can provide a theoretical reference for practical applications. However, land cover types are diverse in urban scenes, so the proposed threshold needs a minor adjustment in accordance with particular scenes.

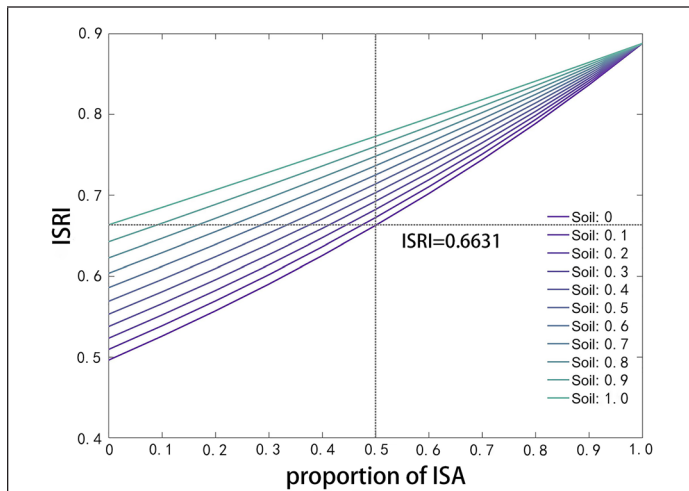


Figure 8. Relationships between the ISRI values and ISA proportions in 11 simulation cases. ISA = impervious surface area; ISRI = impervious surface ratio index.

## Methodology of ISRI Evaluation

### Precision Analysis of ISA Extraction

The purpose of ISRI is to extract ISA accurately and completely from complex urban environments; hence, the precision for ISA mapping by ISRI should be evaluated. The precision analysis of the ISRI classification binary image is conducted by calculating the confusion matrix and classification. Specifically, overall accuracy (OA) and the kappa coefficient are the main evaluation indicators. The testing samples are randomly selected from the original images to ensure the uniform distribution of the samples, and their accuracy is evaluated by the statistical distance among all types. This distance is used to determine the difference degree within the two types, such as separability. The separability indicator (transformed divergence [TD]) will be given later in the article.

### Correlation Analysis Between the ISA Proportion and the ISRI Value

The essence of ISRI is to divide urban areas into ISA and others. Different ISA proportions may cause the spectral value of the mixed pixel to change; therefore, we conduct the experiment to explore the correlation between the ISA proportion and the ISRI value. The visual interpretation results of the high-resolution images from Google Earth are regarded as the reference value for urban land cover types in each pixel of the corresponding Landsat-8 OLI images to calculate the ISA proportion (Figure 9). Specifically, first, we obtain the visual interpretation results of Google Earth images. Second, we calculate the proportions of ISA in each pixel of Landsat-8 OLI images (Figure 9). Finally, we analyze the correlation between the different ISA proportions and the corresponding index values.

### Separability Between ISA and Soil

The spectral curve of ISA is similar to that of soil. Whether ISA and soil can be separated clearly is the important target for ISA index evaluation; hence, the three separability measurements, namely, TD (Mausel *et al.* 1990), Jeffries–Matusita (JM) distance (M. Davis *et al.* 1978), and spectral discrimination index (SDI) (Kaufman and Remer 1994; Pereira 1999), corresponding to Equations 7–9, are introduced to evaluate the separability of ISRI. TD is used to indicate the separability between categories by characterizing the spectral distance of each class. JM distance is a separability measurement based on conditional probability theory; that is, the average distance between two class density functions is calculated (Schmidt and Skidmore 2003). SDI is based on the average index value and standard

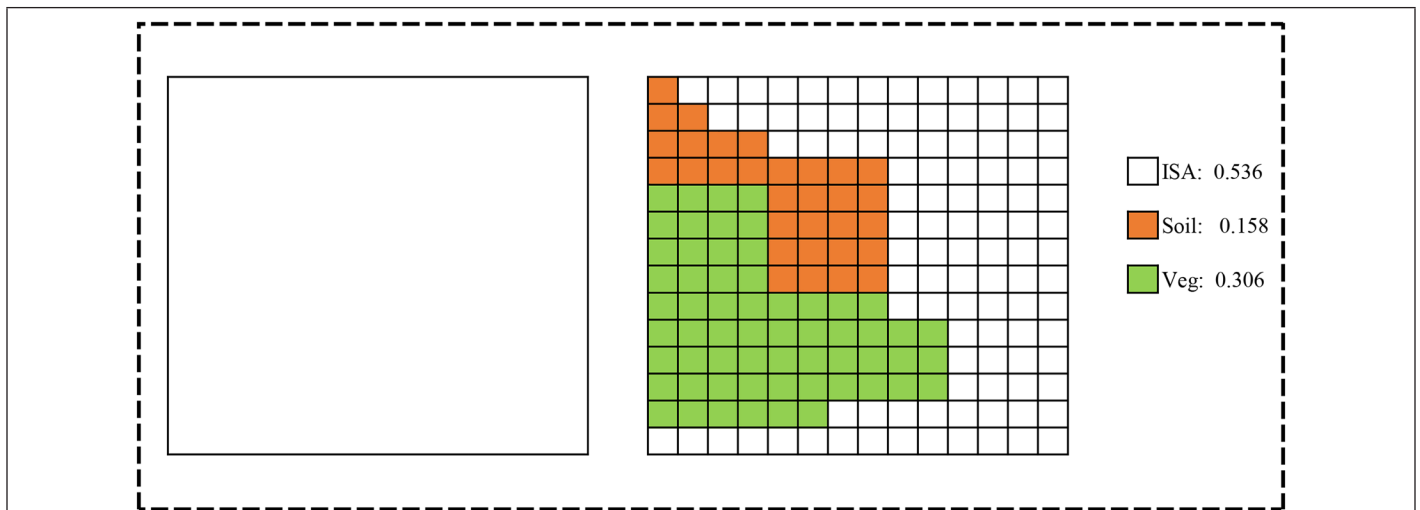


Figure 9. Calculation of the proportion of ISA, soil, and vegetation in one Landsat-8 pixel by using Google Earth images: (a) one pixel of Landsat-8 images; (b) classification of the high-resolution image corresponding to the pixel in (a). ISA = impervious surface area.

deviation of two classes to calculate the spectral separability between them:

$$TD = 2000 \left( 1 - e^{-\frac{\text{Diver}}{8}} \right), \quad (7)$$

$$JM \text{ distance} = \sqrt{2(1 - e^{-a})}, \quad (8)$$

$$SDI = \frac{|M_i - M_j|}{\sigma_i + \sigma_j}, \quad (9)$$

where Diver and  $a$  are

$$\text{Diver} = \frac{1}{2} \text{tr}[(c_i - c_j)(c_i^{-1} - c_j^{-1})] + \frac{1}{2} \text{tr}[(c_i^{-1} + c_j^{-1})(M_i - M_j)(M_i - M_j)^T], \quad (10)$$

$$a = \frac{1}{8} (M_i - M_j)^T \left( \frac{c_i + c_j}{2} \right)^{-1} (M_i - M_j) + \frac{1}{2} \ln \left( \frac{|(c_i + c_j) / 2|}{\sqrt{|c_i| |c_j|}} \right), \quad (11)$$

where  $M$  is the average value,  $\sigma$  denotes the standard deviation,  $c$  refers to the covariance matrix,  $\text{tr}$  signifies the modulus of the matrix, and  $i$  and  $j$  represent a certain object (e.g., ISA and soil). Among the three measurements, when the SDI value and JM distance value of the index are greater than 1, it indicates good separability between the two classes. When the TD value is greater than 1700, the two classes can be well separated. In the separability experiment, the results of the visual interpretation of Google Earth images were used as reference images for selecting the pixels of Landsat-8 OLI images with an ISA proportion of 0.5 or more.

### Comparative Analysis with Other Indices

Meanwhile, ISRI was compared with other indices to evaluate the index performance in urban environments. NDBI is a classic index for extracting ISA, which was constructed by using SWIR and NIR bands, as shown in Equation 12 (Zha *et al.* 2003). BCI, which can effectively highlight the three main urban components (ISA, vegetation, and soil), as shown in Equation 13, was proposed by Deng and Wu (2012). In detail, the separability between ISA and soil will be calculated and compared among these indices:

$$NDBI = \frac{\rho_{\text{SWIR}} - \rho_{\text{NIR}}}{\rho_{\text{SWIR}} + \rho_{\text{NIR}}}, \quad (12)$$

$$BCI = \frac{(H + L) / 2 - V}{(H + L) / 2 + V}, \quad (13)$$

where  $\rho_{\text{SWIR}}$  and  $\rho_{\text{NIR}}$  represent the reflectance of the ground in the SWIR and NIR bands, respectively, and  $H$ ,  $L$ , and  $V$  denote the three components after the TC transformation, where  $H$  is “high albedo,”  $L$  indicates “low albedo,” and  $V$  refers to vegetation.

## Results and Discussion

### ISRI Applications

ISRI was applied to the Landsat-8 OLI to obtain the ISRI grayscale images in four study areas (Figure 10) (the DN values of these images pixels had been converted into surface reflectance). As illustrated in Figure 10, the ISRI grayscale images illustrate that urban areas are brighter than suburban areas, and all urban areas are highlighted in the four study areas. The ISA presents a bright off-white hue entirely, whereas soil is indicated as a gray hue, and vegetation is displayed as dark black-gray hue. Specifically, the ISAs with the large index values are characterized as a white hue in ISRI grayscale images, and the low-value ISAs are displayed as bright gray hues. Further, the ISAs have the highest value, followed by soil, and vegetation has the lowest value (water is masked out in advance).

Xining, surrounded by mountains, has a dry climate, and the urban area is dendritic. The difference in hue between soil and ISA is very obvious and discriminable. Dry mountainous soil and ISA can be nearly separated. In Xi’an, Wuhan, and Fuzhou, although the distinction between ISA and soil is not as good as that of Xining, ISA can be also clearly identified. By observing the ISRI grayscale image of Fuzhou, we can find that the outline of the seawall can be clearly extracted. The shape of the urban area near the mountain is obvious. The gray image map (Figure 3d) highlights the urban morphological characteristics of Wuhan urban distribution. In comparison with other cities, in Xi’an, the difference in hue between the ISA and other land cover types is not obvious, but the outline of ISA is still clear. The reason may be that a large area of farmland without vegetation exists near the suburbs of Xi’an, that is, soil with high water content, which has the similar spectral to the ISA with a low ISRI value. Although

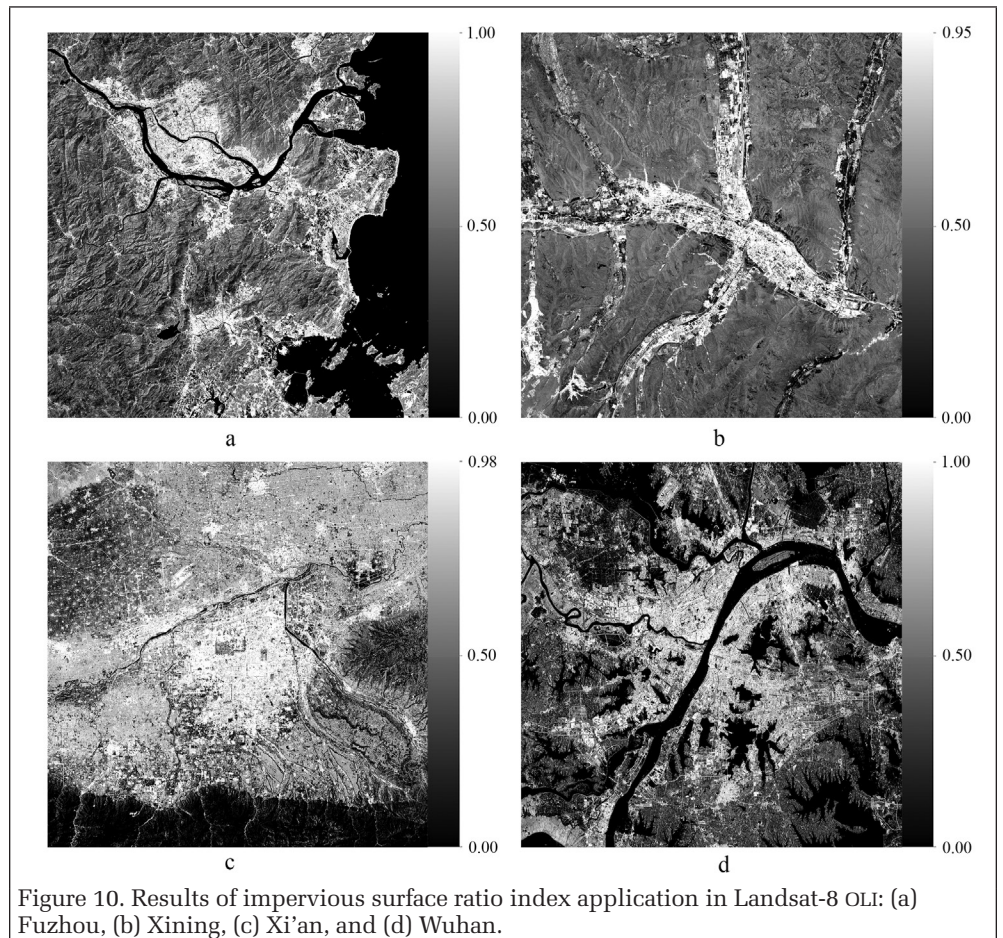


Figure 10. Results of impervious surface ratio index application in Landsat-8 OLI: (a) Fuzhou, (b) Xining, (c) Xi’an, and (d) Wuhan.

the vicinity of Xining has massive soil, the soil type is dry mountain, which is easier to distinguish from ISA than wet soil. Furthermore, most of the suburbs surrounding Fuzhou and Wuhan are covered by vegetation that is distinct from the ISA. Therefore, in terms of difference in hue, the discrimination between ISA and others in Xi'an is inferior to that in other areas. In short, the ISRI grayscale images from Landsat-8 OLI data have a good recognition effect for ISA.

### Results of Comparative Analysis

#### Precision Analysis

With reference to the simulation threshold determined previously and considering the actual images, 0.65 was selected as the ISRI threshold for Landsat-8 OLI by the experiments. The iterative threshold method was applied for the threshold determination of NDBI and BCI. First, the minimum value and the maximum value of index gray images were viewed as the lower and the upper values, respectively. Second, iterative operation in each unit of 0.01 was implemented. Third, the corresponding threshold that has the highest value of OA and kappa coefficient was chosen as the optimal threshold. The classification binary maps were obtained (Figure 11). In Figure 11, from left to right, the images were true-color Landsat-8 OLI images, ISRI, BCI, and NDBI gray images. For Landsat-8 OLI images, the outline of ISA extracted by the threshold of 0.65 is clear and complete, and the overall result was good.

From the overall results (Figure 11a) of the four study areas, the ISA extraction effect of ISRI is better than those of BCI and NDBI. As shown as Figure 11b (the local image), both Fuzhou city and Wuhan city have some obvious soil areas, but both BCI and NDBI wrongly extracted them as ISAs. In Xi'an, ISRI has an obvious effect on ISA extraction. However, BCI and NDBI can hardly separate ISA from soil, especially NDBI.

The confusion matrix was applied to qualitatively evaluate the ISA extraction effect by ISRI. For each study area, a total of 200 checking samples were randomly selected, including 100 ISA and 100 non-ISA samples. The sample accuracy satisfies the standard of the TD. Specifically, all type samples have high separability because the TD values of all of them are above 1900. Table 3 presents the precision by three indices in different study areas. It can be seen from Table 3 that the OAs and kappa coefficients of the extraction result by ISRI are both higher than those of other two indices in all four study areas. Specifically, the OAs in four cities were all above 90%, and the kappa coefficients were all above 0.8.

Although the overall precision in Table 3 is high, differences remain in different cities, which may be related to the wet content of soil. The extraction precision of Xining in dry areas is relatively higher than that in humid areas, such as Fuzhou and Wuhan.

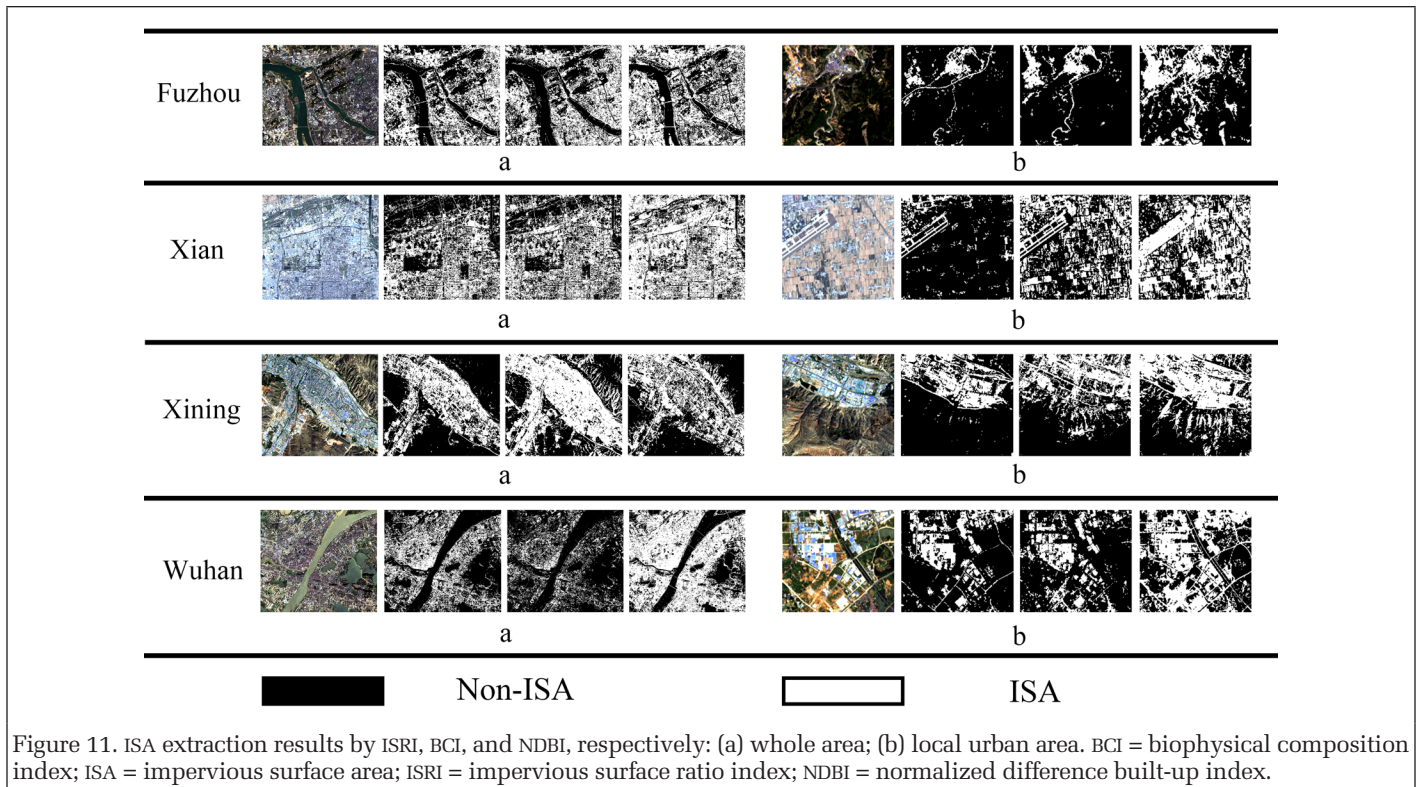


Figure 11. ISA extraction results by ISRI, BCI, and NDBI, respectively: (a) whole area; (b) local urban area. BCI = biophysical composition index; ISA = impervious surface area; ISRI = impervious surface ratio index; NDBI = normalized difference built-up index.

Table 3. Extraction precision by ISRI, BCI, and NDBI in four study areas.

Index	Study Areas							
	Fuzhou		Xi'an		Xining		Wuhan	
	OA (%)	Kappa	OA (%)	Kappa	OA (%)	Kappa	OA (%)	Kappa
ISRI	92.64	0.853	91.82	0.800	95.99	0.917	91.81	0.828
BCI	86.12	0.721	80.38	0.607	87.11	0.745	83.50	0.653
NDBI	79.83	0.591	68.08	0.302	60.04	0.167	79.47	0.572

BCI = biophysical composition index; ISRI = impervious surface ratio index; NDBI = normalized difference built-up index; OA = overall accuracy.

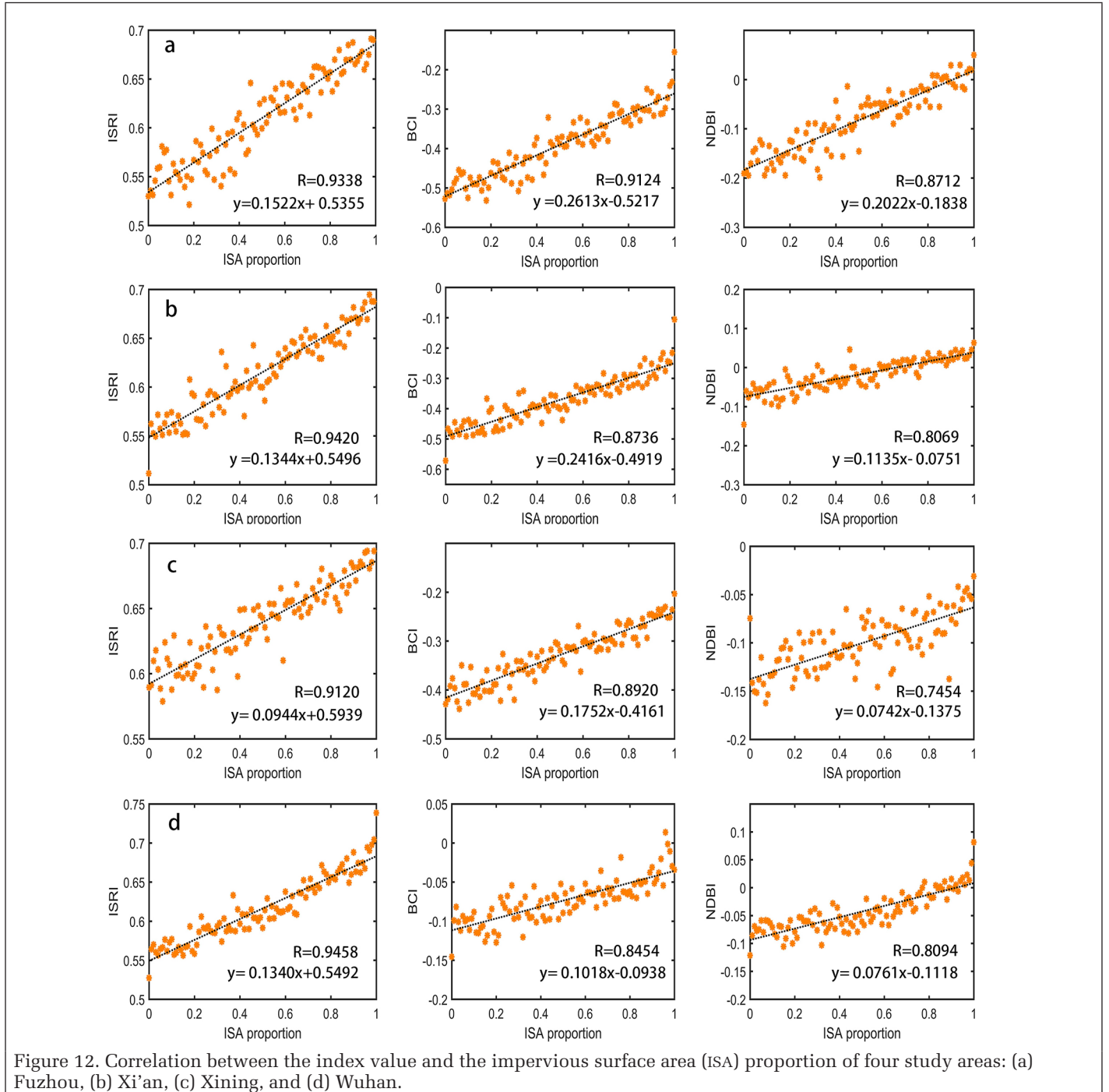
### Correlation Analysis

Results of the visual interpretation of Google Earth high-resolution images were used to calculate the ISA proportion of each pixel of Landsat-8 OLI images. The regression relationship between the ISA proportion and the ISRI value was then established. In fact, heterogeneity also exists in the same land cover type. For example, the ISA types are various, which cause the spectral differences of intraclasses of ISAs. Therefore, the average of ISRI values with the same ISA proportion was used to calculate the regression correlation, and the results are shown in Figure 12. It is found from Figure 12 that the ISA proportions in the four regions of Fuzhou, Xi'an, Xining, and Wuhan have a strong positive correlation with the ISRI values, and their correlation coefficients were 0.9338 ( $p < 0.01$ ), 0.9420 ( $p < 0.01$ ), 0.9120 ( $p < 0.01$ ), and 0.9458 ( $p < 0.01$ ), respectively.

Moreover, the ISRI value gradually increases with the ISA proportion, which is also consistent with the experimental results of threshold simulation presented previously. Meanwhile, the correlations between BCI, NDBI, and ISA proportions under the same experimental conditions were also calculated, respectively. As shown in Figure 12, the correlation coefficient between ISRI and ISA proportion is larger than that of others.

### Separability Analysis

Three indicators, TD, JM distance, and SDI, were selected to evaluate the separability between ISA and soil, and a comparative analysis among ISRI, BCI and NDBI was made. Mixed pixels with an ISA proportion of 0.5 or more were selected to calculate the separability by using three indicators. Separability



experiments were performed on Landsat-8 OLI images, and Figure 13 presents the results. The histograms of three indices showed that soil and ISA corresponded to two distinct peaks. Three indicators were calculated, and the results are shown in Table 4, indicating that the separability of ISRI was generally better than that of BCI and NDBI in four study areas. The soil in Xining has the highest separability from ISA, and all indicators were considerably higher than the standard in presented previously. Except for SDI and JM, the values of TD in Xi'an were low because the farmland without vegetation might have high water content and is easy to confuse with the ISAs. Although the separability does not meet the standards of

TD, the SDI and JM values above the standard prove that it still has good separability. Of course, mixed pixels with the ISA proportions of 0.5 or more were selected instead of ISA pure pixels for separability analysis in order to be more in line with the actual application scenes.

The histograms of NDBI and BCI showed that the degree of discrimination degree of ISA and soil was worse than that of ISRI and that the histogram overlap area between ISA and soil was large, especially in Wuhan. The quantitative analysis of three indicators indicates that, in the study areas of Fuzhou, Xi'an, and Wuhan, the values of TD, JM, and SDI of BCI and NDBI were considerably smaller than that of ISRI. Therefore, their

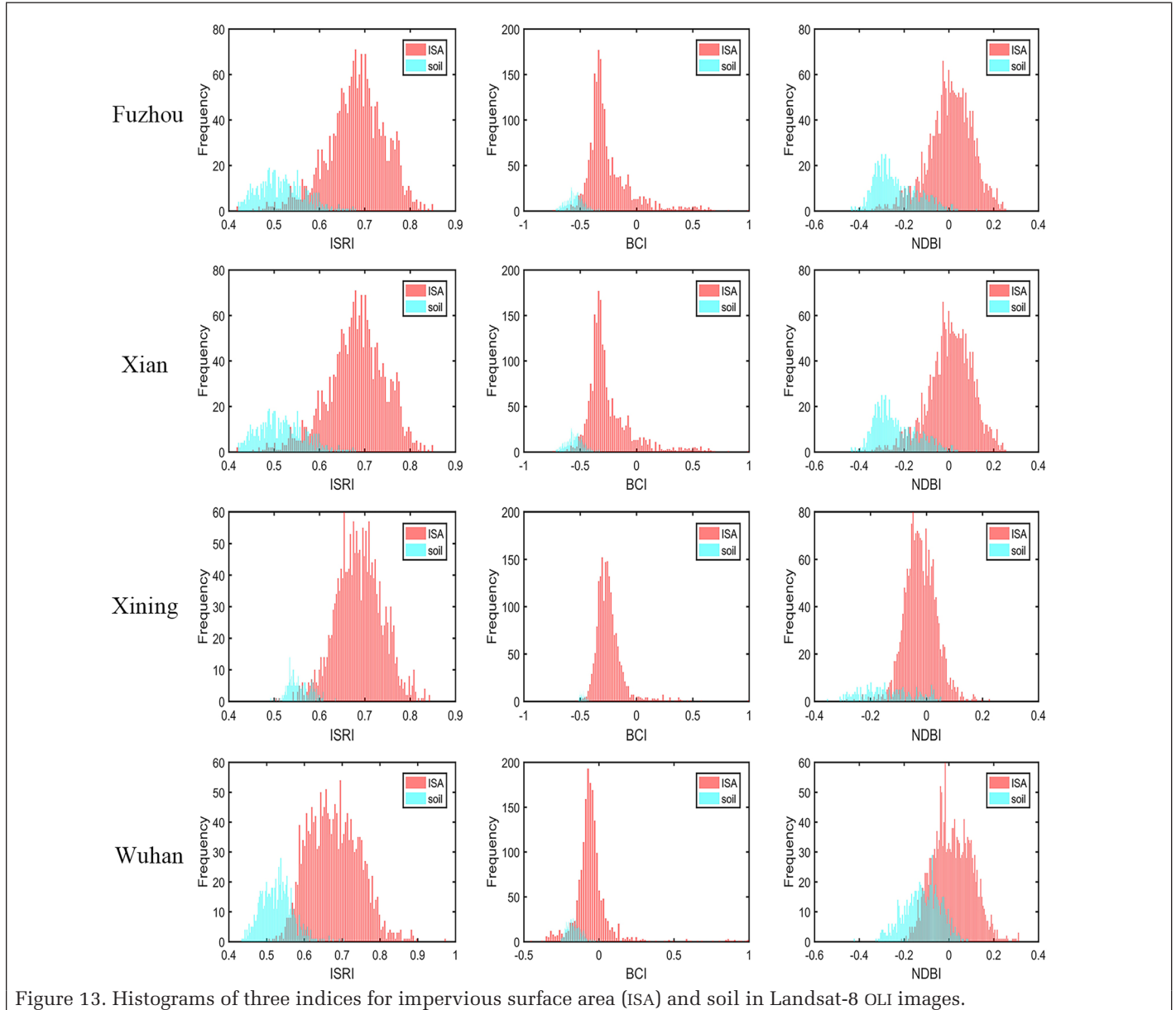


Figure 13. Histograms of three indices for impervious surface area (ISA) and soil in Landsat-8 OLI images.

Table 4. Separability measurements between ISA and soil.

ISA and Soil	Fuzhou			Xi'an			Xining			Wuhan		
	TD	SDI	JM	TD	SDI	JM	TD	SDI	JM	TD	SDI	JM
ISRI	1319.2	1.450	1.140	935.4	1.122	1.018	1778.1	1.785	1.254	1340.7	1.407	1.122
BCI	1080.8	1.065	0.998	659.6	0.886	0.829	1962.2	1.582	1.212	569.3	0.799	0.801
NDBI	1105.5	1.269	1.051	531.8	0.790	0.759	533.2	0.795	0.781	546.3	0.627	0.740

BCI = biophysical composition index; ISA = impervious surface area; ISRI = impervious surface ratio index; JM = Jeffries–Matusita; NDBI = normalized difference built-up index; SDI = spectral discrimination index; TD = transformed divergence.

separability was not better than that of ISRI. To sum up, ISRI performed the best in separability analysis between ISA and soil, followed by BCI and NDBI.

That all separability indicators of NDBI were under the proposed standard showed its poor separability in all areas except Fuzhou. In Xining, the TD value of BCI was slightly larger than that of ISRI. However, BCI had an advantage only in the TD indicator, and the values of JM and SDI in Xining were less than that of ISRI.

Qualitative and quantitative analysis and a comparison result among ISRI, NDBI, and BCI show that ISRI is superior to NDBI and BCI in the separability between ISA and soil. Overall, ISRI separability is more stable and better than others, no matter what kind of study area.

## Discussion

The ISRI aims to amplify the difference between ISA and other types and then maps a relatively complete ISA distribution in complex urban environments. Meanwhile, the ISRI has the characteristics of simple structure, clear physical meaning, and common bands. Specifically, the blue and NIR bands are selected as feature bands, and the coordinate translated ratio form is applied. ISRI is applied to medium-resolution images, and a relatively complete and accurate ISA can be extracted by the threshold proposed in this article. The result of correlation analysis suggests that ISRI has a high significant and positive correlation with the ISA proportion. For the separability analysis, most of the indicators are above the standard discussed here, which comprehensively verifies that ISRI has good separability between ISA and soil. Furthermore, ISRI is better than other indices in reducing the confusion between ISA and soil, and ISRI can obtain relatively stable and complete results under different urban scenes.

Although the extraction results by ISRI are satisfactory, shortcomings remain in the experiments. The verification data use high-resolution images from Google Earth. However, we cannot download the Google images at the same time as the Landsat-8 OLI due to data acquisition limitations. Therefore, minor changes may occur that will lead to errors in the verification experiments. Moreover, the pure sample used in the simulation experiment from the USGS spectral library and the real sample from the actual environment are different. For example, the ISA samples from the USGS spectral library are pure and single artificial materials, but impervious urban surfaces are composed mainly of different artificial materials. Thus, using the spectral samples from the USGS spectral library for

simulation experiments may lead to subtle deviations from the actual value, but the trend is consistent for their high correlation (Table 2). In addition, in situ spectral measurements of ISA require considerable manpower and material resources; therefore, using the spectral library for simulation experiments is a reasonable selection. In this article, ISRI was developed based on a V-I-S conceptual model, so water should be removed in advance by using MNDWI (Xu 2008). Water has a high reflectance in the blue band and a strong absorption rate in the NIR band. In the NIR and blue band space, only the reflectance of water shows a downward trend different from others. Therefore, ISRI could be improved according to the spectral characteristics of water in the future research.

In this article, four different geographic and climatic study areas were selected to testify whether ISRI can be widely applicable. Study areas are macroscopically divided into two types, namely, dry climate and humid climate cities, but actually, the soil moisture measurements are not conducted because the large-scale field measurements are difficult. The existing research shows that the separability between soil and ISA in the wet area is not as good as that in the dry area. It is found that the lower the reflectance of soil in the NIR band, the lower the slope between the blue and NIR bands when the water content of soil is high (Sadeghi *et al.* 2015). For the ISRI, the higher the water content of soil, the higher the ISRI value of soil and the worse the separability between soil and ISA. Rainfall will increase soil humidity and cannot affect ISA. Therefore, the images before and after rain in the same area of Wuhan were selected to evaluate the ISRI separability difference between ISA and soil. The results are shown in Figure 14, where (a) is the relatively dry time period before rainfall (23 July 2016) and (b) is the relatively wet time period after the rainfall (1 March 2016) according to weather forecasting. It is clear that the overlap area of Figure 14a was less than that of Figure 14b. Meanwhile, all separability indicators in Figure 14a are higher than those in Figure 14b (Table 5). This result shows that soil humidity affects the ISA extraction result to some extent. Therefore, we suggest that image acquisition

Table 5. ISRI separability measurements between ISA and soil before and after rainfall in Wuhan.

ISA and Soil	TD	SDI	JM
a	1340.7	1.407	1.122
b	1247.3	1.223	1.034

ISA = impervious surface area; JM = Jeffries–Matusita; SDI = spectral discrimination index; TD = transformed divergence.

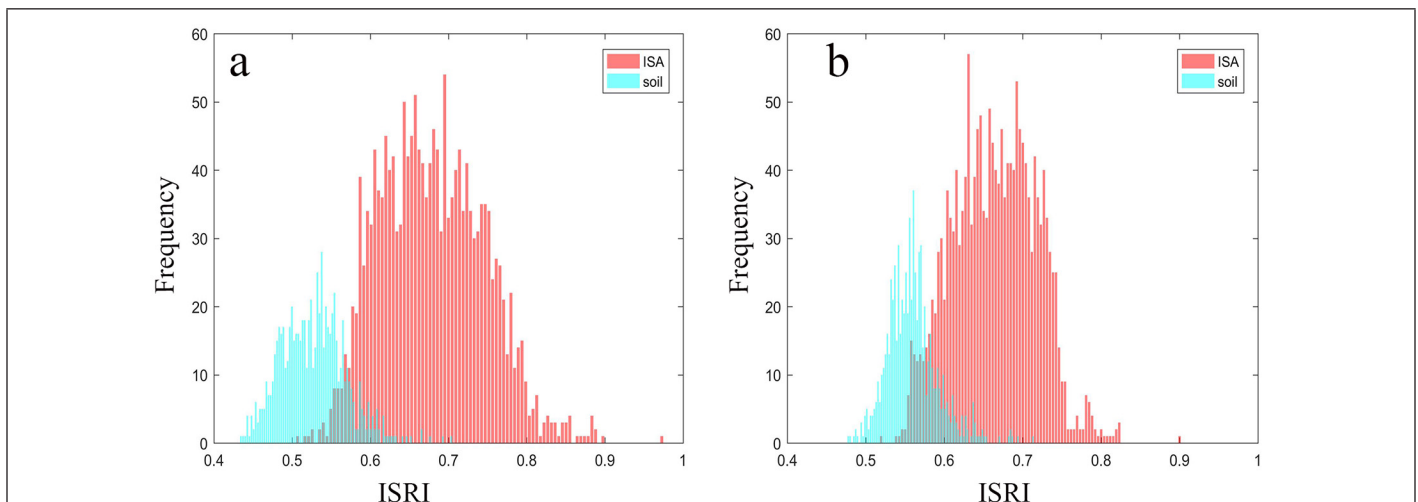


Figure 14. Histograms of ISRI for ISA and soil in Landsat-8 OLI images: (a) dry time period before rainfall; (b) wet time period after rainfall. ISA = impervious surface area; ISRI = impervious surface ratio index.

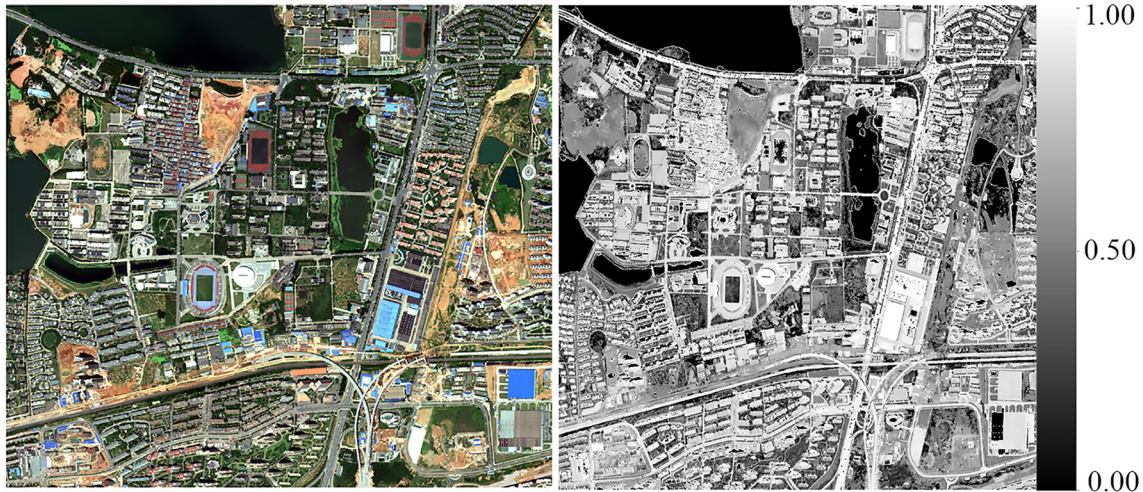


Figure 15. Results of impervious surface ratio index (ISRI) applied in WorldView-2 images. From left to right, true-color composite image and gray image of result using ISRI.

data be selected during the dry seasons or the period of fair weather. Furthermore, we will explore the soil moisture in future research.

Furthermore, ISRI uses only the blue and NIR bands. Therefore, ISRI can be also applied into WorldView-2 images in Zigui County, China, to evaluate the ISRI separability between ISA and soil, and the result is displayed in Figure 15. Similar to the results from Landsat-8 OLI images, the bright off-white hue represents ISA, soil is a gray hue, and vegetation is a darker gray-black hue. However, the hue of bright red roofs is slightly weaker than other ISAs because the bright red roof has lower reflectance in the blue band than other ISAs, but the reflectance in the NIR band is high (Herold and Roberts 2010), which makes the ISRI value too small. In general, the ISRI effect using high-resolution images remains good. The SDI and JM values were 1.455 and 1.143, respectively, indicating that ISRI can also separate the soil from ISA well. Overall, the ISRI separability between soil and ISA in high-resolution images was still good.

## Conclusions

The ISA coverage is usually used as the indicator of urbanization and exerts important impacts on urban eco-environmental systems. Therefore, mapping ISA timely and dynamically is critical for urban planning and governance. The aim of this article is to develop a simple ISA index for minimizing or decreasing the confusion between ISA and soil; therefore, a new ISRI is proposed under the V-I-S conceptual model.

The results demonstrate that ISRI has three characteristics. First, ISRI can represent ISA well, and a strong positive correlation exists between the ISRI value and the ISA proportion. Second, ISRI can efficiently separate ISA from soil under different urban environments. Specifically, the effect of ISRI is best in arid climate regions. Third, ISRI has a clear theoretical basis for its ratio form, and the spectral heterogeneity of ISA is decreased.

It is noticeable that atmospheric correction should be done before ISRI operation and that images should be selected during the dry seasons or a period of fair weather. In addition, although the ISRI threshold value suggested in here could acquire excellent results universally, a minor adjustment might be needed in accordance with particular scenes if optimal results are to be obtained.

## Acknowledgments

The authors are grateful to the editors, reviewers, and all those who helped us during the writing of this article. The research was supported by the National Key Research and Development Program (grant no. 2018YFB1004600).

## References

- Arnold, C. L. and C. J. Gibbons. 1996. Impervious surface coverage: The emergence of a key environmental indicator. *Journal of the American Planning Association* 62 (2):243–258.
- Bauer, M. E., J. K. Doyle, and N. J. Heinert. 2002. Impervious surface mapping using satellite remote sensing. Pages 2334–2336 in *Proceedings of the IEEE International Geoscience and Remote Sensing Symposium*, held Toronto, Ontario, 24–28 June 2002. New York: IEEE.
- Bazi, Y. and F. Melgani. 2006. Toward an optimal SVM classification system for hyperspectral remote sensing images. *IEEE Transactions on Geoscience and Remote Sensing* 44 (11):3374–3385.
- Bhaskaran, S., S. Paramananda, and M. Ramnarayan. 2010. Per-pixel and object-oriented classification methods for mapping urban features using Ikonos satellite data. *Applied Geography* 30 (4):650–665.
- Blair, R. B. 1996. Land use and avian species diversity along an urban gradient. *Ecological Applications* 6 (2):506–519.
- Cai, C., P. Li, and H. Jin. 2016. Extraction of urban impervious surface using two-season WorldView-2 images: A comparison. *Photogrammetric Engineering and Remote Sensing*, 82:335–349.
- Carlson, T. N. and S. Traci Arthur. 2000. The impact of land use–land cover changes due to urbanization on surface microclimate and hydrology: A satellite perspective. *Global and Planetary Change* 25 (1):49–65.
- Chen, Z. and J. Chen. 2006. Investigation on extracting the space information of urban land-use from high spectrum resolution image of ASTER by NDBI method. *Geo-Information Science* 24 (2):213–221.
- Cooper, B., Dymond, R. and Shao, Y., 2017. Impervious comparison of NLCD versus a detailed dataset over time. *Photogrammetric Engineering & Remote Sensing* 83:429–437.
- Davis, S. M., D. A. Landgrebe, T. L. Phillips, P. H. Swain, R. M. Hoffer, J. C. Lindenlaub, and L. F. Silva. 1978. *Remote Sensing: The Quantitative Approach*. New York: McGraw-Hill.
- Deng, C. and C. Wu. 2012. BCI: A biophysical composition index for remote sensing of urban environments. *Remote Sensing of Environment* 127:247–259.

- Durbha, S. S., R. L. King, and N. H. Younan. 2007. Support vector machines regression for retrieval of leaf area index from multiangle imaging spectroradiometer. *Remote Sensing of Environment* 107 (1):348–361.
- Elvidge, C. D., B. T. Tuttle, P. C. Sutton, K. E. Baugh, A. T. Howard, C. Milesi, B. Bhaduri, and R. Nemani. 2007. Global distribution and density of constructed impervious surfaces. *Sensors (Basel, Switzerland)* 7 (9):1962–1979.
- Esch, T., V. Himmler, G. Schorcht, M. Thiel, T. Wehrmann, F. Bachofer, C. Conrad, M. Schmidt, and S. Dech. 2009. Large-area assessment of impervious surface based on integrated analysis of single-date Landsat-7 images and geospatial vector data. *Remote Sensing of Environment* 113 (8):1678–1690.
- Foody, G. M. and M. K. Arora. 1997. An evaluation of some factors affecting the accuracy of classification by an artificial neural network. *International Journal of Remote Sensing* 18 (4):799–810.
- Franke, J., D. A. Roberts, K. Halligan, and G. Menz. 2009. Hierarchical multiple endmember spectral mixture analysis (MESMA) of hyperspectral imagery for urban environments. *Remote Sensing of Environment* 113 (8):1712–1723.
- Grimm, N. B., S. H. Faeth, N. E. Golubiewski, C. L. Redman, W. Jianguo, B. Xuemei, and J. M. Briggs. 2008. Global change and the ecology of cities. *Science* 319 (5864):756–760.
- Haboudane, D., J. R. Miller, N. Tremblay, P. J. Zarco-Tejada, and L. Dextraze. 2002. Integrated narrow-band vegetation indices for prediction of crop chlorophyll content for application to precision agriculture. *Remote Sensing of Environment* 81 (2):416–426.
- Herold, M. and D. A. Roberts. 2010. The spectral dimension in urban remote sensing. In *Remote Sensing of Urban and Suburban Areas*, edited by T. Rashed and C. Jürgens, 47–65. Dordrecht: Springer.
- Hu, X. and Q. Weng. 2009. Estimating impervious surfaces from medium spatial resolution imagery using the self-organizing map and multi-layer perceptron neural networks. *Remote Sensing of Environment* 113 (10):2089–2102.
- Kaufman, Y. J. and L. A. Remer. 1994. Detection of forests using mid-IR reflectance: An application for aerosol studies. *IEEE Transactions on Geoscience and Remote Sensing* 32 (3):672–683.
- Kokaly, R. F., R. N. Clark, G. A. Swayze, K. E. Livo, T. M. Hoefen, N. C. Pearson, R. A. Wise, W. M. Benzel, H. A. Lowers, R. L. Driscoll, and A. J. Klein. 2017. *USGS Spectral Library Version 7, Data Series*, Reston, VA: US Geological Survey.
- Kussul, N., M. Lavreniuk, S. Skakun, and A. Shelestov. 2017. Deep learning classification of land cover and crop types using remote sensing data. *IEEE Geoscience and Remote Sensing Letters* 14 (5):778–782.
- Liu, C., Z. Shao, M. Chen, and H. Luo. 2013. MNDISI: a multi-source composition index for impervious surface area estimation at the individual city scale. *Remote Sensing Letters* 4 (8):803–812.
- Liu, X., G. Hu, B. Ai, X. Li, and Q. Shi. 2015. A normalized urban areas composite index (NUACI) based on combination of DMSP-OLS and MODIS for mapping impervious surface area. *Remote Sensing* 7 (12):17168–17189.
- Lu, D., E. Moran, and S. Hetrick. 2011. Detection of impervious surface change with multitemporal Landsat images in an urban-rural frontier. *ISPRS Journal of Photogrammetry and Remote Sensing* 66 (3):298–306.
- Lu, D. and Q. Weng. 2007. A survey of image classification methods and techniques for improving classification performance. *International Journal of Remote Sensing* 28 (5):823–870.
- Matsushita, B., F. Yang, and T. Fukushima. 2014. Impervious surface area as an indicator for evaluating drainage basins. In *Integrative Observations and Assessments*, edited by S.I. Nakano, T. Yahara, and T. Nakashizuka, 239–252. Tokyo: Springer.
- Mausel, P. W., W. J. Kramber, and J. K. Lee. 1990. Optimum band selection for supervised classification of multispectral data. *Photogrammetric Engineering & Remote Sensing* 56 (1):55–60.
- McIver, D. K. and M. A. Friedl. 2002. Using prior probabilities in decision-tree classification of remotely sensed data. *Remote Sensing of Environment* 81 (2):253–261.
- Miller, J. E., S.A.C. Nelson, and G. R. Hess. 2009. An object extraction approach for impervious surface classification with very-high-resolution imagery. *The Professional Geographer* 61 (2):250–264.
- Nagel, P. and F. Yuan. 2016. High-resolution land cover and impervious surface classifications in the Twin Cities Metropolitan Area with NAIP imagery. *Photogrammetric Engineering & Remote Sensing* 82:63–71.
- Pereira, J.M.C. 1999. A comparative evaluation of NOAA/AVHRR vegetation indexes for burned surface detection and mapping. *IEEE Transactions on Geoscience and Remote Sensing* 37 (1):217–226.
- Phinn, S., M. Stanford, P. Scarth, A. T. Murray, and P. T. Shyy. 2002. Monitoring the composition of urban environments based on the vegetation-impervious surface-soil (VIS) model by subpixel analysis techniques. *International Journal of Remote Sensing* 23 (20):4131–4153.
- Plaza, A., P. Martinez, R. Perez, and J. Plaza. 2004. A quantitative and comparative analysis of endmember extraction algorithms from hyperspectral data. *IEEE Transactions on Geoscience and Remote Sensing* 42 (3):650–663.
- Powell, R. L., D. A. Roberts, P. E. Dennison, and L. L. Hess. 2007. Sub-pixel mapping of urban land cover using multiple endmember spectral mixture analysis: Manaus, Brazil. *Remote Sensing of Environment* 106 (2):253–267.
- Rashed, T., D. Roberts, J. Rogan, and R. Powell. 2003. Measuring the physical composition of urban morphology using multiple endmember spectral mixture models. *Photogrammetric Engineering & Remote Sensing* 69 (9):1011–1020.
- Richards, J. A. 2013. Supervised classification techniques. In *Remote Sensing Digital Image Analysis: An Introduction*, edited by J. A. Richards, 247–318. Berlin: Springer.
- Ridd, M. K. 1995. Exploring a V-I-S (vegetation-impervious surface-soil) model for urban ecosystem analysis through remote sensing: Comparative anatomy for cities. *International Journal of Remote Sensing* 16 (12):2165–2185.
- Roberts, D. A., M. Gardner, R. Church, S. Ustin, G. Scheer, and R. O. Green. 1998. Mapping chaparral in the Santa Monica Mountains using multiple endmember spectral mixture models. *Remote Sensing of Environment* 65 (3):267–279.
- Sadeghi, M., S. B. Jones, and W. D. Philpot. 2015. A linear physically-based model for remote sensing of soil moisture using short wave infrared bands. *Remote Sensing of Environment* 164:66–76.
- Schmidt, K. S. and A. K. Skidmore. 2003. Spectral discrimination of vegetation types in a coastal wetland. *Remote Sensing of Environment* 85 (1):92–108.
- Shao, Z., H. Fu, P. Fu, and L. Yin. 2016. Mapping urban impervious surface by fusing optical and SAR data at the decision level. *Remote Sensing* 8 (11):945.
- Shao, Z., H. Fu, D. Li, O. Altan, and T. Cheng. 2019. Remote sensing monitoring of multi-scale watersheds impermeability for urban hydrological evaluation. *Remote Sensing of Environment* 232:111338.
- Shao, Z. and C. Liu. 2014. The integrated use of DMSP-OLS nighttime light and MODIS data for monitoring large-scale impervious surface dynamics: A case study in the Yangtze River Delta. *Remote Sensing* 6 (10):9359–9378.
- Slonecker, E. T., D. B. Jennings, and D. Garofalo. 2001. Remote sensing of impervious surfaces: A review. *Remote Sensing Reviews* 20 (3):227–255.
- Somers, B., G. P. Asner, L. Tits, and P. Coppin. 2011. Endmember variability in spectral mixture analysis: A review. *Remote Sensing of Environment* 115 (7):1603–1616.
- Sun, G., X. Chen, X. Jia, Y. Yao, and Z. Wang. 2016. Combinational build-up index (CBI) for effective impervious surface mapping in urban areas. *IEEE Journal of Selected Topics in Applied Earth Observations and Remote Sensing* 9 (5):2081–2092.
- Thiemann, S. and H. Kaufmann. 2002. Lake water quality monitoring using hyperspectral airborne data—A semiempirical multisensor and multitemporal approach for the Mecklenburg Lake District, Germany. *Remote Sensing of Environment* 81 (2):228–237.

- Tian, Y., H. Chen, Q. Song, and K. Zheng. 2018. A novel index for impervious surface area mapping: Development and validation. *Remote Sensing* 10 (10):1521.
- Turker, M. and D. Koc-San. 2015. Building extraction from high-resolution optical spaceborne images using the integration of support vector machine (SVM) classification, Hough transformation and perceptual grouping. *International Journal of Applied Earth Observation and Geoinformation* 34:58–69.
- Turner, B.L.I.I., W. B. Meyer, and D. L. Skole. 1994. Global land-use/land-cover change: Towards an integrated study. *Ambio* 23 (1):91–95.
- Utz, R. M., K. N. Eshleman, and R. H. Hilderbrand. 2011. Variation in physicochemical responses to urbanization in streams between two Mid-Atlantic physiographic regions. *Ecological Applications* 21 (2):402–415.
- Van de Voorde, T., T. De Roeck, and F. Canters. 2009. A comparison of two spectral mixture modelling approaches for impervious surface mapping in urban areas. *International Journal of Remote Sensing* 30 (18):4785–4806.
- Wang, Z., C. Gang, X. Li, Y. Chen, and J. Li. 2015. Application of a normalized difference impervious index (NDII) to extract urban impervious surface features based on Landsat TM images. *International Journal of Remote Sensing* 36 (4):1055–1069.
- Weng, Q. 2012. Remote sensing of impervious surfaces in the urban areas: Requirements, methods, and trends. *Remote Sensing of Environment* 117:34–49.
- Weng, Q., D. Lu, and J. Schubring. 2004. Estimation of land surface temperature–vegetation abundance relationship for urban heat island studies. *Remote Sensing of Environment* 89 (4):467–483.
- Wu, C. 2004. Normalized spectral mixture analysis for monitoring urban composition using ETM+ imagery. *Remote Sensing of Environment* 93 (4):480–492.
- Wu, C. and A. T. Murray. 2003. Estimating impervious surface distribution by spectral mixture analysis. *Remote Sensing of Environment* 84 (4):493–505.
- Xian, G. and C. Homer. 2010. Updating the 2001 national land cover database impervious surface products to 2006 using Landsat imagery change detection methods. *Remote Sensing of Environment* 114 (8):1676–1686.
- Xu, H. 2008. A new index for delineating built-up land features in satellite imagery. *International Journal of Remote Sensing* 29 (14):4269–4276.
- Xu, H. 2010. Analysis of impervious surface and its impact on urban heat environment using the normalized difference impervious surface index (NDISI). *Photogrammetric Engineering & Remote Sensing* 76 (5):557–565.
- Zha, Y., J. Gao, and S. Ni. 2003. Use of normalized difference built-up index in automatically mapping urban areas from TM imagery. *International Journal of Remote Sensing* 24 (3):583–594.
- Zhang, Q., B. Li, D. Thau, and R. Moore. 2015. Building a better urban picture: Combining day and night remote sensing imagery. *Remote Sensing* 7 (9):11887–11913.
- Zhang, S., K. Yang, M. Li, Y. Ma, and M. Sun. 2018. Combinational biophysical composition index (CBCI) for effective mapping biophysical composition in urban areas. *IEEE Access* 6:41224–41237.

## IN-PRESS ARTICLES

- Wenfu Wu, Jiahua Teng, Qimin Cheng, and Songjing Guo. Extraction of Impervious Surface Using *Sentinel-1A* Time-Series Coherence Images with the Aid of a *Sentinel-2A* Image.
- Chumbitha Leena, Manoj Saxena, and Ravi Dwivedi. Road Extraction from Cartosat-2F Multispectral Data with Object-Oriented Analysis.
- Wei Wang, Yuan Xu, Yingchao Ren, Gang Wang. Parsing of Urban Façades from 3D Point Cloud Based on A Novel Multi-View Domain.
- Jiali Wang and Yannan Chen. Digital Surface Model Refinement Based on Projected Images.
- John C. Trinder. Remote Sensing for Ecosystem Services and Urban Sustainability.
- Qimin Cheng, Yuan Xu, Peng Fu, Jinling Li, Wei Wang, and Yingchao Ren. Scene Classification of Remotely Sensed Images via Densely Connected Convolutional Neural Networks and an Ensemble Classifier.
- Zhenfeng Shao, Yun Tang, Xiao Huang, and Deren Li. Monitoring Work Resumption of Wuhan in the COVID-19 Epidemic Using Daily Nighttime Light.
- Tao Wang, Deng Lianbin, Li Yuhong, and Peng Hao. Progressive TIN Densification with Connection Analysis for urban LiDAR Data.
- Nahed Osama, Bisheng Yang, Yue Ma, and Mohamed Freeshah. A Digital Terrain Modeling Method in Urban Areas by the ICESat-2.
- Ting Bai, Kaimin Sun, Wenzhuo Li, Deren Li, Yepi Chen, and Haigang Sui. A Novel Class-specific Object-based Method for Urban Change Detection using High-Resolution Remote Sensing Imagery.
- Yang Liu, Yujie Sun, Shikang Tao, Min Wang, Qian Shen, and Jiru Huang. Discovering potential illegal construction within building roofs from UAV images using semantic segmentation and object-based change detection.
- Yongtai Chen, William C. Tang, Jinkui Chu, Ran Zhang, and Song Li. Error Analysis and Optimization of Sky Full-Polarization Imaging Detection System.
- Yang Han, Haiyan Yao, Ziyang Li, Haofang Niu, Tianyi Hao, and Yuyu Zhou. Inversion of Solar-Induced Chlorophyll Fluorescence Using Polarization Measurements of Vegetation.
- Neema Nicodemus Lyimo, Fang Luo, Qimin Cheng, and Hao Peng. Quality Assessment of Heterogeneous Training Datasets for Classification of Urban Area with Landsat imagery.
- Shalini Gakhar and Kailash Chandra Tiwari. Comparative assessment of target detection algorithms for urban targets using hyperspectral data.
- Long Chen, Bo Wu, Yao Zhao, and Yuan Li. A Real-Time Photogrammetric System for Acquisition and Monitoring of 3D Human Body Kinematics.
- Letícia Ferrari Castanheiro, Antonio Maria Garcia Tommaselli, Adilson Berveglieri, Mariana Batista Campos, and José Marcato Junior. Modeling hyperhemispherical points and calibrating a dual-fisheye system for close-range applications.
- Jonathan Li, Qitong Yu, Wei Liu, Wesley Nunes Gonçalves, and José Marcato Junior. Spatial Resolution Enhancement for Large-scale Land Cover Mapping via Weakly Supervised Deep Learning.
- Binbin He, Guoming Li, Liang Li, Miao Yang, Qiongyi Huang, and Zihan Guo. Ecological Functions and Human-activity Interferences Evaluation in Ecological Protection Redline for Urban Environment.
- Fang Gao, Yihui Li, Wentao Li, Peng Zhang, Yuan An, Xing Zhong, and Yuwei Zhai. A High-Resolution Satellite DEM Filtering Method Assisted with Building Segmentation.
- Xueyan Li, Yu Hou, Ruifeng Zhai, Junfeng Song, Xuehan Ma Shuzhao Hou, and Shuxu Guo. Three-dimensional reconstruction of single input image based on point cloud.
- Hui Luo and Nan Chen. A Combined Unmixing Framework for Impervious Surface Mapping on Medium-Resolution Images with Visible Shadows.

# Reclaimed-Airport Surface-Deformation Monitoring by Improved Permanent-Scatterer Interferometric Synthetic-Aperture Radar: A Case Study of Shenzhen Bao'an International Airport, China

Lu Miao, Kailiang Deng, Guangcai Feng, Kaifeng Li, Zhiqiang Xiong, Yuedong Wang, and Shuiyuan He

## Abstract

Reclaimed airports usually have fragile geological structures and are susceptible to the uneven ground settlements caused by filling-material consolidation, underground construction, and dynamic loading from takeoff and landing of aircrafts. Therefore, deformation monitoring is of great significance to the safe operation of reclaimed airports. This study adopts an improved permanent-scatterer interferometric synthetic-aperture radar strategy to map the spatiotemporal deformation of Shenzhen Bao'an International Airport in China using ascending and descending Envisat/ASAR data acquired from 2007 to 2010 and Sentinel-1 data from 2015 to 2019. The results show that uneven settlements of the airport concentrate in the new reclaimed land. Then we explore the settlement characteristics of each functional area. Furthermore, we separate out the dynamic-load settlement of runway No. 2 and confirm the settlements caused by dynamic load. This study provides new ideas for studying deformation in similar fields, and technical references for the future construction of Shenzhen Airport.

## Introduction

Over the past decades, coastal cities have seen fast development, accompanied by large-scale land reclamation. Reclaimed land is usually flat and open, so many airports have been constructed on it, including Shanghai Pudong International Airport (Y. Jiang *et al.* 2016), Kansai International Airport (Mesri and Funk 2015), and LaGuardia Airport (Fornés Martínez 2015). However, due to unstable foundations, these airports commonly suffer land subsidence, so it is necessary to monitor their surface deformation. Especially due to dynamic and static loads and groundwater level changes, the flight area has great potential for subsidence, which threatens the safety of operations of the airport (Yang and Yang 2007; G. Wang *et al.* 2013).

Traditional surveying methods, such as leveling and global navigation satellite systems, can obtain highly accurate and reliable surface deformation at a few control points. But their

Lu Miao, Guangcai Feng, Zhiqiang Xiong, and Yuedong Wang are with the School of Geosciences and Info-Physics, Central South University, Changsha, China.

Kailiang Deng and Kaifeng Li are with the Naval Institute of Hydrographic Surveying and Charting, Tianjin, China (dkl\_hych@163.com).

Shuiyuan He is with the Guangzhou Marine Geological Survey, Guangzhou, China

observation density and efficiency are low, so they cannot be applied in the deformation monitoring of airports. Besides, it is difficult and dangerous for surveyors to work inside the flight area, such as the runway, if the airport starts operation. Interferometric synthetic-aperture radar (InSAR) is a powerful geodetic technique for surface-deformation monitoring (Bamler and Hartl 1998; Rosen *et al.* 2000), as it has wide ground coverage and needs no ground control. Nowadays, it has become an important supplement for traditional surface-deformation measurement of airport areas. Differential InSAR has been used to observe uneven ground-surface settlements at Hong Kong Chek Lap Kok Airport (Ding *et al.* 2001; G. Liu *et al.* 2001) and Iqaluit Airport in Canada (Short *et al.* 2014). Multi-temporal InSAR (MT-InSAR) has also been used to map the time-series deformation of Beijing Capital International Airport (Gao *et al.* 2016, 2019; He *et al.* 2016), Kunming Changshui International Airport (L. Zhang 2018), Nice Côte d'Azur Airport (Cavalié, Sladen, and Kelner 2015), among other. However, these studies have paid little attention to the reclaimed area and the deformation characteristics of different functional areas of the airport. Furthermore, very few efforts have been made to use InSAR technology to separate the composition of runway deformation. Deformation composition separation refers to confirming the magnitudes of settlement caused by different reasons, especially the dynamic-load settlement caused by aircraft taxiing. Shenzhen Bao'an International Airport (hereafter Shenzhen Airport) is one of the biggest airports in China. It has a reclaimed area of up to 13 km<sup>2</sup>. Nowadays, most airport facilities are built on reclaimed foundations. Therefore, this study monitors the subsidence of this airport and elaborates on the issues just raised.

In this study, we process the Envisat/ASAR data set covering Shenzhen Airport from 2007 to 2010 and the Sentinel-1 data set from 2015 to 2019 to obtain the spatial and temporal distribution of the surface deformation of the airport during construction and operation periods. Then we analyze the coupling relationship between surface subsidence and reclamation activities. In addition, taking runway No. 2 as an example, we use the InSAR results to explore the distribution and characteristics of settlements caused by dynamic loading. Finally, the potential and limitations of using InSAR technology for airport monitoring are discussed.

Photogrammetric Engineering & Remote Sensing  
Vol. 87, No. 2, February 2021, pp. 105–116.  
0099-1112/21/105–116

© 2021 American Society for Photogrammetry  
and Remote Sensing  
doi: 10.14358/PERS.87.2.105

## Study Area

### Geological Background

Shenzhen Airport is located on the east bank of the Pearl River Estuary and west of Bao'an District, about 30 km from the city of Shenzhen. Influenced by the subtropical maritime climate, this region has long summers, short winters, and abundant rainfall. The lowest temperature appears in January and the highest in July. The study area is in an alluvial plain with large areas of tidal flats. The marine sediments of the Quaternary Period, dominated by silt, are widely distributed in the low-lying coastal land and the east coast of the Lingdingyang Estuary. Most parts of this layer have a thickness of 3–10 m, but in some areas the thickness is up to 20 m. This kind of soft soil with high water content and relatively large pores is extremely susceptible to external loads and causes surface deformation (H.-M. Zhang, Xu, and Zeng 2002). Therefore, for Shenzhen Airport, it is very important to carry out comprehensive surface-subsidence monitoring over a long period of time (Niu *et al.* 2007).

### Airport Construction Process

Shenzhen has experienced unprecedented development in the past forty years (Yeh and Li 1997), resulting in land-resource insufficiency. Like other coastal cities, Shenzhen began to reclaim land, in 1991 (Seto *et al.* 2002), and the Shenzhen Airport coastline has been extended toward the sea several times, as shown in Figure 1c (Xu *et al.* 2016).

We take the 1979 coastline as the original coastline of the region, and divide the development process of Shenzhen Airport into three stages. The construction of the airport was carried out during the first stage (1979–2006). The old airport, including terminals A and B, runway No. 1, and corresponding supporting facilities, was located inside the 1979 coastline. In 2006, Shenzhen Airport entered the second stage (2006–2013) of its development, by reclaiming land and expanding on the west side of the old airport. The new airport, including terminal T3, runway No. 2, the ground transportation center (GTC), and other related facilities, was built on the reclaimed land. The reclamation project for runway No. 2 was carried out from 2006 to 2010, and the runway was put into operation on June 30, 2011. The T3 terminal building was constructed between February 25, 2010, and the end of November 2012. It officially began operating in 2013, when terminals A and B were closed and the section of Metro Line 11 that runs through the airport area began construction. During the second stage, the expansion project of Shenzhen Airport was completed. After 2013, the new airport started operation and entered the third stage (2013–present) of its development. In 2016, Metro Line 11 started operation. In the same year, the reclamation and soft foundation treatment for the T4 terminal area started on the north of the T3 terminal. The construction of the T4 terminal is expected to start in 2020.

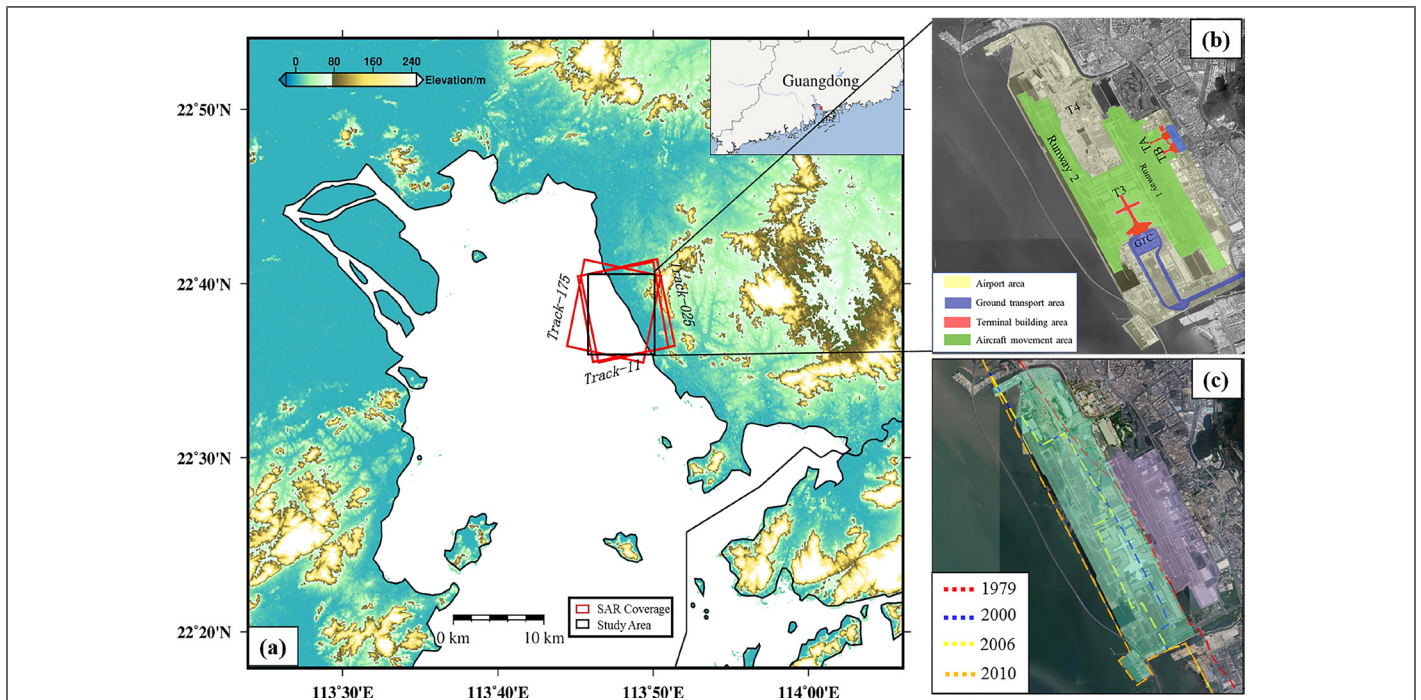


Figure 1. Study area. (a) Synthetic-aperture radar data coverage of the study area: the study area is outlined by the black rectangle, and red rectangles represent the coverage of the data set used. (b) Functional areas of the airport: the yellow, blue, red, and green masks cover the airport, ground transportation, terminal, and flight areas, respectively. (c) The coastline of Shenzhen Airport and its evolution: the purple mask and green masks cover the old airport area and the new airport area, respectively. The red, blue, yellow, and orange dotted lines are the coastline in 1979, 2000, 2006, and 2010, respectively.

Table 1. Image parameters and time coverage.

Sensor	Orbit	LOS Coefficient [E, N, U]	Incidence Angle (°)	Track	Number	Temporal Span
Envisat/ASAR	Ascending	[−0.32, −0.07, 0.94]	22.76	25	29	2/28/2007–7/7/2010
	Descending	[0.40, −0.08, 0.91]	22.82	175	28	6/24/2007–8/22/2010
Sentinel-1	Ascending	[−0.31, −0.09, 0.78]	33.91	11	104	6/15/2015–5/13/2019

LOS = line of sight; E = east–west; N = north–south; U = vertical.

## Data Processing

### Data Set

The data used in this study are Envisat/ASAR data of both ascending and descending orbits acquired from 2007 to 2010 and Sentinel-1 ascending data acquired from 2015 to 2019 (Figure 1; Tables 1, A1, and A2). During the time span of the Envisat/ASAR data, the old airport was completed and the new airport was under construction. During the time span of the Sentinel-1 data, the new airport area began operation.

### Improved PS-InSAR Strategy and Data Processing

In coastal areas, the atmospheric delay of SAR data is always serious. Furthermore, it is hard for the traditional persistent-scatterer InSAR (PS-InSAR) method to choose sufficient interferometric points, due to the poor scattering characteristics of the airport. In order to conduct a more detailed analysis of the study area, an improved PS-InSAR strategy is used to choose more point targets. This improved strategy can enhance the

point density by combining the traditional PS points and distributed points of the SBAS-InSAR. First we use the amplitude dispersion index (Ferretti, Prati, and Rocca 2001) to select PS points. Then the conventional differential interferometric process is applied to the co-registered single-look complex images. The average coherence of the differential interferograms is used to select high-coherence point targets (PTs) according to the threshold. The PS points selected by the traditional method and PTs are used as target candidates for subsequent processing. The flowchart is shown in Figure 2. Figure 3 compares the points selected by the traditional PS method and the improved strategy. The proposed strategy can significantly increase the density of interferometric points. After the point selection, the data information, including interferometric phase and coherence, is stored in vector format for subsequent processing. The interferometric phase of point targets can be expressed as

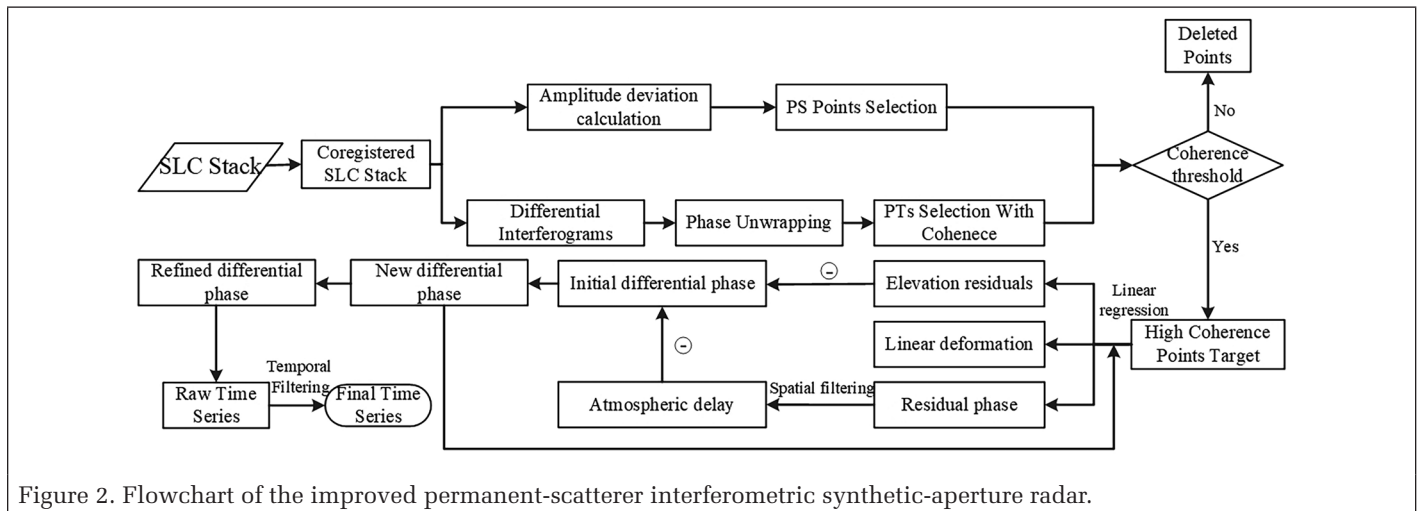


Figure 2. Flowchart of the improved permanent-scatterer interferometric synthetic-aperture radar.

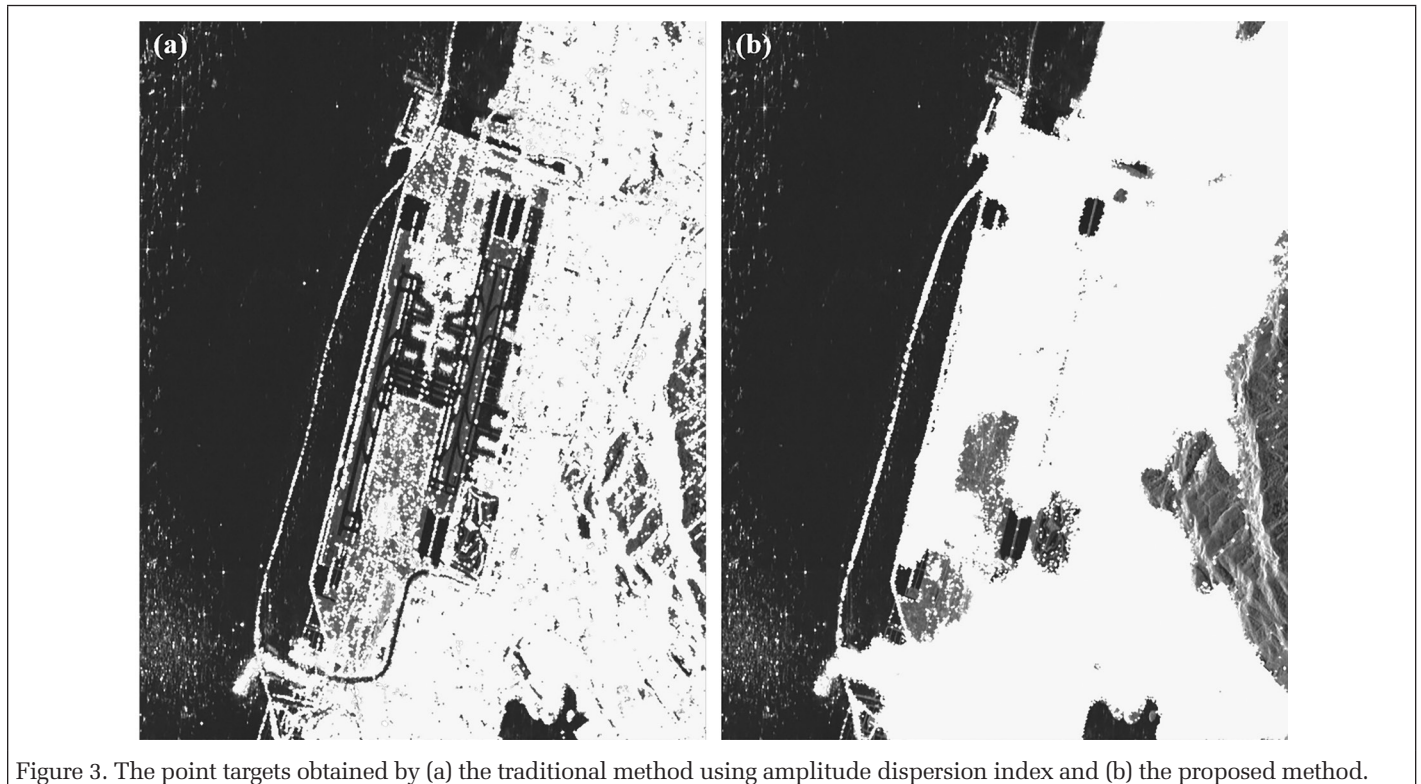


Figure 3. The point targets obtained by (a) the traditional method using amplitude dispersion index and (b) the proposed method.

$$\delta\phi = \frac{4\pi}{\lambda} \Delta T v + \frac{4\pi}{\lambda} \frac{B_{\perp} \Delta z}{r \sin\theta} + \Delta\phi_{\text{atm}} + \Delta_n, \quad (1)$$

where  $\Delta T$  represents the acquisition time difference of two images,  $v$  is the linear deformation rate,  $\lambda$  is the wavelength of the radar data,  $B_{\perp}$  is the perpendicular baseline,  $\Delta z$  denotes the elevation error,  $\theta$  is the incidence angle of the SAR satellite,  $r$  is the distance between the ground target and satellite, and  $\Delta\phi_{\text{atm}}$  and  $\Delta_n$  represent atmospheric delay and noise, respectively. Then singular value decomposition is used to transform the multi-master image into a single master image and obtain the elevation residuals as well as the raw time-series deformation. The raw time-series deformation is inverted using a linear regression model to obtain the average displacement rates. Finally, spatiotemporal filtering is performed to obtain the nonlinear deformation and thus the total time-series displacements.

Because of the side-looking geometry, the final deformation rate is the sum of the projections of the ground three-dimensional deformation in the line-of-sight direction. The projection coefficients are listed in Table 1. For the reclaimed area, the vertical subsidence is the main contribution of the line-of-sight displacement (Xu *et al.* 2016).

We choose stable reference points inside the 1979 coastline for phase unwrapping. The detailed data-process parameters are shown in Table 2, and the spatiotemporal baseline networks are shown in Figure A1.

### Deformation Results and Validation

In this study, the results of Envisat/ASAR data are used to study the settlement characteristics of the reclaimed areas and the areas inside the coastline during the construction stage of the airport. The results of Sentinel-1 data are used to study the uneven settlement of those areas during the operation stage in recent years. Deformation monitoring of the new airport located in the reclaimed area is the focus of this study. The deformation rate in this study is in the line-of-sight direction.

#### Deformation Between 2007 and 2010

The deformation rate generated from the Envisat/ASAR data shows that most of the selected points are distributed on reflectors with strong radar-signal reflection, which proves the reliability of the point-selection methods to some extent. And most of these points are distributed inside the 1979 coastline, because the area outside the coastline was under reclamation and expansion from 2007 to 2010, as shown in the optical images of Figure 1c. During that period, the surface-deformation rate of the whole study area was about  $-7.8$  to  $2.9$  mm/year. The old airport area was generally stable. Small settlements mainly occurred around the Hang Gang golf course to the north of runway No. 1 (region B in Figure 4a, 4b), the surface-compaction area to the south of the south apron (region D in Figure 4a, 4b), and some new reclaimed areas (region A in Figure 4a, 4b).

As Figure 4a and 4b shows, the deformation rates generated from the ascending and descending results have good consistency. The coherence points are mainly distributed inside the original coastline, and the overall deformation magnitude of the airport is small, so we select a profile

(profile AB in Figure 4) inside the original coastline to further explore the consistency of the two results. As Figure 5 shows, there is no obvious settlement in the selected profile. The settlement magnitude slightly fluctuates between 2 and  $-2$  mm/year, which also confirms the uncertainty of the estimation of the deformation rate. Therefore, the ascending and descending results are reliable.

#### Deformation Between 2015 and 2019

During 2015–2019, the airport experienced obvious uneven settlement (shown by the yellow dotted box in Figure 4c), especially in the reclaimed area, such as the under-construction T4 terminal (regions A, B), runway No. 2 and its taxiway (region C), the airport road along the south side of the GTC, and some unused land (region F). Deformation rates of these areas are up to  $-20$  mm/year, and in some points even exceed  $-40$  mm/year. However, the old airport within the 1979 coastline is stable except some areas affected by the excavation of deep foundation pits (regions D and E). Therefore, reclamation subsidence relating to human activities is the main cause of the uneven settlement. The reclaimed area has high risk of surface subsidence, needing continuous deformation monitoring.

Since there are no external data to validate the results of the Sentinel-1 data in the period 2015–2019, we assess their reliability by the uncertainty of the deformation rate. As shown in Figure 4d, the uncertainty of the deformation rate of most selected point targets is smaller than 1 mm/year, especially the area inside the 1979 coastline and the T3 terminal. Only a few points located in the T4 terminal area have a deformation-rate uncertainty larger than 1 mm/year. Therefore, the reliability of the Sentinel-1 deformation results is confirmed.

### Analysis of the Deformation Results

In terms of function, the airport can be divided into three parts: flight areas, terminals, and ground transportation areas. In the Shenzhen Airport, the flight areas include runways No. 1, No. 2, and No. 3 (under construction), the apron, and the taxiway system. The terminals include terminals A, B, and T3. The ground transportation system consists of the aboveground and underground parking lots, as well as airport road systems. The time span of the Sentinel-1 data used in this study is from 2015 to 2019, when the new airport was completed and put into operation. In the following, specific settlement characteristics are analyzed using the Sentinel-1 results.

#### Terminal Areas

As Figure 6 shows, terminals A, B, and T3 are generally stable between June 2015 and May 2019, especially terminals A and B, located inside the 1979 coastline. Terminal T3, built on the reclaimed foundation, is also relatively stable, with minor settlement in some areas, such as the No. 2 main finger corridor (MC2), the Northeast Hall, and the Southwest Hall.

We selected some PTs (P1, P2, P3, and P4) to study the time-series subsidence characteristics in these terminals. As Figure 6e and 6f shows, all four points have nonlinear periodic deformations. These periodic deformations are mainly due to the thermal expansion effect of the terminal building materials. P3 and P4, located in the old terminals, fluctuate

Table 2. Parameters in data processing.

Sensor	Orbit	Master Image	Perpendicular Baseline (m)	Temporal Baseline (day)	Filter	Multi-look	DEM
Envisat/ASAR	Ascending	10/15/2008	0–250	0–350	NL	1:5	SRTM
	Descending	9/21/2008	0–250	0–300	NL	1:5	SRTM
Sentinel-1	Ascending	6/15/2015	—	—	NL	4:1	SRTM

DEM = digital elevation model; NL = nonlocal; SRTM = Shuttle Radar Topography Mission.

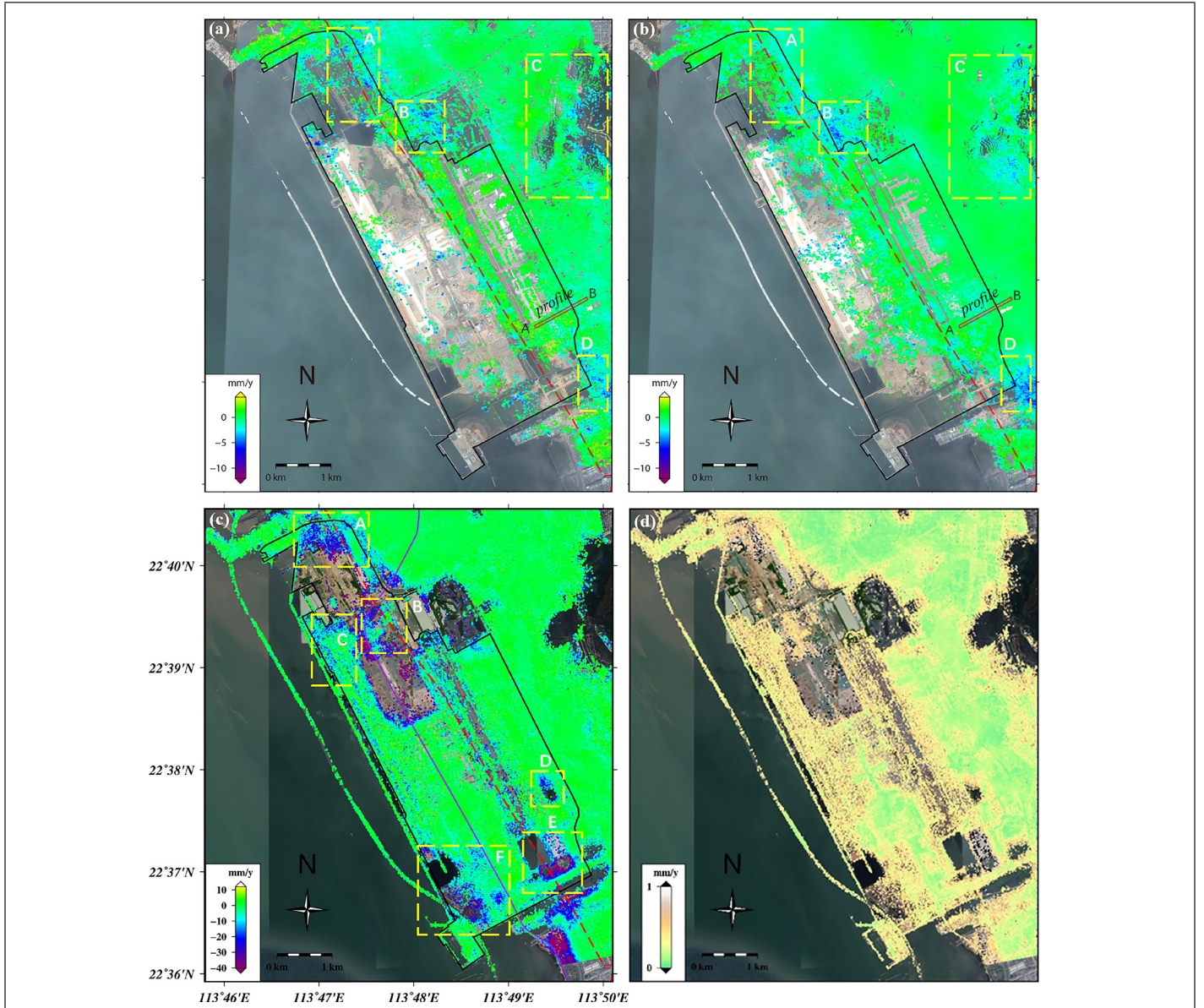


Figure 4. Deformation-rate maps generated from (a) track 025 data set, (b) track 175 data set, and (c) Sentinel-1 data set; and (d) deformation-rate uncertainty map of the results of the Sentinel-1 data. The solid black line indicates the outline of Shenzhen Airport, the solid purple line is Metro Line 11, and the red dotted line is the coastline in 1979. The yellow dotted frame is the subsidence area. The base images of the results of ASAR and Sentinel-1 are the optical images in 2010 and 2019, respectively. Profile AB is analyzed in Figure 5.

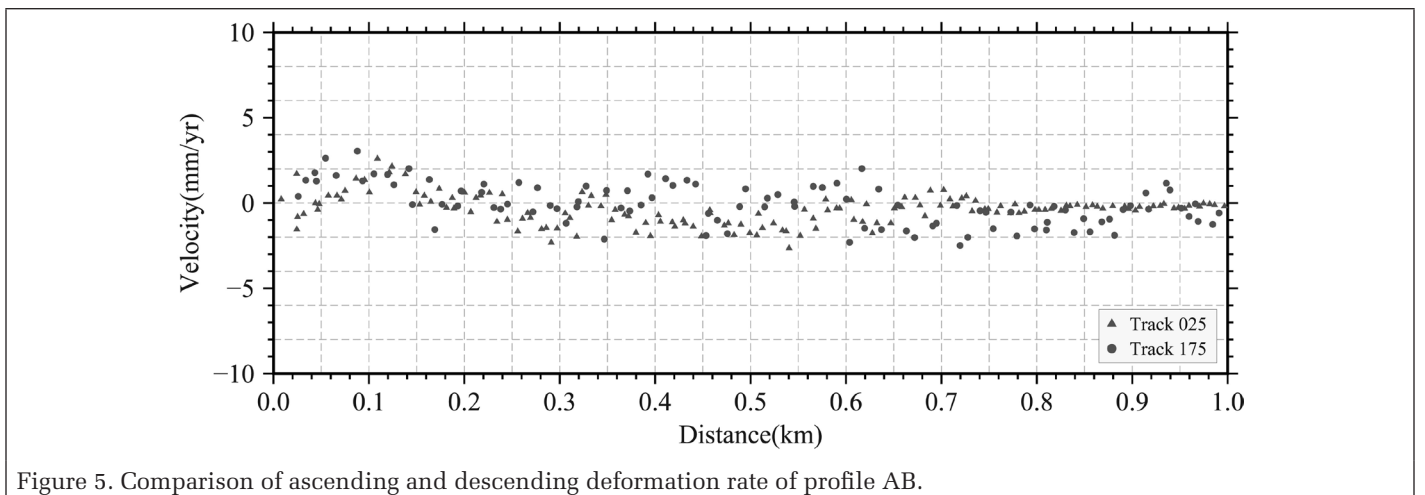


Figure 5. Comparison of ascending and descending deformation rate of profile AB.

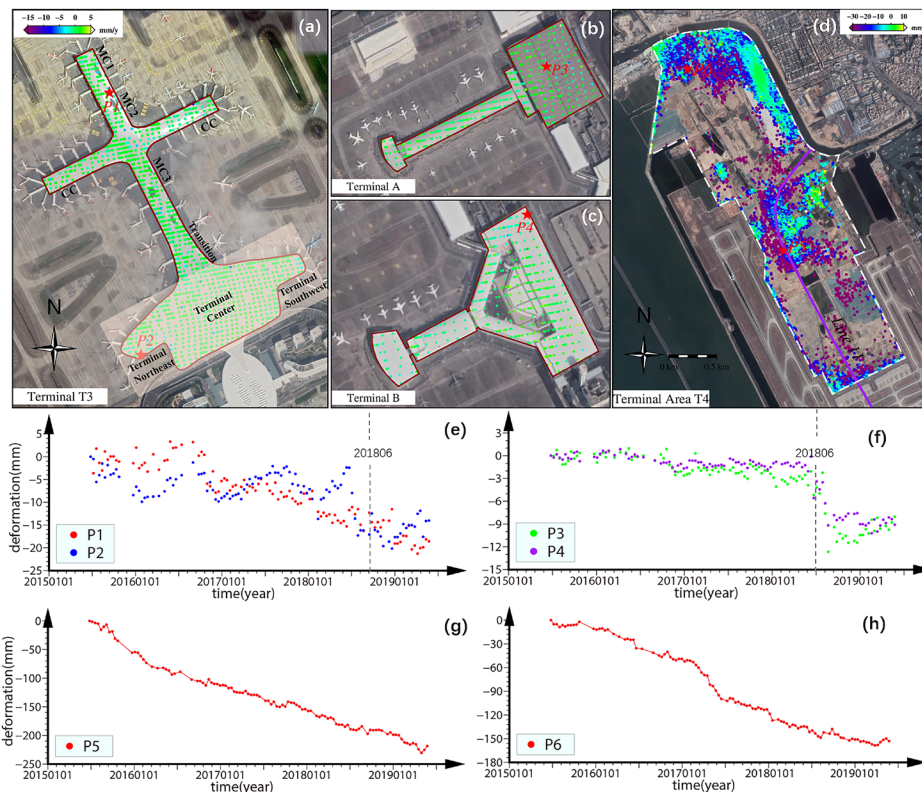


Figure 6. Deformation-rate map of terminals (a) T3, (b) A, (c) B, and (d) T4 between 2015 and 2019. (e and f) Time series of the deformation at P1, P2, P3, and P4. (g and h) Time series of the deformation at P5 and P6.

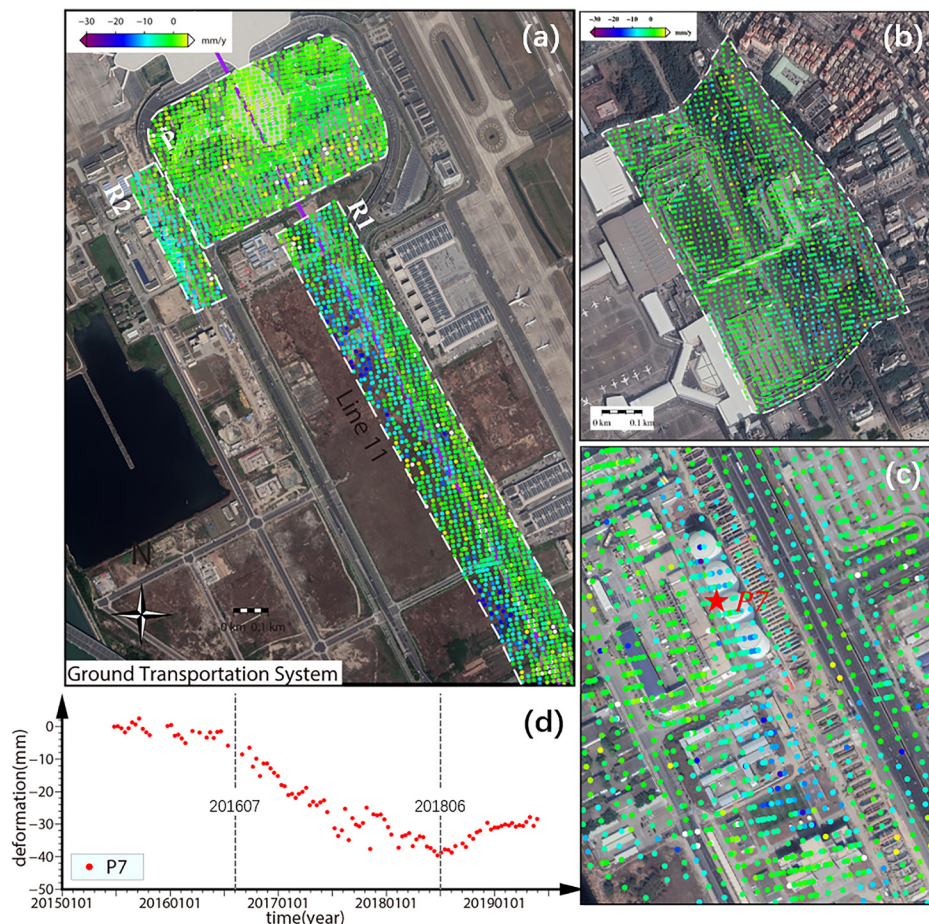


Figure 7. (a and b) Deformation zone of the ground transportation system between 2015 and 2019. (c) Zoom-in of region R2. (d) Time series of the deformation at P7.

less than P1 and P2. In addition to the periodic deformation, P1 and P2 have a general tendency of subsidence. The maximum cumulative settlement is 21.2 mm. The newly reclaimed areas are still undergoing slow consolidation settlement, but the foundation of the old airport area has been compacted and reached a stable state. After June 2018, there is obvious settlement at all four points. According to local meteorological data, during this period a couple typhoons landed at Shenzhen, including the super-typhoon Mangkhut, which caused the worst typhoon disaster in the past 30 years (S. Chen *et al.* 2018). These typhoons might have caused some small-magnitude motion of the terminal.

To further ease the pressure of air transportation, the airport planned to build terminal T4 on the north of terminal T3, where the Guangzhou-Dongguan-Shenzhen intercity railway and Metro Line 20 were under construction and Metro Line 11 runs underground. So there are many cross operations. Due to the ground construction, InSAR observation is seriously decoherent, and PTs cannot be selected in most areas. As the deformation-rate map (Figure 6d) shows, there is obvious settlement in the T4 terminal area, and the deformation rate of some points even exceeds  $-30$  mm/year. The cumulative settlement of the points P5 and P6 is more than 150 mm. According to the Terzaghi theory of consolidation (Liu *et al.* 2016), the T4 terminal area is still in the primary consolidation stage, and settlement will continue for some time before the area enters the secondary compression stage.

### Ground Transportation System

To analyze the deformation characteristics of the ground transportation area, we select the GTC and its attached parking lot (region P in Figure 7a), parking lot A/B (Figure 7b), and some sections of the airport roads (regions R1 and R2 in Figure 7a), which are undergoing significant subsidence. As the deformation-rate map (Figure 7) shows, both the old parking lots inside the 1979 coastline and the new parking lots on the reclaimed foundation, as well as the GTC, are in a stable state. That means the surface soil of the parking lots has reached a compacted state after consolidation,

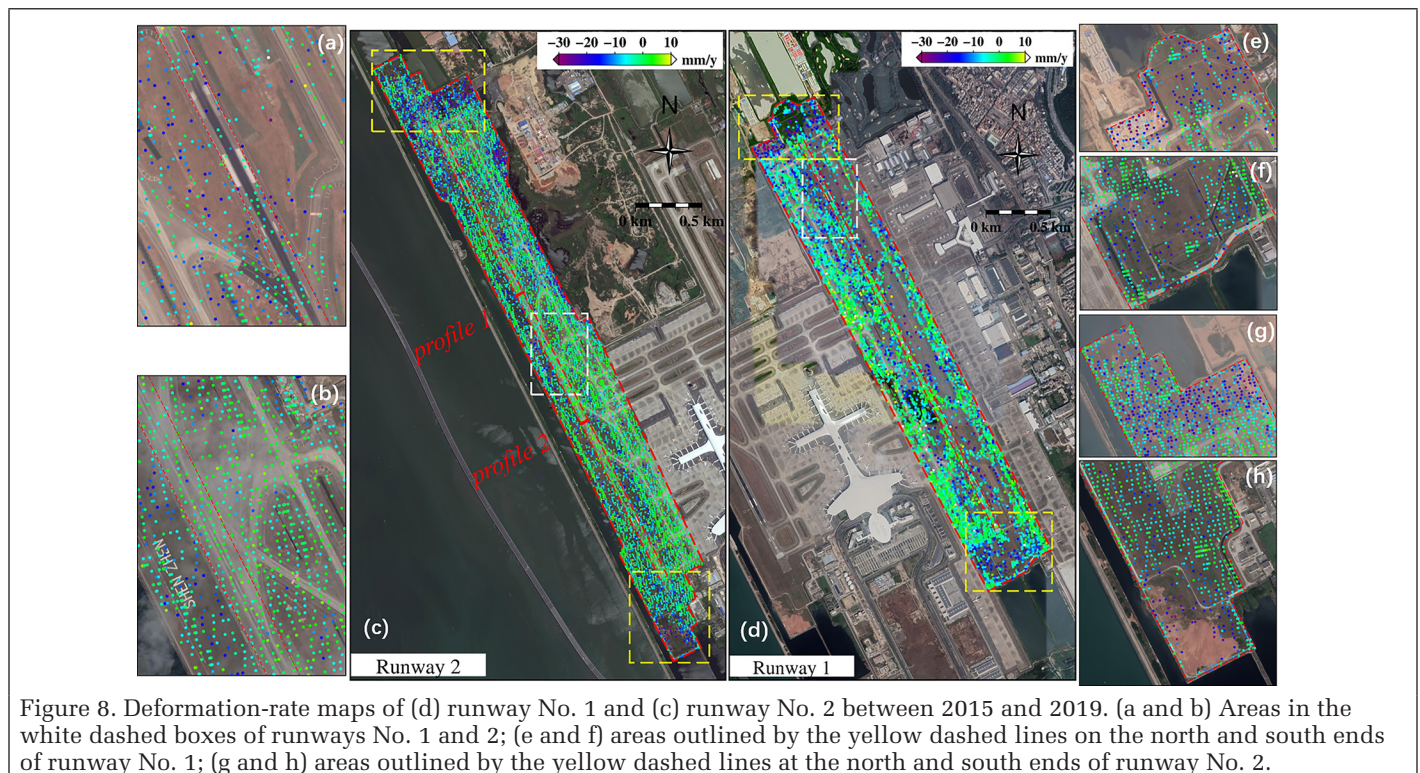
and the dynamic load from vehicles will not cause ground subsidence.

In Figure 7a, R1 is a road section along Metro Line 11. The average deformation rate of some points on it reaches  $-20$  mm/year. The subsiding points are distributed along the subway. Therefore, the construction and operation of the subway should be the main reason for settlement in this section. Line 11 started operation in June 2016, less than three years before 2019. Generally speaking, the settlement of the subway follows the logistic model in the time dimension (H. Wang *et al.* 2017), so this section should gradually stabilize in the future. R2 is a section along the Linghang No. 5 Road. During 2015–2019, the surrounding buildings (Figure 7c) experienced great settlement. The largest settlement occurred at an oil company southwest of the T3 terminal. The settlement around the four large fixed-top tanks is particularly noticeable, with the cumulative settlement over 40 mm (see point P7 in Figure 7). Around July 2016, the construction of Shenzhen Airport section of the Guangzhou-Dongguan-Shenzhen intercity railway started, and point P7 also started continuous settlement. Therefore, the construction of the intercity railway has an impact on the surface stability. The settlement here is a typical example of the surrounding ground subsidence due to excavation of the foundation pit (C. Jiang *et al.* 2003).

### Flight Areas

The flight areas, especially the runway, are the key zone of the airport, and their stability is very important to the safety of plane takeoff and landing. However, monitoring the deformation of the flight areas by ground-measurement methods is very difficult. It is also hard for traditional MT-InSAR to obtain the deformation information, due to the poor scattering characteristics. The proposed method can greatly increase the density of the selected deformation points in this area, and help the deformation analysis.

From Figure 8, a clear settlement trend can be observed. Runway No. 1 has more serious settlement than runway No. 2, with a maximum rate of  $-39.9$  mm/year and a large area of settlement in the northern section (Figure 8a). Runway No. 1



is located along the 1979 coastline and is in the transition area between the reclaimed land and the inland area, where the Quaternary marine sedimentary layers are distributed with deep soft soil. Runway No. 1 was built in 1990. During construction, dynamic compaction of the ground was used to strengthen the shallow soil layer, but caused settlement of the underlying silty soft soil layer. This settlement continued during 2015–2019, and will continue for the next few years with the compaction of soft soil. For runway No. 2, the settlement is mainly distributed in the reserved area outside the two ends of the runway (Figure 8g, 8h). The main cause of the settlement is the consolidation of the landfill soil. In the main body of the runway and the taxiway area, the surface is relatively stable, and no significant settlement occurs in a large area. The reason is that the replacement method was used in the foundation construction. It can be seen that this method can maintain higher stability of the ground than the general foundation treatment process. Of course, the replacement method is more complicated.

## Discussion

### Dynamic-Load Settlement Analysis of Runway

Due to dynamic and static loads as well as ground consolidation, airport runways are prone to settlement, which will directly affect the takeoff and landing security of aircraft. In general, the loads that cause the airport's surface settlement are the dynamic loads caused by aircraft taxiing, takeoff, and landing, the static loads caused by primary and secondary consolidation of soil, and additional loads caused by groundwater level changes (G. Wang *et al.* 2012). The latter two

kinds of loads act on the entire pavement, while the dynamic load often has a specific range of action, causing uneven settlement in the runway surface. We establish a foundation dynamic-load settlement model for runway No. 2 and use the InSAR results to separate the dynamic-load settlement (Yang and Yang 2007).

Runway No. 2 was completed in August 2010 and officially opened to traffic on July 26, 2011 (Figure 9). During the time between construction completion and operation, the airport pavement slowly settled due to consolidation of the soil. After operation, the impact of dynamic loads increased with the growing number of aircraft, causing the ground to undergo dynamic-load settlement. The dynamic load is usually only applied within a certain distance from the centerline of the runway, which is called the dynamic-load action zone in this study (G. Wang *et al.* 2012). Shenzhen Airport is a 4F civil airport, and the total width of runway is 60 m. The planes taking off and landing there have main landing gear with an outer

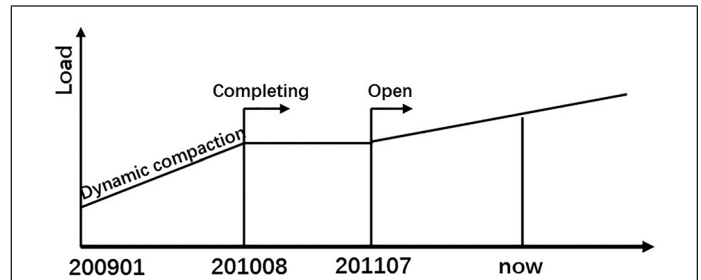


Figure 9. Load change of the foundation of runway No. 2.

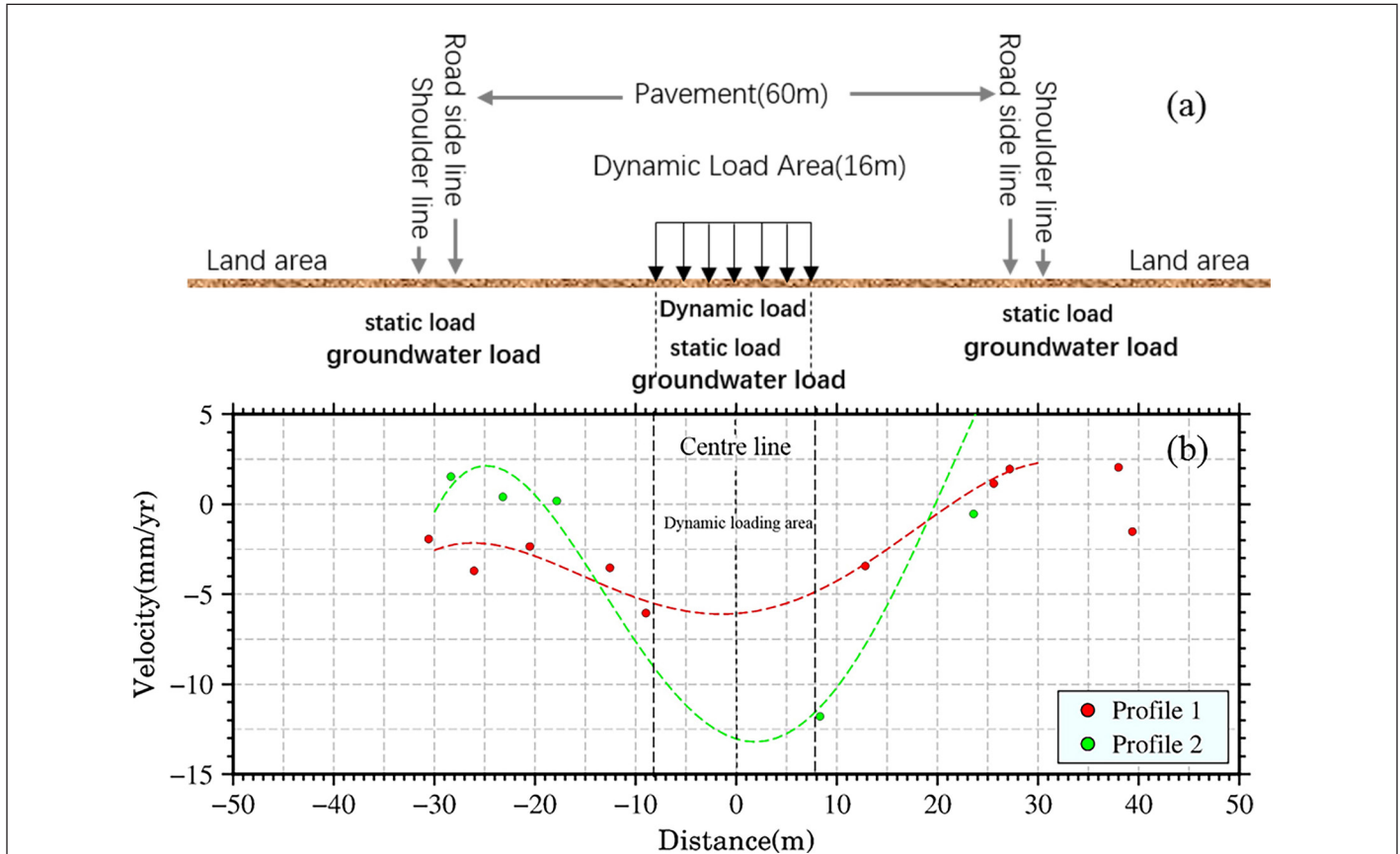


Figure 10. (a) Dynamic-load settlement model and (b) deformation rate of point targets in two profiles of runway No. 2. The ordinate represents the deformation rate of the point target in the profile, and the abscissa represents the distance of the point target from the centerline.

contour interval of 16 m. Therefore, the differential settlement between the point within 8 m and the point more than 30 m from the centerline can be used to approximate the dynamic-load settlement of the airport runway. The physical model is shown in Figure 10.

We attempt to separate the dynamic deformation of runway No. 2 from 2015 to 2019 using time-series results of Sentinel-1. Figure 10b is the deformation-rate diagram of two profiles (profiles 1 and 2 in Figure 8) selected from runway No. 2. The range of the dynamic-load action zone of runway No. 2 is  $\pm 8$  m.

On these two profiles, from the road sideline to the dynamic-load area, the settlement rate gradually increases. In the fitting curve, the valley values of the settlement velocities of the two profiles are located in the dynamic-load zone, confirming the existence of dynamic-load settlement of runway No. 2. The differential settlement (the difference between the mean values of the PT deformation rate inside and outside the dynamic-load action zone) in profile 1 is about  $-4.8$  mm/year, and profile 2 is about  $-11.4$  mm/year, with cumulative differential settlement of about  $-21$  mm and  $-54$  mm, respectively.

This is the first demonstration of separating the dynamic-load settlement components of airport runways using MT-InSAR results. Our results are consistent with the characteristics of runway dynamic-load subsidence obtained by traditional measurements, such as the dynamic-load subsidence of runway No. 1 at Shanghai Pudong Airport obtained using GPS data (G. Wang *et al.* 2012). However, the PTs in the profile are not sufficient to quantitatively determine the dynamic-load settlement of the whole runway, because the width of the runway is only about 60 m and the resolution of the SAR image is  $5 \text{ m} \times 20 \text{ m}$  (range  $\times$  azimuth). In the future, the dynamic-load deformation of the airport runway can be studied using SAR data of higher spatiotemporal resolutions.

#### Potential and Limits of MT-InSAR in Mapping Airport Subsidence

In this study, the SAR observations cover both the construction and operation phases of the Shenzhen Airport. In the Envisat/ASAR results, high-density PTs can be selected in the stable area (the old airport area) but not in the construction area, due to temporal decorrelation. This problem is also found in the deformation monitoring of Beijing Capital International Airport (Gao *et al.* 2016). However, we can obtain part of the surface-deformation information of the T4 terminal area during the construction period from the Sentinel-1 data from 2015 to 2019, because Sentinel-1 has a shorter revisit cycle than that of Envisat/ASAR (12 days vs. 35 days). This advantage of Sentinel-1 has also been demonstrated at the new Xiamen airport and Kuala Lumpur International Airport's land-reclamation monitoring (Marshall *et al.* 2018; X. Liu *et al.* 2019). So we can conclude that InSAR technology can extract surface-deformation information well in the high-coherence area during the operational phase. However, in the construction phase it is susceptible to the influence of temporal decorrelation, which makes its deformation-monitoring ability limited. The use of SAR data with high temporal resolution can improve the surface-measurement capability.

The SAR data selection is also an important factor for surface-deformation monitoring in airport areas. High-spatial-resolution images (such as TerraSAR-X or COSMO-SkyMed data sets) can usually provide much more detail for deformation monitoring. For instance, in identifying the deformation of a single infrastructure, the high-resolution COSMO-SkyMed will detect 3 to 6 times more points than the medium-resolution Envisat and RADARSAT satellites (Bonano *et al.* 2013; M. Chen and Shao 2013; Ma *et al.* 2019). In this study, C-band medium-spatial-resolution SAR data are used to extract the settlement information in the airport's high-coherence area, but they do not perform well for the runway areas because

of low point density. The Envisat/ASAR data were also used to delineate the main areas with subsidence at Hong Kong Airport, but the overall density of points in the airport areas is still too sparse to study the deformation details in local areas, especially the runway area (L. Zhang, Ding, and Lu 2011; Zhao *et al.* 2011). Generally, the width of the airport runway is  $\leq 60$  m, and the medium-resolution images of Envisat/ASAR and Sentinel-1 data are smaller than  $5 \text{ m} \times 20 \text{ m}$ , so they cannot provide sufficient points for runway-area deformation monitoring.

The InSAR data-processing strategy is another issue that needs to be considered in airport deformation monitoring. Traditional MT-InSAR (such as interferometric point-target analysis and SBAS-InSAR) usually performs well in monitoring the deformation of airport facilities, but it fails to select sufficient PS points in the low-scattering area (L. Zhang *et al.* 2011), like the runway area. For example, some scholars have used high-resolution TerraSAR-X images to investigate the deformation of Beijing Capital International Airport and adopted some methods to reduce the unwrapping error and increase the density of selected points (Gao *et al.* 2016, 2019; He *et al.* 2016). In this study, the proposed improved PS-InSAR strategy can partly increase the PS density by combining the observations of SBAS-InSAR, but it would reduce the spatial resolution of the result because of multi-look processing. Therefore, how to obtain sufficient points in an area with low-scattering characteristics (such as runway and expressway) needs further study. In addition, reclaimed airport area usually lacks a high-spatial-resolution digital elevation model, which would affect the accuracy of the InSAR processing. Therefore, using three-dimensional laser scanning technology (Shao *et al.* 2016) to obtain a digital elevation model—or using a data-processing method that is not assisted by a digital elevation model—to retrieve time-series displacements in reclaimed areas may be a good solution.

#### Conclusions

We proposed an improved PS-InSAR technique to measure the long-term (2007–2019) surface deformation of Shenzhen Airport. By comparing the results in different time domains, we found that uneven settlement is mainly distributed outside the 1979 coastline. The surface-deformation patterns of different functional areas are as follows: (1) the terminal zone is the most stable area of the airport; (2) in the ground transportation zone, some sections of the road have undergone surface deformation due to aboveground or underground engineering construction, such as a subway; (3) the flight zone is the most unstable area due to a combination of factors. We confirm settlement caused by the dynamic load on runway No. 2 by InSAR measurement, which is the first time such an operation has been performed. This study provides references for studying the general settlement characteristics of functional areas of the airport, and makes a meaningful attempt to use InSAR results to separate the composition of the runway settlement.

#### Acknowledgments

This research was supported by the National Key R&D Program of China (No.2016YFC0303004), Fundamental Research Funds for the graduate student of Central South University (1053320190999) and National Science Foundation of China (41574005). The authors would like to thank the European Space Agency (ESA) for providing Envisat/ASAR data and Sentinel-1 data. General Mapping Tools (version 5.1.2) was used to produce several figures.

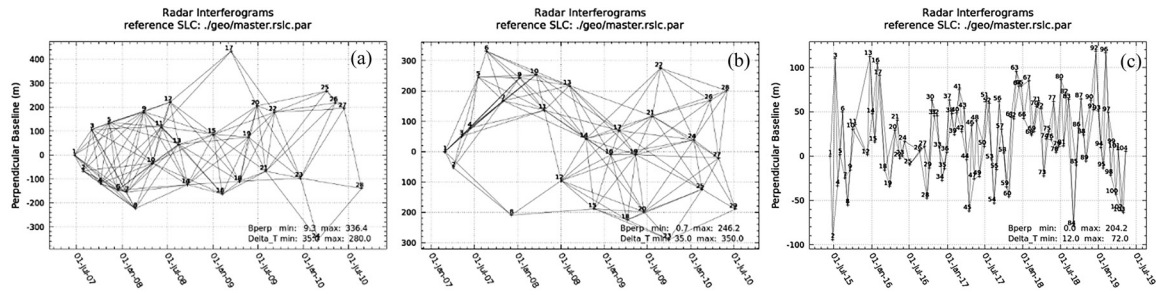


Figure A1. Spatiotemporal baseline network of (a) track 025, (b) track 175, and (c) Sentinel-1.

Table A1. Image data sets of Envisat/ASAR (tracks 025 and 175).

No.	Orbit	Acquisition Date	Temp_B (day)	Perp_B (m)	Orbit	Acquisition Date	Temp_B (day)	Perp_B (m)
1	Ascending	2/28/2007	0	0	Descending	6/24/2007	0	0
2	Ascending	4/4/2007	35	-52.946	Descending	7/29/2007	35	-66.300
3	Ascending	5/9/2007	70	50.641	Descending	9/2/2007	70	106.796
4	Ascending	6/13/2007	105	78.616	Descending	10/7/2007	105	-119.240
5	Ascending	7/18/2007	140	246.176	Descending	11/11/2007	140	134.998
6	Ascending	8/22/2007	175	331.313	Descending	12/16/2007	175	-146.594
7	Ascending	10/31/2007	244	167.866	Descending	1/20/2008	210	-155.877
8	Ascending	12/5/2007	280	-209.482	Descending	2/24/2008	245	-223.888
9	Ascending	1/9/2008	315	243.667	Descending	3/30/2008	280	180.496
10	Ascending	3/19/2008	385	254.215	Descending	5/4/2008	315	-33.914
11	Ascending	4/23/2008	420	136.498	Descending	6/8/2008	350	118.656
12	Ascending	7/2/2008	490	-95.718	Descending	7/13/2008	385	220.918
13	Ascending	8/6/2008	525	217.723	Descending	8/17/2008	420	45.229
14	Ascending	10/15/2008	595	42.313	Descending	9/21/2008	455	-124.066
15	Ascending	11/19/2008	630	-188.648	Descending	1/4/2009	560	86.144
16	Ascending	1/28/2009	700	-10.936	Descending	2/8/2009	595	-162.996
17	Ascending	3/4/2009	735	69.285	Descending	3/15/2009	630	433.797
18	Ascending	4/8/2009	770	-225.182	Descending	4/19/2009	665	-109.997
19	Ascending	5/13/2009	805	-10.186	Descending	5/24/2009	700	74.463
20	Ascending	6/17/2009	840	-198.921	Descending	6/28/2009	735	205.113
21	Ascending	7/22/2009	875	117.409	Descending	8/2/2009	770	-67.835
22	Ascending	8/26/2009	910	275.600	Descending	9/6/2009	805	179.186
23	Ascending	9/30/2009	945	-289.911	Descending	12/20/2009	910	-97.186
24	Ascending	1/13/2010	1050	38.944	Descending	2/28/2010	980	-353.220
25	Ascending	2/17/2010	1085	-124.264	Descending	4/04/2010	1015	267.683
26	Ascending	3/24/2010	1120	169.293	Descending	5/09/2010	1050	218.822
27	Ascending	4/28/2010	1155	-21.175	Descending	6/13/2010	1085	194.234
28	Ascending	6/2/2010	1190	200.777	Descending	8/22/2010	1155	-139.752
29	Ascending	7/7/2010	1225	-189.857				

References

Bamler, R. and P. Hartl. 1998. Synthetic aperture radar interferometry. *Inverse Problems* 14 (4):R1.

Bonano, M., M. Manunta, A. Pepe, L. Paglia, and R. Lanari. 2013. From previous C-band to new X-band SAR systems: Assessment of the DInSAR mapping improvement for deformation time-series retrieval in urban areas. *IEEE Transactions on Geoscience and Remote Sensing* 51 (4):1973–1984.

Cavalié, O., A. Sladen and M. Kelner. 2015. Evidence of ground subsidence at the Nice Côte d’Azur International airport from InSAR time series analysis. Number 8140 in *EGU General Assembly*, held in Vienna, Austria, 12–17 April 2015. Edited by J. Editor. City, St.: Publisher.

Chen, S., G. Tian, H. Li, Q. Zhang, Y. Bai and L. Wang. 2018. Impact of Typhoon “Mangosteen” no. 1822 on rainfall erosivity in Guangdong Province. *Bulletin of Soil and Water Conservation* 39 (3):231–236.

Chen, M. and Z. Shao. 2013. Robust affine-invariant line matching for high resolution remote sensing images. *Photogrammetric Engineering and Remote Sensing* 79 (8):753–760.

Ding, X., G. Liu, Z. Li, Z. Li and Y. Chen. 2004. Monitoring ground Settlement in Hong Kong with satellite SAR interferometry. *Photogrammetric Engineering and Remote Sensing* 70(10): 1151–1156.

Ferretti, A., C. Prati and F. Rocca. 2001. Permanent scatterers in SAR interferometry. *IEEE Transactions on Geoscience and Remote Sensing* 39 (1):8–20.

Fornés Martínez, H. 2015. Analysis of potential implementations of pushback control at LaGuardia Airport (master’s thesis). *Massachusetts Institute of Technology*, Cambridge.

Gao, M., H. Gong, B. Chen, C. Zhou, W. Chen, Y. Liang, M. Shi and Y. Si. 2016. InSAR time-series investigation of long-term ground displacement at Beijing Capital International Airport, China. *Tectonophysics* 691 (B):271–281.

Gao, M., H. Gong, X. Li, B. Chen, C. Zhou, M. Shi, L. Guo, Z. Chen, Z. Ni and G. Duan. 2019. Land subsidence and ground fissures in Beijing Capital International Airport (BCIA): Evidence from quasi-PS InSAR analysis. *Remote Sensing* 11 (12):1466.

He, Y., L. Zhu, H. Gong and R. Wang. 2016. Analysis of land subsidence features based on TerraSAR images in Beijing-Capital International Airport. *Science of Surveying and Mapping* 41 (12):14–18.

Table A2. Image data sets of Sentinel-1 (track 11).

No.	Acquisition Date	Temp_B (day)	Perp_B (m)
1	6/15/2015	0	0.000
2	6/27/2015	12	-94.203
3	7/9/2015	24	109.951
4	7/21/2015	36	-33.315
5	8/2/2015	48	1.708
6	8/14/2015	60	49.775
7	8/26/2015	72	-24.614
8	9/7/2015	84	-55.167
9	9/19/2015	96	-15.485
10	10/1/2015	108	30.777
11	10/13/2015	120	35.277
12	12/12/2015	180	1.512
13	12/24/2015	192	112.586
14	1/5/2016	204	47.813
15	1/17/2016	216	15.826
16	1/29/2016	228	104.570
17	2/10/2016	240	90.943
18	3/5/2016	264	-15.604
19	3/29/2016	288	-34.186
20	4/22/2016	312	29.207
21	5/4/2016	324	40.648
22	5/16/2016	336	-2.071
23	5/28/2016	348	0.460
24	6/9/2016	360	16.717
25	7/3/2016	384	-9.775
26	8/20/2016	432	6.040
27	9/13/2016	456	10.845
28	9/25/2016	468	-47.446
29	10/07/2016	480	-13.413
30	10/19/2016	492	63.266
31	10/31/2016	504	45.752
32	11/12/2016	516	45.703
33	11/24/2016	528	9.109
34	12/06/2016	540	-27.193
35	12/18/2016	552	-13.991
36	12/30/2016	564	4.545
37	1/11/2017	576	63.453
38	1/23/2017	588	48.045
39	2/04/2017	600	24.661
40	2/16/2017	612	48.737
41	2/28/2017	624	74.813
42	3/12/2017	636	27.897
43	3/24/2017	648	53.933
44	4/5/2017	660	-3.875
45	4/17/2017	672	-61.813
46	4/29/2017	684	34.380
47	5/11/2017	696	-25.669
48	5/23/2017	708	40.017
49	6/4/2017	720	-22.873
50	6/28/2017	744	11.276
51	7/10/2017	756	65.547
52	7/22/2017	768	59.250

Table A2 continued

No.	Acquisition Date	Temp_B (day)	Perp_B (m)
53	8/3/2017	780	-4.237
54	8/15/2017	792	-52.815
55	8/27/2017	804	-14.917
56	9/8/2017	816	61.721
57	9/20/2017	828	30.432
58	10/2/2017	840	3.580
59	10/14/2017	852	-34.467
60	10/26/2017	864	-45.922
61	11/7/2017	876	43.785
62	11/19/2017	888	42.472
63	12/1/2017	900	95.767
64	12/13/2017	912	78.704
65	12/25/2017	924	79.294
66	1/6/2018	936	42.931
67	1/30/2018	960	85.010
68	2/11/2018	972	23.813
69	2/23/2018	984	27.663
70	3/7/2018	996	55.965
71	3/19/2018	1008	60.334
72	3/31/2018	1020	53.081
73	4/12/2018	1032	-22.313
74	4/24/2018	1044	19.258
75	5/6/2018	1056	27.675
76	5/18/2018	1068	18.710
77	5/30/2018	1080	61.901
78	6/11/2018	1092	4.071
79	6/23/2018	1104	10.494
80	7/5/2018	1116	86.058
81	7/17/2018	1128	11.680
82	7/29/2018	1140	69.030
83	8/10/2018	1152	63.737
84	9/3/2018	1176	-79.355
85	9/15/2018	1188	-9.861
86	9/27/2018	1200	31.813
87	10/9/2018	1212	64.665
88	10/21/2018	1224	23.921
89	11/2/2018	1236	-5.579
90	11/26/2018	1260	63.171
91	12/8/2018	1272	52.303
92	12/20/2018	1284	118.446
93	1/1/2019	1296	50.913
94	1/13/2019	1308	10.179
95	1/25/2019	1320	-13.247
96	2/6/2019	1332	116.855
97	2/18/2019	1344	49.426
98	3/2/2019	1356	-21.518
99	3/14/2019	1368	12.795
100	3/26/2019	1380	-42.983
101	4/7/2019	1392	7.726
102	4/19/2019	1404	-61.030
103	5/1/2019	1416	-63.716
104	5/13/2019	1428	5.450

Jiang, C., Y. He, Y. Gai and J. Huang. 2003. Monitoring and initial analysis of surface settlement neighboring to excavation works. *Architecture Technology* 34 (2):102-103.

Jiang, Y., M. Liao, H. Wang, L. Zhang and T. Balz. 2016. Deformation monitoring and analysis of the geological environment of Pudong International Airport with persistent scatterer SAR interferometry. *Remote Sensing* 8 (12):1021.

Liu, G., X. Ding, Y. Chen, Z. Li and Z. Li. 2001. Using satellite radar differential interference technology to measure the settlement field at Hong Kong Chek Lap Kok Airport. *Chinese Science Bulletin* 46 (14):1224-1228.

Liu, X., C. Zhao, Q. Zhang, C. Yang and J. Zhang. 2019. Characterizing and monitoring ground settlement of marine reclamation land of Xiamen New Airport, China with Sentinel-1 SAR datasets. *Remote Sensing* 11 (5):585.

Ma, P., W. Wang, B. Zhang, J. Wang, G. Shi, G. Huang, F. Chen, J. Jiang and H. Lin. 2019. Remotely sensing large- and small-scale ground subsidence: A case study of the Guangdong-Hong Kong-Macao Greater Bay Area of China. *Remote Sensing of Environment* 232:111282.

Marshall, C., D. J. Large, A. Athab, S. L. Evers, A. Sowter, S. Marsh and S. Sjögersten. 2018. Monitoring tropical peat related settlement using ISBAS InSAR, Kuala Lumpur International Airport (KLIA). *Engineering Geology* 244:57-65.

- Mesri, G. and J. R. 2015. Settlement of the Kansai International Airport islands. *Journal of Geotechnical and Geoenvironmental Engineering* 141 (2):04014102.
- Niu, R., L. Zhang, Z. Shao and Q. Chang. 2007. Web-based geological hazard monitoring in the Three Gorges area of China. *Photogrammetric Engineering and Remote Sensing* 73 (6):709–719.
- Rosen, P. A., S. Hensley, I. R. Joughin, F. K. Li, S. N. Madsen, E. Rodriguez and R. M. Goldstein. 2000. Synthetic aperture radar interferometry. *Proceedings of the IEEE* 88 (3):333–382.
- Seto, K. C., C. E. Woodcock, C. Song, X. Huang, J. Lu and R. K. Kaufmann. 2002. Monitoring land-use change in the Pearl River Delta using Landsat TM. *International Journal of Remote Sensing* 23 (10):1985–2004.
- Shao, Z., N. Yang, X. Xiao, L. Zhang and Z. Peng. 2016. A multi-view dense point cloud generation algorithm based on low-altitude remote sensing images. *Remote Sensing* 8 (5):381.
- Short, N., A.-M. LeBlanc, W. Sladen, G. Oldenborger, V. Mathon-Dufour and B. Brisco. 2014. RADARSAT-2 D-InSAR for ground displacement in permafrost terrain, validation from Iqaluit Airport, Baffin Island, Canada. *Remote Sensing of Environment* 141:40–51.
- Wang, G., L. Han, Z. Chai, J. Cao and Z. Zhou. 2013. The runway subgrade settlement induced by moving aircraft loading. *Chinese Journal of Underground Space and Engineering* 9 (4):939–945.
- Wang, G., L. Han, Z. Chai, Y. Wei, J. Cao and Z. Zhou. 2012. Subgrade settlement rules of first runway of Pudong Airport in Shanghai. *Journal of Engineering Geology* 20 (1):131–137.
- Wang, H., G. Feng, B. Xu, Y. Yu, Z. Li, Y. Du and J. Zhu. 2017. Deriving spatio-temporal development of ground subsidence due to subway construction and operation in delta regions with PS-InSAR data: A case study in Guangzhou, China. *Remote Sensing* 9 (10):1004.
- Xu, B., G. Feng, Z. Li, Q. Wang, C. Wang and R. Xie. 2016. Coastal subsidence monitoring associated with land reclamation using the point target based SBAS-InSAR method: A case study of Shenzhen, China. *Remote Sensing* 8 (8):652.
- Yang, F. and L. Yang. 2007. The effect analysis of traffic loads on post construction settlement of subgrade. *Chinese Journal of Underground Space and Engineering* 3 (7):1338–1341.
- Yeh, A.G.O. and X. Li. 1997. An integrated remote sensing and GIS approach in the monitoring and evaluation of rapid urban growth for sustainable development in the Pearl River Delta, China. *International Planning Studies* 2 (2):193–210.
- Zhang, H.-M., Y.-S. Xu and Q.-L. Zeng. 2002. Deformation behavior of Shenzhen soft clay and post-construction settlement. *Chinese Journal of Geotechnical Engineering* 24 (4):509–514.
- Zhang, L. 2018. The deformation monitoring of Kunming Changshui International Airport based on PS-InSAR. *Journal of Kunming Metallurgy College* 34 (1):6–10.
- Zhang, L., X. Ding and Z. Lu. 2011. Ground settlement monitoring based on temporarily coherent points between two SAR acquisitions. *ISPRS Journal of Photogrammetry and Remote Sensing* 66 (1):146–152.
- Zhao, Q., H. Lin, W. Gao, H. A. Zebker, A. Chen and K. Yeung. 2011. InSAR detection of residual settlement of an ocean reclamation engineering project: A case study of Hong Kong International Airport. *Journal of Oceanography* 67 (4):415–426.

# Fully Convolutional Neural Network for Impervious Surface Segmentation in Mixed Urban Environment

Joseph McGlinchy, Brian Muller, Brian Johnson, Maxwell Joseph, and Jeremy Diaz

## Abstract

*The urgency of creating appropriate, high-resolution data products such as impervious cover information has increased as cities face rapid growth as well as climate change and other environmental challenges. This work explores the use of fully convolutional neural networks (FCNNs)—specifically UNet with a ResNet-152 encoder—in mapping impervious surfaces at the pixel level from WorldView-2 in a mixed urban/residential environment. We investigate three-, four-, and eight-band multispectral inputs to the FCNN. Resulting maps are promising in both qualitative and quantitative assessment when compared to automated land use/land cover products. Accuracy was assessed by F1 and average precision (AP) scores, as well as receiver operating characteristic curves, with area under the curve (AUC) used as an additional accuracy metric. The four-band model shows the highest average test-set accuracies (F1, AP, and AUC of 0.709, 0.82, and 0.807, respectively), with higher AP and AUC than the automated land use/land cover products, indicating the utility of the blue-green-red-infrared channels for the FCNN. Improved performance was seen in residential areas, with worse performance in more densely developed areas.*

## Introduction

Impervious surface extent is increasingly being considered as an indicator of urban sprawl and surface-water run-off, as well as a contributor to the urban heat island effect (Wang and Li 2019). The potential for increased urban run-off, with the corresponding reduction in urban canopy, is cause for concern in watersheds containing urban environments. Thus, impervious surface data have proven valuable for environmental management and land use planning and policy.

Impervious cover data are used in key regulatory and planning functions in local government. Perhaps most important, they are used in establishing the impervious cover fee. This fee is a charge on landowners to cover costs of water management resulting from higher-volume and more rapid flows of stormwater over impervious cover such as streets and parking lots. The amount of the fee is based on evaluation of the area of impervious cover within an ownership parcel. Remotely

---

Joseph McGlinchy and Maxwell Joseph are with the Earth Lab, CIRES, University of Colorado – Boulder, Boulder, CO 80303 (joseph.mcglinchy@colorado.edu).

Brian Muller is with Environmental Sciences, University of Colorado – Boulder, Boulder, CO 80303.

Brian Johnson is with Aerospace Corp., Longmont, CO (previously with the Earth Lab, CIRES, University of Colorado – Boulder, Boulder, CO 80303).

Jeremy Diaz is with The Pennsylvania State University, State College, PA (previously with the Earth Lab, CIRES, University of Colorado – Boulder, Boulder, CO 80303).

sensed data, along with data from other sources, are used as a basis for this determination. Moreover, urban development and densification typically result in expansion of impervious cover, leading to increased water run-off. Without mitigation, additional run-off is associated with increases in the concentration of key pollutants in surface waters and increased risk of flood, injury, and property damage. Thus, in addition to fee assessments, impervious cover data are employed in urban planning activities including stormwater and water-quality planning, capital-improvement planning, flood preparedness, and development management. The need to create appropriate, high-resolution data products such as impervious cover information has increased in urgency as cities face rapid growth as well as climate change and other environmental challenges.

The availability of high-resolution satellite imagery (i.e., less than 5 m/pixel) has allowed for the delineation of urban features such as roadways, sidewalks, paved areas, rooftops, and other impervious surface types which are typically mixed with other materials in imagery acquired from systems with lower spatial resolution, for example, Landsat at 30 m/pixel. Past work has focused on pixel-based (image classification, regression, etc.), subpixel-based (linear spectral unmixing, imperviousness as the complement of vegetation fraction, etc.), and object-based algorithms (i.e., image segmentation and classification), as well as artificial neural networks, for mapping impervious surface extent (Wang and Li 2019). Shao *et al.* (2019) have shown success in mapping impervious surface coverage specifying topographical units such as watersheds using the Landsat archive. Typically, these methods involve a supervised image-classification approach and aggregation of the classification results, which involves the collection of training samples for each class, with many possible distinct classes representative of impervious surface cover. The classification results are then analyzed for accuracy, and all classes indicative of impervious surface cover are aggregated to the same superclass.

Object-based approaches require image segmentation as a preprocessing step. Each image segment, or object, is then used to calculate a feature vector from the image data contained within it. The objects are used as input to a classification algorithm given a set of labeled training data. Wieland and Pittore (2014) calculated features on a per-segment basis and used them as inputs to four classification methods: normal Bayes, K-nearest neighbor, random trees, and support vector machine. All classifiers showed promising results on the test data coming from the same data set as the training data, but showed limited transferability to different sensors with similar spectral and spatial characteristics such as

---

Photogrammetric Engineering & Remote Sensing  
Vol. 87, No. 2, February 2021, pp. 117–123.  
0099-1112/21/117–123

© 2021 American Society for Photogrammetry  
and Remote Sensing  
doi: 10.14358/PERS.87.2.117

*QuickBird*, *IKONOS*, and *WorldView-2*. Wieland and Pittore found that the generally large variability of spectral signatures within the built environment and regional differences in predominant roof materials may also lead to limitations on the transferability of trained classifiers and should be considered when applying such classifiers in new, unseen geographies.

Wieland and Pittore (2014) have shown that the impervious cover class comprises numerous subclasses due to various materials which make up roofs, pavement, and sidewalks. They also have shown that spectral- and texture-based image features account for the greatest percentage of explanation of the impervious cover class. Medium-resolution systems such as Landsat are not able to resolve these features, but high-resolution systems such as Maxar's *WorldView* can resolve these features at the pixel level. Convolutional neural networks (CNNs), by design, account for the texture characteristics of images, and they have been used extensively in the computer-vision community for tasks such as scene classification, object detection, and segmentation due to the integration of many stages of kernel-based convolutional filters. CNNs have also recently emerged as a useful tool for similar tasks using remote-sensing imagery (Zhu *et al.* 2017). Specifically, for image segmentation, the initial work of Ronneberger, Fischer, and Brox (2015) introduced the UNet fully convolutional neural network (FCNN) as a solution to binary segmentation of electron-microscope images into foreground and background classes. Li *et al.* (2018) expanded upon the original UNet architecture to segment Google Earth base map image tiles (e.g., RGB images) into sea and land classes, and the FCNN architecture has also been used to map houses from similar imagery sources (Igloukov and Shvets 2018).

This work evaluates the application of the UNet FCNN, specifically with the ResNet-152 encoder, to the task of binary image segmentation of high-resolution commercial satellite imagery into impervious and pervious surface classes. The rest of this article is organized as follows: the next section describes the study area(s) used in this work, then the proposed methods are presented, followed by their results. The final two sections discuss conclusions and potential future work.

## Study Area and Source Data

A *WorldView-2* scene was acquired over Denver, Colorado, USA, at 10:49 A.M. local time on 24 July 2016, with 0% cloud cover. Maxar *WorldView-2* data were made accessible through GBDX, Maxar's geospatial big-data platform. *WorldView-2* data contains eight spectral bands (coastal blue, blue, green, yellow, red, red edge, and two near-infrared channels) and have a nominal ground sample distance of approximately 2 m. The scene used in this work was captured with a view angle of 10.5° off-nadir, resulting in a pixel size of 1.9 m. This area of Denver, covering approximately 10 km<sup>2</sup>, is characterized by residential, dense urban, and mixed residential and urban land use.

Polygons were derived from orthoimagery collected by the Denver Regional Aerial Photography Project managed by the Denver Regional Council of Governments. The orthoimagery includes four-band multispectral images (RGB and NIR) collected in 2016 at submeter resolutions. These images were used to digitize planimetric data such as building footprints and streets. We clipped these data to a study area in west-central Denver and aggregated impervious units into polygons attributed as impervious or pervious cover. This polygon data set served as the labeled training, test, and validation data set. All polygons were given a label of 1 or 0 to represent impervious or pervious surface type, respectively. ArcMap 10.6 (Esri, Inc.) was used to convert the geometries with label values 1 and 0 to a raster with the same pixel size as the *WorldView-2* image,

utilizing the Snap Raster environment variable. This ensured alignment of the ground-truth data to the remotely sensed image. Visual inspection of polygons labeled "building" and "driveway" overlaid with the *WorldView-2* imagery confirmed that the data sets were well aligned (Figure 1, top left) and sufficient to consider each data set for model training.

## Methods

Impervious surface mapping has traditionally been approached as a hierarchical image-classification task. Pixel- and object-based approaches are prevalent in the literature (e.g., Weng 2012; Wieland and Pittore 2014; and references therein). These classification approaches are often treated as a supervised classification task which requires collecting training samples of all classes. Samples from classes such as roads, roofs (typically a single class for each roof type or color), pavement (typically a single class for each type of paved material), vegetation (typically a single class for each type of vegetation: grass, tree, senescent grass, etc.), water, and shadow are collected and used to train the classifier. The classification results, if satisfactory, are then aggregated into two classes which contain subclasses deemed appropriate for impervious or pervious surface identification.

Materials which fall into the impervious surface category, such as concrete, brick, metal, painted surfaces, asphalt, and plastics, tend to have similar spectral reflectance curves. This spectral similarity, along with the range of magnitude across samples from the same material class, can be a source of confusion in traditional supervised classification algorithms. Examples from the United States Geological Survey spectral library (Kokaly *et al.*, 2017) for samples of different impervious surface materials, along with the range of the reflectance curves, are shown in Figure 2, overlaid with the *WorldView-2* band centers. To demonstrate this in a mapping sense, an unsupervised *k*-means classification (*k* = 5) on a pair of image sets from the data used in this study is shown in Figure 3, along with the distribution of class labels which intersect the

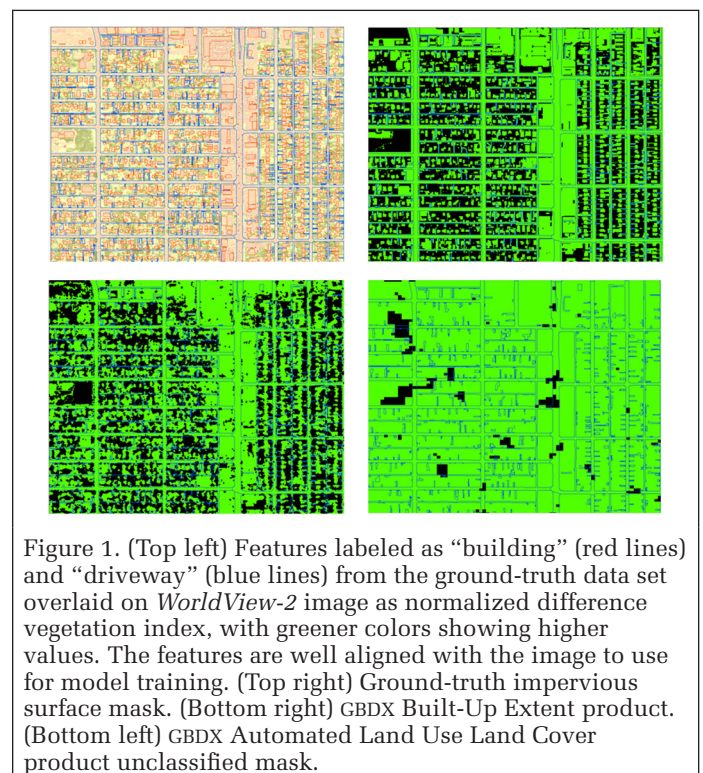


Figure 1. (Top left) Features labeled as "building" (red lines) and "driveway" (blue lines) from the ground-truth data set overlaid on *WorldView-2* image as normalized difference vegetation index, with greener colors showing higher values. The features are well aligned with the image to use for model training. (Top right) Ground-truth impervious surface mask. (Bottom right) GBDX Built-Up Extent product. (Bottom left) GBDX Automated Land Use Land Cover product unclassified mask.

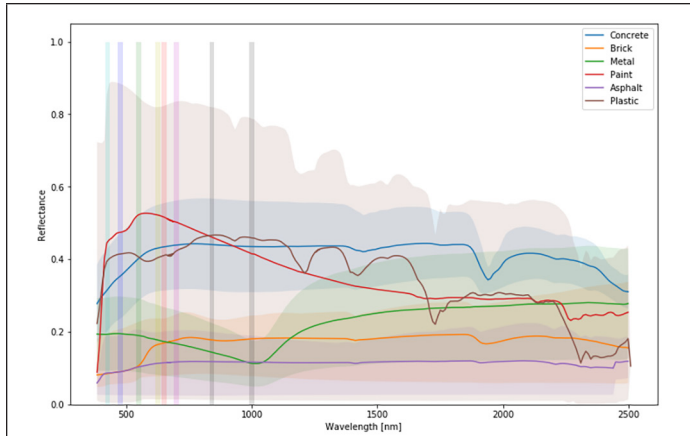


Figure 2. Plot of material spectra from United States Geological Survey spectral library. Solid lines are the average reflectance from the family of spectral curves for the material type. Shaded areas represent variability within the material spectra. Vertical bars identify wavelength positions of *WorldView-2* spectral bands.

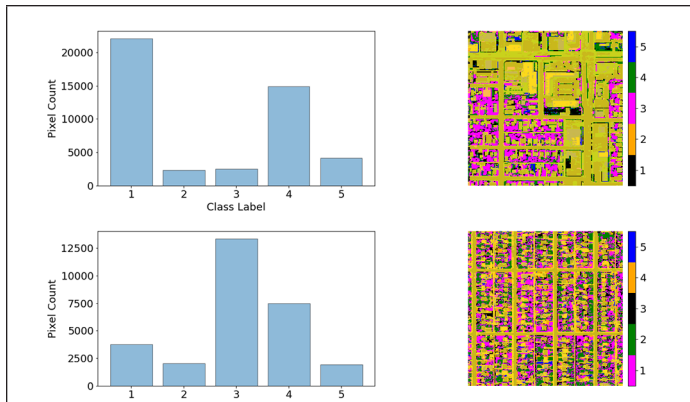


Figure 3. Example of unsupervised  $k$ -means ( $k = 5$ ) classification in mixed urban and residential areas. The ground-truth mask is overlaid in yellow. Note that every class label is present in the ground-truth mask, with the road class being the most prevalent (class 1 in top scene, class 3 in bottom scene).

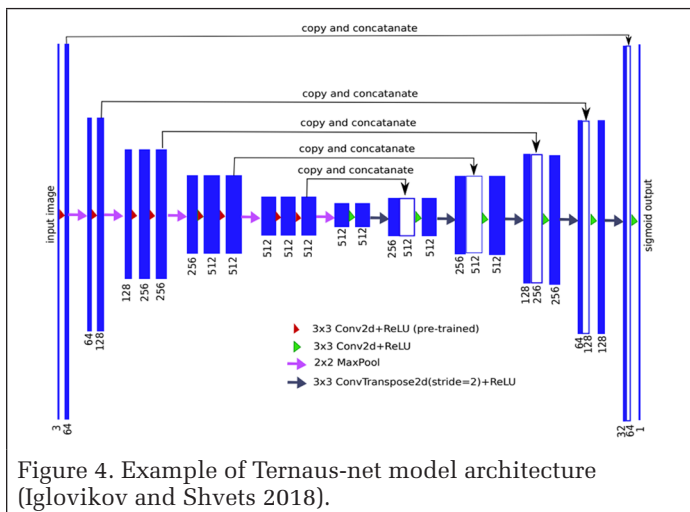


Figure 4. Example of Teraus-net model architecture (Igloukov and Shvets 2018).

ground-truth data from the same area. It is clear that all class labels are present in the ground-truth mask, and an aggregation of pixels to represent the impervious cover would require much care to include the correct pixels and classes.

Data products accessed from Maxar’s GBDX platform were considered reference data sets for the segmentation of impervious surfaces. Two automated GBDX processing tasks available at the time of this work were selected for their utility in mapping impervious surfaces from *WorldView-2* scenes: Built-Up Extent (BUE) and Automated Land Use Land Cover (LULC). Both tasks required an atmospherically corrected *WorldView-2* scene. The BUE task uses eight-band imagery to identify human built-up areas. This process creates a binary image, where intensity 255 shows that a pixel is likely part of a built-up area and intensity 0 shows that a pixel is likely not part of a built-up area (DigitalGlobe 2016b). The Automated LULC task performs unsupervised land use/land cover classification on the GBDX platform. There are six classes: vegetation, water, bare soil, clouds, shadows, and unclassified. The unclassified class can be used as a rough approximation of built-up (DigitalGlobe 2016a).

The pixels containing the “unclassified” value from the Automated LULC task, as well as the pixels containing the value 255 from the BUE task, are assigned as impervious surface pixels and used for comparison as a baseline to the UNet segmentation results. The area in Figure 1 shows a variety of features which are considered as impervious surface; there are many different roof types, sidewalks, and roads present. The BUE product (bottom right) vastly overestimates the coverage of these surfaces, whereas the Automated LULC result (bottom left), while more closely delineating some of the salient features, still shows pixel classification noise and tends to over- or underestimate in different areas, thus decreasing the accuracy of impervious surface segmentation when compared to the ground-truth mask (top right).

### Model Description

The UNet model used in this work follows Teraus-net (Igloukov and Shvets 2018; Shvets *et al.* 2018) due to its previous success in segmenting buildings in natural-color base map imagery. A UNet architecture with ResNet-152 encoder, made available by the TorchSat library (<https://github.com/sshuair/torchsat>), was specified for all band combinations. The model architecture was adapted from the Teraus-net architecture, which is constructed as shown in Figure 4. The loss function for per-pixel segmentation was selected as the binary cross entropy loss  $H$ , calculated by the negative log-likelihood of the target  $y_i$  and output for each sample  $n$  per batch, defined as

$$H = -\frac{1}{n} \sum_{i=1}^n \left( y_i \log \hat{y}_i + (1 - y_i) \log (1 - \hat{y}_i) \right). \quad (1)$$

The loss  $H$  is updated with the Jaccard index, which is defined as the intersection-over-union between two sets, to optimize the two-class image segmentation. In this case, the two sets consist of the target and model output. It is represented for two sets  $A$  and  $B$  as

$$J(A, B) = \frac{|A \cap B|}{|A \cup B|} = \frac{|A \cap B|}{|A| + |B| - |A \cap B|}. \quad (2)$$

For a set of target  $y_i$  and output  $\hat{y}_i$  image pixels, Equation 2 can be written as

$$J = \frac{1}{n} \sum_{i=1}^n \left( \frac{y_i \hat{y}_i}{y_i + \hat{y}_i - y_i \hat{y}_i} \right). \quad (3)$$

As in the work of Iglovikov and Shvets (2018), these two metrics are combined to produce a generalized loss function  $L$ :

$$L = H - \log(J). \quad (4)$$

### Training, Validation, and Test Data

Our previous work has shown satisfactory segmentation using a 64×64-pixel window, but the spatial distribution of the training, validation, and test points were dense and overlapping (McGlinchy *et al.* 2019). In the present work, we specify spatial blocking of the training data to allow for extrapolation of the model for application outside of the training set.

The geographic boundary of the ground-truth polygons was used to constrain the generation of 1000 randomly distributed point locations. These points were divided into training, validation, and test sets using a  $k$ -means blocking approach, resulting in 500 points for training, 269 points for validation, and 231 points for testing, as shown in Figure 5. The point locations were used as center coordinates to extract 256×256-pixel windows from the eight-band *WorldView-2* surface reflectance image and from the ground-truth raster. The *WorldView-2* surface reflectance data were used as is, i.e., no image normalization was applied to the data, since we assume that the surface reflectance product is self-normalized. Random rotations were applied to each image/target pair during training. Separate UNet models with ResNet-152 encoder were trained with the following band combinations:

- Blue-Green-Red
- Blue-Green-Red-NIR1
- All eight *WorldView-2* bands

The Blue-Green-Red model was also trained separately by loading the pretrained ImageNet weights to evaluate the utility of the features learned from the ImageNet data set in the segmentation task with the limited training data.

### Training Parameters

The model was trained on an Amazon Web Services (AWS) p3.8xlarge instance with four GPUs configured with the AWS Deep Learning Amazon Machine Image. The PyTorch 3.6 environment was used and configured with spatial libraries (e.g., rasterio, gdal, and fiona) as well as the gbdxtools Python package (<https://gbdxtools.readthedocs.io/en/latest/>) to support loading and extracting of image data with more than three bands using geospatial coordinates. The model training was distributed across four GPUs on the AWS instance. The number of training epochs was chosen arbitrarily as 500, and a batch size of 32 was specified. The model used the Adam optimizer with a learning rate of 0.001, and the loss function  $L$  as defined in Equation 4.

The training loss was recorded for each training iteration and summed as a running loss for each epoch. Also, average precision (AP) and F1 scores were calculated using scikit-learn (Pedregosa *et al.* 2011) for every training iteration and averaged for each epoch, and receiver operating characteristic curves—which compute the false alarm rate and the true positive rate of the prediction—were used to compute the area under the curve (AUC) for each training iteration and averaged over each epoch. Higher segmentation accuracy is represented by AUC closer to 1.0 for a single curve.

### Results and Discussion

Plots showing the running loss, mean F1 score, mean AP (mAP), and mean AUC across

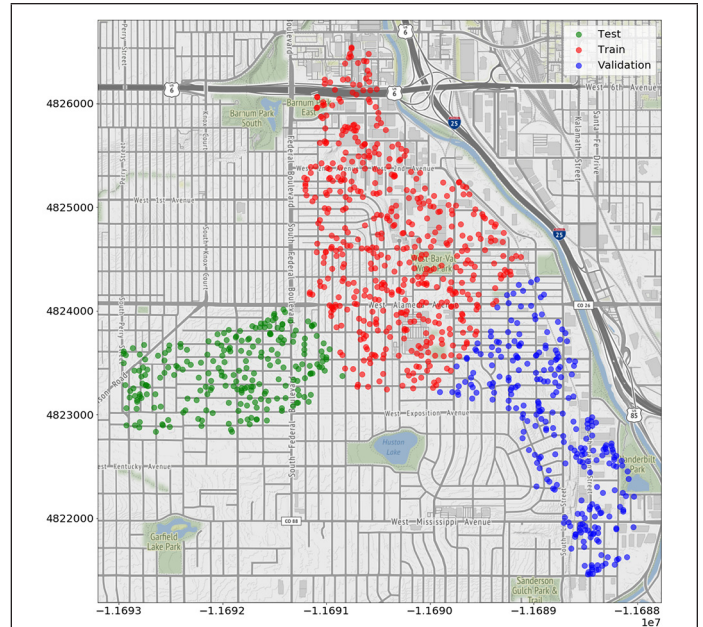


Figure 5. Distribution of training, validation, and test point locations. Windows of 256×256 pixels were extracted from each point location. Denver metro area focused on base map.

the 500 training epochs are shown in Figure 6 and summarized in Table 1 for models using the four band combinations. Based on this information alone, there is no clear separation between models trained with subsets of *WorldView-2* bands and all bands; all model and input combinations converge to a similar value.

Table 1. F1, mean average precision (mAP), area under the receiver operating characteristic curve (AUC), and running loss after 500 training epochs for models considering all band combinations.

Bands	F1	mAP	AUC	Loss
B-G-R	0.932	0.933	0.972	6.171
B-G-Ra	0.950	0.952	0.983	4.565
B-G-R-N1	0.933	0.931	0.963	6.116
All eight	0.888	0.871	0.945	9.762

<sup>a</sup> Three-band model pretrained with ImageNet.

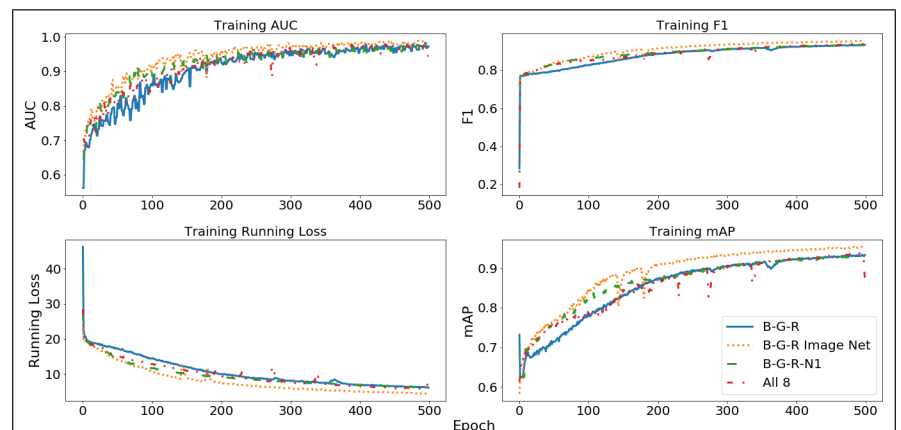


Figure 6. (Clockwise from top left) Mean area under the receiver operating characteristic curve, F1, average precision, and running loss across 500 training epochs.

Table 2. Minimum, mean, and maximum F1, average precision (AP), and area under the receiver operating characteristic curve (AUC) scores across the test data set considering all band combinations and considering only the Automated Land Use Land Cover (LULC) and Built-Up Extent (BUE) products. \*indicates the 3-band model pretrained with Image Net, and bottom two rows showing scores across test dataset considering only automated LULC and BUE products. Rightmost column has the average of all accuracy metrics. The UNet model with B-G-R-N1 input bands has the highest average score, and is in bold.

Bands	Test F1			Test AP			Test AUC			Total Average <sup>a</sup>
	Minimum	Mean	Maximum	Minimum	Mean	Maximum	Minimum	Mean	Maximum	
<b>B-G-R</b>	0.497	0.666	0.917	0.559	0.715	0.887	0.646	0.723	0.825	0.701
<b>B-G-R<sup>b</sup></b>	0.593	0.714	0.886	0.646	0.746	0.901	0.706	0.768	0.835	0.743
<b>B-G-R-N1</b>	0.556	0.709	0.906	0.736	0.82	0.915	0.736	0.807	0.855	<b>0.779</b>
<b>All eight</b>	0.483	0.629	0.788	0.767	0.845	0.933	0.734	0.795	0.856	0.756
<b>LULC</b>	0.733	0.793	0.878	0.684	0.767	0.864	0.733	0.765	0.820	0.775
<b>BUE</b>	0.644	0.719	0.846	0.481	0.574	0.744	0.530	0.560	0.630	0.647

Boldface indicates the highest average score (for B-G-R-N1).

<sup>a</sup> Average of all accuracy metrics.

<sup>b</sup> Three-band model pretrained with ImageNet.

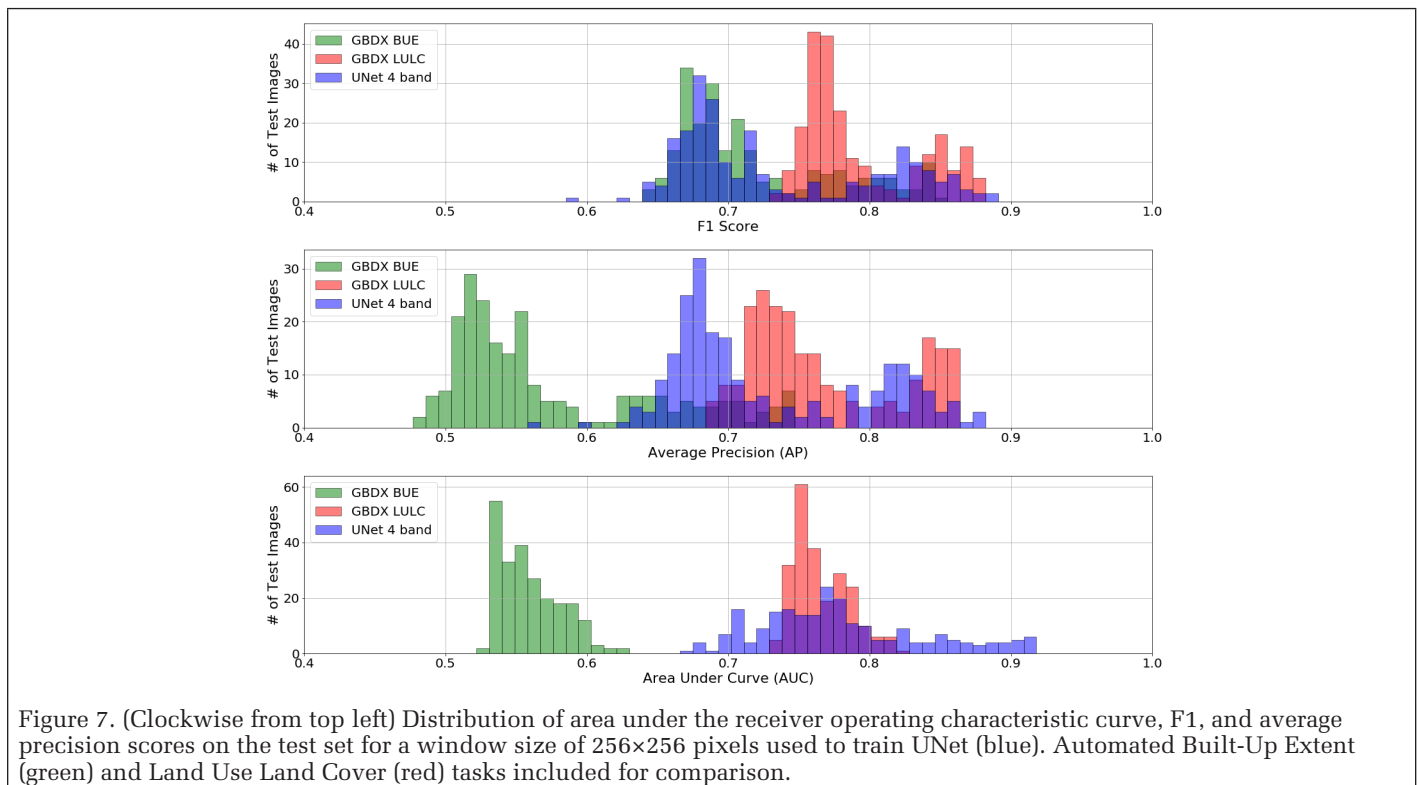


Figure 7. (Clockwise from top left) Distribution of area under the receiver operating characteristic curve, F1, and average precision scores on the test set for a window size of 256×256 pixels used to train UNet (blue). Automated Built-Up Extent (green) and Land Use Land Cover (red) tasks included for comparison.

The mean and range of values for F1, AP, and AUC for the test set were recorded and give a better indication of which set of bands gives the best performance for this model architecture. The model did not see these data sets during training, and thus scores derived from the test data allow for conclusions to be drawn about the different band combinations used to train the model. These values are presented in Table 2. It is clear from this table that the four-band model is on the higher end of mean and range of F1 scores across the test set. If the average of all accuracy metrics is considered, the four-band model has the highest average among all scores. The bottom two rows of Table 2 show the accuracy metrics for the test set when considering only the Automated LULC and BUE products compared to the ground-truth masks. The higher mean F1 score can be misleading, as the AP and AUC scores are categorically lower for these products than for the four-band UNet model. Interestingly, the three-band model using the pretrained ImageNet weights did not perform as well on the test set as the four-band model, although it was also not significantly worse, so features learned for the ImageNet

classification task may still be useful for the image-segmentation task. This suggests that even with a limited training data set, fully training a multi-band UNet model still performs well.

Histograms showing the distribution of F1, AP, and AUC scores on the test data set are shown in Figure 7 and indicate that the UNet classifier (blue) outperforms both automated tasks (green and red). A sample result with an image chip over a residential area is shown in Figure 8, and a mixed residential/commercial area is shown in Figure 9. The F1, AP, and AUC scores for these examples are, respectively, 0.820, 0.818, and 0.918 and 0.846, 0.835, and 0.817, when considering the result from the four-band model.

The distribution of accuracy scores for the four-band model is presented Figure 7. Even with a deep ResNet-152 encoder, the UNet model does not perform well in all cases. High training accuracy suggests that the model may be overfitting to the training data, and a larger and more diverse set of training data may be needed to establish higher test-set accuracies and model generalization. Additionally, a different encoding architecture may be required for the task of

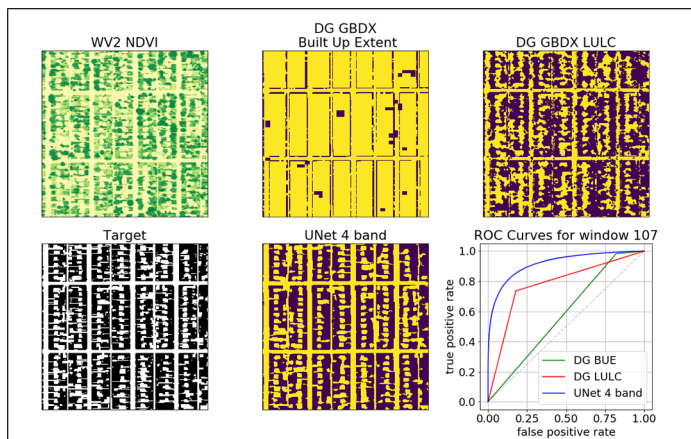


Figure 8. Sample result for image chip over a residential area from the test set after the model was trained on Blue-Green-Red-NIR1 channels. (Left to right, top to bottom) Normalized difference vegetation index representation; Built-Up Extent result; Automated Land Use Land Cover result; ground-truth labeled image; four-band UNet result; receiver operating characteristic curve for Built-Up Extent (green), Automated Land Use Land Cover (red), and UNet (blue). UNet outperforms the other two tasks in this example.

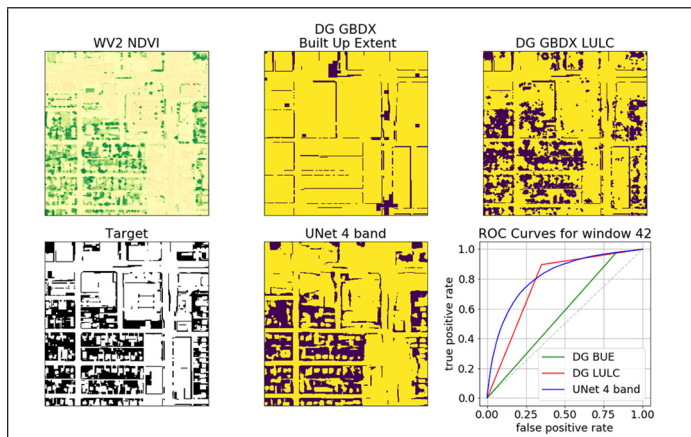


Figure 9. Sample result for image chip over a more densely urbanized area from the test set after the model was trained on Blue-Green-Red-NIR1 channels. (Left to right, top to bottom) Normalized difference vegetation index representation; Built-Up Extent result; Automated Land Use Land Cover (LULC) result; ground-truth labeled image; four-band UNet result; receiver operating characteristic curve for Built-Up Extent (green), Automated LULC (red), and UNet (blue). UNet does not significantly outperform the Automated LULC task in this example.

segmenting impervious surfaces to take advantage of all available spectral information.

The four-band UNet model performs markedly better in residential and less densely developed areas, where there is more contrast in the impervious surface class, but has trouble with the binary classification in more densely developed areas. An example of where the four-band UNet model struggles to segment the impervious surface class is shown in Figure 9, where the image chip presented to the model contains a mixture of densely developed and residential areas. This could be due to the challenging aspect of image segmentation with crisp edges in the ground-truth masks (Ma *et al.* 2019), and suggests that a different approach to encoding the image data may be necessary.

The decreased performance of the eight-band model is counterintuitive, as with more spectral information available to the model, one may expect improved classification accuracy of the pixels. The additional bands (coastal blue, yellow, red edge, and a second near-infrared channel) may not be able to provide enough information to the network to enhance the impervious surface classification at the pixel level; indeed, there is no clear separation in Figure 2 for the corresponding materials. Additionally, a model architecture designed and optimized for natural-color data, while extensible to include more channels, may not be the appropriate architecture to encode information from the additional spectral bands. However, the inclusion of a near-infrared band does increase performance for a UNet with ResNet encoder over the traditional natural-color channels, likely due to its separation between vegetated and non-vegetated areas.

## Conclusions

This work has shown successful application of the UNet FCNN architecture to the problem of impervious surface segmentation from high-resolution multispectral satellite imagery. We were able to train a UNet model with ResNet-152 encoder considering multiple band combinations on input. Similar performance across the different input combinations suggests that different encoder approaches may need to be considered, more and diverse training samples added, or both.

Segmentation of impervious surfaces from high-resolution satellite imagery is a complex task, as the materials comprising this surface classification are many, e.g., asphalt, metal, concrete, brick, and stone. The spectral signatures of these surfaces are similar, and traditional image-classification algorithms struggle to differentiate between them. The FCNN approach to classifying impervious surfaces inherently incorporates neighboring information when classifying each pixel. Additionally, the best-performing FCNN model used in this work operates on more spectral information than the traditional RGB data sets used in computer vision; we are able to incorporate an infrared channel. The FCNN has been trained to operate on surface reflectance data, a common data product in the remote-sensing community which does not need additional normalization of the input data. The efforts of this project have been made openly available, including code ([https://github.com/joemcglinchy/IS\\_UNet\\_Resnet152](https://github.com/joemcglinchy/IS_UNet_Resnet152)) and model weights (<https://rb.gy/n4rkjy>) for the four-band input as well as three- and eight-band inputs.

Ideally, FCNN models such as the UNet used in this work could be applied to other imaging platforms and geographic locations in an effort to reduce the need to train new models for a specific scenario and data set. There is much room for future work in this application area, and such work will consider different approaches to the encoding problem, additional training data, the integration of image-acquisition metadata such as solar and viewing geometry, ensemble models which incorporate specific band sets in order to take advantage of the full spectral depth of data acquired from systems like *WorldView-2* and *WorldView-3* where there are more than three or four spectral bands, and portability to surface reflectance products generated from different imaging platforms, such as Planet and Sentinel-2.

## Acknowledgments

This work was supported by Earth Lab through the University of Colorado Boulder's Grand Challenge Initiative, in partnership with Maxar for imagery access.

## References

- DigitalGlobe. 2016a. Automated Land Cover Classification. <<http://web.archive.org/web/20170311233956/https://gbdxdocs.digitalglobe.com/docs/automated-land-cover-classification>> Accessed DD June 2019.
- DigitalGlobe. 2016b. Built Up Extent. <<http://web.archive.org/web/20170311234001/https://gbdxdocs.digitalglobe.com/docs/built-up-extent>> Accessed DD June 2019.
- Iglovikov, V. and A. Shvets. 2018. TeraNet: U-Net with VGG11 encoder pre-trained on ImageNet for image segmentation. arXiv:1801.05746.
- Kokaly, R. F., R. N. Clark, G. A. Swayze, K. E. Livo, T. M. Hoefen, N. C. Pearson, R. A. Wise, W. M. Benzel, H. A. Lowers, R. L. Driscoll and A. J. Klein. 2017. *USGS Spectral Library Version 7: U.S. Geological Survey Data Series 1035*. Reston, Va.: U.S. Geological Survey.
- Li, R., W. Liu, L. Yang, S. Sun, W. Hu, F. Zhang and W. Li. 2018. DeepUNet: A deep fully convolutional network for pixel-level sea-land segmentation. *IEEE Journal of Selected Topics in Applied Earth Observations and Remote Sensing* 11 (11):3954–3962.
- Ma, L., Y. Liu, X. Zhang, Y. Ye, G. Yin and B. A. Johnson. 2019. Deep learning in remote sensing applications: A meta-analysis and review. *ISPRS Journal of Photogrammetry and Remote Sensing* 152:166–177.
- McGlinchy, J., B. Johnson, B. Muller, M. Joseph and J. Diaz. 2019. Application of UNet fully convolutional neural network to impervious surface segmentation in urban environment from high resolution satellite imagery. Pages PP–PP in *IGARSS 2019–2019 IEEE International Geoscience and Remote Sensing Symposium*, held in Yokohama, Japan, 28 July–2 August 2019. Edited by J. Editor. City, St.: IEEE.
- Pedregosa, F., G. Varoquaux, A. Gramfort, V. Michel, B. Thirion, O. Grisel, M. Blondel, P. Prettenhofer, R. Weiss, V. Dubourg, J. Vanderplas, A. Passos, D. Cournapeau, M. Brucher, M. Perrot and É. Duchesnay. 2011. Scikit-learn: Machine learning in Python. *Journal of Machine Learning Research* 12:2825–2830.
- Ronneberger, O., P. Fischer and T. Brox. 2015. U-Net: Convolutional networks for biomedical image segmentation. Pages 234–241 in *Medical Image Computing and Computer-Assisted Intervention—MICCAI 2015*. Edited by N. Navab, J. Hornegger, W. Wells and A. Frangi. 18th International Conference, held in Munich, Germany, 5–9 October 2015. Lecture Notes in Computer Science vol. 9351. Cham, Switzerland: Springer.
- Shao, Z., H. Fu, D. Li, O. Altan and T. Cheng. 2019. Remote sensing monitoring of multi-scale watersheds impermeability for urban hydrological evaluation. *Remote Sensing of Environment* 232:111338.
- Shvets, A., A. Rakhlin, A. A. Kalinin and V. I. Iglovikov. 2018. Automatic instrument segmentation in robot-assisted surgery using deep learning. arXiv:1803.01207.
- Wang, Y., and M. Li. 2019. Urban impervious surface detection from remote sensing images: A review of the methods and challenges. *IEEE Geoscience and Remote Sensing Magazine* 7 (3):64–93.
- Weng, Q. 2012. Remote sensing of impervious surfaces in the urban areas: Requirements, methods, and trends. *Remote Sensing of Environment* 117:34–49.
- Wieland, M. and M. Pittore. 2014. Performance evaluation of machine learning algorithms for urban pattern recognition from multi-spectral satellite images. *Remote Sensing* 6 (4):2912–2939.
- Zhu, X. X., D. Tuia, L. Mou, G.-S. Xia, L. Zhang, F. Xu and F. Fraundorfer. 2017. Deep learning in remote sensing: A comprehensive review and list of resources. *IEEE Geoscience and Remote Sensing Magazine* 5 (4):8–36.

# SUSTAININGMEMBERS

## **Aerial Services, Inc.**

Cedar Falls, Iowa  
www.AerialServicesInc.com  
Member Since: 5/2001

## **Ayres Associates**

Madison, Wisconsin  
www.AyresAssociates.com  
Member Since: 1/1953

## **Cardinal Systems, LLC**

Flagler Beach, Florida  
www.cardinalsystems.net  
Member Since: 1/2001

## **Dewberry**

Fairfax, Virginia  
www.dewberry.com  
Member Since: 1/1985

## **Esri**

Redlands, California  
www.esri.com  
Member Since: 1/1987

## **F.R. Aleman & Associates, Inc.**

Miami, Florida  
https://fr-aleman.com  
Member Since: 7/2020

## **Geographic Imperatives LLC**

Centennial, Colorado  
http://geographicimperativesllc.com  
Member Since: 9/2021

## **GeoWing Mapping, Inc.**

Richmond, California  
www.geowingmapping.com  
Member Since: 12/2016

## **GPI Geospatial Inc.**

formerly **Aerial Cartographics of America, Inc. (ACA)**  
Orlando, Florida  
www.aca-net.com  
Member Since: 10/1994

## **Green Grid Inc.**

San Ramon, California  
www.greengridinc.com  
Member Since: 1/2020

## **Half Associates, Inc.**

Richardson, Texas  
www.half.com  
Member Since: 8/2021

## **Keystone Aerial Surveys, Inc.**

Philadelphia, Pennsylvania  
www.kasurveys.com  
Member Since: 1/1985

## **Kucera International**

Willoughby, Ohio  
www.kucerainternational.com  
Member Since: 1/1992

## **L3Harris Corporation**

Broomfield, Colorado  
www.harris.com  
Member Since: 6/2008

## **Pickett and Associates, Inc.**

Bartow, Florida  
www.pickettusa.com  
Member Since: 4/2007

## **Quantum Spatial, Inc.**

Sheboygan Falls, Wisconsin  
www.quantumspatial.com  
Member Since: 1/1974

## **Sanborn Map Company**

Colorado Springs, Colorado  
www.sanborn.com  
Member Since: 10/1984

## **Surveying And Mapping, LLC (SAM)**

Austin, Texas  
www.sam.biz  
Member Since: 12/2005

## **T3 Global Strategies, Inc.**

Bridgeville, Pennsylvania  
https://t3gs.com/  
Member Since: 6/2020

## **Teledyne Optech**

Vaughan, Ontario, Canada  
TeledyneOptech.com  
Member Since: 12/2020

## **Terra Remote Sensing (USA) Inc.**

Bellevue, Washington  
www.terraremotecom  
Member Since: 11/2016

## **Towill, Inc.**

San Francisco, California  
www.towill.com  
Member Since: 1/1952

## **Wingtra**

Zurich, Switzerland  
https://wingtra.com/  
Member Since: 6/2020

## **Woolpert LLP**

Dayton, Ohio  
www.woolpert.com  
Member Since: 1/1985

# SUSTAININGMEMBERBENEFITS

## **Membership**

- ✓ Provides a means for dissemination of new information
- ✓ Encourages an exchange of ideas and communication
- ✓ Offers prime exposure for companies

## **Benefits of an ASPRS Membership**

- Complimentary and discounted Employee Membership\*
- E-mail blast to full ASPRS membership per year\*
- Professional Certification Application fee discount for any employee
- Discounts on *PE&RS* Classified Ad
- Member price for ASPRS publications
- Discount on group registration to ASPRS virtual conferences
- Sustaining Member company listing in ASPRS directory/website
- Hot link to company website from Sustaining Member company listing page on ASPRS website
- Press Release Priority Listing in *PE&RS* Industry News
- Priority publishing of Highlight Articles in *PE&RS* plus, 20% discount off cover fee, one per year
- Discount on *PE&RS* full-page advertisement
- Exhibit discounts at ASPRS sponsored conferences (exception ASPRS/ILMF)
- Free training webinar registrations per year\*
- Discount on additional training webinar registrations for employees
- Discount for each new SMC member brought on board (Discount for first year only)

\*quantity depends on membership level

# An Improved GPU-Based Parallel Computing Method for Landscape Index Calculation in Urban Area

Mengjun Kang, Yunlong Ma, Qingyun Du, and Min Weng

## Abstract

*With the development of urbanization in the world, dealing with the problems caused by urban expansion is becoming more and more important. The data that need to be processed in urbanization studies have increased with the improvement of the spatial and temporal resolution of remote sensing satellites, exerting considerable pressure on traditional software used for landscape index computation. In this article, an improved landscape index-computing algorithm is proposed. Based on CUDA, a pixel-group parallelization strategy is adopted to optimize the algorithm. The results show that the proposed algorithm increases the efficiency by more than a factor of three as the amount of data to be processed increases to 50 million pixels, thus providing a new way to calculate large-scale landscape index values on personal computers to study urbanization.*

## Introduction

In recent years, urban expansion has brought about great advancement in the development of all countries in the world. At the same time, the clustering of large urban populations has brought new problems to urban development, such as natural hazards, declining natural vegetation cover, loss of arable land, urban heat islands, and air pollution (Shao *et al.* 2020; Y. Zhang and Shao 2020). Therefore, urban expansion has become an important issue in urban development (H. Zhang *et al.* 2019; Shao *et al.* 2020). In many scholars' research on urban expansion, raster data and landscape indexes are widely used (C.-X. Li *et al.* 2010; X. Liu *et al.* 2010; Huyan *et al.* 2017). Ouyang and Zhu (2020) analyzed the spatial expansion mode of urban land and the dispersion, dominance, scale, and fragmentation of urban land based on the landscape expansion index and partial landscape pattern index. J. Liu *et al.* (2018) put forward the Multi-Order Adjacent Index, which was used to analyze the overall expansion degree and spatial-change process of Wuhan city from a macro perspective.

With the improvement of the quantity and quality of the analysis of urban expansion and the rapid growth of geospatial data, landscape indexes are developing in a high-dimensional and dynamic direction. Because increasing amounts of data must be processed, more powerful and efficient computing mechanisms are needed for landscape analysis. However, faced with large-scale raster data, traditional landscape index-computing software applications (such as FRAGSTATS, a desktop software that calculates a variety of landscape indexes)

that run on personal computers have difficulty completing the analysis effectively due to the data volume and computing efficiency limitations caused by insufficient computer memory and algorithms that execute serially (Y. Liu and Guan 2017). Therefore, the main goal of this study was to design a connected-component labeling (CCL) algorithm for multi-valued images oriented toward landscape index computing.

Generally, basic parameters such as the number of patches, patch area, and perimeter must be obtained before the landscape index can be calculated; calculating these parameters requires the CCL of images. The CCL process involves labeling connected pixels with the same value, while disconnected pixels are labeled with different values. This labeling process is both the most important and the most time-consuming aspect of landscape index computing. Therefore, optimizing landscape index computing ability and efficiency can be accomplished primarily by optimizing the efficiency of the CCL algorithm.

CCL algorithm development can be roughly divided into two stages:

The first stage is the improvement of the algorithm structure. The earliest CCL algorithm needed to traverse an image many times, which led to high time complexity; therefore, early CCL algorithm optimizations focused on the high time complexity of the algorithm itself. A common way to reduce the time complexity is to reduce the number of times the algorithm must traverse an image; this aspect was addressed by various algorithms (He, Chao, and Suzuki 2008; Kalentev *et al.* 2011; Gao, Wang, and Hu 2014). The classical “two-pass” algorithm (Gotoh *et al.* 1990; Wu, Otoo, and Suzuki 2009; Zhao *et al.* 2015) requires only two traversals. The two-pass technique was an improvement over the original algorithm; nevertheless, serial algorithms are inefficient at processing large-scale data. In contrast to the two-pass algorithm, the run-based labeling algorithm is based on a different processing concept that is similar to the run-length encoding process of raster data. In this scheme, run lengths (rather than individual pixels) serve as the basic unit to be labeled. Consequently—particularly for images with large numbers of continuous pixels—the number of units to be marked is greatly reduced, and the traversal time is shorter (He *et al.* 2008).

The second stage of optimization involves applying parallel algorithm design. The processing results of the optimized algorithms developed in the first stage show that although run-based coding improves the processing efficiency compared with the original CCL algorithm, the essence of the traditional serial algorithm remains unchanged, and the level of improvement is not ideal. Therefore, in recent years, efforts

Mengjun Kang, Yunlong Ma, Qingyun Du, and Min Weng are with the School of Resource and Environmental Sciences, Wuhan University, Wuhan, China.

Mengjun Kang is also with the Key Laboratory of Urban Land Resources Monitoring and Simulation, Ministry of Natural Resources, Shenzhen 518034, China.

Corresponding author: Min Weng (wengmin@whu.edu.cn).

Photogrammetric Engineering & Remote Sensing  
Vol. 87, No. 2, February 2021, pp. 125–132.  
0099-1112/21/125–132

© 2021 American Society for Photogrammetry  
and Remote Sensing

doi: 10.14358/PERS.87.2.125

to optimize the CCL algorithm have shifted toward parallel designs. C.-X. Li *et al.* (2010) designed an algorithm suitable for fast labeling of connected components in binary images achieved through a field-programmable gate array (see also Y. Li 2015). Although this algorithm is highly efficient, its universality is poor due to its dependence on circuit hardware.

Since then, computer hardware developments have elevated general-purpose computing on a graphics processing unit (GPU) into a common approach for solving general large-scale data problems due to GPUs' many-core characteristics. GPU-based computing has also been used to solve numerous problems in the image-processing field (Harish and Narayanan 2007; Cheng 2013; Zhu *et al.* 2014). Considering the simplicity and repeatability of the CCL task for a single pixel, which matches the characteristics of a multi-core GPU, and to reduce the run time and cost as much as possible, researchers who study CCL algorithm optimization have increasingly turned to general-purpose computing using GPUs. These studies can be divided into two main categories: single-pixel-based and multiple-pixel-based parallel strategies.

Kalentev *et al.* (2011) adopted a pixel-based parallel strategy that allocated one thread for each pixel. In the algorithm, for each pixel only the pixels in its neighborhood were scanned, and the label was corrected by judging the relationship between the current pixel label and the minimum label value of the connected neighborhood pixels, until the label no longer needed to be modified. Qin and Fang (2010) also adopted a pixel-based parallel strategy to update vertex identification and patch position through iteration; they determined a connected component by the connected-component vertex. The iteration continued until the vertex position no longer changed. While a pixel-based parallel strategy maximizes the utilization of the GPU's parallel capability, it is still unable to effectively address large-scale data, due to the limited number of available threads.

The other parallel strategy is based on groups of pixels. Under this parallel strategy, nearby closely linked pixels are grouped together as the minimum labeling unit. Researchers have designed several algorithms based on this idea (Yonehara and Aizawa 2015). Mu and Yang (2013) divided an image into blocks, adopted a 2×2-pixel unit as the minimum connector and then merged the edges between blocks. Lu, Ding, and Sun

(2008) split images into rows and organized the smallest labeling unit by run length. The latter scheme not only achieved higher processing efficiency but also provided a new parallel computing strategy for CCL. However, adopting a matrix of relations to store the equivalent run lengths wastes memory and is unsuitable for large-scale multi-valued image computing.

In general, the efficiency improvements of the various labeling algorithms based on CPU single-thread sequential processing are quite limited, because the problems are still addressed by traditional serial algorithms. At present, studies of parallel CCL algorithms are almost all aimed at binary images. Moreover, device thread and memory limitations make it difficult to apply these algorithms to large-scale multi-valued image-labeling tasks. Designing a suitable parallel version of an algorithm and optimizing the GPU acceleration techniques enables rapid labeling of large-scale multi-valued images even in a stand-alone environment more efficiently, making it easier to process data when studying urbanization.

This article is organized into five sections. The first section introduces the research background and purpose of the article. The second section presents the experimental design, including the experimental data and environment. The third section introduces the algorithm design, mainly including serial labeling algorithm design and algorithm parallelization. The fourth section reports the experimental results and offers some discussion, mainly of the correctness of the algorithm and the time-consumption analysis of the serial and parallel algorithms. (The two-pass algorithm is used for comparison because it is generally considered to be efficient in serial algorithm.) The last section summarizes the whole article, lists the advantages and disadvantages of the proposed algorithm, and proposes future research directions.

## Experimental Data and Environment

### Study Area

The adopted experimental data are based on the classified data of a certain land use; the data format consists of raster data in TIFF format. The experimental data were sourced from the second land investigation performed in Hubei Province in 2009. Hubei Province, located in central China,

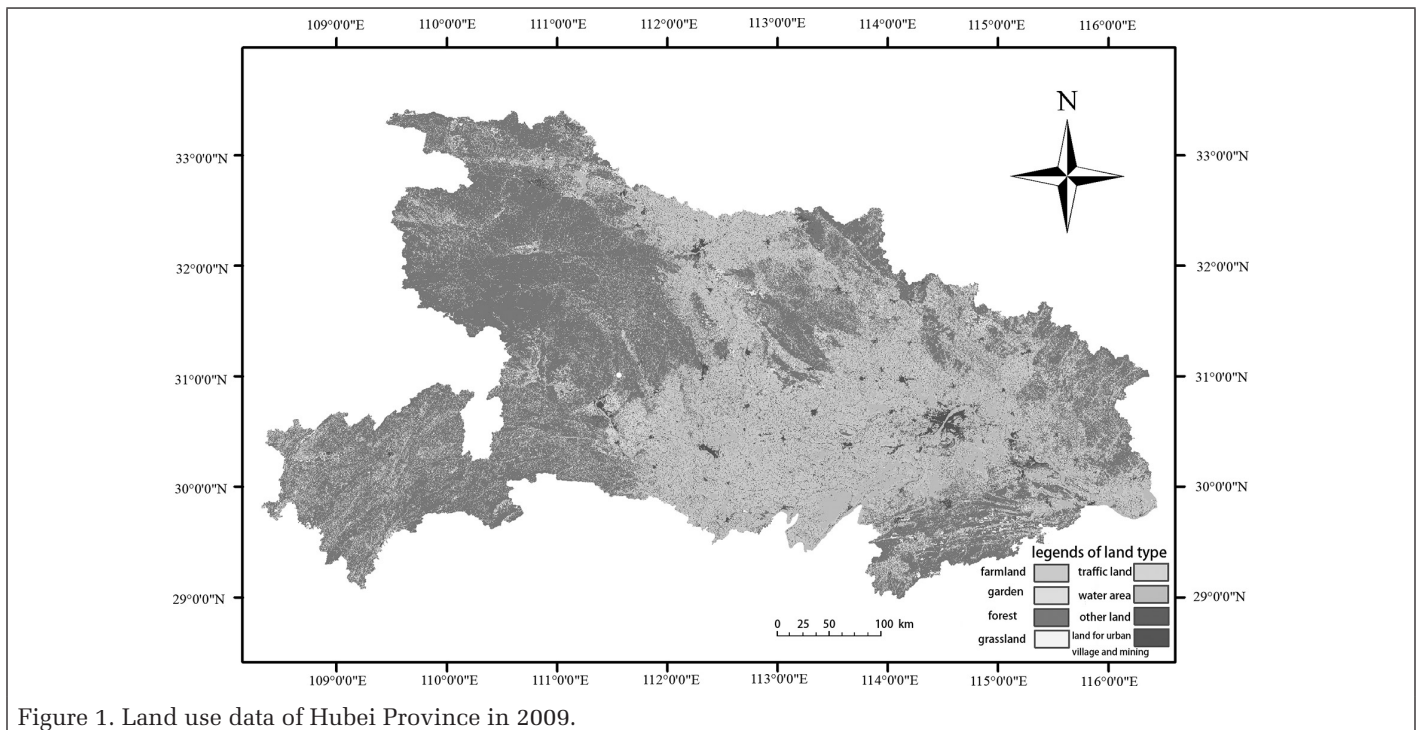


Figure 1. Land use data of Hubei Province in 2009.

is famous for its numerous lakes. Therefore, its land patches are fragmentary, and the data consist of complex, multi-valued images (as shown in Figure 1) that meet the research requirements of this study. The data and code that support the findings of this study are available through Figshare (at doi:10.6084/m9.figshare.10007489 and doi:10.6084/m9.figshare.10007477). However, because data4 and data5 have higher resolutions, they cannot be made publicly available, due to data-privacy concerns.

The experimental data are transformed from the vector format into raster images with five different resolutions. The pixel values are the land use types from Hubei Province (36 categories in total). The data used in the experiment are described in Table 1.

Table 1. Experimental data description (land use classification raster image, including 36 land types).

Data	Resolution	File Size (MB)
Image 1	467×255	0.14
Image 2	936×511	0.54
Image 3	2012×1023	2.08
Image 4	5628×3071	17.1
Image 5	9381×5119	48.7

The experiments were carried out on a stand-alone computer equipped with an Intel Core i5-8500 processor running at 3.00 GHz and an NVIDIA GeForce GT 1030 with 2 GB of memory. The code was written using the CUDA C programming language. The maximum number of threads supported by a block is 1024, and a thread warp contains 32 threads (that is, 32 threads make up a thread warp and execute together). The operating system was Windows 10, and the parallel algorithm was based on CUDA version 10.0. The details of the experimental environment are listed in Table 2.

Table 2. Experimental hardware and software environment.

CPU	GPU	Environment
Intel Core i5-8500	NVIDIA GeForce GT 1030	Windows 10 Pro
3.00 GHz	GDDR5	Visual Studio 2013
16 GB	2 GB	CUDA 10.0
6 cores	Warp size 32	GDAL 2.4.0

## Methods

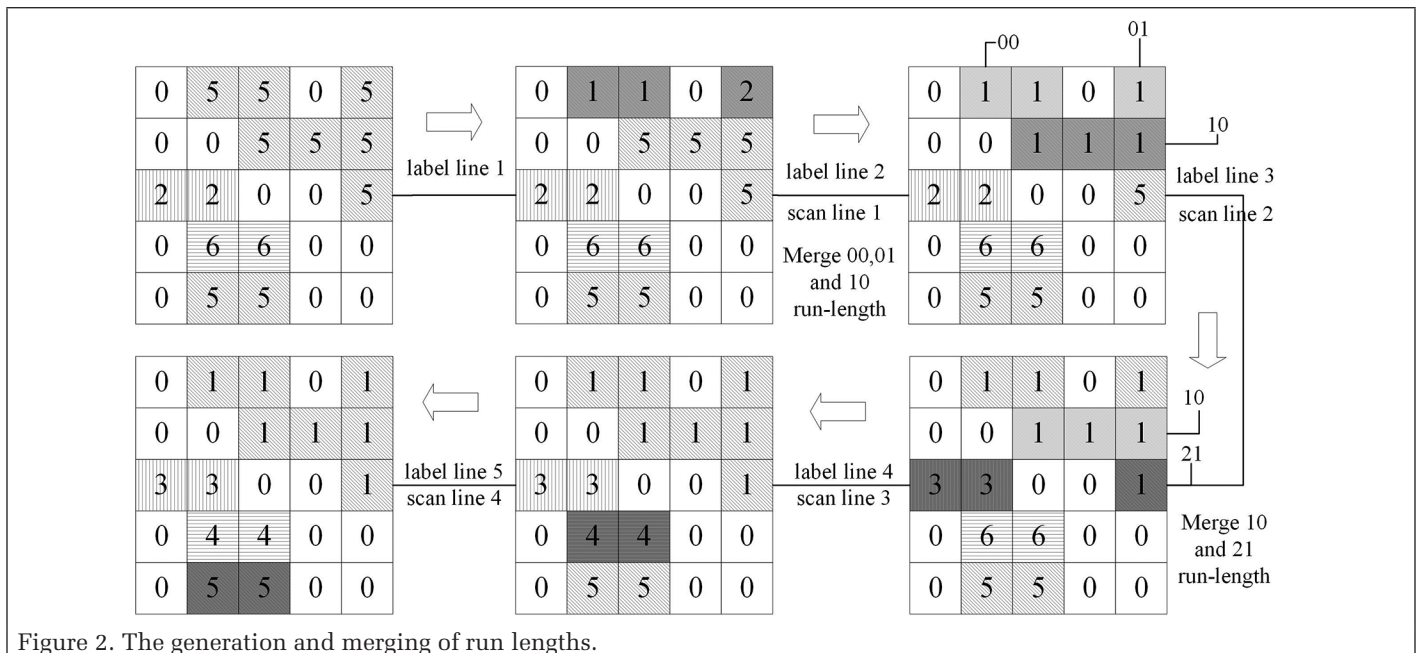
To improve the traditional CCL algorithm for binary images, a serial CCL algorithm for computing the landscape index based on run length was designed and implemented. The parallel strategy and the selection of parallel technology are discussed in the following subsections. Finally, the GPU-based parallel algorithm was implemented based on CUDA.

### Serial Labeling Algorithm for Computing the Landscape Index

In Figure 2, it is assumed that 0 values represent nonurban area and nonzero values represent subtypes of urban area; the connected subtypes of urban area need to be labeled with the same value. The run-length algorithm uses run lengths as the smallest processing units rather than pixels; therefore, an initial scan is needed to convert the processing unit from pixels to run lengths. Considering the order in which a serial algorithm scans the image, after the current row has been scanned the previous row has completed the conversion of the processing unit from pixels to run lengths. Therefore, the previous row can be retrieved when the subsequent line is scanned to process the equivalence families, as shown in Figure 2.

The entire algorithm can be roughly divided into the following parts:

1. Read pixel data into memory and store them in a two-dimensional array.
2. Scan all the image pixels line by line; pixels whose adjacent-pixel values are the same are recorded as a run length. The starting and ending positions, pixel values, and number of pixel points in the run length are recorded and stored in memory. Each target run length needs to determine only its own connectivity based on the consecutive points judged to be connected, and each run-length scan operation needs to scan only the previous row's run lengths.
3. Calculate the perimeter of the connected domain using point connectivity. If the data were counted when the traversal is finally merged into the connected domain, the image pixel points would need to be traversed again, which would affect algorithm efficiency. Generating the run lengths also requires image traversal; consequently, the point-connectivity process can be performed in conjunction with the run-length generation.
4. Merge run lengths into patches for groups with equivalent run lengths. Specifically, the method operates as follows:



starting from the second row, all the run lengths of the previous row are removed while the traversal is scanned. If the current traversal is connected to the previous traversal, an equivalent label record and label-value correction are required.

5. Compute auxiliary information. In contrast to other connected-component marking algorithms, in order to simplify landscape computing this algorithm needs to count the number of patches and add the number of pixels contained in the run length already processed by the equivalent group to the data structure under the corresponding label to calculate the patch perimeters and areas.

### Design and Realization of the Improved Parallel Algorithm

The concurrent execution characteristics of parallel algorithms make parallel computing approaches more suitable for solving independent repetitive computing problems. In the serial CCL algorithm based on run length, the run lengths of each line need to be updated based on their overlapping relationship with the previous line. The run lengths are often closely related. However, each run-length label depends only on the previous line. For each run length, or each row, the operation is repetitive. Even if the currently executing row cannot determine whether the previous line has been processed, it can still be corrected through global variables used to monitor whether a run length needs to be corrected to determine whether to repeat the trip correction; therefore, the algorithm can be parallelized.

Based on comprehensive research and prior studies, the following three parallel strategies for CCL algorithms should be considered.

The first strategy is a parallel strategy based on pixels. Each pixel is assigned to a thread, which handles it independently. The GPU core utilization of this parallel strategy is high, and its processing efficiency is also relatively high. However, when processing large-scale image data, the number of threads required may exceed the number of threads supported by the GPU. Therefore, this parallel strategy can be used only for small-scale image-recognition fields and is unsuitable for landscape analysis of large-scale raster data.

The second strategy is based on pixel blocks—that is,  $N \times N$  ( $2 \times 2$  or  $3 \times 3$ ) pixels are taken as a pixel group, forming the minimum processing unit. Each pixel group is allocated to a thread. However, this strategy is not ideal for accelerating CCL mainly because after the end of the parallel process, more boundaries will exist that also need to be considered for merging the 2D regions. The different minimum marking units cause greater complexity during edge merging, which in turn introduces greater difficulties in merging the equivalent minimum units.

Based on these problems and the run-length labeling algorithm, a parallel strategy based on row pixels was designed. This strategy divides pixels into groups using a 1D rather than a 2D region. Thus, it reduces the complexity of run-length merging and converts the minimum processing unit from pixel units to run-length units through run-length coding, which greatly reduces the number of minimum processing units. Similar to the serial algorithm, all the run lengths of the adjacent rows on one side of each row are scanned, and label correction is conducted according to the relation between the run lengths and the label values.

The algorithm splits the input raster data into rows. Each row is allocated to one thread for processing. After data segmentation is complete, the image data are preprocessed and the label units converted from pixels to run lengths. Then, by traversing the run lengths, all the equivalent pairs are recorded. Finally, the process of equivalent-pair merging is executed iteratively until the run-length labels no longer change. At this point, the label result has been obtained. Finally, the patch numbers are acquired by relabeling, and the perimeters and areas of the patches are calculated simultaneously. A flowchart of the entire algorithm is shown in Figure 3. The whole flowchart is shown in Figure 4.

### Run-Length Generation

This algorithm uses the run length rather than the pixel as the smallest unit for labeling. Therefore, the pixels must first be converted into run lengths. In the serial algorithm, because its execution order is known, run-length generation and the process for combining equivalent run lengths can be processed sequentially.

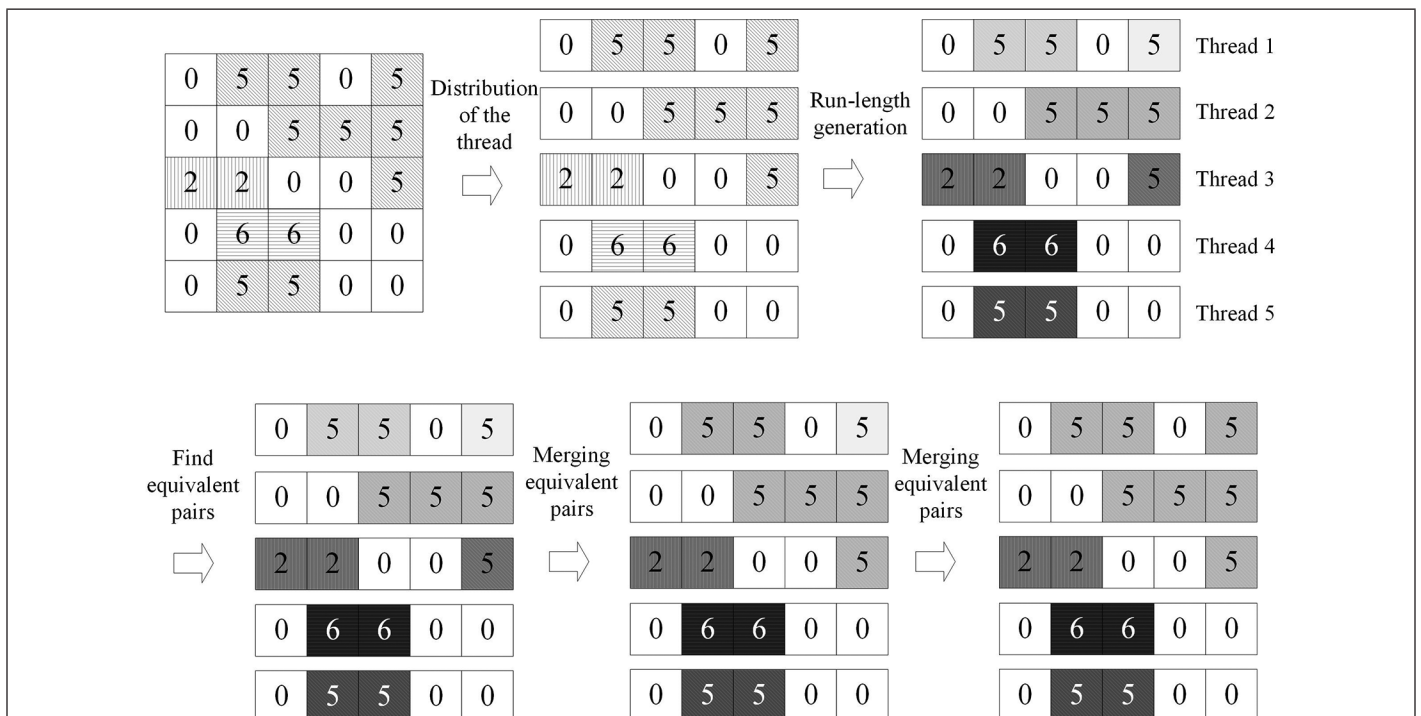


Figure 3. Schematic diagram of the parallel algorithm.

However, the concurrence of parallel computing makes it necessary to complete all the run-length generation operations before the process of combining equivalent run lengths. The rows are completely independent of one another and do not affect each other while run lengths are being generated. Each thread independently processes one line; the connected pixels are grouped into run lengths, and a unique label is assigned to the run length.

The run lengths of each row are stored in a 2D array corresponding to the row number. Finally, thread synchronization is needed to ensure that all the rows have been completed; at that point, the run-length arrays have been generated successfully.

Because the record of run-length generation and the process of determining the point connectivity are independent operations and rows do not affect one another, just as in the serial algorithm, run-length generation can be executed simultaneously via computing point connectivity in the parallel

algorithm—that is, each thread processes a line of run-length generation and calculates the point connectivity.

During this operation, the entire image needs to be traversed only once; the corresponding run-length array is generated according to the input image matrix. The labeled units are converted from pixels to run lengths, and the 2D image array is converted into a run-length array. Each run length is marked by a unique value. For line  $I$ , the label values increase in sequence from  $i \times \text{width}$  (where “width” denotes the image width and  $i$  starts from 0). Thus, the entire line of pixels from front to back is scanned to determine whether the current pixel value is equal to the previous pixel value. When it is equal, it belongs to the same run length; otherwise, it belongs to a different run length. In other words, consecutive pixels with the same value belong to one run length, and independent pixels also belong to one run length. At the end of the run-length generation process, the pixel array on the device has been converted to an array of run lengths. Considering

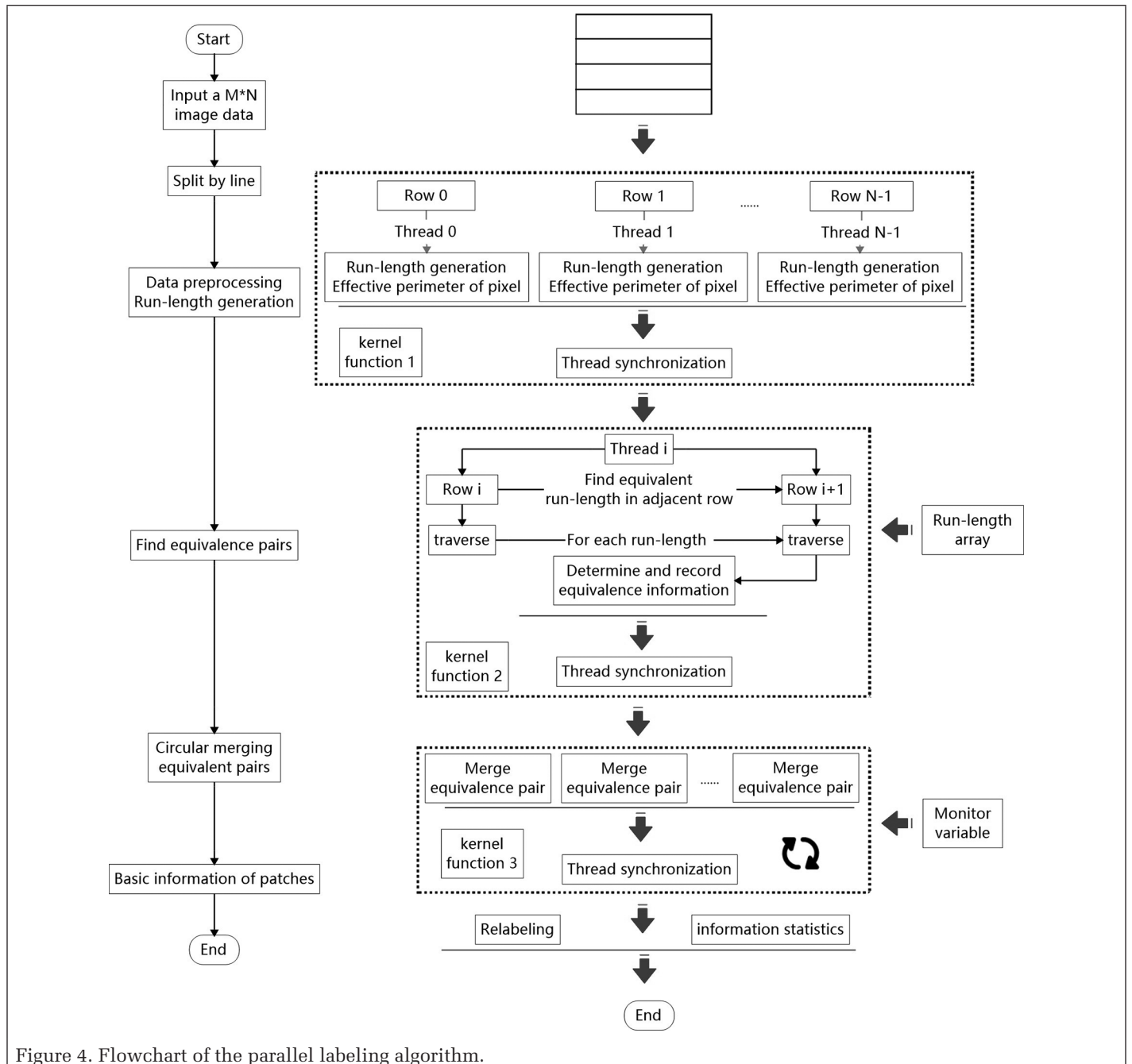


Figure 4. Flowchart of the parallel labeling algorithm.

the limited device memory, the pixel-array memory should be released as soon as possible.

#### Finding Equivalent Pairs

Finding equivalent pairs requires a single traversal of all the run lengths, which is also performed in parallel. The eigenvalue of the pixel can be used to obtain equivalent pairs. The eigenvalue of a pixel is defined here as the difference between the pixel of the point and the four points at the top, left, bottom left, and bottom right (note that all nonzero values are converted to 1):

$$\text{value} = 10^2(\text{pt} - \text{pt}_{\text{left-top}}) + 10(\text{pt} - \text{pt}_{\text{left}}) + 10(\text{pt} - \text{pt}_{\text{left-bottom}}) + (\text{pt} - \text{pt}_{\text{bottom}}). \quad (1)$$

All the pixels processed by thread  $i$  are scanned from front to back, and for each pixel, the equivalent pairs can be found by the eigenvalue of the pixel. An equivalent pair must satisfy the conditions

$$\text{value} \neq 1111 \cap \text{value} \neq 1011.$$

Considering the limitations of GPU memory and its data processing, rather than using an equivalent family to record equivalent run lengths, a pointer and eigenvalue of the pixel are adopted to record equivalent run lengths by using equivalent pairs. The merge of equivalent pairs is achieved meanwhile.

#### Merging Equivalent Pairs

After the second step, merging equivalent pairs does not require another traversal of all the run lengths, because the run lengths whose labels need to be modified have already been identified by the eigenvalue. Thus, merging the equivalent pairs requires traversing each line.

Before the merging operations, monitor variables must first be copied to the device. Each thread processes the equivalent array of one row, and for each thread the process can be divided into several parts (as shown in Figure 5):

1. Scan the run-length in sequence and process the equivalent pairs in turn.
2. Locate the target run lengths by the eigenvalue of the pixel and determine whether the label values are equal. If the label values are equal, it means that the label of the run length does not need to be modified and the monitor variable will be false. Otherwise, the label of the run length must be modified to the smaller labels of the two target run lengths, and the monitor variable will be true.
3. Repeat the preceding steps until the monitor variable is false.

#### Basic Patch Information

Acquiring the statistics for the basic patch information requires relabeling all the run lengths, adding the basic information of run lengths with the same label value, and obtaining the basic information of the patches with a corresponding label. This process is executed on the CPU. The specific method is as follows:

1. Scan the run lengths in sequence, assign the new label value for the run length, and record the old and new label-value pairs. The array subscript corresponds to the old label value, while the array value corresponds to the new label value.
2. When traversing the next run length of the same label value, modify values directly to the corresponding array value. When traversing a run length with a different label value, provide new label values in order. After relabeling is complete, all the run lengths have been labeled in order. Calculate the patch perimeter and area information of the patch array during relabeling.

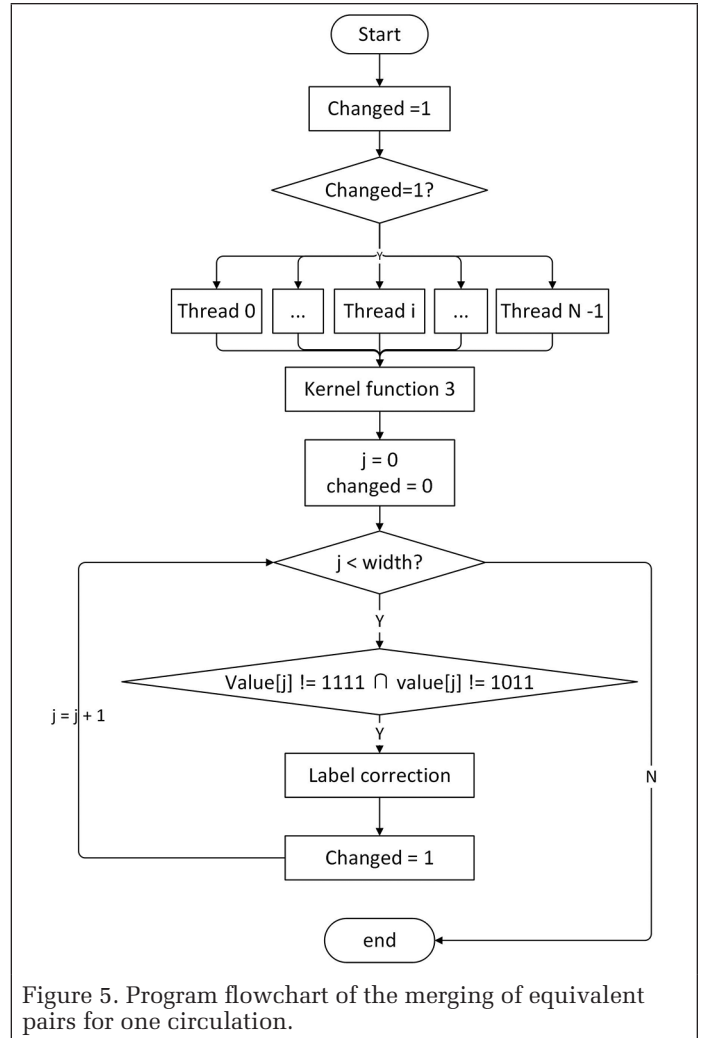


Figure 5. Program flowchart of the merging of equivalent pairs for one circulation.

## Results and Discussion

To comprehensively evaluate the proposed method, the following three aspects were considered:

1. The correctness of the algorithm results was investigated.
2. The proposed algorithm was executed on the five different data sets listed in Table 1, and the cycle times of each data set were collected. Then the relationship between the patches identified from each data set and the cycle times was discussed.
3. The times consumed by the serial algorithm, parallel algorithm, and FRAGSTATS software were collected for the five different data sets. Then their computational efficiencies were compared and analyzed, and the speed ratio of the parallel algorithm to the serial algorithm (that is, the running time of the serial algorithm divided by the running time of the parallel algorithm) was calculated.

#### Correctness of the Algorithm Results

First, the correctness of the patch number was verified. The CPU serial algorithm, the GPU parallel algorithm, and FRAGSTATS were applied to the data sets. The experimental results are shown in Table 3. They show that the computational results of FRAGSTATS and the serial and parallel algorithms are identical from data1 to data4. For data 5, FRAGSTATS cannot process the data, and the serial and parallel algorithm results are consistent.

Table 3. Comparison of the three algorithms in terms of patch number.

Data Set	CPU (Patches)	GPU (Patches)	FRAGSTATS (Patches)
data1	16 809	16 809	16 809
data2	58 382	58 382	58 382
data3	197 534	197 534	197 534
data4	1 119 943	1 119 943	1 119 943
data5	2 136 833	2 136 833	Unable to handle the data volume

### Analysis of Cycle Times

In terms of the algorithm itself, the number of cycle times is related to the image complexity. In general, a larger image means more complex patches and more cycle times. According to the label results obtained from the first 10 cycles (as shown in Figure 6), all the data used in the experiment approached the true value at a faster speed during the first several cycles, while changes in subsequent cycles were slower. That is, a large number of merge operations were completed during the first few executions of the circular merge operation of equivalent pairs, while only a small amount of work was completed in the subsequent cycles, indicating that few rows needed to be processed in the later cycles and that a large number of rows were already in a constant state.

Therefore, row-monitoring variables were added to the parallel algorithm in this study to monitor the number of modifications to a row during the cycle process. As soon as the

adjacent rows of a row are no longer modified, the next cycle execution is not required, which effectively improves the efficiency of the algorithm. In addition, this algorithm can make a trade-off between labeling time and accuracy by controlling the execution times to meet specific requirements.

### Efficiency Analysis of the Three Algorithms

Table 4 shows the running times on the experimental data for FRAGSTATS, the serial algorithm, and the parallel algorithm designed in this study. None of the parallel timings include memory allocation or data-copying operations—only the time required for parallel program execution. To improve the accuracy of the experimental results, Table 4 shows the average time consumption for 10 runs.

Table 4. Statistical table of experimental time-consumption results (ms).

Data Set	FRAGSTATS	Serial Algorithm	Parallel Algorithm	Speedup Ratio
data1	320	20.6	50.2	0.41
data2	920	32.2	68.3	0.47
data3	3400	803.3	482.3	1.66
data4	49 300	5458.5	2196.1	2.49
data5		13 253	4189.3	3.16

According to the results in Table 4, because the parallel algorithm adopts the parallel strategy based on rows, when the data volume is small the parallel algorithm's time

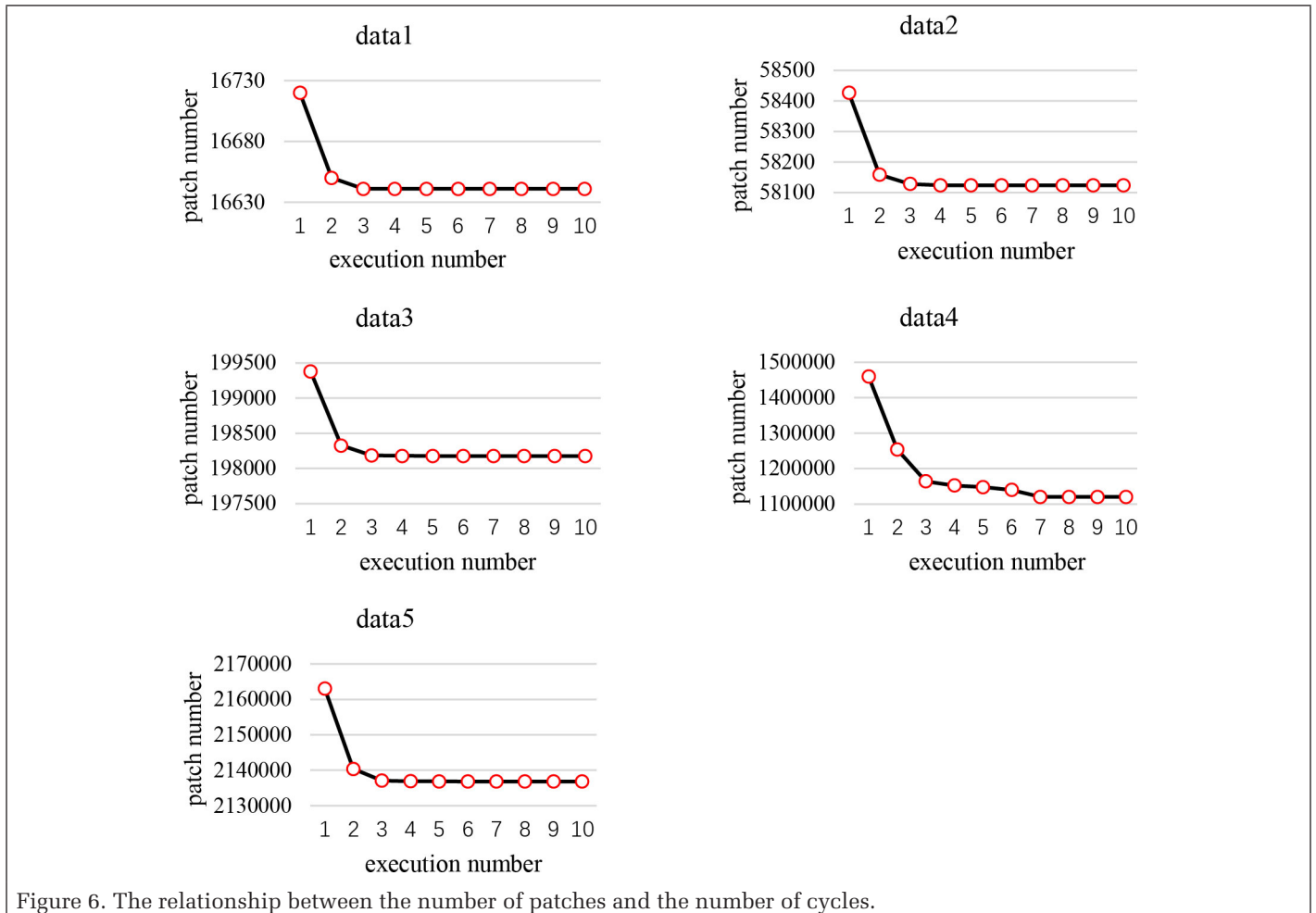


Figure 6. The relationship between the number of patches and the number of cycles.

consumption suffers due to the number of concurrent execution threads and limited GPU thread-operation capability, which fails to maximize the use of a processor core. However, as the volume of data increases, the GPU core utilization rate gradually increases, and the speedup ratio of the parallel algorithm also increases steadily compared with that of the serial algorithm.

## Conclusions

Based on run-length coding, this article proposed an improved CCL algorithm suitable for multi-valued image-data labeling and landscape index computing. The results show that the parallel algorithm further improves efficiency by more than three times, which enables it to efficiently calculate raster data consisting of tens of millions of pixels in a short time, providing a new way to perform landscape index computing on large-scale raster data.

The improved parallel algorithm proposed in this article can be executed on a stand-alone computing environment on any GPU that supports CUDA. The algorithm fully capitalizes on the processing power of the GPU multi-core architecture for data-intensive and computationally intensive tasks, reduces the computing cost of large-scale raster data, and improves the processing capacity and efficiency. This is crucial for the study of urbanization, which needs to deal with raster data with higher resolution and larger data volumes efficiently.

Due to the limitations of the device memory on the equipment used in this study, the parallel algorithm fails when the number of pixels reaches 100 million. Future research will focus primarily on reducing the data-storage requirements to further optimize the algorithm.

## Acknowledgements

The Project Supported by the Open Fund of Key Laboratory of Urban Land Resources Monitoring and Simulation, ministry of Natural Resources (grant number: KF-2019-04-064), and the National Key Research and Development Program of China, grant number 2017YFB0503500

## References

- Cheng, T. 2013. Accelerating universal Kriging interpolation algorithm using CUDA-enabled GPU. *Computers & Geosciences* 54:178–183.
- Gao, Y., F. Wang and X. Hu. 2014. Connected components labeling algorithm based on run-length table searching. Pages PP–PP in *2014 9th International Conference on Computer Science & Education*, held in Vancouver, British Columbia, 22–24 August 2014. Edited by J. Editor. City, St.: IEEE.
- Gotoh, T., Y. Ohta, M. Yoshida and Y. Shirai. 1990. High speed algorithm for component labeling. *Systems and Computers in Japan* 21 (5):74–84.
- Harish, P. and P. J. Narayanan. 2007. Accelerating large graph algorithms on the GPU using CUDA. Pages 197–208 in *High Performance Computing—HiPC 2007*, held in Goa, India, 18–21 December 2007. Edited by S. Aluru, M. Parashar, R. Badrinath and V. K. Prasanna. Lecture Notes in Computer Science vol. 4873. Berlin: Springer.
- He, L., Y. Chao and K. Suzuki. 2008. A run-based two-scan labeling algorithm. *IEEE Transactions on Image Processing* 17 (5):749–756.
- He, L., Y. Chao, K. Suzuki and K. Wu. 2009. Fast connected-component labeling. *Pattern Recognition* 42 (9):1977–1987.
- Huyan, F., S. Zhenfeng, F. Peng and C. Qimin. 2017. The dynamic analysis between urban nighttime economy and urbanization using the DMSP/OLS nighttime light data in China from 1992 to 2012. *Remote Sensing* 9 (5):416.
- Kalentev, O., A. Rai, S. Kemnitz and R. Schneider. 2011. Connected component labeling on a 2D grid using CUDA. *Journal of Parallel and Distributed Computing* 71 (4):615–620.
- Li, C.-X., Y.-P. Huang, X.-X. Han and J. Pang. 2010. Algorithm of binary image labeling and parameter extracting based on FPGA. Pages 542–545 in *2010 2nd International Conference on Computer Engineering and Technology, Vol. 3*, held in Chengdu, China, 16–18 April 2010. Edited by J. Editor. City, St.: IEEE.
- Li, Y. 2015. Fast multi-level connected component labeling for large-scale images. Pages PP–PP in *2015 International Conference on Optoelectronics and Microelectronics (ICOM)*, held in Changchun, China, 16–18 July 2015. Edited by J. Editor. City, St.: IEEE.
- Liu, J., L. Jiao, T. Dong, G. Xu, B. Zhang and L. Yang. 2018. A novel measure approach of expansion process of urban landscape: Multi-order Adjacency Index. *Scientia Geographica Sinica* 38 (11):1741–1749.
- Liu, X., X. Li, Y. Chen, Z. Tan, S. Li and B. Ai. 2010. A new landscape index for quantifying urban expansion using multi-temporal remotely sensed data. *Landscape Ecology* 25 (5):671–682.
- Liu, Y. and Q. Guan. 2017. A parallel algorithm for landscape metrics. *Journal of Geo-Information Science* 19 (4):457–466.
- Lu, K.-Z., F.-X. Ding and H.-Y. Sun. 2008. Parallel algorithm of region labeling based on run-length coding. *Computer Engineering and Applications* 44 (16):49–51.
- Mu, T. H. and Y. Yang. 2013. A method for binary image component parallel labeling algorithm based on cuda. *Advanced Materials Research* 811:538–542.
- Ouyang, X. and X. Zhu. 2020. Spatio-temporal characteristics of urban land expansion in Chinese urban agglomerations. *Acta Geographica Sinica* 75 (3):571–588.
- Qin, F.-T. and B. Fang. 2010. GPU accelerated parallel labeling algorithm of connected-domains in binary images. *Journal of Computer Applications* 30 (10):2774–2776.
- Shao, Z., L. Ding, D. Li, O. Altan, M. E. Huq and C. Li. 2020. Exploring the relationship between urbanization and ecological environment using remote sensing images and statistical data: A case study in the Yangtze River Delta, China. *Sustainability* 12 (14):5620.
- Shao, Z., C. Li, D. Li, O. Altan, L. Zhang and L. Ding. 2020. An accurate matching method for projecting vector data into surveillance video to monitor and protect cultivated land. *ISPRS International Journal of Geo-Information* 9 (7):448.
- Wu, K., E. Otoo and K. Suzuki. 2009. Optimizing two-pass connected-component labeling algorithms. *Pattern Analysis and Applications* 12 (2):117–135.
- Yonehara, K. and K. Aizawa. 2015. A line-based connected component labeling algorithm using GPUs. Pages PP–PP in *2015 International Symposium on Computing and Networking (CANDAR)*, held in Sapporo, Japan, 8–11 December 2015. Edited by J. Editor. City, St.: IEEE.
- Zhang, H., X. Ning, Z. Shao and H. Wang. 2019. Spatiotemporal pattern analysis of China's cities based on high-resolution imagery from 2000 to 2015. *ISPRS International Journal of Geo-Information* 8 (5):241.
- Zhang, Y. and Z. Shao. 2020. Assessing of urban vegetation biomass in combination with LiDAR and high-resolution remote sensing images. *International Journal of Remote Sensing NN (NN):PP–PP*. doi: 10.1080/01431161.2020.1820618
- Zhao, X., L. He, B. Yao and Y. Chao. 2015. A new connected-component labeling algorithm. *IEICE Transactions on Information and Systems* 98 (11):2013–2016.
- Zhu, Z., Z. Ge, S. Chen, X. Sun and Y. Shang. 2014. Research on CUDA-based image parallel dense matching. Pages PP–PP in *2013 Chinese Automation Congress*, held in Changsha, China, 7–8 November 2013. Edited by J. Editor. City, St.: IEEE.

# Exploring the Performance of Different Texture Information and Polarization Features from PolSAR Images in Urban Land Cover Classification

Songjing Guo, Jiahua Teng, and Qimin Cheng

## Abstract

With the improvement of spatial resolution of polarimetric synthetic aperture radar (PolSAR) images, there was more research on texture features extracted from PolSAR images; however, the performance of texture features derived from different descriptors in PolSAR images was not fully explored. In this study, the performance of combining polarization features with texture features extracted by four descriptors, respectively, in land cover classification was explored. The experimental results indicated that: (1) different texture features have different abilities to distinguish ground objects; (2) with the improvement of spatial resolution of PolSAR images, texture features should not be ignored; (3) polarization features are very important for land cover classification, texture features can be used as auxiliary features to further improve the classification accuracy. This study could serve as a meaningful reference for information extraction from PolSAR images.

## Introduction

The United Nations has developed a comprehensive agenda for meeting its urban development goals (Anderson *et al.* 2017; Scott and Rajabifard 2017). Urban land cover classification is one of the main fields of remote sensing applications and contributes to the implementation of the United Nations comprehensive agenda. The classification results can be used to measure urbanization rate and evaluate urban ecological environment (Trinder and Liu 2020), provide data support for urban hydrological model (Shao *et al.* 2019) and monitor the cultivated land (Shao *et al.* 2020). Due to the imaging ability of all-day and all-weather, synthetic aperture radar (SAR) can make effective earth observations in areas where optical sensors fail to work, such as cloudy, rainy, or foggy areas (Jun *et al.* 2014; Shao *et al.* 2017; Shao *et al.* 2019). Compared with single- or dual-polarization SAR systems, a fully polarimetric synthetic aperture radar (PolSAR) image contains more information, such as polarization information, scattering information, and texture information (Jin *et al.* 2014; Du *et al.* 2015; Xiang *et al.* 2016). Therefore, PolSAR has the potential to identify land cover types (Chen *et al.* 2017; Chen *et al.* 2019).

Songjing Guo is with the School of Geography and Information Engineering, China University of Geosciences, 388 Lumo Road, Wuhan, China.

Jiahua Teng is with the Ministry of Ecology and Environment Center for Satellite Application on Ecology and Environment, 4 Fengde East Road, Beijing, China.

Qimin Cheng is with the School of Electronics Information and Communications, Huazhong University of Science and Technology, 1037 Luoyu Road, Wuhan, China (chengqm@hust.edu.cn).

Generally, in the PolSAR image polarization target decomposition method is widely used to identify land cover types. Polarization target decomposition is proposed by Huynen firstly, which divides the coherence/covariance matrix into several basic scattering models (Huynen 1978). Then, various modified polarization decomposition methods have been proposed (Yajima *et al.* 2008; Zhang *et al.* 2008; An *et al.* 2011; Arii *et al.* 2011; Si-Wei *et al.* 2014; Bhattacharya *et al.* 2015; Xiang *et al.* 2015; Zou *et al.* 2015; Xiang *et al.* 2017; Quan *et al.* 2018; Fan *et al.* 2019). However, while different polarization target decomposition methods try to illustrate the PolSAR image from different perspectives, none of them is superior to others in all cases. Hence, it is necessary to make full use of the complementarity of different decomposition methods and combine the polarization features obtained by various decomposition methods to classify ground objects.

With the development of earth observation technology, a wealth of higher quality data are available for the research (Shao *et al.* 2020). The spatial resolution of PolSAR images has also been improved. Therefore, the spatial information should not be ignored in PolSAR images. Texture features extracted from different descriptors were firstly proposed for optical images. Since the imaging mechanism of the SAR system is obviously different from that of optical sensors, it is not clear whether these texture features are applicable to PolSAR data (Sun *et al.* 2016; Deng *et al.* 2018). Although there was some research on texture features extracted from PolSAR images, they usually use only one texture descriptor and the performance of the spatial information in the PolSAR image was not fully explored (Zhai *et al.* 2015; Chen *et al.* 2017; Li *et al.* 2018; Yang *et al.* 2019; Zhai *et al.* 2019). Exploring the performance of different texture features and polarization features from a PolSAR image in urban land cover classification is important but not clear.

Therefore, in this study, Radarsat-2 and experimental airborne SAR (ESAR) data were selected as our experimental data set. Four common descriptors, gray-level co-occurrence matrix (GLCM), Gaussian Markov random fields (GMRF), local binary pattern (LBP), and Gabor filters (Gabor), were used to extract texture features. Then we made a comprehensive analysis of these texture features and polarization features in land cover classification using random forests (RF) classifier. The overall accuracy (OA), the producer's accuracy (PA), the user's accuracy (UA), and the Kappa coefficient based on the

Photogrammetric Engineering & Remote Sensing  
Vol. 87, No. 2, February 2021, pp. 133–142.  
0099-1112/21/133–142

© 2021 American Society for Photogrammetry  
and Remote Sensing  
doi: 10.14358/PERS.87.2.133

confusion matrix were calculated to assess the accuracy of classification results.

### Data Source

Two data sets were used in this study (Figure 1), one of which was Radarsat-2. Radarsat-2 launched on 14 December 2007 and has a capacity for imaging in a variety of polarization modes. It operates in the C band. In this study, a Radarsat-2 data partly covered Wuhan city was employed. The image has four polarization modes including HH, HV, VH, and VV. It was acquired on 5 June 2015 and has a spatial resolution of  $8 \times 8$  m.

The other PolSAR data was obtained by the ESAR sensor. The sensor has five operating frequency bands: X-, C-, S-, L- and P-band. Three measurement modes including single channel operation, SAR polarimetry, and SAR interferometry modes can be selected. In this study, the L-band data acquired by the German Aerospace Centre covering Oberpfaffenhofen in 1999 was used. The size of this imagery is  $1408 \times 1540$  pixels and with a spatial resolution of  $3 \times 3$  m. The land cover types of this study area are mainly buildings, forest, roads, farmland, and other targets.

Basic preprocessing steps, such as speckle filtering, radiometric calibration, terrain correction, and multi-look were conducted in the software Sentinel Application Platform (SNAP) 6.0. Various polarization features were extracted using the software Polarimetric SAR data processing and educational tool and SNAP, and texture features extraction was implemented by Python programming. Detailed information about these features are described in the sections “Polarization Features Extraction” and “Texture Features Extraction”.

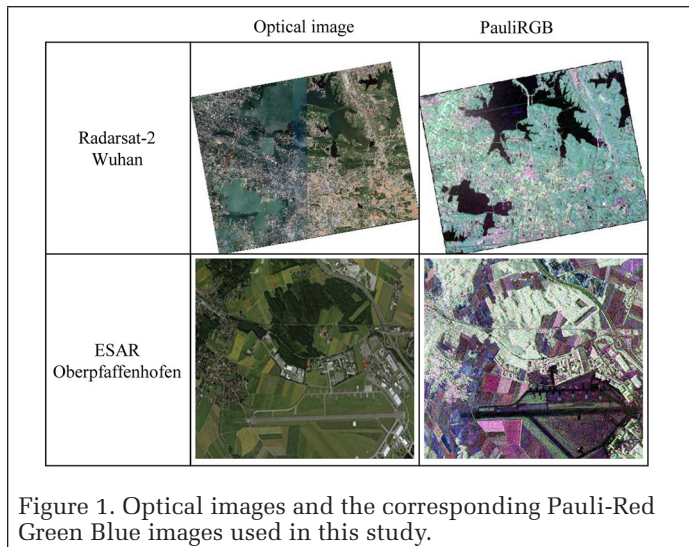


Figure 1. Optical images and the corresponding Pauli-Red Green Blue images used in this study.

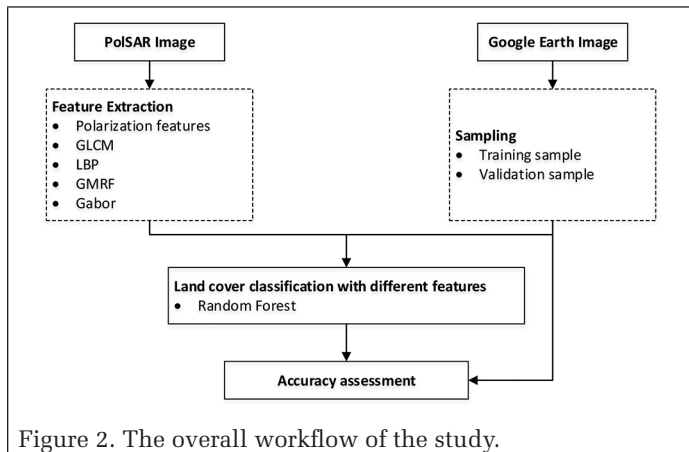


Figure 2. The overall workflow of the study.

## Methods

Figure 2 illustrates the overall workflow of this study. Different features, including polarization features and texture features derived from four texture descriptors were first extracted from both PolSAR images. Training and validation samples were then randomly selected with the aid of Google Earth images. Finally, land cover classification was performed on different combinations of the features using random forest classifier. Detailed descriptions are provided in the following sections.

### Polarization Features Extraction

Compared with conventional single- or multi-polarization SAR, fully PolSAR data can provide plenty of scattering mechanism information about targets, which plays an important role in land cover classification. A PolSAR system can measure the complete scattering matrix  $S$  of ground objects, which is given by the following Sinclair matrix (Lee *et al.* 1993):

$$S = \begin{bmatrix} S_{hh} & S_{hv} \\ S_{vh} & S_{vv} \end{bmatrix} \quad (1)$$

The elements in the matrix  $S$  represent the backscatter coefficients of ground objects on different polarization channels. For each element, the subscripts reflect the polarization mode of the received signal and transmitted signal, respectively. Under the reciprocity assumption  $S_{hv} = S_{vh}$ , the scattering vector  $\kappa_p$  of the target is formed by vectoring the scattering matrix as follows:

$$\kappa_p = [S_{hh} + S_{vv}, S_{hh} - S_{vv}, 2S_{hv}]^T \quad (2)$$

Then the coherency matrix  $\langle [T] \rangle$  can be formed as follows:

$$[T] = \kappa_p \kappa_p^* = \begin{bmatrix} T_{11} & T_{12} & T_{13} \\ T_{21} & T_{22} & T_{23} \\ T_{31} & T_{32} & T_{33} \end{bmatrix} \quad (3)$$

To facilitate interpretation of PolSAR data, various polarization target decomposition methods which can divide a received radar signal into several scattering responses of basic and simple ground objects were proposed, which have been widely used in many fields, such as polarization enhancement, change detection, and target recognition, and a series of valuable research results have been achieved (Li *et al.* 2018; Sun *et al.* 2018). At present, these polarization target decomposition methods can be divided into two categories: coherent target decomposition and incoherent target decomposition. Because ground objects in urban areas are usually distributed targets, incoherent target decompositions are more suitable. Therefore, we extracted polarization features mainly using incoherent target decompositions in this study.

Generally, polarization features can be obtained from PolSAR data and polarization target decomposition. In recent years, many incoherent polarization decomposition methods have been developed and applied to extract polarization features. Since each decomposition method was proposed from different aspects, there is no method which can fully describe the scattering mechanism of all ground objects. So, in this study, we selected the widely used and classic decomposition methods, such as H-A-Alpha decomposition, Yamaguchi decomposition, Freeman three-component decomposition, and so on to extract polarization features for urban land cover classification. Moreover, the Span images were also added to polarization features and used to extract texture features from them. The polarization features extracted in this study were listed in Table 1. There were 18 polarization features in total.

Table 1. Polarization features used in this study.

Name	Polarization Information			
Freeman3	Freeman_Dbl	Freeman_Odd	Freeman_Vol	—
Yamaguchi4	Yamaguchi4_Dbl	Yamaguchi4_Hlx	Yamaguchi4_Odd	Yamaguchi4_Vol
VanZyl3	VanZyl3_Dbl	VanZyl3_Odd	VanZyl3_Vol	—
HAA	Alpha Entropy	Anisotropy Gamma	Beta Lambda	Delta
Span	Span	—	—	—

**Texture Features Extraction**

With the improvement of PolSAR image spatial resolution, more spatial information can be extracted. Texture as a natural property of object surface is an important basis for human visual systems to distinguish ground objects. Due to the capability of texture to the surface roughness, regularity, and directionality of objects, extracting texture features to classify land cover types is very necessary and important. Texture features have been widely used in optical images. However, due to the difference between SAR and optical sensors imaging mechanism, texture features are not deeply explored in PolSAR images. This is what this study concerned about.

There are many studies on texture features in the field of image processing (Zhai *et al.* 2015). Texture extraction methods can be divided into four categories, including statistical-based methods, signal processing-based methods, model-based methods, and structure-based methods. However, these texture features were first proposed for optical images, so comprehensively evaluating and analyzing the advantages and disadvantages of the different texture extraction techniques in a PolSAR image is also important and necessary. Texture features finally used in this study are listed in Table 2.

GLCM was first proposed by Haralick (Haralick *et al.* 1973) and has become the most classic and commonly used texture descriptor. The GLCM is created from a grayscale image by selecting either a horizontal (0°), vertical (90°), or diagonal (45° or 135°) direction, and thus we can adopt all these directions and average them to obtain texture features. Texture is generally depicted by the second-order statistics of the GLCM. In Haralick’s research, there were 14 texture features totally derived from the GLCM. But only some texture features were most widely used. In this study, six texture features, dissimilarity, angular second moment, contrast, entropy, correlation, and homogeneity, were used. The effect of the size of image block for computing texture features could not be ignored. Here, the window size is finally set to 7 × 7 according to experiment results and previous studies (Puissant *et al.* 2005; Zhang *et al.* 2014).

LBP is an operator used to describe local texture features of images. Ojala first proposed this method and then demonstrated the high discrimination of LBP in texture classification (Ojala and Harwood 1996). As a simple but effective descriptor, the LBP method has been successfully applied in

Table 2. Texture features used in this study.

Features	Symbol	Description
GLCM	ASM	Angular second moment
	CON	Contrast
	DIS	Dissimilarity
	EN	Entropy
	COR	Correlation
	HOM	Homogeneity
LBP	$P_1, P_2, \dots, P_{10}$	Enhanced rotation-invariant local binary patterns
GMRF	$\theta_1, \theta_2, \dots, \theta_{12}$	GMRF model parameters
Gabor	$\mu_1, \mu_2, \dots, \mu_{24}$ $s_1, s_2, \dots, s_{24}$	Means and variances of the Gabor features (four scales and six orientations)

many fields, such as face analysis and texture classification (Ahonen *et al.* 2006; Zhenhua *et al.* 2010). The basic idea of LBP operator is to threshold a 3 × 3 neighborhood with the value of the center pixel and convert it into binary code, thus forming an LBP, which is shown in Figure 3a. The value of LBP depends on the difference between the center pixel value and its neighbor pixel values. The probability of occurrence of different local patterns in an image is represented by a histogram, thereby obtaining the texture features of the image for subsequent land cover classification. According to the theory of LBP, the original LBP histogram has 256-dimension. To overcome the variation caused by rotation, rotation invariant LBP was proposed (as shown in Figure 3b), the dimension of LBP features is decreased to 36. However, in practical application, the nine patterns in the first row of Figure 3b are the most common, while the other patterns are not. If the last 27 patterns are classified separately, they will have a certain randomness due to the small probability of their occurrence, which leads to the classification results not being stable. So, the enhanced rotation invariant LBP was proposed, and the 27 unusual patterns were classified into one class, with the dimension of features reduced to 10. In this study, enhanced rotation invariant LBP was employed to extract texture features.

GMRF, from the Markov random field (MRF) model, is an extension of Markov stochastic process in a two-dimensional parameter set. As a probability model to describe graphic structure, it is a better method to describe texture and has

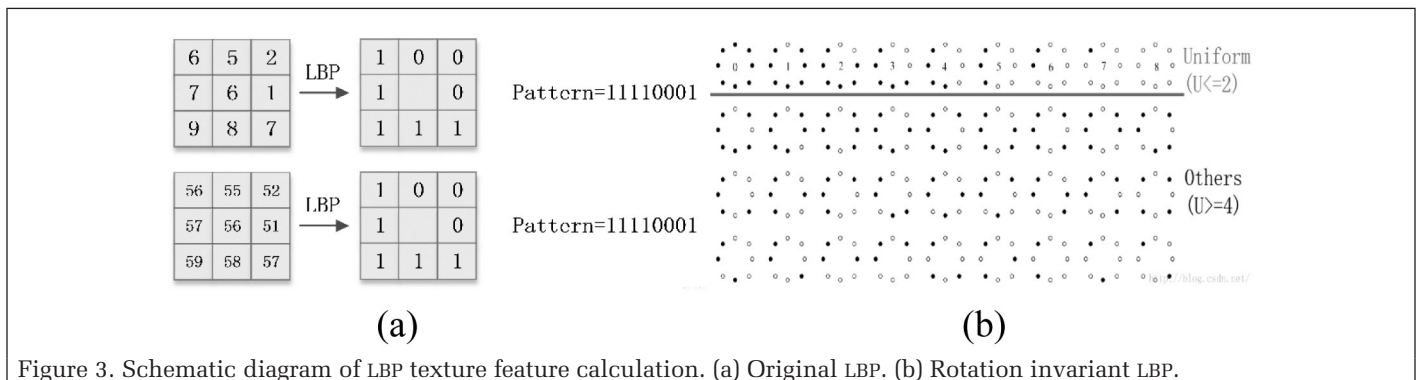


Figure 3. Schematic diagram of LBP texture feature calculation. (a) Original LBP. (b) Rotation invariant LBP.

been successfully applied in many fields, such as image segmentation, image recognition, and so on (Clausi and Yue 2004). Due to the randomness of texture, all textures are composed of different texture primitives which are local and relatively stable, so the randomness of texture can be described by MRF (Chellappa and Chatterjee 1985). Its outstanding characteristic is to introduce the structural information through the neighborhood system properly defined and express the interaction between related random variables in space using a general model. The parameters generated from this model can describe the clustering characteristics of textures in different directions and forms, which is consistent with human's sensory perception. Furthermore, the value of the pixel is just considered as a function of the values of the pixels in its surrounding area. If these pixel values follow a Gaussian distribution, a set of linear equations are expressed by the values of the neighborhood pixels, which is called Gaussian Markov Random Field model. Using a least-squares approach can estimate these parameters that were employed to express the textural features. In general, the order five model is sufficient. Therefore, a fifth-order model was also applied, and 12 parameters totally are estimated in this study. It is worth noting that symmetrical adjacent pixels always share the same parameters in the GMRF model.

Gabor filters come from the function of Gabor that was first proposed by Dennis Gabor, which is a kind of short-time Fourier transform model and a common method in signal processing field. Due to the similarity between the frequency and direction of the Gabor filter and the human visual system, it is appropriate to represent and discriminate the texture (Bovik et al. 1990; Jemaa and Khanfir 2009; Yang and Zhang 2010; Kamarainen 2012). In the spatial domain, two-dimensional Gabor filters can be regarded as a Gaussian kernel function, which is modulated by sinusoidal plane wave. Gabor filter can extract texture information from different directions and has certain robustness to light and attitude. Furthermore, the image rotation and deformation in a certain degree will not affect the extraction and representation of image texture features. However, the choice of parameters (scale, orientation, and frequency) for the function is difficult. In this study, we set the scale and direction to 4 and 6 empirically. The features we used in this study are the mean and variance of the Gabor features, which are 48 features totally.

### Random Forest Algorithm

RF is a typical ensemble learning algorithm that can be used to resolve multiple classification problems (Breiman 2001). It consists of multiple decision trees which are trained by bootstrap sample technique. The final result of the RF model is obtained by voting according to the output of each decision tree. Compared with decision tree, RF conquers the problem of over-fitting and is not sensitive to the noise and outliers, and has scalability and parallelism for high-dimensional data classification. Beyond that, it is a nonparametric, data-driven model without any prior knowledge (Breiman 2001). RF will correctly classify the same type of ground objects with different distribution characteristics. In the RF model, two important parameters, the number of total decision trees and the number of variables for splitting each node, will affect the final result and need to be set carefully. However, this study does not focus on the classification algorithm, so we set the total number of decision trees to 20 and set the number of features used to split in each node to one-half of the input features. In addition, random forest can also evaluate the importance of the feature by adding noise randomly to the variable, and then compare the accuracy changes before and after adding random noise using the out-of-bag data. The larger the change is, the more important the feature is, and vice versa. For more information on RF, please refer to Breiman (2001).

### Land Cover Classification and Accuracy Assessment

In this study, urban land cover classification was employed to investigate the performance of different texture features in PolSAR images. Land cover types of the two study areas are different. In the Wuhan area, five land cover types, buildings, vegetation, water bodies, soils, and roads were identified. And the typical land cover types of the Oberpfaffenhofen area includes buildings, forest, farmland, roads, and other land cover types.

In the process of land cover classification using RF model, sample selection is first necessary. In this study, with the aid of high spatial resolution Google Earth images, a set of samples with all land cover types were selected randomly through visual interpretation. The number of samples of each study area are shown in Table 3. Two thirds of these samples were selected randomly to train the RF classifier and the remaining samples were used for model validation. Four popular indices based on the confusion matrix, UA, PA, OA, and Kappa coefficient were used to assess the classification accuracy in this study. Note that our purpose is exploring the performance of texture features derived from different descriptors in the PolSAR image and their combination with polarization features in land cover classification. The experiments needed to be performed in this study are shown in Table 4.

## Results and Discussion

### Land Cover Classification with Different Features

In this study, we calculated the UA, PA, OA, and Kappa coefficients to estimate the accuracy of the urban land cover classification results with polarization features and different texture features from the Radarsat-2 and ESAR data. The OA and Kappa coefficients of the results using different features are shown in Figure 4. We could discover that the OA and Kappa coefficients of polarization features are higher than the

Table 3. The number of training and testing samples in each PolSAR image.

Samples of	Land Cover Classes				
	Buildings	Vegetation	Water	Soil	Road
<b>Radarsat-2</b>					
Training samples	255	299	513	153	98
Testing samples	126	163	266	68	35
<b>ESAR</b>					
Training samples	675	453	376	391	1007
Testing samples	377	198	183	189	504

Table 4. The tests needed in this study for the Radarsat-2 and ESAR data sets using an RF algorithm.

Test No.	Polarization Features	GLCM	LBP	GMRF	Gabor
1	√				
2		√			
3			√		
4				√	
5					√
6	√	√			
7	√		√		
8	√			√	
9	√				√

results of texture features. The performance of texture features from PolSAR images with different bands and spatial resolutions in land cover classification shows significant differences. For C-band Radarsat-2 image, the values of OA and the Kappa coefficient are in the following sequence: GLCM > Gabor > LBP > GMRF. GLCM, the most widely used texture feature descriptor, achieves the highest accuracy with an OA of 85.26% and a Kappa coefficient of 0.7954. However, for the L-band ESAR image, the OA and the Kappa coefficient difference are in the following sequence: Gabor > LBP > GMRF > GLCM. GLCM obtains the lowest accuracy with an OA of 63.82% and a Kappa coefficient of 0.5024. Using Gabor textures obtain relatively high accuracy in the data and achieves the highest in the ESAR data. The accuracy of LBP and GMRF in the two data are very steady but low. The OA and Kappa coefficients of LBP in the two data are about 75% and 0.65, respectively. The OA of GMRF in the data ranges from 60% to 65%, and the Kappa coefficient of GMRF in the data ranges from 0.40 to 0.53.

Figure 5 shows the UA and PA of all land cover types from both data sets. Compared with texture features, polarization features have a better ability to identify ground objects. The ability of texture features to identify some ground objects is acceptable, but poor in some ground objects. Compared with the Radarsat-2 image, the ability of some texture features to distinguish ground objects is obviously improved in the ESAR image. This indicates that with the increase of the spatial resolution, texture features make an increasing contribution to land cover classification, which should not be ignored. For the Radarsat-2 image, the UA and PA of buildings identified using polarization features and different texture features, respectively are similar and basically up to 80% (except the GMRF). For vegetation, the UA and PA of results with polarization features are over 80%. The UA of the GLCM and Gabor results is about 70% and the PA is about 80%. The UA and PA of vegetation using LBP are about 60%. However, vegetation result classified by GMRF has a low accuracy with a UA of 54.17% and a PA of 7.98%. The UA and PA of water from all results are similar and very high. However, for road and bare soil, the UA and PA of results using texture features and polarization features are all very low; some different phenomena can be found compared with Radarsat-2 data. On the whole, the results using polarization features and Gabor texture features, respectively are similar and have higher accuracy. The UA and PA of buildings from the results are similar to that from Radarsat-2 data. For vegetation, the UA and PA with GLCM and GMRF texture features are very low. Although LBP has high UA of 76%, its PA is still very low. However, for roads and other ground objects, the UA and PA with different texture features are not very low. Based on the results of Radarsat-2 and ESAR, we can find that GLCM and Gabor have a similar ability to distinguish ground

objects, especially for artificial ground targets like buildings. LBP has considerable ability to identify natural ground targets such as vegetation and farmland. And GMRF has the worst performance, which may be caused by the fact that the pixel value in the Span image does not conform to the Gaussian distribution.

### Land Cover Classification with Polarization and Texture Features Combination

In this section, land cover classification combining polarization features with the different texture features are performed. Figure 6 shows the OA and Kappa coefficient of the results using texture and polarization features from Radarsat-2 and ESAR data. The OA and Kappa coefficients of results from Radarsat-2 data range from 90.12% to 92.15% and from 0.8631 to 0.8927, respectively. That from ESAR data range from 90.7% to 95.8% and from 0.8773 to 0.9446, respectively. The OA of the results combining polarization features and texture features are over 90%. And the difference of the OA and Kappa coefficients between these results is not very significant. For Radarsat-2 data, the best result is with the combination of polarization features and LBP texture features. For ESAR data, the best result is with the combination of polarization features and GLCM texture features. The results combining

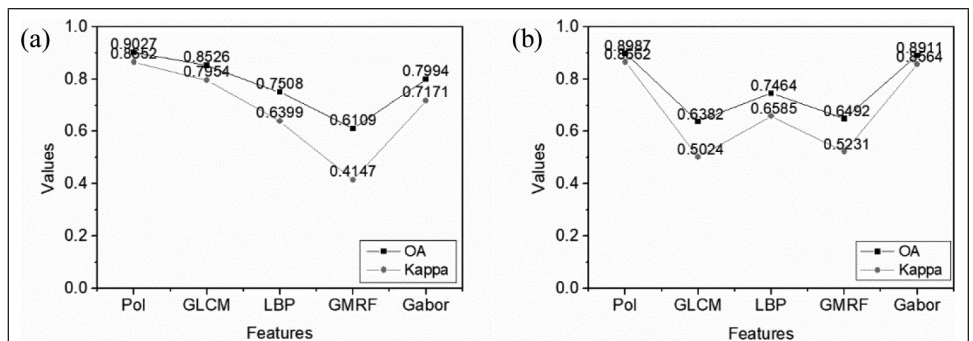


Figure 4. The OA and Kappa coefficients of land cover classification with different features, (a) is for Radarsat-2 data and (b) is for ESAR data.

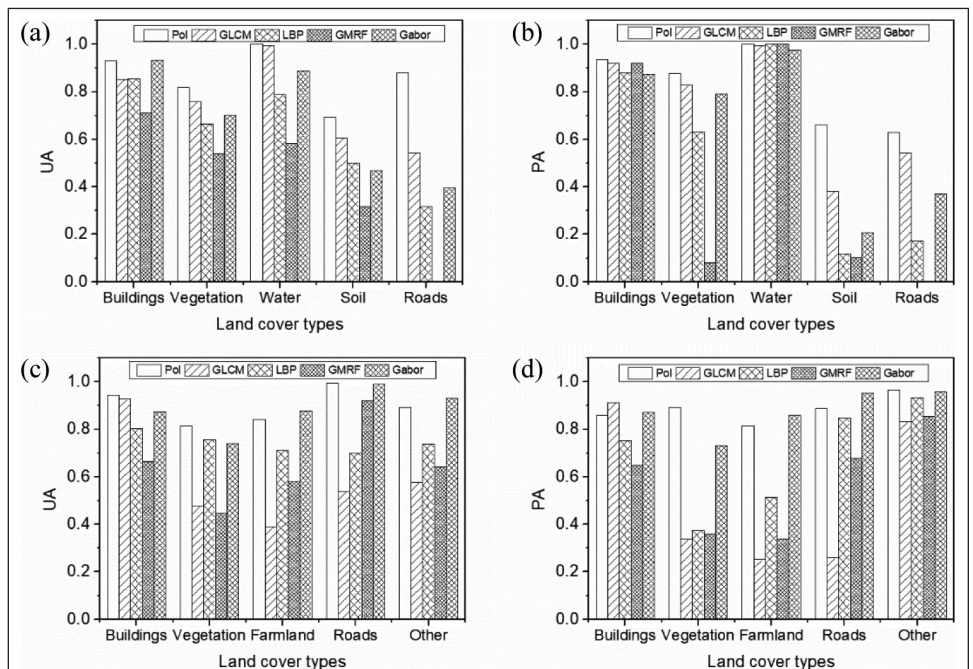


Figure 5. The UA and PA of land cover classification with different features, (a)–(b) are for the Radarsat-2 image and (c)–(d) are for the ESAR image.

polarization features and GMRF texture features from the two data both have the lowest accuracy.

Figure 7 shows the UA and PA of land cover types. In the Radarsat-2 data, the UA and PA of soil and roads are relatively low, while others are high. However, the UA and PA of all ground objects in ESAR data are very high, more than 80%. This shows that texture features are important in high resolution PolSAR images. In addition, according to Figures 6 and 7, the UA, PA, OA, and Kappa coefficients under different feature combination from the data are basically higher than the results of individual features in the previous section. This indicates that for a PolSAR image, polarization features are more important, and texture features can assist polarization features to further improve the accuracy of land cover classification.

### Performance of Polarization and Texture Features Combination in Land Cover Classification

In order to better understand the performance of different features combinations in land cover classification, the results using polarization features alone were taken as reference data and compared with that from different features combination. The comparison results are shown in Figures 8 and 9. From Figure 8, adding texture features can improve the accuracy, but the degree of the improvement difference exists. For Radarsat-2 data, the improvement of combining polarization features and LBP texture features is highest, but only about 2%. However, when GMRF are added, the OA and Kappa coefficient are reduced. These indicate that the contribution of texture features to land cover classification in the Radarsat-2 image is not obvious. For ESAR data, the improvement is remarkable. The improvement of combining polarization features and GMRF features is the lowest, with OA and Kappa coefficient both increasing by 1%, which is slightly below the highest improvement in the Radarsat-2 data. The best improvement with an OA of more than 6% and a Kappa coefficient of 8% is the result with the combination of polarization features and GLCM texture features.

Figure 9 demonstrates the improvement of the UA and PA for each land cover type under different feature combinations. For Radarsat-2 data, there are no rules to follow in the improvement of different land cover types. The improvement has both positive and negative values. This is consistent with the previous findings, which is that adding texture features cannot significantly increase the accuracy of classification in a Radarsat-2 image. It is worth noting that the combination of LBP and polarization features improves all kinds of

land cover types. This indicates that LBP texture features can make up for the deficiency of polarization features, thereby obtaining the highest classification accuracy. For ESAR data, some findings different from the Radarsat-2 data set can be found. The texture features have different degrees of improvement in ground objects identification. The improvement of combining polarization features and GLCM texture features is considerable for all land cover types, especially for buildings, vegetation, and farmland. Adding Gabor texture features can

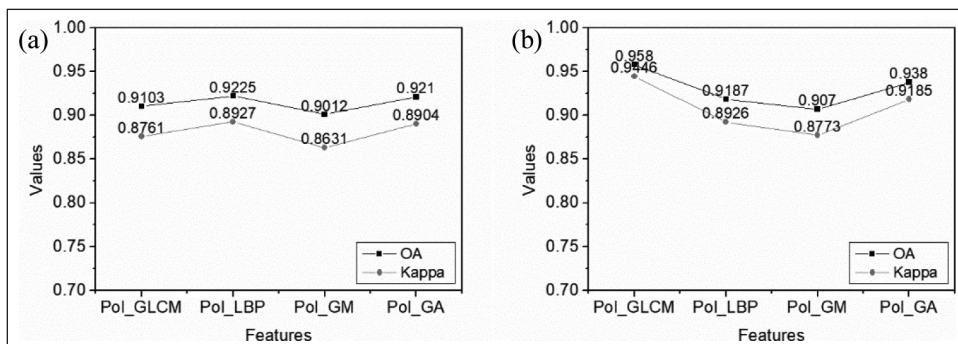


Figure 6. The OA and Kappa coefficients of land cover classification with features combination, (a) is for Radarsat-2 data and (b) is for ESAR data.

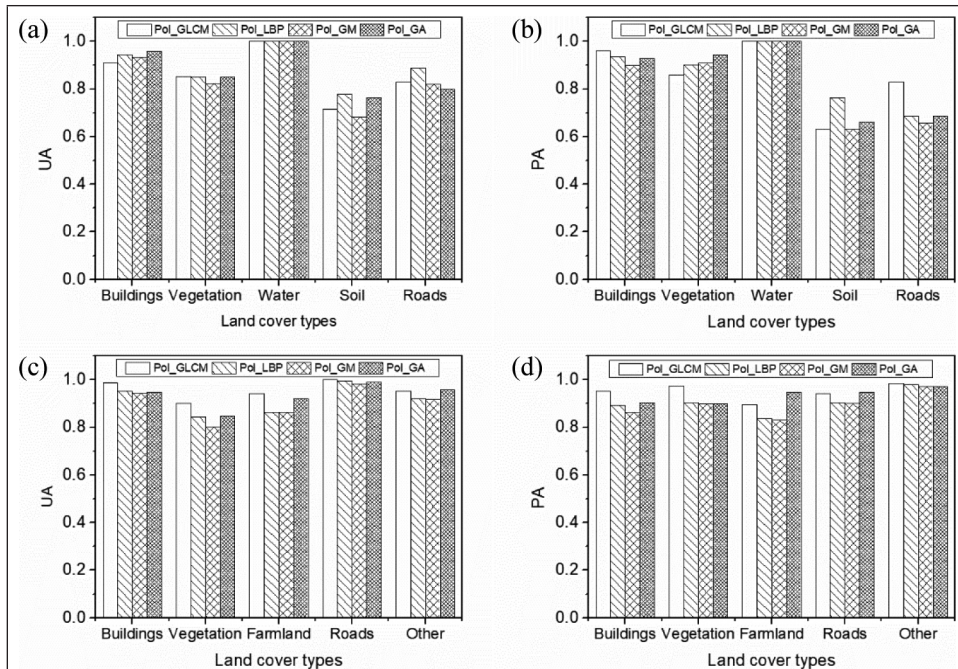


Figure 7. The UA and PA of land cover classification with features combination, (a)–(b) are for the Radarsat-2 image and (c)–(d) are for the ESAR image.

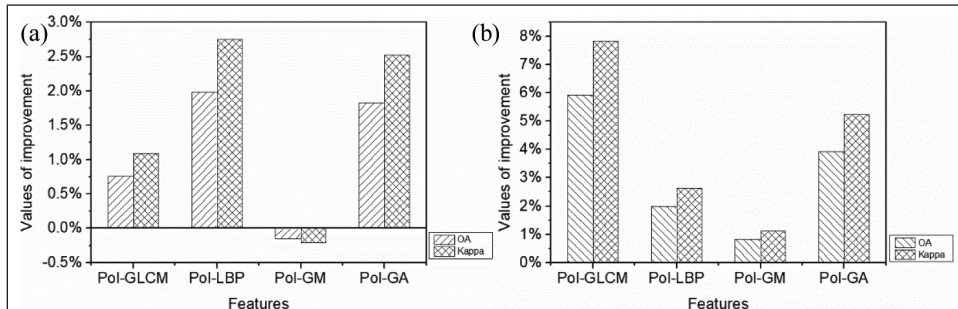


Figure 8. Comparison of the accuracy of results with different features combination, (a) is for Radarsat-2 and (b) is for ESAR.

also improve the accuracy of classification to some extent. However, the improvement of adding LBP texture features and GMRF texture features is not satisfied.

### Discussion of the Contributions of Polarization and Texture Features

Polarization and texture features are the two most important features in PolSAR images, which are widely used in land cover classification (Zhao *et al.* 2013; Zhai *et al.* 2015). But texture features they widely used were GLCM, while LBP, Gabor, and GMRF texture features commonly used in optical images (Chellappa and Chatterjee 1985; Ahonen *et al.* 2006; Jemaa and Khanfir 2009) are not involved. Therefore, in this study, we fully studied the performance of these four texture features from PolSAR images in land cover classification. Figures 10 and 11 illustrate the classification results from Radarsat-2 and ESAR data using different features, respectively. Even for an ESAR image with high spatial resolution, it is difficult to get satisfactory classification results by using texture features alone. And the performance of different texture features is different and GLCM has the best results. From Figure 10, we found that in the results using LBP, GMRF, or Gabor texture features alone, some vegetation was misclassified as water (the rectangular area in Figure 10) and buildings are basically identified, which indicates that texture features are suitable for distinguishing targets with obvious geometric features. However, due to the complex scattering mechanism of vegetation in SAR images, texture features performed poorly in vegetation areas. The results of using polarization features or combining with different texture features are very similar visually. That is, when the spatial resolution is not very high, adding texture features may not improve the accuracy of classification results significantly. Figure 11 shows the results from ESAR data. Compared with Radarsat-2 data, ESAR data has a higher spatial resolution, but also causes more speckle noise problems. The area A, B, and C in Figure 11 represent forest area, dense buildings, and oriented buildings separately. GLCM texture features are a benefit to extract buildings and fail to classify other ground objects. And Gabor texture features are also better for identifying buildings. Based on classification results from Radarsat-2 and ESAR data, GLCM and Gabor are more suitable for the extraction of man-made targets, so some studies have used them to extract collapsed

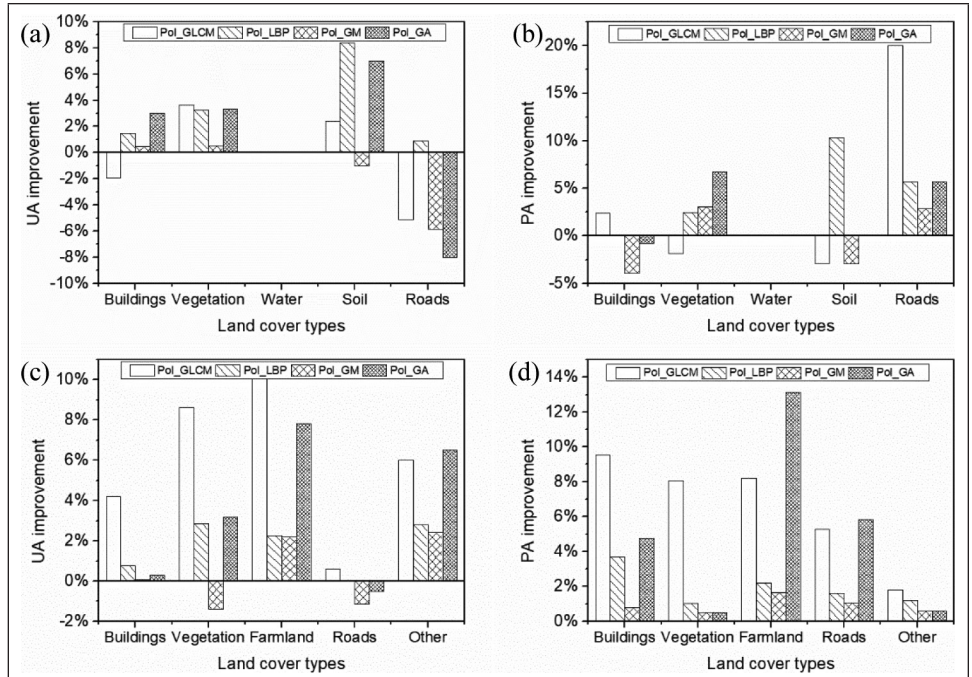


Figure 9. Improvement of the UA and PA under different feature combination, (a)–(b) are for Radarsat-2 and (c)–(d) are for ESAR.

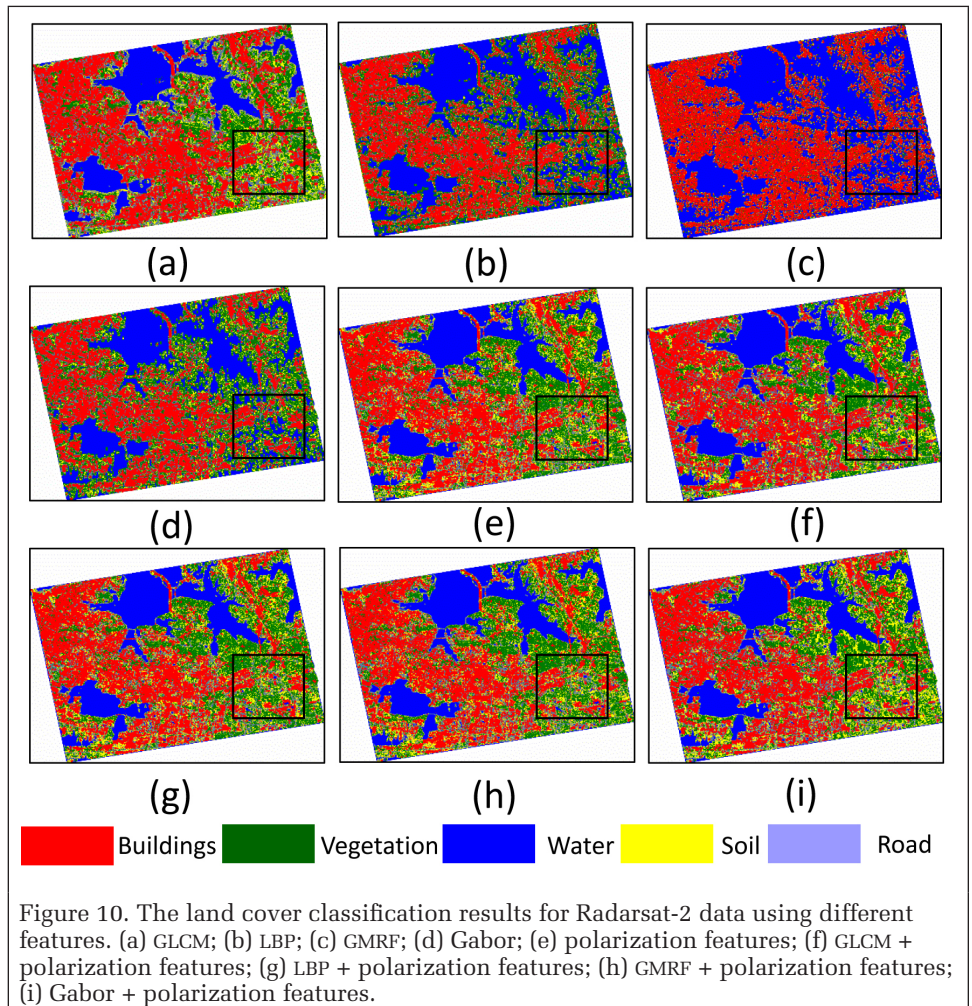


Figure 10. The land cover classification results for Radarsat-2 data using different features. (a) GLCM; (b) LBP; (c) GMRF; (d) Gabor; (e) polarization features; (f) GLCM + polarization features; (g) LBP + polarization features; (h) GMRF + polarization features; (i) Gabor + polarization features.

buildings from PolSAR images (Sun *et al.* 2016; Li *et al.* 2018). Figure 11 demonstrated that texture features derived from LBP and GMRF texture descriptors are not suitable in high resolution PolSAR data and the outline of buildings was not fully extracted. Buildings in optical images is relatively easy to extract (Shao *et al.* 2020), but the polarized radar signals are sensitive to building orientation angle in PolSAR images; using polarization features alone cannot extract buildings fully, especially oriented buildings (Figure 11e). The oriented buildings are easily confused with vegetation (Xiang *et al.* 2017; Quan *et al.* 2018; Sun *et al.* 2018). As it happens, GLCM and Gabor texture features can be used as an auxiliary data in addition to polarization features, which can improve the accuracy of land cover classification (Figure 11f, Figure 11i). Note that some trees whose trunks and the ground formed double-bounce scattering are misclassified as buildings, which cannot be solved effectively.

To better understand the contribution of each feature to the classification results, Figure 12 shows the results of the feature importance score based on RF model from Radarsat-2 and ESAR data. Note that in Figure 12, the numbers on the horizontal axis represent feature numbering, with the first 18 being the polarization features and the rest being the texture features, all of which are arranged in ascending order according to the feature name. According to Figure 12a–d, we can discover that the eighth feature (Freeman\_Vol polarization feature) from Radarsat-2 data makes the most contribution to the land cover classification, and the importance score of the remaining polarization features has little difference. The contribution of texture features derived from the four texture descriptors is very small compared to polarization features, and some texture features do not even contribute at all. The phenomenon in this study is consistent with the previous findings. Figure 12e–h shows the importance score of each feature from ESAR data; the results are obviously different from that of Radarsat-2 data. The importance score of the polarization feature is higher. However, compared with polarization features, the importance score of texture features is not low. We found that some texture features are even more important than some polarization features for land cover classification. These indicate that in PolSAR images, texture features play a very important role. Besides, with the increasing of spatial resolution, the contribution of texture features to land cover classification will

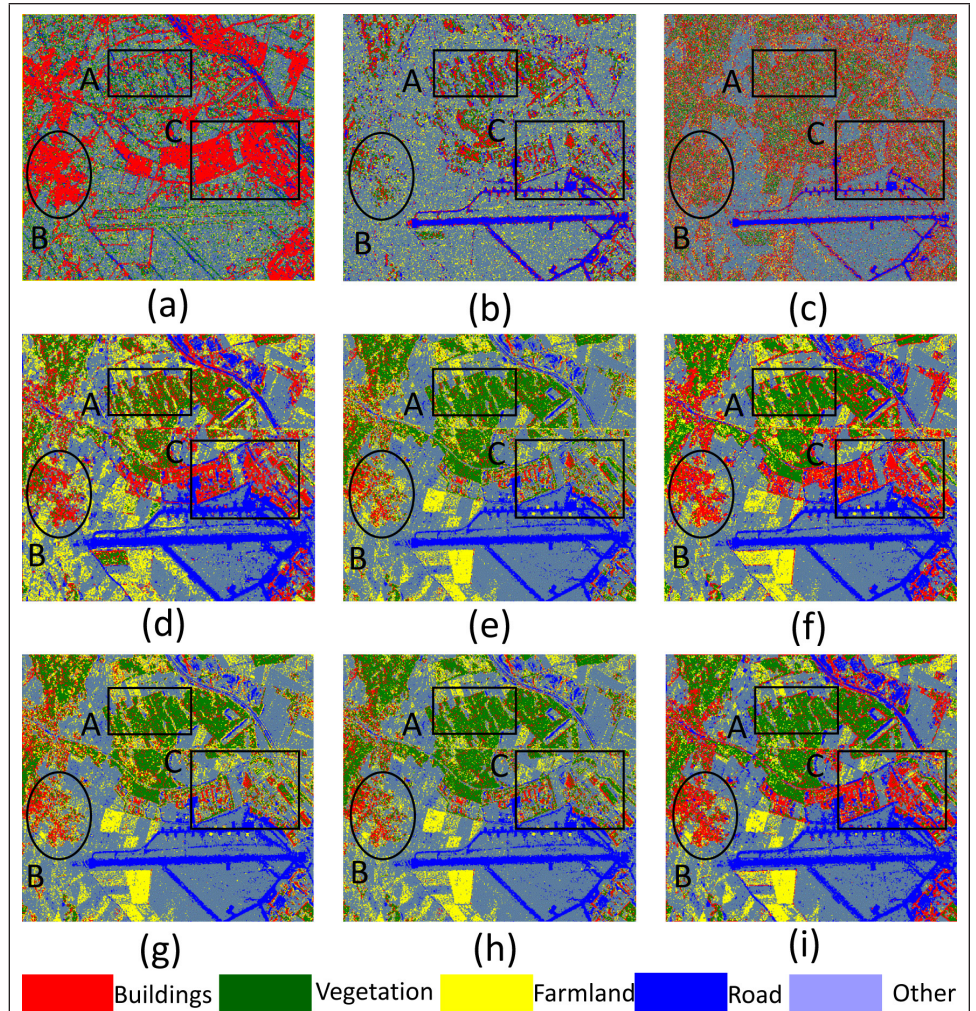


Figure 11. The land cover classification results for ESAR data using different features. (a) GLCM; (b) LBP; (c) GMRF; (d) Gabor; (e) polarization features; (f) GLCM + polarization features; (g) LBP + polarization features; (h) GMRF + polarization features; (i) Gabor + polarization features.

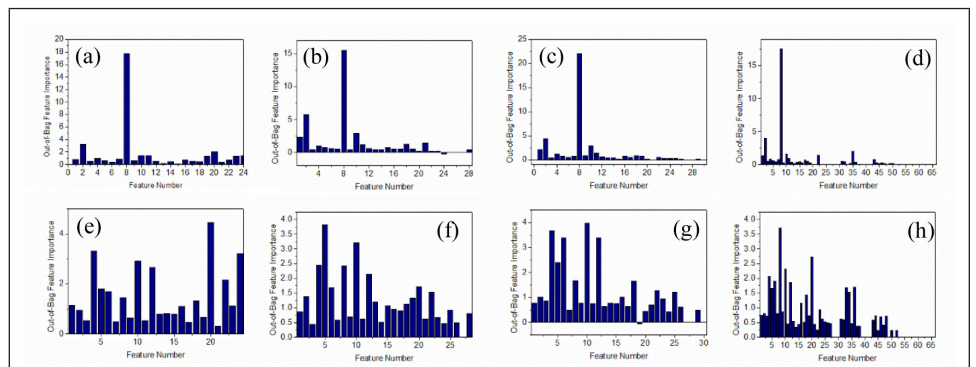


Figure 12. The feature importance score, (a)–(d) are for Radarsat-2 and (e)–(h) are for ESAR data; (a) and (e): polarization features + GLCM; (b) and (f): polarization features + LBP; (c) and (g): polarization features + GMRF; (d) and (h): polarization features + Gabor.

be improved. However, some texture features derived from Gabor and GMRF texture descriptors do not make a contribution to land cover classification.

Polarization features can reflect geometric and physical information of ground objects. Due to the difference of the imaging mechanism between optical and PolSAR images, texture

features of PolSAR images are quite messy. As Figure 12 reflected, for a PolSAR image, polarization features are relatively important to classify land covers, and texture features can be used as auxiliary data. The results of this study showed that the accuracy of land cover classification can be improved to some extent through adding texture features. In this study, we aim to explore the performance of different texture features and their combination with polarization features in land cover classification. In future work, we can focus on investigating new and effective features and develop a new classifier to further improve the accuracy of classification based on this research. Besides, according to the feature importance score analysis, some features contribute little to the land cover classification. We can employ some algorithms such as manifold learning to decrease the dimension of features, which can be beneficial to saving the time of training the classifier and improving the accuracy of classification.

## Conclusions

Urban land cover classification is one of the most important applications of remote sensing. It plays a key role in national economy and military field. With the improvement of spatial resolution of the PolSAR image, the spatial information should be paid attention to. Although there was some research on texture features extracted from the PolSAR image, the performance of texture features derived from different descriptors in a PolSAR image was not fully explored. In this study, we explored the performance of GLCM, LBP, GMRF, and Gabor texture features and their combination with polarization features in land cover classification. From the experiment results, we found that: firstly, the ability of different texture features to distinguish ground objects is different. Secondly, with the improvement of spatial resolution, texture features play a more important role in land cover classification and should not be ignored. Thirdly, for the PolSAR image, polarization features are relatively more important and texture features can be used as auxiliary features to further improve the accuracy of land cover classification. It is worth pointing out that the purpose of this paper is not to tell the readers that the texture features used in this paper are the most appropriate and can be used directly, but to help the readers better understand the complex spatial features of ground objects in PolSAR images. This study could serve as a meaningful reference for information extraction from PolSAR images. In future work, we can extract more effective features and develop a new classification algorithm to improve the accuracy of land cover classification in PolSAR images.

## Acknowledgments

The authors are sincerely grateful to the editors as well as the anonymous reviewers for their valuable suggestions and comments that helped us improve this paper significantly. This work is supported by the National Key Research and Development Program of China under Grant 2018YFB0505401, the Research Project from the Ministry of Natural Resources of China under Grant 4201-240100123, the National Natural Science Foundation of China under Grants 41771452, 41771454, and 41890820, and the Natural Science Fund of Hubei Province in China under Grant 2018CFA007.

## References

Ahonen, T., A. Hadid and M. Pietikäinen. 2006. Face recognition with local binary patterns. *IEEE Transactions on Pattern Analysis & Machine Intelligence* 28 (12):2037–2041.

An, W., C. Xie, X. Yuan, Y. Cui and J. Yang. 2011. Four-component decomposition of polarimetric SAR images with deorientation. *IEEE Geoscience and Remote Sensing Letters* 8 (6):1090–1094.

Anderson, K., B. Ryan, W. Sonntag, A. Kavvada and L. Friedl. 2017. Earth observation in service of the 2030 agenda for sustainable development. *Geo-spatial Information Science* 20 (2):77–96.

Arii, M., J. J. van Zyl and Y. Kim. 2011. Adaptive model-based decomposition of polarimetric SAR covariance matrices. *IEEE Transactions on Geoscience and Remote Sensing* 49 (3):1104–1113.

Bhattacharya, A., A. Muhuri, S. De, S. Manickam and A. C. Frery. 2015. Modifying the Yamaguchi four-component decomposition scattering powers using a stochastic distance. *IEEE Journal of Selected Topics in Applied Earth Observations and Remote Sensing* 8 (7):3497–3506.

Bovik, A. C., M. Clark and W. S. Geisler. 1990. Multichannel texture analysis using localized spatial filters. *IEEE Transactions on Pattern Analysis and Machine Intelligence* 12 (1):55–73.

Breiman, L. 2001. Random forests. *Machine Learning* 45 (1):5–32.

Chellappa, R. and S. Chatterjee. 1985. Classification of textures using Gaussian Markov random fields. *IEEE Transactions on Acoustics Speech & Signal Processing* 33 (4):959–963.

Chen, Y., L. Jiao, Y. Li, L. Li, D. Zhang, B. Ren and N. Marturi. 2019. A novel semicoupled projective dictionary pair learning method for PolSAR image classification. *IEEE Transactions on Geoscience and Remote Sensing* PP (4):1–12.

Chen, Y., L. Jiao, Y. Li and J. Zhao. 2017. Multilayer projective dictionary pair learning and sparse autoencoder for PolSAR image classification. *IEEE Transactions on Geoscience & Remote Sensing*:1–12.

Clausi, D. A. and B. Yue. 2004. Comparing cooccurrence probabilities and Markov random fields for texture analysis of SAR sea ice imagery. *IEEE Transactions on Geoscience & Remote Sensing* 42 (1):215–228.

Deng, X., J. Chen, H. Li, P. Han and W. Yang. 2018. Log-cumulants of the finite mixture model and their application to statistical analysis of fully polarimetric UAVSAR data. *Geo-spatial Information Science* 21 (001):45–55.

Haralick, R. M., K. Shanmugam and I. H. Dinstein –Du, P., A. Samat, B. Waske, S. Liu and Z. Li. 2015. Random forest and rotation forest for fully polarized SAR image classification using polarimetric and spatial features. *ISPRS Journal of Photogrammetry & Remote Sensing* 105 (Jul.):38–53.

Fan, H., S. Quan, D. Dai, X. Wang and S. Xiao. 2019. Seven-component model-based decomposition for PolSAR data with sophisticated scattering models. *Remote Sensing* 11 (23):2802.

Haralick, R. M., K. Shanmugam and I. H. Dinstein. 1973. Textural features for image classification. *IEEE Transactions on Systems, Man, and Cybernetics* SMC-3 (6):610–621.

Huynen, J. R. 1978. Phenomenological theory of radar targets. *Electromagnetic Scattering*:653–712.

Jemaa, Y. B. and S. Khanfir. 2009. Automatic local Gabor features extraction for face recognition. *Computer Science*:1–6.

Jin, H., G. Mountrakis and S. V. Stehman. 2014. Assessing integration of intensity, polarimetric scattering, interferometric coherence and spatial texture metrics in PALSAR-derived land cover classification. *ISPRS Journal of Photogrammetry & Remote Sensing* 98:70–84.

Jun, L., W. Xing, C. Min, L. Shuguang, Z. Xiran, S. Zhenfeng and L. Ping. 2014. Thin cloud removal from single satellite images. *Optics Express* 22 (1):618–632.

Kamarainen, J.-K. 2012. Gabor features in image analysis. Pages 13–14 in *Proceedings International Conference on Image Processing Theory*, held in Istanbul, Turkey, 15–18 Oct. 2012.

Lee, J.-S., M. R. Grunes and R. Kwok. 1993. Classification of multi-look polarimetric SAR imagery based on complex Wishart distribution. *International Journal of Remote Sensing* 15 (1):2299–2311.

Li, L., X. Liu, Q. Chen and S. Yang. 2018. Building damage assessment from PolSAR data using texture parameters of statistical model. *Computers & Geosciences* 113:115–126.

Ojala, T. and I. Harwood. 1996. A comparative study of texture measures with classification based on feature distributions. *Pattern Recognition* 29 (1):51–59.

- Puissant, A., J. Hirsch and C. Weber. 2005. The utility of texture analysis to improve per pixel classification for high spatial resolution imagery. *International Journal of Remote Sensing* 26 (4):733–745.
- Quan, S., B. Xiong, D. Xiang, L. Zhao, S. Zhang and G. Kuang. 2018. Eigenvalue-based urban area extraction using polarimetric SAR data. *IEEE Journal of Selected Topics in Applied Earth Observations and Remote Sensing* 11 (2):458–471.
- Scott, G. and A. Rajabifard. 2017. Sustainable development and geospatial information: A strategic framework for integrating a global policy agenda into national geospatial capabilities. *Geospatial Information Science* 20 (002):1–18.
- Shao, Z., J. Deng, L. Wang, Y. Fan, N. Sumari and Q. Cheng. 2017. Fuzzy autoencode based cloud detection for remote sensing imagery. *Remote Sensing* 9 (4):311.
- Shao, Z., H. Fu, D. Li, O. Altan and T. Cheng. 2019a. Remote sensing monitoring of multi-scale watersheds impermeability for urban hydrological evaluation. *Remote Sensing of Environment* 232:111338.
- Shao, Z., C. Li, D. Li, O. Altan, L. Zhang and L. Ding. 2020a. An accurate matching method for projecting vector data into surveillance video to monitor and protect cultivated land. *ISPRS International Journal of Geo-Information* 9:448.
- Shao, Z., Y. Pan, C. Diao and J. Cai. 2019b. Cloud detection in remote sensing images based on multiscale features-convolutional neural network. *IEEE Transactions on Geoscience and Remote Sensing* 57 (6):4062–4076.
- Shao, Z., P. Tang, Z. Wang, N. Saleem, S. Yam and C. Sommai. 2020b. BRRNet: A fully convolutional neural network for automatic building extraction from high-resolution remote sensing images. *Remote Sensing* 12:1050.
- Shao, Z., W. Zhou, X. Deng, M. Zhang and Q. Cheng. 2020c. Multilabel remote sensing image retrieval based on fully convolutional network. *IEEE Journal of Selected Topics in Applied Earth Observations and Remote Sensing* 13:318–328.
- Si-Wei, C., W. Xue-Song, X. Shun-Ping and M. Sato. 2014. General polarimetric model-based decomposition for coherency matrix. *IEEE Transactions on Geoscience and Remote Sensing* 52 (3):1843–1855.
- Sun, W., L. Shi, J. Yang and P. Li. 2016. Building collapse assessment in urban areas using texture information from postevent SAR data. *IEEE Journal of Selected Topics in Applied Earth Observations and Remote Sensing* 9 (8):3792–3808.
- Sun, X., H. Song, R. Wang and N. Li. 2018. High-resolution polarimetric SAR image decomposition of urban areas based on a POA correction method. *Remote Sensing Letters* 9 (4):363–372.
- Trinder, J. and Q. Liu. 2020. Assessing environmental impacts of urban growth using remote sensing. *Geo-spatial Information Science* (6):1–20.
- Xiang, D., Y. Ban and Y. Su. 2015. Model-based decomposition with cross scattering for polarimetric SAR urban areas. *IEEE Geoscience and Remote Sensing Letters* 12 (12):2496–2500.
- Xiang, D., T. Tang, Y. Ban, Y. Su and G. Kuang. 2016. Unsupervised polarimetric SAR urban area classification based on model-based decomposition with cross scattering. *ISPRS Journal of Photogrammetry and Remote Sensing* 116:86–100.
- Xiang, D., W. Wang, T. Tang and Y. Su. 2017. Multiple-component polarimetric decomposition with new volume scattering models for PolSAR urban areas. *IET Radar, Sonar & Navigation* 11 (3):410–419.
- Yajima, Y., Y. Yamaguchi, R. Sato, H. Yamada and W. M. Boerner. 2008. POLSAR image analysis of wetlands using a modified four-component scattering power decomposition. *IEEE Transactions on Geoscience and Remote Sensing* 46 (6):1667–1673.
- Yang, M. and L. Zhang. 2010. Gabor feature based sparse representation for face recognition with Gabor occlusion dictionary. Pages 448–461 in *Proceedings Computer Vision—ECCV 2010*, held in Crete, Greece, 5–11 September 2010. Berlin, Heidelberg, Germany: Springer, Berlin, Heidelberg.
- Yang, R., X. Xu, Z. Xu, H. Dong, R. Gui and F. Pu. 2019. Dynamic fractal texture analysis for PolSAR land cover classification. *IEEE Transactions on Geoscience and Remote Sensing*:1–12.
- Zhai, W., C. Huang and W. Pei. 2019. Building damage assessment based on the fusion of multiple texture features using a single post-earthquake PolSAR image. *Remote Sensing* 11 (8).
- Zhai, W., H. Shen, C. Huang and W. Pei. 2015. Fusion of polarimetric and texture information for urban building extraction from fully polarimetric SAR imagery. *Remote Sensing Letters* 7 (1):31–40.
- Zhang, L., B. Zou, H. Cai and Y. Zhang. 2008. Multiple-component scattering model for polarimetric SAR image decomposition. *IEEE Geoscience and Remote Sensing Letters* 5 (4):603–607.
- Zhang, Y., H. Zhang and H. Lin. 2014. Improving the impervious surface estimation with combined use of optical and SAR remote sensing images. *Remote Sensing of Environment* 141:155–167.
- Zhao, L., J. Yang, P. Li, L. Zhang, L. Shi and F. Lang. 2013. Damage assessment in urban areas using post-earthquake airborne PolSAR imagery. *International Journal of Remote Sensing* 34 (24):8952–8966.
- Zhenhua, G., Z. Lei and Z. David. 2010. A completed modeling of local binary pattern operator for texture classification. *IEEE Transactions on Image Processing* 19 (6):1657–1663.
- Zou, B., Y. Zhang, N. Cao and N. P. Minh. 2015. A four-component decomposition model for PolSAR data using asymmetric scattering component. *IEEE Journal of Selected Topics in Applied Earth Observations and Remote Sensing* 8 (3):1051–1061.

# PE&RS Media Kit 2021

## Special Advertising Opportunities

### FRONT COVER SPONSORSHIP

A *PE&RS* cover sponsorship is a unique opportunity to capture the undivided attention of your target market through three premium points of contact.

#### 1— *PE&RS* FRONT COVER

(Only twelve available, first-come, first-served)

*PE&RS* is world-renowned for the outstanding imagery displayed monthly on its front cover—and readers have told us they eagerly anticipate every issue. This is a premium opportunity for any company, government agency, university or non-profit organization to provide a strong image that demonstrates their expertise in the geospatial information industry.

#### 2— FREE ACCOMPANYING “HIGHLIGHT” ARTICLE

A detailed article to enhance your cover image is welcome but not a condition of placing an image. Many readers have asked for more information about the covers and your article is a highly visible way to tell your story in more depth for an audience keenly interested in your products and services. No article is guaranteed publication, as it must pass ASPRS editorial review. For more information, contact Rae Kelley at rkelley@asprs.org.

#### 3— FREE TABLE OF CONTENTS COVER DESCRIPTION

Use this highly visible position to showcase your organization by featuring highlights of the technology used in capturing the front cover imagery. Limit 200-word description.

**Terms:** Fifty percent nonrefundable deposit with space reservation and payment of balance on or before materials closing deadline.

Cover Specifications:

**Bleed size:** 8 5/8" × 11 1/4" Trim: 8 3/8" × 10 7/8"

Offprints of the cover, Table of Contents page, and highlight article are available at the time of publication. These must be ordered and paid for in advance.

For front cover offprints or other quantities, contact Rae Kelley, ASPRS Assistant Director – Publications 505-819-3599 e-mail rkelley@asprs.org.

### PRICING

	Corporate Member Exhibiting at a 2021 ASPRS Conference	Corporate Member	Exhibitor	Non Member
Cover 1	\$1,850	\$2,000	\$2,350	\$2,500

### Belly Bands, Inserts, Outserts & More!

Make your material the first impression readers have when they get their copy of *PE&RS*. Contact Bill Spilman at bill@innovativemediasolutions.com

### VENDOR SEMINARS

ASPRS Sustaining Members now have the opportunity to hold a 1-hour informational session as a Virtual Vendor Seminar that will be free to all ASPRS Members wishing to attend. There will be one opportunity per month to reach out to all ASPRS Members with a demonstration of a new product, service, or other information. ASPRS will promote the Seminar through a blast email to all members, a notice on the ASPRS web site home page, and ads in the print and digital editions of *PE&RS*.

The Virtual Seminar will be hosted by ASPRS through its Zoom capability and has the capacity to accommodate 500 attendees.

Vendor Seminars	
Fee	\$2,500 (no discounts)

### EMPLOYMENT PROMOTION

When you need to fill a position right away, use this direct, right-to-the-desktop approach to announce your employment opportunity. The employment opportunity will be sent once to all ASPRS members in our regular Wednesday email newsletter to members, and will be posted on the ASPRS Web site for one month. This type of advertising gets results when you provide a web link with your text.

Employment Opportunity	Net Rate
30-Day Web + 1 email	\$500/opportunity
Web-only (no email)	\$300/opportunity

*Do you have multiple vacancies that need to be filled? Contact us for pricing details for multiple listings.*

### NEWSLETTER DISPLAY ADVERTISING

Your vertical ad will show up in the right hand column of our weekly newsletter, which is sent to more than 3,000 people, including our membership and interested parties. **Open Rate: 32.9%**

Newsletter vertical banner ad	Net Rate
180 pixels x 240 pixels max	\$500/opportunity

## PE&RS Digital Edition

### Digital Edition E-mail Blast: 5,800+

*PE&RS* is available online in both a public version that is available to anyone but does not include the peer-reviewed articles, and a full version that is available to ASPRS members only upon login.

The enhanced version of *PE&RS* contains hot links for all ASPRS Sustaining Member Companies, as well as hot links on advertisements, ASPRS Who's Who, and internet references.

### Become a sponsor today!

The e-mail blast sponsorship opportunity includes a **180 x 240 pixel ad** in the email announcement that goes out to our membership announcing the availability of the electronic issue.

Digital Edition Opportunities	Net Rate
E-mail Blast Sponsorship*	\$1,000

For more information, contact Bill Spilman at bill@innovativemediasolutions.com | (877) 878-3260 toll-free | (309) 483-6467 direct | (309) 483-2371 fax

## PE&RS 2021 Advertising Rates & Specs

**THE MORE YOU ADVERTISE THE MORE YOU SAVE!** PE&RS offers frequency discounts. Invest in a three-times per year advertising package and receive a 5% discount, six-times per year and receive a 10% discount, 12-times per year and receive a 15% discount off the cost of the package.

	Corporate Member Exhibiting at a 2021 ASPRS Conference	Corporate Member	Exhibitor	Non Member
<i>All rates below are for four-color advertisements</i>				
Cover 1	\$1,850	\$2,000	\$2,350	\$2,500
<i>In addition to the cover image, the cover sponsor receives a half-page area to include a description of the cover (maximum 500 words). The cover sponsor also has the opportunity to write a highlight article for the journal. Highlight articles are scientific articles designed to appeal to a broad audience and are subject to editorial review before publishing. The cover sponsor fee includes 50 copies of the journal for distribution to their clients. More copies can be ordered at cost.</i>				
Cover 2	\$1,500	\$1,850	\$2,000	\$2,350
Cover 3	\$1,500	\$1,850	\$2,000	\$2,350
Cover 4	\$1,850	\$2,000	\$2,350	\$2,500
Advertorial	1 Complimentary Per Year	1 Complimentary Per Year	\$2,150	\$2,500
Full Page	\$1,000	\$1,175	\$2,000	\$2,350
2 page spread	\$1,500	\$1,800	\$3,200	\$3,600
2/3 Page	\$1,100	\$1,160	\$1,450	\$1,450
1/2 Page	\$900	\$960	\$1,200	\$1,200
1/3 Page	\$800	\$800	\$1,000	\$1,000
1/4 Page	\$600	\$600	\$750	\$750
1/6 Page	\$400	\$400	\$500	\$500
1/8 Page	\$200	\$200	\$250	\$250
Other Advertising Opportunities				
Wednesday Member Newsletter Email Blast	1 Complimentary Per Year	1 Complimentary Per Year	\$600	\$600

A 15% commission is allowed to recognized advertising agencies

Ad Size	Width	Height
Cover (bleed only)	8.625"	11.25"
Full Page (bleed)	8.625"	11.25"
Full Page (trim)	8.375"	10.875"
2/3 Page Horizontal	7.125"	6.25"
2/3 Page Vertical	4.58"	9.625"
1/2 Page Horizontal	7.125"	4.6875"
1/2 Page Vertical	3.4375"	9.625"
1/3 Page Horizontal	7.125"	3.125"
1/3 Page Vertical	2.29"	9.625"
1/4 Page Horizontal	7.125"	2.34"
1/4 Page Vertical	3.4375"	4.6875"
1/8 Page Horizontal	7.125"	1.17"
1/8 Page Vertical	1.71875"	4.6875"

- Publication Size: 8.375" × 10.875" (W x H)
- Live area: 1/2" from gutter and 3/8" from all other edges
- No partial page bleeds.
- Publication Style: Perfect bound
- Printing Method: Web offset press
- Software Used: PC InDesign CS6
- Supported formats: TIFF, EPS, BMP, JPEG, PDF, PC InDesign, Illustrator, and Photoshop

Source: PE&RS Readership Survey, Summer 2017

For more information, contact Bill Spilman at bill@innovativemediasolutions.com | (877) 878-3260 toll-free | (309) 483-6467 direct | (309) 483-2371 fax

**Send ad materials to:**  
 ASPRS/PE&RS Production  
 425 Barlow Place, Suite 210  
 Bethesda, Maryland 20814  
 505-819-3599  
 rkelly@asprs.org

**Ship inserts to:**  
 Alicia Coard  
 Walsworth  
 2180 Maiden Lane  
 St. Joseph, MI 49085  
 888-563-3220 (toll free)  
 269-428-1021 (direct)  
 269-428-1095 (fax)  
 alicia.coard@walsworth.com

# Digital Elevation Model Technologies and Applications: The DEM Users Manual, 3<sup>rd</sup> Edition

Edited by David F. Maune, PhD, CP  
and Amar Nayegandhi, CP, CMS

To order, visit  
<https://www.asprs.org/dem>

The 3rd edition of the DEM Users Manual includes 15 chapters and three appendices. References in the eBook version are hyperlinked. Chapter and appendix titles include:

1. Introduction to DEMs  
*David F. Maune, Hans Karl Heidemann, Stephen M. Kopp, and Clayton A. Crawford*
  2. Vertical Datums  
*Dru Smith*
  3. Standards, Guidelines & Specifications  
*David F. Maune*
  4. The National Elevation Dataset (NED)  
*Dean B. Gesch, Gayla A. Evans, Michael J. Oimoen, and Samantha T. Arundel*
  5. The 3D Elevation Program (3DEP)  
*Jason M. Stoker, Vicki Lukas, Allyson L. Jason, Diane F. Eldridge, and Larry J. Sugarbaker*
  6. Photogrammetry  
*J. Chris McGlone and Scott Arko*
  7. IfSAR  
*Scott Hensley and Lorraine Tighe*
  8. Airborne Topographic Lidar  
*Amar Nayegandhi and Joshua Nimetz*
  9. Lidar Data Processing  
*Joshua M. Novac*
  10. Airborne Lidar Bathymetry  
*Jennifer Wozencraft and Amar Nayegandhi*
  11. Sonar  
*Guy T. Noll and Douglas Lockhart*
  12. Enabling Technologies  
*Bruno M. Scherzinger, Joseph J. Hutton, and Mohamed M.R. Mostafa*
  13. DEM User Applications  
*David F. Maune*
  14. DEM User Requirements & Benefits  
*David F. Maune*
  15. Quality Assessment of Elevation Data  
*Jennifer Novac*
- Appendix A. Acronyms  
Appendix B. Definitions  
Appendix C. Sample Datasets

This book is your guide to 3D elevation technologies, products and applications. It will guide you through the inception and implementation of the U.S. Geological Survey's (USGS) 3D Elevation Program (3DEP) to provide not just bare earth DEMs, but a full suite of 3D elevation products using Quality Levels (QLs) that are standardized and consistent across the U.S. and territories. The 3DEP is based on the National Enhanced Elevation Assessment (NEEA) which evaluated 602 different mission-critical requirements for and benefits from enhanced elevation data of various QLs for 34 Federal agencies, all 50 states (with local and Tribal input), and 13 non-governmental organizations.

The NEEA documented the highest Return on Investment from QL2 lidar for the conterminous states, Hawaii and U.S. territories, and QL5 IfSAR for Alaska.

Chapters 3, 5, 8, 9, 13, 14, and 15 are "must-read" chapters for users and providers of topographic lidar data. Chapter 8 addresses linear mode, single photon and Geiger mode lidar technologies, and Chapter 10 addresses the latest in topobathymetric lidar. The remaining chapters are either relevant to all DEM technologies or address alternative technologies including photogrammetry, IfSAR, and sonar.

As demonstrated by the figures selected for the front cover of this manual, readers will recognize the editors' vision for the future – a 3D Nation that seamlessly merges topographic and bathymetric data from the tops of the mountains, beneath rivers and lakes, to the depths of the sea.

Co-Editors

David F. Maune, PhD, CP and  
Amar Nayegandhi, CP, CMS

---

## PRICING

Student (must submit copy of Student ID)	\$50 +S&H
ASPRS Member	\$80 +S&H
Non-member	\$100 +S&H
E-Book (only available in the Amazon Kindle store)	\$85

---

LEARN  
DO  
GIVE  
BELONG

**ASPRS Offers**

- » Cutting-edge conference programs
- » Professional development workshops
- » Accredited professional certifications
- » Scholarships and awards
- » Career advancing mentoring programs
- » *PE&RS*, the scientific journal of ASPRS

[asprs.org](http://asprs.org)

ASPRS